Experimental Investigation on Conventional and Non-Conventional Machining of Sintered Advanced Ceramics Using CVD Diamond Coated End Mills and Electroplated Diamond Grinding Points

by

Mohammed Alharbi

A thesis submitted to the University of Birmingham for the degree of
DOCTOR OF PHILOSOPHY

School of Mechanical Engineering
University of Birmingham
June 2023

UNIVERSITY OF
BIRMINGHAM

University of Birmingham Research Archive

e-theses repository

This unpublished thesis/dissertation is copyright of the author and/or third parties. The intellectual property rights of the author or third parties in respect of this work are as defined by The Copyright Designs and Patents Act 1988 or as modified by any successor legislation.

Any use made of information contained in this thesis/dissertation must be in accordance with that legislation and must be properly acknowledged. Further distribution or reproduction in any format is prohibited without the permission of the copyright holder.

ABSTRACT

The superior properties of advanced ceramics of ZrO_2, Al_2O_3, Si_3N_4, and SiC, such as high hardness, strength, functioning under high temperatures of up to 2500°C, wear resistance, and corrosion resistance, have made them good alternative for metallic materials. Due to better durability and functionality that could exhibit compared to metals, in several applications, such as dental implants, hip joint replacement, body armours, and break discs. However, machining advanced ceramics to its final shape with high dimension precision and without defects is a challenging process, because of their brittleness and high hardness that makes them difficult to cut. Therefore, ceramic components are often machined before sintering, but this remains challenging because sintering causes unpredictable volume shrinkage of up to 5%.

This study investigated the machinability of the four commonly used advanced ceramics, using two different tooling. The assessment criteria included the tool life, surface roughness, material removal mechanism, and cutting forces. In addition, the effect of cutting fluid was investigated, where in **phase 1**, Al_2O_3, Si_3N_4, and SiC were benchmarked against ZrO_2 using a 4-mm-diameter chemical vapor-deposited (CVD) diamond-coated (15µm thick) end mill at the following parameters: cutting speed *V*, 60 m/min; feed *fz***,** 0.5 µm/tooth; cutting depth, 0.25 mm; and cutting width, 0.5 mm. In **phase 2**, for benchmarking, 4-mm-diameter D126 diamond grinding point to machine slot was used at the following parameters: *V*, 1 m/s; *F*, 1 mm/ min; and cutting depth, 0.1 mm. Moreover, the machinability was investigated using a non-conventional machining technique: ultrasonic assisted milling/grinding that referred improving the machinability of hard materials. This study is the first to benchmark the four advanced ceramics using CVD diamond-coated end mills and diamond grinding points by conventional and non-conventional machining technique.

The findings from **phase 1** show that end milling in a wet environment increased the tool life five times. Among the four ceramics, ZrO_2 showed the best machinability, where the cutter machined for 1500 mm. For Al_2O_3, Si_3N_4, and SiC, the tool lives were 100, 40, and 10 mm, respectively. The average surface roughness Ra achieved for the four ceramics were 0.33, 0.47, 0.24, and 0.28 µm, respectively. Compared with those of the other ceramics, the resulting surface of ZrO_2 was dominated by ductile fractures. The cutting forces were proportional to the tool life, as the forces increased as the tool life decreased, where the obtained Euclidean norm *F* values of ZrO_2, Al_2O_3, Si_3N_4, and SiC were 51, 61, 96, and 118 N, respectively. Tool life was markedly improved using the ultrasonic assisted machining method. The tool life of used cutters that machined Al_2O_3, Si_3N_4, and SiC were improved by 1900%, 25%, and 900%, respectively. However, the cutter that machined ZrO_2 did not show any improvement in tool life, as it was reduced from 1500 mm to 1300 mm, because of what believed thermal softening of the cutter.

In **phase 2**, the findings show that a lower cutting speed is better for grinding ZrO_2. Also, the benchmarking showed that the grinding points markedly reduced the influence of hardness on the grinding forces. SiC, the hardest ceramic, obtained the lowest grinding force, with Euclidean norm *F* value of 31.5 N, whereas ZrO_2, Al_2O_3, and Si_3N_4 obtained *F* values of 107, 63, and 339 N, respectively. These were clearly reflected on the tool wear of the four diamond points, where the SiC cutter showed the lowest wear rate. The obtained Ra values of ZrO_2, Al_2O_3, Si_3N_4, and SiC were 0.33, 0.53, 0.16, and 0.08 µm, respectively. None of the resulting surfaces of the four ceramics were dominated by ductile fractures. However, the reduction in grinding force caused by the use of a non-conventional method (ultrasonic assisted grinding [UAG]) was noticeable. The *F* values for ZrO_2, Al_2O_3, and Si_3N_4 were reduced by 30%, 26%, and 24%, respectively. However, the *F* value for SiC was almost similar to that with the conventional method. However, grinding using the UAG method resulted in a shorter tool life.

ACKNOWLEDGEMENTS

The author thanks the following people and organisations for their help and assistance during this project:

The Ministry of Education in the Kingdom of Saudi Arabia and Umm Al-Qura University in Saudi Arabia for sponsoring the project financially.

Dr. Richard Hood, Associate Professor in the Department of Mechanical Engineering, for his guidance, support, encouragement, and supervision.

Dr. Sein Leung Soo, Reader in the Department of Mechanical Engineering, for his support and supervision.

Dr. Ali Abdelhafeez Hassan, Lecturer in the Department of Mechanical Engineering in Teesside University, for his encouragement, assistance, and advice.

The technical staff of the Department of Mechanical Engineering, especially Mr. Andy Loat for his technical support and advice.

My colleagues in the Machining Research Group, Dr. Ramy Abdallah, Rakan, Fernanda, Luis, Gib, Ming, and Mohammed, for their support and advice.

The staff of the Saudi Arabian Cultural Bureau in London for their guidance, support, and advice.

This thesis was copy edited for conventions of language, spelling and grammar by Scribendi Inc.

TABLE OF CONTENTS

LIST OF FIGURES ix

LIST OF TABLES xvii

LIST OF NOMENCLATURE xviii

1. INTRODUCTION 1

1.1 Background 1

1.2 Advanced Ceramic Production Challenge 2

1.3 Aim and Objectives of the Study 4

2. LITERATURE REVIEW 5

2.1 Theoretical Background 5

2.1.1 Definition of Ceramics 5

2.1.2 Advanced Ceramics 5

2.1.2.1 Advanced Ceramics Classification 6

2.1.2.2 Zirconia (ZrO_2) 7

2.1.2.3 Alumina (Al_2O_3) 7

2.1.2.4 Silicon Nitride (Si_3N_4) 7

2.1.2.5 Silicon Carbide (SiC) 8

2.1.3 Mechanical Properties of Ceramics 8

2.1.3.1 Fracture Toughness 9

2.1.4 Advanced Ceramic Machining 10

2.1.4.1 Conventional Material Removal Mechanism 11

2.1.4.2 UAM Mechanism 15

2.1.5 Tool Wear 16

2.1.5.1 Tool Wear Types 17

2.1.5.2 Tool Wear Mechanisms 18

2.1.5.3 Grinding Wheel Wear 19

2.2 Previous Studies 21
2.2.1 End Milling 21
2.2.2 Grinding 26
2.2.2.1 Conventional Diamond Grinding 26
2.2.2.2 Ultrasonic Assisted Grinding 34
2.3 Summary 47
3. RESEARCH METHODOLOGY 49
3.1 Materials and Tools 52
3.1.1 Workpieces 52
3.1.2 Cutting Tools 53
3.1.2.1 Phase 1, End Milling 53
3.1.2.2 Phase 2, Point Grinding 55
3.1.3 Testing Equipment 56
3.2 Measuring Procedure 60
3.2.1 Phase 1, End Milling 60
3.2.2 Phase 2, Point Grinding 61
3.3 Experimental Procedure 62
3.3.1 Phase 1, End Milling 62
3.3.1.1 Phase 1.A: Investigating the Operating Parameters for End Milling ZrO_2 62
3.3.1.2 Phase 1.B: Benchmarking Al_2O_3, Si_3N_4, and SiC against ZrO_2 64
3.3.1.3 Phase 1.C: Investigating the Operating Parameters for End Milling ZrO2 Using UAM 64
3.3.1.4 Phase 1.D: Benchmarking Al_2O_3, Si_3N_4, and SiC against ZrO_2 Using UAM in Comparison with Conventional Milling 66
3.3.2 Phase 2, Point Grinding 67
3.3.2.1 Phase 2.A: Investigating the Operating Parameters for 67

Point Grinding ZrO_2
3.3.2.2 Phase 2.B: Benchmarking Al_2O_3, Si_3N_4, and SiC against ZrO_2 68
3.3.2.3 Phase 2.C: Investigating the Operating Parameters for Point Grinding ZrO_2 Using UAG 68
3.3.2.4 Phase 2.D: Benchmarking Al_2O_3, Si_4N_3, and SiC against ZrO_2 Using the UAG Method and Comparing Conventional Point Grinding with UAG 69
3.3.3 Testing Statistics 70

4. RESULTS AND DISCUSSION: PHASE 1, END MILLING 71

4.1 The Effect of Cutting Fluid on Tool Life 71
4.2 Phase 1.A: Investigating the Operating Parameters for End Milling ZrO_2 72
4.3 Phase 1.B: Benchmarking Al_2O_3, Si_3N_4, and SiC against ZrO_2 79
4.4 Phase 1.C: Investigating the Operating Parameters for End Milling ZrO_2 Using UAM 89
4.5 Phase 1.D: Benchmarking Al_2O_3, Si_3N_4, and SiC against ZrO_2 Using UAM in Comparison with Conventional Milling 96
4.6 Summary of Results 107

5. RESULTS AND DISCUSSION: PHASE 2, POINT GRINDING 108

5.1 Phase 2.A: Investigating the Operating Parameters for Point Grinding ZrO_2 108
5.2 Phase 2.B: Benchmarking Al_2O_3, Si_3N_4, and SiC against ZrO_2 113

5.3 Phase 2.C: Investigating the Operating Parameters for Point Grinding ZrO_2 Using Ultrasonic Assisted Grinding 121

5.4 Phase 2.D: Benchmarking Al_2O_3, Si_4N_3, and SiC against ZrO_2 Using UAG and Comparing Conventional Point Grinding with UAG 127

4.6 Summary of Results 136

6. CONCLUSIONS 137

7. SUGGESTIONS FOR FUTURE WORK 141

8. REFERENCES 142

APPENDICES 146

APPENDIX A: Additional Experimental Results 146

A.1 Phase 1, End Milling 146

A.2 Phase 2, Point Grinding 158

LIST OF FIGURES

Figure 1.1	Advanced ceramic products [1]	1
Figure 2.1	Ceramics classification [11]	7
Figure 2.2	Classical loading modes of crack faces [18]	9
Figure 2.3	Chip formation mechanism in cutting and grinding of ductile material [26]	12
Figure 2.4	Chip formation mechanism in brittle material cutting [27]	12
Figure 2.5	Patterns of the growth of two cracks in a brittle material under a concentrated load: radial-median (R) and lateral (L) [18]	14
Figure 2.6	Chip formation in a brittle material [18]	14
Figure 2.7	Comparison between USM and UAM [28]	15
Figure 2.8	Material removal mechanism by UAM **[**29**]**	16
Figure 2.9	Tool wear types [32]	18
Figure 2.10	Grinding wheel micro-topography changes during grinding [26]	20
Figure 2.11	Grinding wheel wear curve [36]	21
Figure 2.12	Illustration of (a) end mill geometry, (b) cutting edge radius, (c) tool side view, (d) tool before coating, (e) tool after diamond coating [46]	23
Figure 2.13	CVD diamond-coated end mill [47]	24
Figure 2.14	Tool wear area at a speed of 4000 rpm and feed rates of (a) 11 mm/min and (b) 21 mm/min [47]	25
Figure 2.15	Normal grinding force of the ceramics according to grinding speed [49]	27
Figure 2.16	Surface roughness of the ceramics according to grinding speed [49]	27
Figure 2.17	ZrO_2 ground surface at speeds of (a) 40 m/s, (b) 80 m/s, (c)120 m/s, and (d) 160 m/s [49]	28
Figure 2.18	SiC ground surface at speeds of (a) 40 m/s, (b) 80 m/s, (c)120 m/s, and (d) 160 m/s [49]	28
Figure 2.19	Al_2O_3 ground surface at speeds of (a) 40 m/s, (b) 80 m/s, (c)120 m/s, and (d) 160 m/s [49]	29
Figure 2.20	Si_3N_4 ground surface at speeds of (a) 40 m/s, (b) 80 m/s, (c)120 m/s, and (d) 160 m/s [49]	29

Figure 2.21	Normal grinding forces according to wheel speed [50]	30
Figure 2.22	Surface roughness according to wheel speed [50]	31
Figure 2.23	Ground surfaces of different ceramics at different wheel speeds (grit size of 35/35, cutting depth of 40 µm, and feed rate of 3 m/min) [50]	31
Figure 2.24	Ground surfaces of different ceramics at different wheel speeds (grit size of 50/60, cutting depth of 40 µm, and feed rate of 3 m/min) [50]	32
Figure 2.25	Conical abrasive tool [28]	35
Figure 2.26	Main effects on the cutting forces [27]	37
Figure 2.27	Main effects on the surface roughness [27]	37
Figure 2.28	Main effects on MRR [27]	38
Figure 2.29	UAG setup of K9 optical glass machining [30]	38
Figure 2.30	Effects of the variable parameters, (a) feed, (b) speed, and (c) cutting depth, on the cutting forces in conventional diamond milling compared with UAG at a cutting depth range of A = <10 µm [30]	39
Figure 2.31	Tool wear in experiment 1, obtained with (a) UAG and (b) conventional milling [30]	40
Figure 2.32	Effects of the variable parameters, (a) feed, (b) speed, and (c) cutting depth, on the cutting forces in conventional diamond milling compared with UAG at cutting depth range of A = >10 µm [30] with conventional cooling [58]	41
Figure 2.33	Cutting tool [63]	43
Figure 2.34	Experiment setup [64]	44
Figure 2.35	End face of (a) a new tool and (b) a worn tool after a dimensional error of 5% was reached [64]	45
Figure 2.36	SEM image of the machined pockets at tool overlapping percentages of (a) 0%, (b) 10%, and (c) 20% [64]	45
Figure 3.1	Project workflow	51
Figure 3.2	Sintered advanced ceramics used in the project	52
Figure 3.3	CVD diamond-coated end mill images (grind, end, and side view)	54
Figure 3.4	Thickness measurement of the CVD diamond coating	55
Figure 3.5	Electroplated diamond grinding point of D126 grit size: side and end views	56
Figure 3.6	Five-axis DMG Ultrasonic 20 Linear	57

Figure 3.7	Three-axis Matsuura FX-5 CNC machine	58
Figure 3.8	Microscopes used: (a) Alicona Infinite Focus microscope and (b) optical microscope for tool wear observation (c) Keyence digital microscope	59
Figure 3.9	The surface roughness measurement variation between Alicona and stylus profilometer of Si3N4 sample that end milled at V=60 m/min, fz=0.5 µm/tooth, DOC=0.25 mm, and WOC=0.5 mm	59
Figure 3.10	Example of one measurement of peak-to-peak value of approximately 38 N	61
Figure 3.11	Schematic illustrating the milling process in (a) slot milling (tests 1 and 3) and (b) side milling (tests 2 and 4), (phase 1.A)	63
Figure 3.12	Experimental setup (phase 1.A)	63
Figure 3.13	Illustration of (a) experimental setup, (b) machining process (phase 1.B)	64
Figure 3.14	Illustration of (a) experiment setup, (b) Ultrasonic Assisted Milling (phase1.C)	66
Figure 3.15	Illustration of (a) experimental setup, (b) machining process (phase 2.A)	68
Figure 3.16	Illustration of (a) experimental setup, (b) Ultrasonic Assisted Grinding (phase 2.C)	69
Figure 4.1	Tool wear in ball-nose end mills of (a) VB > 0.3 mm in a dry environment after cutting 20 mm and (b) VB of 0.016 mm in a wet environment after cutting 50 mm	72
Figure 4.2	Tool flank wear according to cutting length (phase 1.A)	74
Figure 4.3	Tool flank wear according to cutting time (phase 1.A)	74
Figure 4.4	Illustration of engagement angles for test 2 & 4	75
Figure 4.5	Tool flank wear of Test 1 after cutting 10 mm at V = 60 m/min, f z= 0.5 µm/tooth, WOC = 4 mm, and DOC = 0.12 mm (phase 1.A)	76
Figure 4.6	Tool flank wear of Test 2 after cutting 80 mm at V = 60 m/min, f z= 0.5 µm/tooth, WOC = 0.5 mm, and DOC = 0.25 mm (phase 1.A)	77
Figure 4.7	Tool flank wear of Test 3 after cutting 30 mm at V = 60 m/min, f z= 0.5 µm/tooth, WOC = 4 mm, and DOC = 0.06 mm (phase 1.A)	77
Figure 4.8	Tool flank wear of Test 4 after cutting 1800 mm at V = 60 m/min, f z= 0.5 µm/tooth, WOC = 0.5 mm, and DOC = 0.25 mm (phase 1.A)	78
Figure 4.9	Average surface roughness Ra of ZrO_2 obtained under conventional	79

machining conditions (phase 1.A)

Figure 4.10 Tool flank wear according to cutting length & time (phase 1.B) 80

Figure 4.11 Tool flank wear of the cutter of ZrO_2 after cutting 1500 mm at V = 60 m/min, f z= 0.5 µm/tooth, WOC = 0.5 mm, and DOC = 0.25 mm (phase 1.B) 82

Figure 4.12 Tool flank wear of the cutter of Al_2O_3 after cutting 100 mm at V = 60 m/min, f z= 0.5 µm/tooth, WOC = 0.5 mm, and DOC = 0.25 mm (phase 1. B 83

Figure 4.13 Tool flank wear of the cutter of Si_3N_4 after cutting 40 mm at V = 60 m/min, f z= 0.5 µm/tooth, WOC = 0.5 mm, and DOC = 0.25 mm (phase 1.B) 83

Figure 4.14 Tool flank wear of the cutter of SiC after cutting 10 mm at V = 60 m/min, f z= 0.5 µm/tooth, WOC = 0.5 mm, and DOC = 0.25 mm (phase 1.B) 84

Figure 4.15 Tool wear at the cutting edge of the cutters of (a) ZrO_2, (b) Al_2O_3, (c) Si_3N_4, (d) SiC by conventional machining (phase 1.B) 84

Figure 4.16 Average surface roughness Ra of ZrO_2, Al_2O_3, Si_3N_4, and SiC obtained by conventional milling (phase 1.B) 85

Figure 4.17 Microscopic images of the machined surfaces of (a) ZrO_2, (b) Al_2O_3, (c) Si_3N_4, and (d) SiC (phase 1.B) 87

Figure 4.18 Average maximum absolute peak-to-peak cutting forces of the conventionally machined ZrO_2, Al_2O_3, Si_3N_4, and SiC (phase 1.B) 89

Figure 4.19 Tool flank wear according to cutting length & time (phase 1.C) 90

Figure 4.20 Tool flank wear of the cutter with low US amplitude (0.5–2 µm) after cutting 1200 mm (phase 1.C) 92

Figure 4.21 Tool flank wear of the cutter with a high US amplitude (2–4 µm) after cutting 150 mm (phase 1.C) 92

Figure 4.22 Average surface roughness Ra at the conventional, low, and high US amplitudes obtained with ZrO_2 machining by UAM (phase 1.C) 93

Figure 4.23 Microscopic images of ZrO_2 surfaces machined by (a) conventional milling (vibration amplitude = 0 µm), (b) a cutter with low US vibration amplitude (0.5 –2 µm), and (c) a cutter with high US vibration amplitude (2–4 µm), (phase 1.C) 94

Figure 4.24 Average maximum absolute peak-to-peak cutting forces of the 95

	conventional, low-amplitude US, and high-amplitude US machining of ZrO_2 (phase 1.C)	
Figure 4.25	Tool flank wear trends according to the cutting length & time of ZrO_2, Al_2O_3, Si_3N_4, and SiC by UAM (phase 1.D)	96
Figure 4.26	Tool flank wear trends according to the cutting length & time of ZrO_2, Al_2O_3, Si_3N_4, and SiC by conventional machining and UAM (phase 1.D)	98
Figure 4.27	Tool flank wear of the cutter of Al_2O_3 at US amplitudes of 0.5–2 µm after cutting 2000 mm (phase 1.D)	99
Figure 4.28	Tool flank wear of the cutter of Si_3N_4 at US amplitudes of 0.5–2 µm after cutting 50 mm (phase 1.D)	100
Figure 4.29	Tool flank wear of the cutter of SiC at US amplitudes of 0.5–2 µm after cutting 100 mm (phase 1.D)	100
Figur 4.30	Tool wear at the cutting edge of the cutters of (a) ZrO_2, (b) Al_2O_3, (c) Si_3N_4, (d) SiC by UAM **(**phase 1.D)	101
Figur 4.31	Average surface roughness Ra values of ZrO_2, Al_2O_3, Si_3N_4, and SiC obtained using conventional machining and UAM (phase 1.D)	102
Figur 4.32	Microscopic images of surfaces machined using UAM at US amplitudes of 0.5–2 µm: (a) ZrO_2, (b) Al_2O_3, (c) Si_3N_4, and (d) SiC (phase 1.D)	103
Figure 4.33	Average maximum absolute peak-to-peak cutting forces of ZrO_2, Al_2O_3, Si_3N_4, and SiC using conventional machining and UAM (phase 1.D)	104
Figure 5.1	Tool wear at a speed of 5 m/s and feed rate of 5 mm/min after grinding for 20 mm (phase 2.A)	109
Figure 5.2	Tool wear at a speed of 1 m/s and feed rate of 1 mm/min after grinding for 100 mm (phase 2.A)	110
Figure 5.3	Average surface roughness Ra of ZrO_2 obtained using conventional point grinding at a high-speed V = 5 m/s and low speed V = 1 m/s (phase 2.A)	111
Figure 5.4	Microscopic images of the ZrO_2 surfaces machined by the grinding point at (a) V = 5 m/s and feed rate = 5 mm/min, and (b) V = 1 m/s and feed rate = 1 m/s (phase 2.A)	112
Figure 5.5	Average maximum absolute peak-to-peak grinding forces of conventional point grinding of ZrO_2 at a high speed of V = 5 m/s and low speed of V = 1 m/s (phase 2.A)	113

Figure 5.6	Tool wear of the Al_2O_3 grinding point after grinding 100 mm (phase 2.B)	115
Figure 5.7	Tool wear of the Si_3N_4 grinding point after grinding 100 mm (phase 2.B)	116
Figure 5.8	Tool wear of the SiC grinding point after grinding 100 mm (phase 2.B)	117
Figure 5.9	Average surface roughness Ra of ZrO_2, Al_2O_3, Si_3N_4, and SiC machined using conventional grinding points (phase 2.B)	118
Figure 5.10	Microscopic images of (a) ZrO_2, (b) Al_2O_3, (c) Si_3N_4, and (d) SiC ground using conventional grinding points at V = 1 m/s and F = 1 mm/min (phase 2.B)	119
Figure 5.11	Average maximum absolute peak-to-peak grinding forces of conventional point grinding of ZrO_2, Al_2O_3, Si_3N_4, and SiC at V = 5 m/s and V = 1 m/s (phase 2.B)	120
Figure 5.12	Side view of the utilised grinding point showing the effects of the geometry of the grains on material removal (phase 2.B)	121
Figure 5.13	Tool wear of the ZrO_2 grinding point after grinding 100 mm at high US amplitudes of 5–6 µm, V = 1 m/s, and F = 1 mm/min (phase 2.C)	123
Figure 5.14	Tool wear of the ZrO_2 grinding point after grinding 100 mm at low US amplitudes of 1–2 µm, V = 1 m/s, and F = 1 mm/min (phase 2.C)	124
Figure 5.15	Average surface roughness Ra of ZrO_2 obtained using UAG at high and low US amplitudes of 5–6 µm and 1–2 µm, respectively (phase 2.C)	125
Figure 5.16	Microscopic images of ZrO_2 ground using UAG at (a) high US amplitudes of 5–6 µm and (b) low US amplitude of 1–2 µm (phase 2.C)	126
Figure 5.17	Average maximum absolute peak-to-peak grinding forces of UAG for ZrO_2 using a grinding point at high and low US amplitudes of 5–6 µm and 1–2 µm, respectively (phase 2.C)	127
Figure 5.18	Tool wear of the Al_2O_3 grinding point after grinding 100 mm at US amplitudes of 1–2 µm, V = 1 m/s, and F = 1 mm/min (phase 2.D)	129
Figure 5.19	Tool wear of Si_3N_4 grinding point after grinding for 100 mm, at US amplitude of (1-2) µm, V= 1 m/s, and F= 1 mm/min (phase 2.D)	130
Figure 5.20	Tool wear of the SiC grinding point after grinding 100 mm at US amplitudes of 1–2 µm, V = 1 m/s, and F = 1 mm/min (phase 2.D)	131
Figure 5.21	Average surface roughness Ra of ZrO_2, Al_2O_3, Si_3N_4, and SiC machined using the conventional grinding points and UAG (phase 2.D)	132

Figure 5.22	Microscopic images of the surfaces machined using UAG at US amplitudes of 1–2 µm: (a) ZrO_2, (b) Al_2O_3, (c) Si_3N_4, and (d) SiC (phase 2.D)	133
Figure 5.23	Average maximum absolute peak-to-peak grinding forces of ZrO_2, Al_2O_3, Si_3N_4, and SiC obtained using conventional grinding points and UAG (phase 2.D)	134
Figure A1	Cutting force signal of ZrO_2 in X axis F_X (end milling)	146
Figure A2	Cutting force signal of ZrO_2 in Y axis F_Y (end milling)	146
Figure A3	Cutting force signal of ZrO_2 in Z axis F_Z (end milling)	147
Figure A4	Cutting force signal of Al_2O_3 in X axis F_X (end milling)	147
Figure A5	Cutting force signal of Al_2O_3 in Y axis F_Y (end milling)	148
Figure A6	Cutting force signal of Al_2O_3 in Z axis F_Z (end milling)	148
Figure A7	Cutting force signal of Si_3N_4 in X axis F_X (end milling)	149
Figure A8	Cutting force signal of Si_3N_4 in Y axis F_Y (end milling)	149
Figure A9	Cutting force signal of Si_3N_4 in Z axis F_Z (end milling)	150
Figure A10	Cutting force signal of SiC in X axis F_X (end milling)	150
Figure A11	Cutting force signal of SiC in Y axis F_Y (end milling)	151
Figure A12	Cutting force signal of SiC in Z axis F_Z (end milling)	151
Figure A13	Cutting force signal of ZrO_2 in X axis F_X (UAM)	152
Figure A14	Cutting force signal of ZrO_2 in Y axis F_Y (UAM)	152
Figure A15	Cutting force signal of ZrO_2 in Z axis F_Z (UAM)	153
Figure A16	Cutting force signal of Al_2O_3 in X axis F_X (UAM)	153
Figure A17	Cutting force signal of Al_2O_3 in Y axis F_Y (UAM)	154
Figure A18	Cutting force signal of Al_2O_3 in Z axis F_Z (UAM)	154
Figure A19	Cutting force signal of Si_3N_4 in X axis F_X (UAM)	155
Figure A20	Cutting force signal of Si_3N_4 in Y axis F_Y (UAM)	155
Figure A21	Cutting force signal of Si_3N_4 in Z axis F_Z (UAM)	156
Figure A22	Cutting force signal of SiC in X axis F_X (UAM)	156
Figure A23	Cutting force signal of SiC in Y axis F_Y (UAM)	157
Figure A24	Cutting force signal of SiC in Z axis F_Z (UAM)	157
Figure A25	Cutting force signal of ZrO_2 in X axis F_X (point grinding)	158
Figure A26	Cutting force signal of ZrO_2 in Y axis F_Y (point grinding)	158
Figure A27	Cutting force signal of ZrO_2 in Z axis F_Z (point grinding)	159

Figure A28 Cutting force signal of Al_2O_3 in X axis F_X (point grinding) 159
Figure A29 Cutting force signal of Al_2O_3 in Y axis F_Y (point grinding) 160
Figure A30 Cutting force signal of Al_2O_3 in Z axis F_Z (point grinding) 160
Figure A31 Cutting force signal of Si_3N_4 in X axis F_X (point grinding) 161
Figure A32 Cutting force signal of Si_3N_4 in Y axis F_Y (point grinding) 161
Figure A33 Cutting force signal of Si_3N_4 in Z axis F_Z (point grinding) 162
Figure A34 Cutting force signal of SiC in X axis F_X (point grinding) 162
Figure A35 Cutting force signal of SiC in Y axis F_Y (point grinding) 163
Figure A36 Cutting force signal of SiC in Z axis F_Z (point grinding) 163
Figure A37 Cutting force signal of ZrO_2 in X axis F_X (UAG) 164
Figure A38 Cutting force signal of ZrO_2 in Y axis F_Y (UAG) 164
Figure A39 Cutting force signal of ZrO_2 in Z axis F_Z (UAG) 165
Figure A40 Cutting force signal of Al_2O_3 in X axis F_X (UAG) 165
Figure A41 Cutting force signal of Al_2O_3 in Y axis F_Y (UAG) 166
Figure A42 Cutting force signal of Al_2O_3 in Z axis F_Z (UAG) 166
Figure A43 Cutting force signal of Si_3N_4 in X axis F_X (UAG) 167
Figure A44 Cutting force signal of Si_3N_4 in Y axis F_Y (UAG) 167
Figure A45 Cutting force signal of Si_3N_4 in Z axis F_Z (UAG) 168
Figure A46 Cutting force signal of SiC in X axis F_X (UAG) 168
Figure A47 Cutting force signal of SiC in Y axis F_Y (UAG) 169
Figure A48 Cutting force signal of SiC in Z axis F_Z (UAG) 169

LIST OF TABLES

Table 2.1	Fracture Toughness of advanced ceramics [19]	10
Table 2.2	Grinding parameter levels [50]	30
Table 2.3	Machining parameters levels [28]	35
Table 2.4	Experiment 1 parameters [30]	39
Table 2.5	Experiment 2 parameters [30]	41
Table 2.6	Machining parameters levels [62]	42
Table 2.7	Machining parameters levels [63]	43
Table 3.1	The properties of the experimental ceramics with stainless steel 316	53
Table 3.2	CVD diamond-coated end mill specifications	54
Table 3.3	Technical data of DMG Ultrasonic 20 Linear	57
Table 3.4	Machining parameter sets at cutting speed of 60 m/min (4777 rpm), (phase1.A)	62
Table 3.5	Amplitude levels at a resonance frequency of 33.5 kHz (phase 1.C)	65
Table 3.6	Machining parameters (phase 2.A)	67
Table 3.7	Amplitude levels at a resonance frequency of 29 kHz (phase 2.C)	69
Table 3.8	Summary of project's testing number	70
Table 4.1	Summary of the technical results of Phase 1	107
Table 5.1	Summary of the technical results of Phase 2	136

LIST OF NOMENCLATURE

Al_2O_3	Alumina
AWJ	Abrasive water jet
a_0	Interatomic spacing
C^o	Celsius
C	Crack length
CBN	Cubic boron nitride
Cl	Lateral crack length
CNC	Computer numerical control
CVD	Chemical vapor deposition diamond
DOC	Depth of cut
EDM	Electrical discharge machining
F	Feed rate
f	Feed per revolution
HPSN	Hot pressed silicon nitride
HSM	High-speed machining
K	Stress intensity factor
L	Cutting length
l	Liter
LAM	Laser assisted milling
LBM	Laser beam machining
m	Meter
min	Minute
mm	Millimeter
MRR	Material removal rate
N	Newton
n	Rotational speed
nm	Nano meter
P	Load of indentation
PCD	Polycrystalline diamond
PVD	Physical vapor deposition

Q	Flow rate
Ra	The average roughness of a surface
rpm	Revolution per minutes
RUM	Rotary ultrasonic machining
s	Second
SEM	Scanning electron microscopy
Si	Silicon
SiC	Silicon carbide
Si_3N_4	Silicon nitride
tc	Critical depth of cut
UAG	Ultrasonic assisted grinding
UAM	Ultrasonic assisted machining
USM	Ultrasonic machining
V	Cutting speed
VB	Flank wear width
vol.	Volume
WOC	Width of cut
ZrO_2	Zirconia
µm	Micro meter
ρ	Crack tip radius
σ	Tensile stress

1. INTRODUCTION

1.1 Background: Ceramic materials are inorganic, non-metallic composites containing mostly crystalline that have been used for thousands of years since mankind found that clay can be used to form objects after mixing with water and fired. The research and development over the past decade in the field of ceramic manufacturing have resulted in the production of high-performance or advanced ceramics. Nowadays, advanced ceramics are used in many sectors of modern industries, as shown in **Figure 1.1**. They are good substitutes for metallic materials and super alloys owing to their competitive mechanical and chemical properties.



Figure 1.1 Advanced ceramic products [1]

Ceramics have a wide spectrum of properties, but their most common characteristics are high hardness, brittleness, and resistance to deformation. In addition, they are chemically stable materials that can resist corrosion and oxidation. They have long-term durability, high strength in terms of compressive load, high stiffness, and high wear resistance. They are non-magnetic,

electrically and thermally insulating, light-weight, and refractory. Their melting points are high, allowing them to perform and functioning well at elevated temperatures of up to 2500°C.

Owing to the superior characteristics of advanced ceramics, they are at the top of the list of needed materials for modern industries, because of the good durability and functionality that exhibit comparing to metallic materials, such as the following [1]:

- aerospace (jet engine igniters, radomes of missiles, hydraulic wear components, and thermal protection shield)
- nuclear (waste containment and bearing)
- military (body armour, vehicle armour, and ballistic transparent ceramics)
- automotive (tire pressure sensors, engine O_2 sensors, turbocharger impeller, break discs, lining, valves, and pistons)
- semiconductors
- heat exchanger
- medical (hip replacement, dental implants, digital hearing aid, and cardiac valves)
- industrial ware product
- oil industry (pipes and nozzles)
- renewable energy (solar cells, fuel cells, and battery membrane)
- refractories (furnace parts, insulators, crucibles, and rocket lining)

1.2 Advanced Ceramic Production Challenge

The process of manufacturing advanced ceramic products starts from compacting refined powder, followed by pre-sintering machining, sintering, and finally, machining using abrasive diamond tooling [2]. The final stage of machining could include grinding, polishing, milling, and drilling, depending on what the product needs. The big challenge for advanced ceramic production is the high cost of machining, which can reach up to 50% of the overall production cost [3]. The difficulty of machining hard to cut materials increases machining cost by reducing MRR, also

reducing in tool life due to higher forces that needed to form chips which means higher number of consumed tools, and by using expensive tool that contained diamond to resist the abrasive nature of hard materials. Especially when conventional methods such as grinding, milling, turning, and drilling are applied, which results in the chipping of edges, cracks, and brittle fractures. Thus, these surface defects are responsible for the poor surface integrity of advanced ceramic products, which limits MRR during the processing, that is, the mass production rate of advanced ceramics. However, some studies have indicated that the use of newly developed tools could improve the MRR without affecting the surface quality [4-6]. By improving the tool resistance toward hardness and wear, since cutting forces increases as MRR increases, and the tool wear increases as cutting forces increases, and surface quality decreases as tool wear rate increases thus cutting with tool that exhibiting higher wear resistance it will allow help to cut at higher MRR with good surface quality.

In recent years, besides the conventional machining methods, non-conventional methods such as electrical discharge machining (EDM), abrasive water jet (AWJ), ultrasonic machining (USM), ultrasonic assisted milling (UAM), ultrasonic assisted grinding (UAG), laser-assisted milling (LAM), electron beam machining, ion beam machining, electrochemical machining have been used extensively for advanced ceramic machining. These methods exhibit good improvements in terms of MRR. However, these methods have not yet reached the desired economical level for mass production. Therefore, further investigation and studies are needed to improve them [7]. Studies have benchmarked different numbers of ceramics because advanced ceramics differ in performance and properties, each one having its own unique properties that result in a different performance with every machining method.

1.3 Aim and Objectives of the Study

The aim of this study was to evaluate the machinability of advanced ceramics commonly used in industrial applications and commercial products. The focus of this study was on advanced ceramics, including zirconia (ZrO_2), alumina (Al_2O_3), silicon nitride (Si_3N_4), and silicon carbide (SiC). The study involved the use of conventional coated solid carbide and abrasive grinding tools with a small diameter of 4.00 mm. In addition, a phase of this work was aimed at investigating the effect of using non-conventional methods of UAM and UAG the machinability. Because it has stated that using ultrasonic assisted machining has improved the machinability of some hard to cut materials [7]. Also, UAM/UAG produces no thermal damage on ceramic workpieces with relatively high MRR and dimensional accuracy, making it a suitable machining method. To achieve the goal of this study, the following objectives were set:

1. Conduct a literature review to establish the current state of the art for research on the machinability of advanced ceramics.

2. Investigate the machining parameters for the use of diamond-coated end mills on ZrO_2 with a 4-mm-diameter tool. And benchmark Al_2O_3, Si_3N_4, and SiC against ZrO_2 for the use of diamond-coated end mills conventionally. The assessment criteria included tool wear, surface roughness, material removal mechanism, and cutting forces.

3. Investigate the effect of using electroplated diamond grinding points with a small diameter (4 mm) on ZrO_2 at a relatively high cutting speed. And benchmark Al_2O_3, Si_3N_4, and SiC against ZrO_2 for the use of diamond grinding points conventionally. The assessment criteria include tool wear, surface roughness, material removal mechanism, and cutting forces.

4. Investigate the improvements that can be achieved using non-conventional methods of UAM and UAG.

2. LITERATURE REVIEW

2.1 Theoretical Background

2.1.1 Definition of Ceramics

Ceramics are an important material group. They belong to one of the three super groups of materials other than metals and polymers [8]. The word *ceramics* originated from the Greek word *keramicos*, which means burnt stuff. According to the American Ceramic Society's Ceramic Glossary [9], ceramics would be defined scientifically as:

> "Ceramic sing., n.; ceramics pl. n. (1) a general term applied to the art or technique of producing articles by a ceramic process, or to the articles so produced. C-242 (2) any of a class of inorganic, non-metallic products which are subjected to a high temperature during manufacture or use. (High temperature usually means a temperature above a barely visible red, approximately 540°C (1000°F)). Typically, but not exclusively, a ceramic is a metallic oxide, boride, carbide, or nitride, or a mixture or compound of such materials; that is, it includes anions that play important roles in atomic structures and properties". (pp. 13-14)

2.1.2 Advanced Ceramics

The ceramic group has a wide range of compounds and components with widely varied characteristics, applications, and processing. Thus, a detailed and specific definition of advanced ceramics is needed to distinguish them from other compounds. According to the Versailles Project on Advanced Materials and Standards (VAMAS) [10], advanced ceramics should be defined as follows:

> "An inorganic, non-metallic (ceramic), basically crystalline material of rigorously controlled composition and manufactured with detailed regulation from highly refined and/or characterised raw materials giving precisely specified attributes"

The given definition reveals the following characteristics of ceramics:

- They have a crystalline microstructure, which means that they have no glassy (amorphous) components.
- The characteristics of their compositions and microstructures, such as porosity, grain size, and phase, are highly engineered and controlled.

- Their manufacturing processes require highly regulated clean conditions.
- Their manufacturing processes require the use of highly refined, pure synthetic materials rather than naturally occurring materials such as quartz sand and clay.
- Their superior properties are obtained from good quality-controlled processes and are required for specific, precise applications.

2.1.2.1 Advanced Ceramics Classification

Depending on their chemical compositions, advanced ceramics are divided into two main types: **non-silicate oxides** i.e. (ZrO_2 and Al_2O_3) and **non-oxides** i.e. (Si_3N_4 and SiC), as shown in **Figure 2.1**. The molecules in ceramics are unlike those in metals, as they have more complicated and larger structures held together by ionic, covalent, or mixed bonding. Most ceramic structures are bonded together by a mixed bonding mechanism but with different ratios, of which the bond component is more dominant. The ratio of covalent to ionic bonding is approximately 4:6 in oxides i.e. (ZrO_2 and Al_2O_3) and 9:1 in non-oxides i.e. (Si_3N_4 and SiC). The difference in electronegativity between the compound elements is mainly responsible for the ratio of dominancy. The dominance of covalent bonding is the main factor responsible for the higher hardness and melting point of non-oxide ceramic structures than those of oxide ceramics.

In metallic bonding, a free covalent electron is responsible for thermal/electrical conductivity. Ionic and covalent bonding do not have this free electron. Therefore, ceramics exhibit low thermal/electrical conductivity. In addition, the strength of this bonding is responsible for the high hardness and brittleness of ceramics, as it restricts the dislocation motion in the ceramic crystal system.

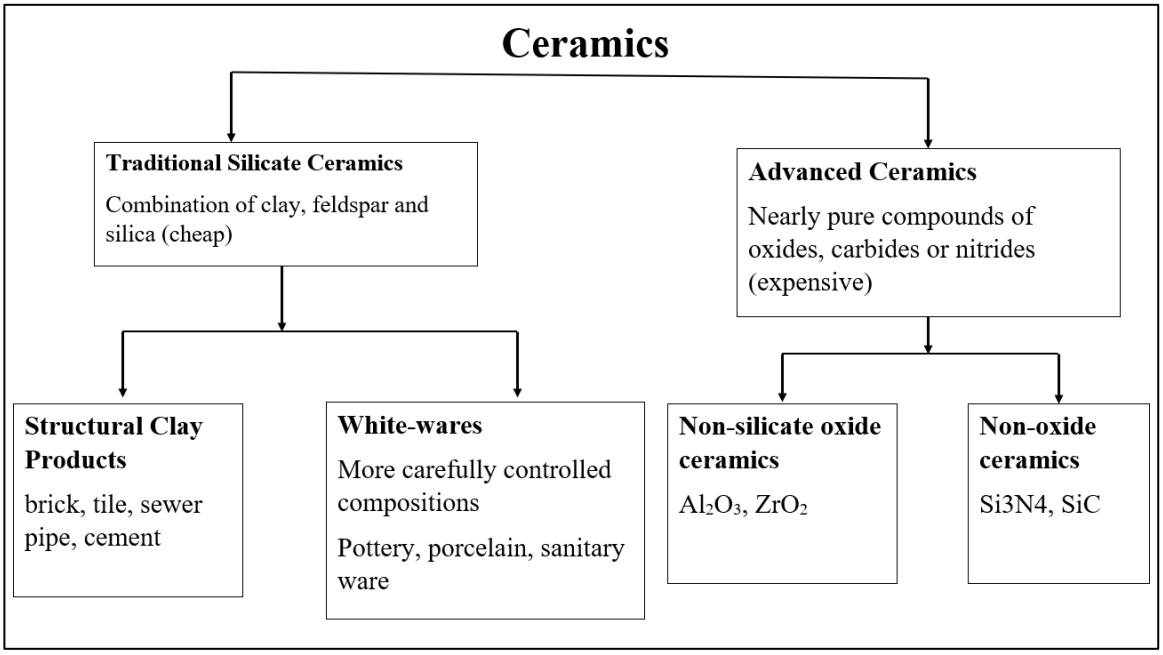


Figure 2.1 Ceramics classification [11]

2.1.2.2 Zirconia (ZrO_2)

Zirconia-based ceramics have been developed over the past decade and used in so many important applications owing to their unique properties, one of which is transformation toughening, which increases their toughness and strength. This transformation affects only the crystal structure, without any changes in the chemical composition [12].

2.1.2.3 Alumina (Al_2O_3)

Aluminium oxide is considered one of the most commonly used synthetic raw materials in ceramic production. Owing to its wide range of good chemical, mechanical, electrical, and thermal properties, it can be used in cutting tools, integrated circuits, and furnaces. Al_2O_3 is produced from bauxite using Bayer's method [8].

2.1.2.4 Silicon Nitride (Si_3N_4)

Since silicon nitride was developed, it has become a target for research and investigation over the last few decades. This is a result of the new challenges that emerged from newly developed

technologies such as gas turbines that require materials that can stand elevated temperatures and have good mechanical and chemical properties [14]. In 1955, the first Si_3N_4 was developed [15] for use in the manufacturing of rocket nozzles, crucibles, and thermocouple tubes.

Hot-Pressed Silicon Nitride

This process depends on the pressure used during heating to produce products with simple shapes. The limitation of this process is the relatively expensive machining that follows pressing [16].

2.1.2.5 Silicon Carbide (SiC)

Silicon carbide is a ceramic compound composed of 50% C and 50% Si, which can be found in nature as SiC but in small amounts and rare geographical locations. The bonding type in the SiC compound is mixed: approximately 12% ionic and 88% covalent. Therefore, it exhibits more hardness and is more refractory than other ceramics, which makes it useful in a wide range of applications [17].

2.1.3 Mechanical Properties of Ceramics

Generally, ceramics are known by their high brittleness, low fracture toughness, high Young's modulus, high hardness, and high compressive strength. However, two important elements, which are fracture mechanism and toughness, must be fully understood and investigated in studying the mechanical properties of ceramic materials. They are important in evaluating the performance of ceramics used in various applications. Also, the brittleness or low fracture toughness of ceramics limit the exploitation of their high strength because once a fracture starts, it cannot be stopped. A fracture develops in an almost instantaneous process, without any indication of when, where, or on what condition it will occur [18].

2.1.3.1 Fracture Toughness

Crack length and applied stress are the parameters that determine brittle fractures in ceramics. Therefore, the stress intensity factor can be determined as:

$$K = Y\sigma\sqrt{\pi c} \qquad 2.1$$

Where; $\boldsymbol{\sigma}$ the applied stress, ***C*** crack length, and ***Y*** dependent on the orientation and location of the crack during loading. In **Figure 2.2**, three loading modes of crack faces are shown. **Mode I** is the opening mode; **mode II**, the sliding mode; and **mode III**, the tearing mode. These modes have their own stress intensity factors: ***K* I**, ***K* II**, and ***K* III**, respectively. The most critical loading mode responsible for most ceramic fractures is the opening or tensile mode. Thus, the stress intensity equation that describes the ceramic fracture toughness can be expressed as:

$$K = Y\sigma c\sqrt{\pi c} \qquad 2.2$$

where the ***Y*** value ranges from 1 to 1.1 [18].

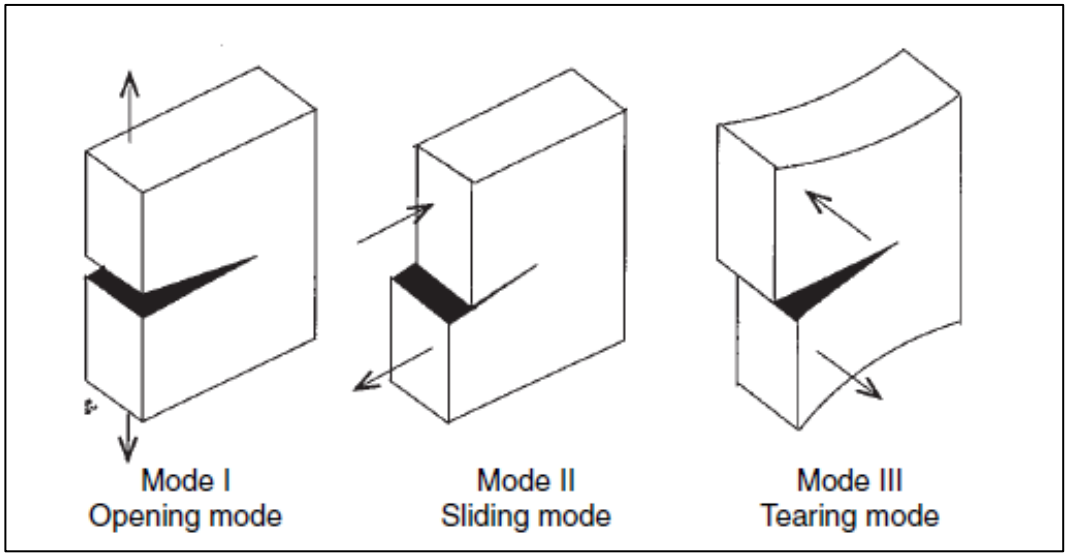


Figure 2.2 Classical loading modes of crack faces [18]

Table 2.1 lists the stress intensity factors for the four main advanced ceramics and diamond. Al_2O_3 and SiC clearly show lower fracture toughness (2.5 to 4.5 MPam½) than ZrO_2 and Si_3N_4 (5 to 9 MPam½). The material microstructure features such as grain size/shape and crystal type/phase significantly affect the fracture toughness. Therefore, a well-controlled microstructure design of ceramics could improve fracture toughness, especially in multi-component ceramics [19].

Table 2.1 Fracture Toughness of advanced ceramics [19]

Materials	**Fracture Toughness KIc (MPam½)**
Diamond	9–10
Zirconia Mg-PSZ	6–9
Alumina Al_2O_3	2.5–4.5
Silicon Nitride HPSN	5–8
Silicon Carbide SiC	2.5–4.0

2.1.4 Advanced Ceramic Machining

The machining of ceramic products to their final shapes with high dimension precision and without surface defects is a time- and labour-consuming and thus expensive process. Therefore, ceramic products are sometimes machined before sintering to induce shrinkage of the product size by approximately 3-5%, as the product at this stage has high MRR and could reach its minimum dimension tolerance before sintering. Usually, during the pre-sintered stage, conventional machining is applied either by using high-speed steel and coated tungsten carbide tools for milling or diamond grinding wheel for grinding [20-23].

In the post-sintered stage, abrasive diamond grinding is the most common machining method used for the surface finishing of ceramic products. During grinding, an abrasive wheel that removes the material from the workpiece surface is used, while a non-stop cooling fluid is flooded into the contact zone to reduce the generated heat, removing debris while reducing the friction force. The MRR of the diamond grinding process is relatively low at this stage.

Apart from the conventional abrasive diamond machining, more techniques have been developed to improve the machinability of ceramics, such as US machining (**USM**), in which a slurry containing abrasive particles is used to hit the workpiece surface under the load of a vibrating tool to fracture the workpiece surface and remove the material.

From **USM**, another machining method, **UAM** was developed by merging the conventional machining with US vibration machining. In this technique, a core drill tool made of metal-bonded abrasive diamond is rotated while vibrating at certain US frequencies and fed to the workpiece surface to drill holes. It is basically used for drilling, but its use has been extended to perform milling in some studies. The following section provides an explanation of the material removal mechanism in both conventional machining and **UAM** [24] [25].

2.1.4.1 Conventional Material Removal Mechanism

The most common machining processes applied to ceramics are grinding, lapping, polishing, and drilling with core drill tools, which is the most frequently used process for machining advanced ceramics. The turning and milling processes can be considered as cutting processes. The mechanisms of the material removal in the cutting and grinding of ductile material are similar to that shown in **Figure 2.3**. where in cutting ductile material the area of uncut chip ahead tool tip is subjected to compression in different directions and the tool forces on the chip developed friction and normal force which resulted in formation of a shear zone. When the shear stress reaches or

exceeds the shear strength of the material, yielding begins to form chips by starting cracks at shear plane. For grinding it mainly distinguished by the negative rake angle, wider edge angle, lower cutting depth, and limited space between the abrasive grain and machined surface, which requires the use of a smaller chip size than that that used in the cutting process by reducing cutting depth to range of 10 to 50 µm [26]. For cutting brittle material, shown in **Figure 2.4,** the crack immediately propagated along irregulated plane and separate chips. Brittle material has discontinuous and irregular chips, unlike that of ductile material of continuous and smooth chips.

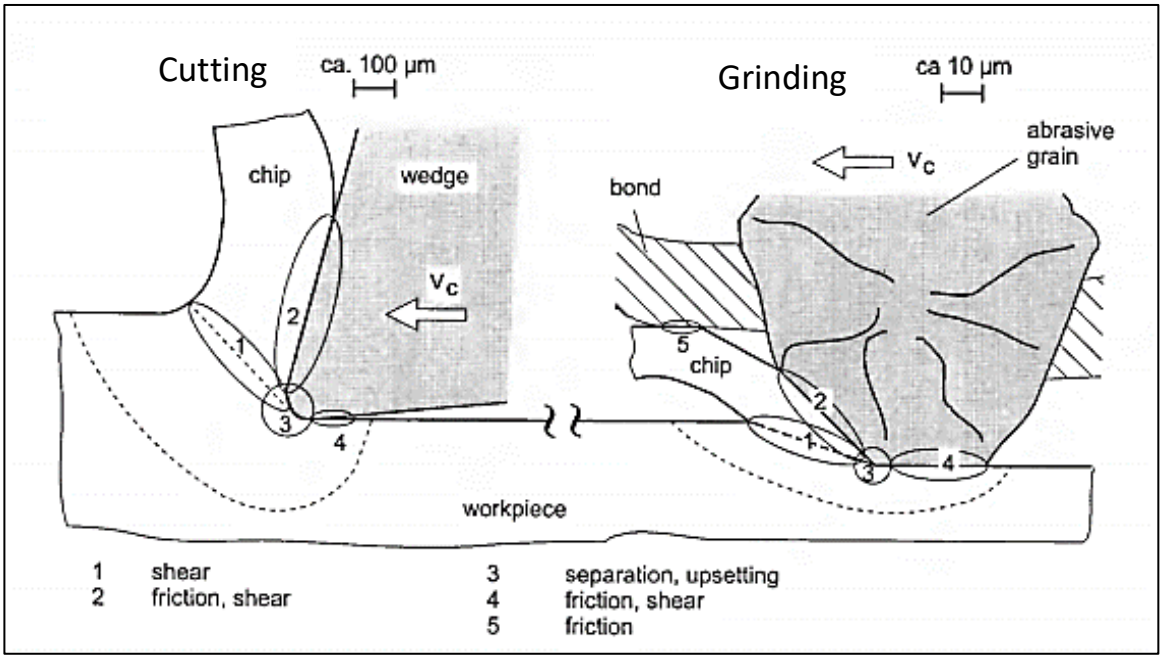


Figure 2.3 Chip formation mechanism in cutting and grinding of ductile material [26]

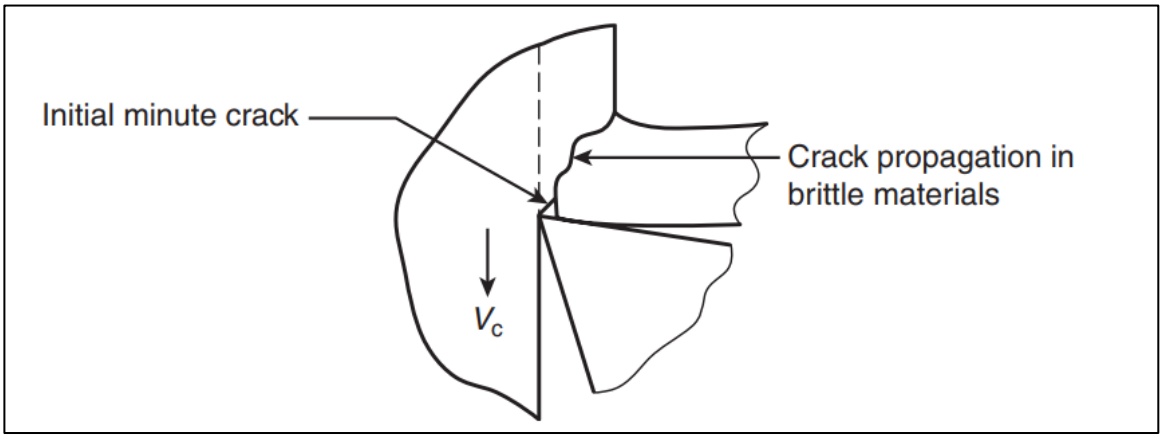


Figure 2.4 Chip formation mechanism in brittle material cutting [27]

When grinding brittle material it subjected to concentrated load by sharp ends like Vickers indentation, two patterns of cracks will develop: **lateral** and **radial-median cracks**. At the beginning of loading, radial-median cracks will form under the indentation area and start to propagate during the loading period. When unloading starts, a lateral crack will start to develop and grow until the end of unloading, where these cracks eventually meet the outer surface of the material, as shown in **Figure 2.5**. Therefore, during an abrasion or wear process, when a harder material scratches a relatively softer one, multiple concentrated loading overlaps, resulting in multiple overlapped lateral cracks intersecting on the outer surface and surrounding lateral cracks, which eventually lead to material removal, as shown in **Figure 2.6** [18]. The damage in a material highly depends on the length of the lateral cracks, which has a linear relationship with the load of indentation, which could be expressed after many experimental works as:

$$\boldsymbol{P \propto Cl^{\frac{3}{2}}} \qquad 2.3$$

where $\boldsymbol{P}$ is the load of indentation and $\boldsymbol{Cl}$ is the lateral crack length.

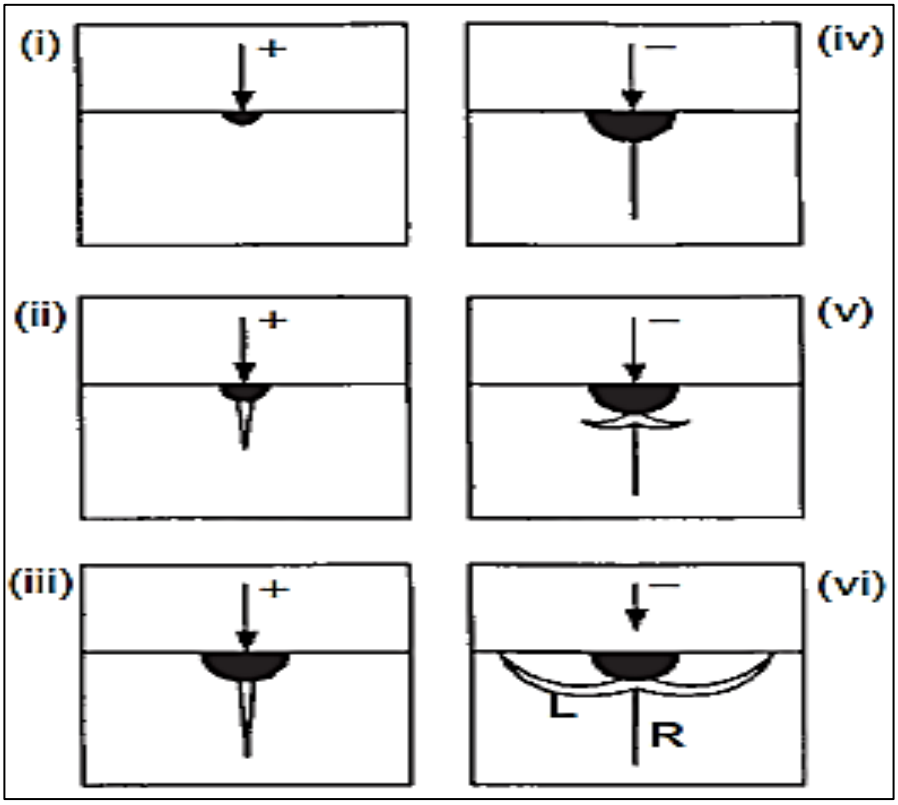


Figure 2.5 Patterns of the growth of two cracks in a brittle material under a concentrated load: radial-median **(R)** and lateral **(L)** [18]

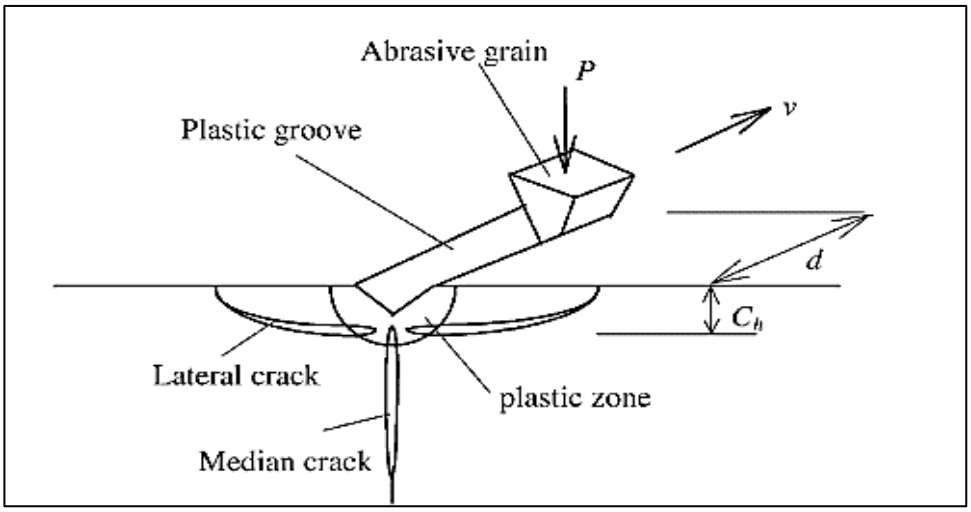


Figure 2.6 Chip formation in a brittle material [18]

2.1.4.2 UAM Mechanism

The concept of ultrasonic machining (**USM**) depends on the tool tip vibration, shaped conversely to the desired machined cavity fed toward into workpiece while a slurry consisting of water and abrasive particles is fed into the contact zone between the tool and the workpiece. These abrasives will hit the workpiece and induce brittle fracture under tool pressure, removing the material from the surface, as shown in **Figure 2.7**.

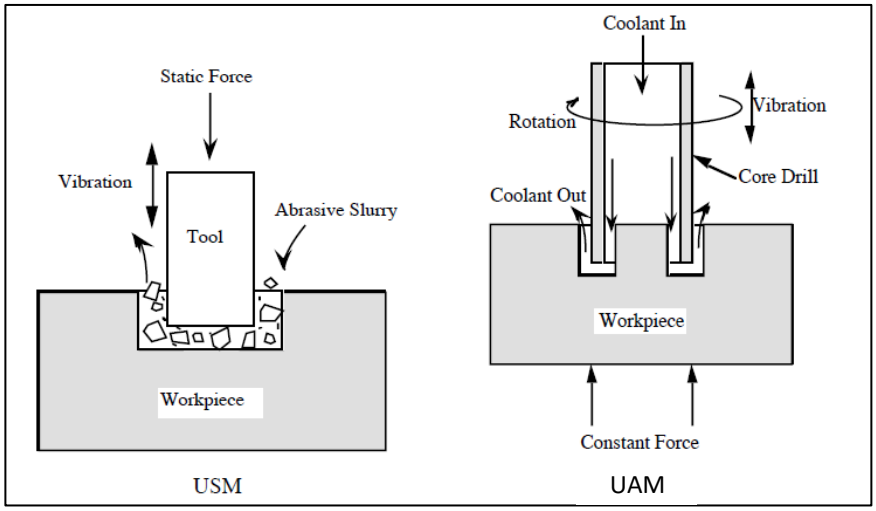


Figure 2.7 Comparison between **USM** and **UAM** [28]

However, UAM a developed version of USM machining where a core drill tool with a bonded diamond tip rotates and vibrates vertically at the same time while it is fed toward in workpiece. The cutting fluid is supplied through the core into the contact zone to reduce heat and remove swarfs and debris to prevent jamming. UAM is basically used for drilling has been used for grinding-milling operations. The mechanism of material removal by UAM is shown in **Figure 2.8**, where three mechanisms included: hammering [29] resulted by vertical ultrasonic vibration that induced indentation and crushing. Abrasion that resulted from the rotation of spindle and could be modelled as grinding. Extraction that produced from simultaneous actions of US vibration and spindle rotation.

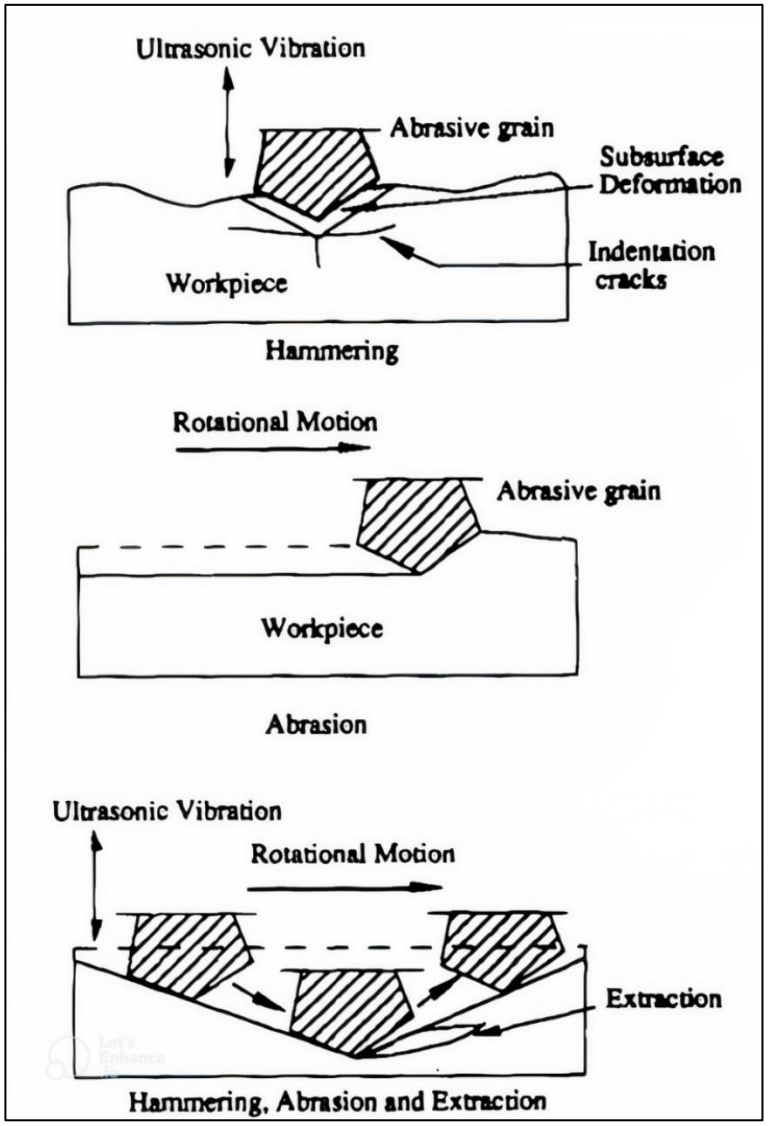


Figure 2.8 Material removal mechanism by UAM **[**29**]**

2.1.5 Tool Wear

Tool wear is an important factor in evaluating cutting tools, which directly influence the economy of the machining process and workpiece surface integrity. The variables that affect the mechanism of tool wear are complex and interact with each other, such as the machined material, tool material, machining conditions, and cutting fluid. During the machining process, the tool cuts the workpiece surface by shearing, generating heat in the contact zone of both the surface

and the tool. As the machining and frictions progress, the heat continues to increase and transfers to the tool material, which eventually leads to tool failure due to thermo-mechanical stresses [31].

2.1.5.1 Tool Wear Types

Tool wear is related to the concept of tool life/failure, where tool life refers to the period that the tool is in a useable condition for cutting, while tool failure refers to the end of tool life. Tool failure can occur by plastic deformation, gross fracture, or gradual deformation, called 'tool wear'. Generally, tool wear is due to multiple and simultaneous wear mechanisms such as adhesion, abrasion, diffusion, dissolution, and chemical reaction. The common method to characterise tool wear types is observing the cutting tool surface area, as shown in **Figure 2.9**, with the following wear types: (a) flank wear, (b) crater wear, (c) notch wear, (d) nose radius wear, (e) thermal cracking, (f) parallel cracking, (g) built-up edge (BUE), (h) gross plastic deformation, (i) edge chipping, (j) chip hammering, and (k) gross fracture. Each type takes place depending on the process conditions, tool/workpiece material, and cutting fluid. The most common wear type in conventional machining is flank and carter wear, while thermal/parallel cracking occurs in an interrupted process. Built-up edge is not a wear but induces adhesion or abrasion wear. Gross plastic deformation wear is also not a wear but changes the tool shape, thereby changing the friction forces and generated heat, which eventually leads to tool failure. Gross fracture is not gradual deformation, but catastrophic gross failure is suddenly ending tool life at any point of the process [32].

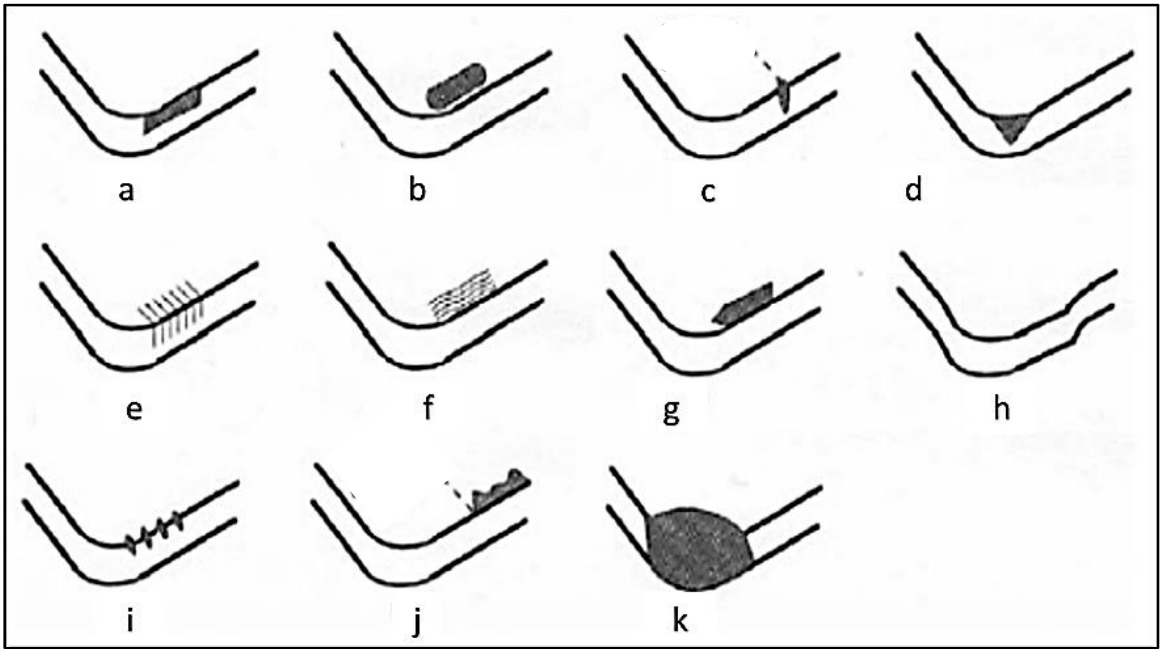


Figure 2.9 Tool wear types [32]

2.1.5.2 Tool Wear Mechanisms

a) Adhesion

Adhesion wear occurs between two surfaces, one of which is sliding on the other, where a fragment in one surface adheres to the other one and gets pulled out from its original place because of the increasing adhesive force between the atoms at the contact zone. The adhesion wear law states that wear is inversely proportional to the hardness of the workpiece material and directly proportional to the distance slide and load between the two surfaces [33]. It could be seen as attrition, crater wear, and built-up edge.

b) Mechanical Wear

- Abrasion wear occurs when a rough surface containing abrasive particles slides on a softer workpiece or a workpiece of equal hardness to remove the material. As a result, the tool material will also be removed because of the hardness of the workpiece material. For instance, flank wear, crater wear, and nose wear.
- Microfracture
- Delamination

- Chipping at sharp cutting edges [27]

c) Diffusion

Diffusion in the solid state takes place between two interfaced surfaces at high temperatures, where the surface of high atomic concentration moves to the regions of lower atomic concentrations. This results in the weakening of the tool structure, and this wear increases exponentially with increasing temperature [34]. This mechanism mostly wears crater face of the tool.

d) Dissolution

This wear occurs on the rake face of the tool under high temperatures and severe machining conditions, where the generated chips form with tool a solid solution that removes the tool material constantly as it forms chips during machining. Dissolution wear occurs depending on the chemical inertness and material compositions of the tool and workpiece [35]. Thus, the tool wear in ceramics machining is rarely showing diffusion or dissolution mechanisms, because of the chemical stability that advanced ceramics exhibits.

e) Chemical Reaction

Even though chemical reaction is not a wear mechanism, it can affect tool life tremendously, as it occurs between two interfaced surfaces, and a compound is formed from the generated chips of workpiece and cutting tool such as oxidation. It occurs when the tool material interacts with the surrounding oxygen. It is usually observed as a notch crack on a tool surface, is propagated during the process, and leads to tool failure [35].

2.1.5.3 Grinding Wheel Wear

Wheel wear during the grinding process is highly dependent on the grinding conditions, where many physical and chemical wear mechanisms are attributed to wheel wear. The interaction of the workpiece chips with the wheel bond during the process produces changes in wheel micro-topography, such as grain pullout, bond removal, flat grain, and grain fracture, which can occur

in a steady mode or suddenly, as shown in **Figure 2.10**. Generally, wear of the grinding wheel can be classified as follows:

- attrition wear, where the diamond grits lose their cutting edges and become dull, resulting in lower grinding ability and severe operation conditions that generate excessive heat;
- fracture wear of the grit or/and bond, where part of the grit breaks off, improving the grinding ability of the wheel by sharpening the grits and removing the worn grits [26].

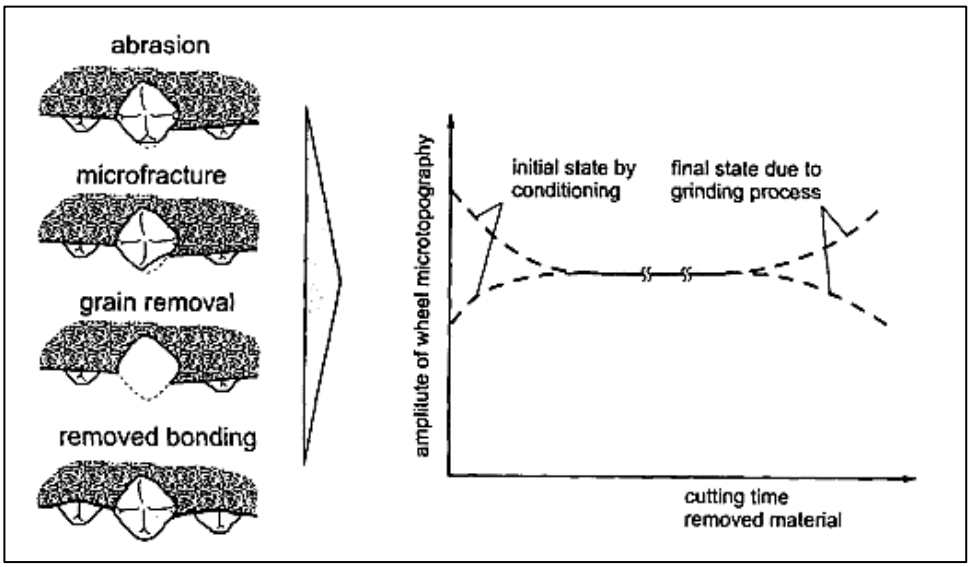


Figure 2.10 Grinding wheel micro-topography changes during grinding [26]

A basic difference exists between attrition and fracture wear. Attrition wear is unwanted wear because it deteriorates the grinding efficiency, whereas fracture wear improves the grinding ability. The sequence of events in wheel wear during the grinding process is depicted in the wheel life curve shown in **Figure 2.11**, where in the first stage, the wear rate is high because of fracture wear that sharpens the grits. In the second stage or steady-state region, the wear occurs by attrition with minor fractures in the grits and bond. Most of the workpiece material is removed during this stage. In the final stage, the grits become dull, and the amount of cutting is decreased relative to rubbing and ploughing.

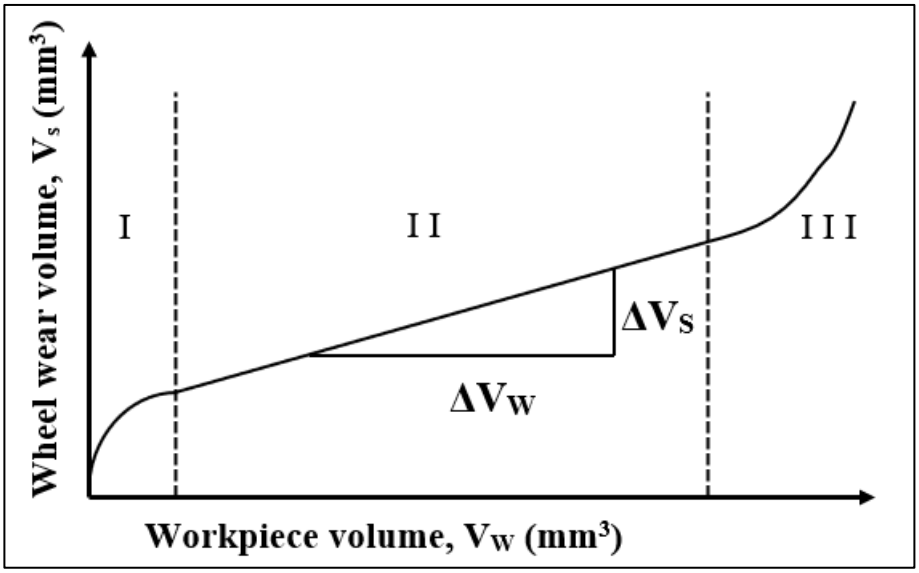


Figure 2.11 Grinding wheel wear curve [36]

Wheel wear is measured using the *G* ratio expressed as:

$$G = \frac{\text{Volume of removed material}}{\text{Volume of wheel wear}},$$

where the G value depends on the wheel type, cutting fluid, and grinding conditions; as the grinding forces increase, the *G* ratio decreases [26].

2.2 Previous Studies

2.2.1 End Milling

Several experiments have been conducted on milling hard-to-cut materials using ultra-hard end mills. Matsumura et al. [42] investigated the machining of micro-grooves in glass using the CBN ball-nose end mill. The tool is tilted to a certain angle to improve the surface finish. According to the results, the obtained un-deformed chip thickness was less than 1 μm during the whole process. A crack-free surface is also obtained with an axial cutting depth ranging from 15 to 20 μm. Cheng [43] machined a three-dimensional workpiece made of tungsten carbide using a PCD

tool in ductile cutting mode, where the obtained surface roughness values were Ra = 10 nm and Ry = 30 nm.

Wu [44] studied the wear characteristics of the PCD micro end mills used in the micro milling of tungsten carbide and found that worn tools increase the cutting forces and surface brittle fracture defects. Bian et al. [45] studied the performance of PCD micro end mills on sintered engineering zirconia ZrO_2 ceramics in ductile machining mode. The impacts of the milling parameters such feed per tooth, axial cutting depth, and particle size of the tool on surface integrity were investigated. The tool wear mechanism and its characteristics were observed. The findings of the study showed that the mean surface roughness Ra value was less than 70 nm for all the machined workpieces. The parameter with the most influence on surface roughness was feed per tooth. Moreover, the main wear mechanism in the tool was the peeling off of the diamond particles during friction in the contact zone. The tool consisted of larger diamond particles, which last longer than of smaller ones.

Bian [46] also conducted another investigation in ductile cutting mode for ZrO_2 using a diamond-coated micro end mill of 1 mm in diameter, as shown in **Figure 2.12**. The findings from the experiment were that ZrO_2 can be machined in ductile mode using the diamond-coated tool and achieve a mirror-quality surface finish with an Ra value of 20 nm. Tool wear involved diamond coating delamination and substrate, which correlated with the feed rate. In micro milling, the compressive stress is high because of the small cutting edge, which means that the cutting forces in the *z*-axis are larger than the forces in the other axes.

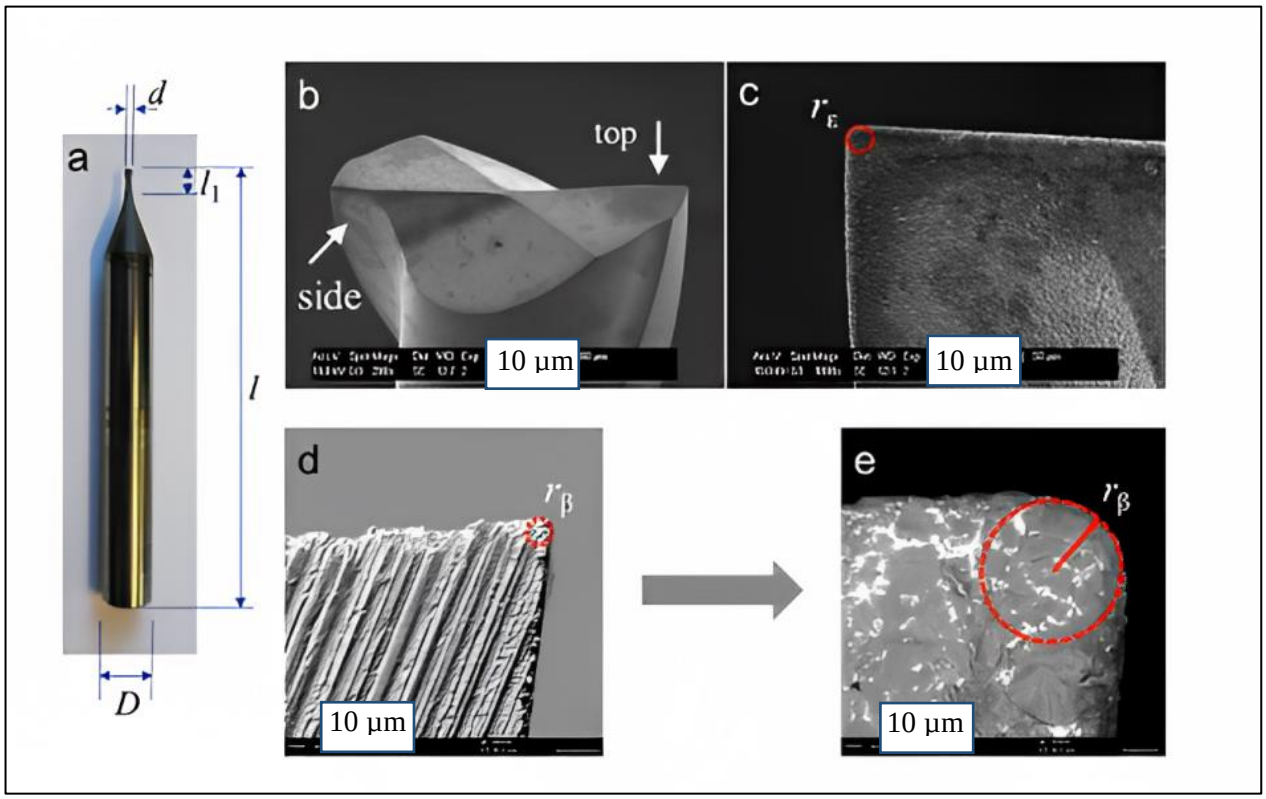


Figure 2.12 Illustration of (a) end mill geometry, (b) cutting edge radius, (c) tool side view, (d) tool before coating, (e) tool after diamond coating [46]

Another investigation on sintered advanced ceramic (Al_2O_3) using end mills was conducted by Liu et al. [47]. Their experimental work was performed using a three-axis CNC machine and tungsten carbide end mills with chemical vapor-deposited (CVD) diamond coating, as shown in **Figure 2.13**. The diamond coating thickness ranged from 10 to 15 µm. The Al_2O_3 workpiece utilised had a hardness value of 1000 Knoop and purity of 99%. The study performed machining in dry environment. 12.7-mm diameter end mills were utilised at a spindle speed of 3000 rpm (V = 119 m/min) and 4000 rpm (V = 159 m/min), with a fixed cutting depth of 0.254 mm and a variable WOC.

Surface Roughness and MRR: the surface that machined at a speed of 3000 rpm obtained a maximum surface roughness of Ra of 2.01 µm at a MRR of 4 mm^3/min. At a speed of 4000 rpm,

maximum Ra of 1.26 µm was obtained at a MRR of 3.71 mm^3/min, which is close to 4 mm^3/min. The surface roughness at the high MRR was similar to the surface roughness at the low MRR. At speed of 4000 rpm, the tool failed faster at feed rate of 21 mm/min and MRR of 13.01 mm^3/min, where high noises and vibration were observed before the tool failed.

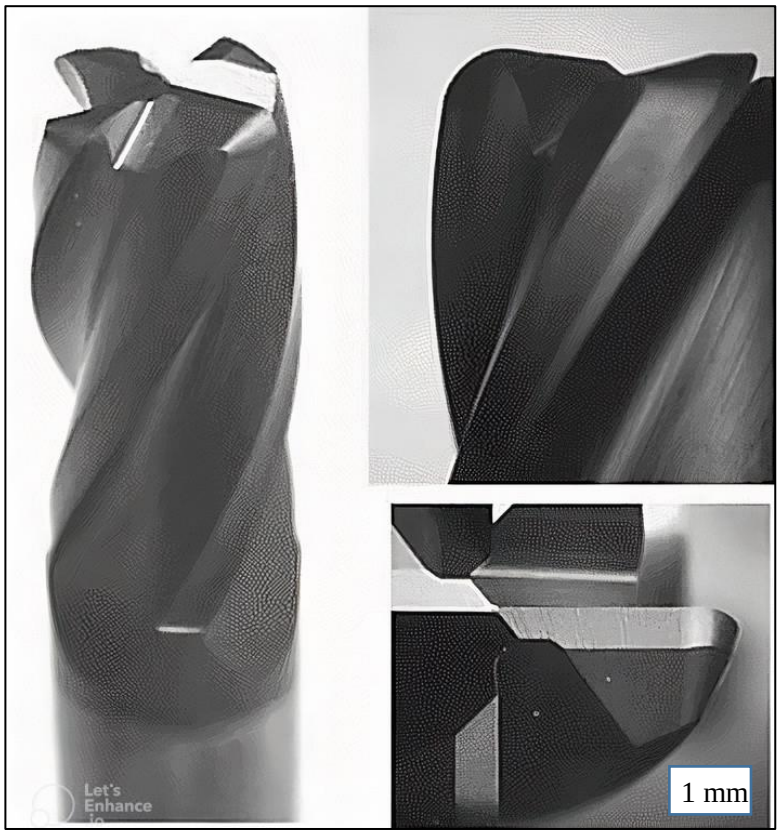


Figure 2.13 CVD diamond-coated end mill [47]

Tool Wear*:* The sizes of the tool wear at the flank face were measured after machining at a speed of 4000 rpm (V = 159 m/min). For a feed rate of 11.9 mm/min and WOC of 2.54 mm, the wear area was 0.00645 mm^2, as shown in **Figure 2.14(a)**. The wear area increased to 0.0323 mm^2 at a feed rate of 21 mm/min (**Figure 2.14 b**). At this high feed rate, the tool life ended faster, and the surface of the Al_2O_3 was severely damaged.

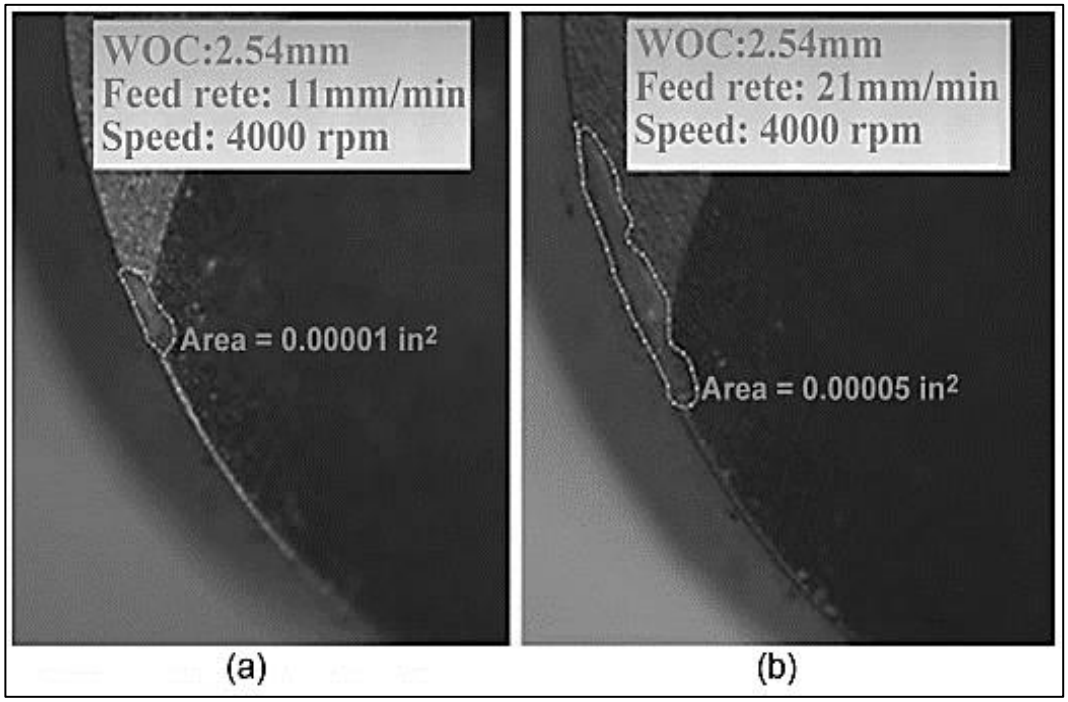


Figure 2.14 Tool wear area at a speed of 4000 rpm and feed rates of (a) 11 mm/min and (b) 21 mm/min [47]

Cutting Forces*:* At a WOC of 0.254 mm, the variation of the forces was stable with time, and the cutting force F_Y was less than 5 N, At WOC of 2.54 mm, F_Y was approximately 21 N, and the variation in peak was higher and unstable with time, which indicates that the tool life will be shorter. At a WOC of 3.81 mm F_Y exceeded 200 N, and the tool failed immediately. The tool tip was chipped as it touched the surface of the material.

Cutting forces according to MRR: The peaks of the cutting forces in the *y*-axis F_Y and the MRR at different WOC has indicated linear relationship, as the MRR increased as the cutting force F_Y increased. When the F_Y value reached 100 N, the tool failed immediately. The most important finding in this work was that CVD diamond-coated cutters are good for machining Al_2O_3 but only under specific controlled conditions such machining at MRRs of 5–6 mm^3/min. The surface roughness was highly affected by the tool substrate texture. Thus, the diamond coating need to be thicker than 15 µm to achieve a better surface finish and to extend the tool life.

2.2.2 Grinding

The superior mechanical properties of advanced ceramics that make ceramic machinability challenging, such as high hardness and brittleness, have made abrasive grinding the most commonly applied machining process. Many studies and works over the past years have been conducted to investigate ceramic grinding ability to develop more efficient grinding methods such as creep feed, high-speed grinding, and **UAG**. Moreover, the operation parameters that affect the grinding characteristics (wheel speed, feed rate, cutting depth, diamond concentration, grit size, cooling method, and cutting fluid type) have been optimise in several works. In the most recent and relevant studies, conventional and non-conventional grinding have been investigated.

2.2.2.1 Conventional Diamond Grinding

Inasaki [48] investigated the most frequently utilised advanced ceramics in the industry, including alumina (Al_2O_3), zirconia (ZrO_2), silicon nitride (Si_3N_4), and silicon carbide (SiC). Two grinding methods were applied in the work. The findings indicated that the creep-feed method resulted in high specific grinding energy and high grinding forces over time. Thus, creep feed is not suitable for grinding ceramics. On the other hand, the high-speed stroke method has been considered more suitable owing to its resulting efficient grinding. All the observed material removal mechanism occurred mainly by brittle fracture.

Yin [49] investigated the response of the four ceramics (Al_2O_3, ZrO_2, Si_3N_4, and SiC) to high-speed grinding at a wheel speed of up to 160 m/s. The diamond wheel utilised had a diameter of 200 mm, width of 6.7 mm, and grit size of 160 µm. The four cutting speeds were 40, 80,120, and 160 m/s at a cutting depth of 40 µm and feed rate of 500 mm/min.

The findings show that the normal grinding forces were reduced by up to 2.5 times as the wheel speed increased. The normal forces were variable depending on the ceramic. The normal force of

ZrO_2 at a speed of 40 m/s was almost four times the force of SiC, as shown in **Figure 2.15**. For Al_2O_3 and SiC, the surface roughness Ra values decreased as the wheel speed increased, and for Si_3N_4, no significant improvement was observed. However, for ZrO_2, the surface roughness decreased at a low speed and increased as the speed increased, as shown in **Figure 2.16**.

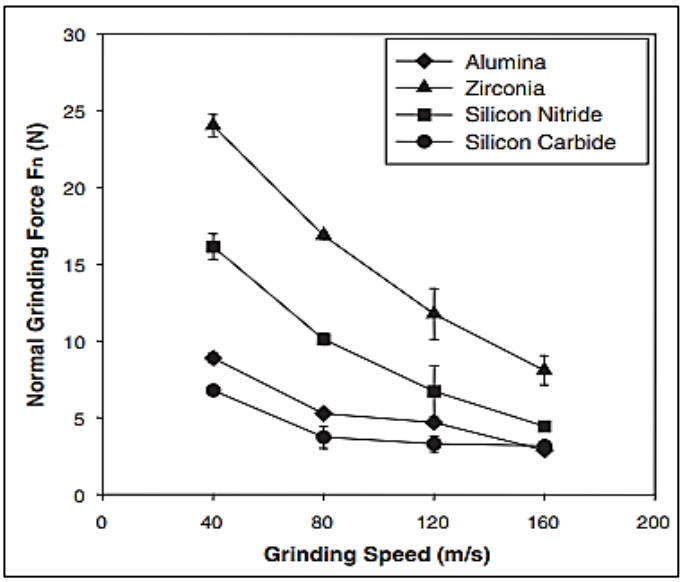


Figure 2.15 Normal grinding force of the ceramics according to grinding speed [49]

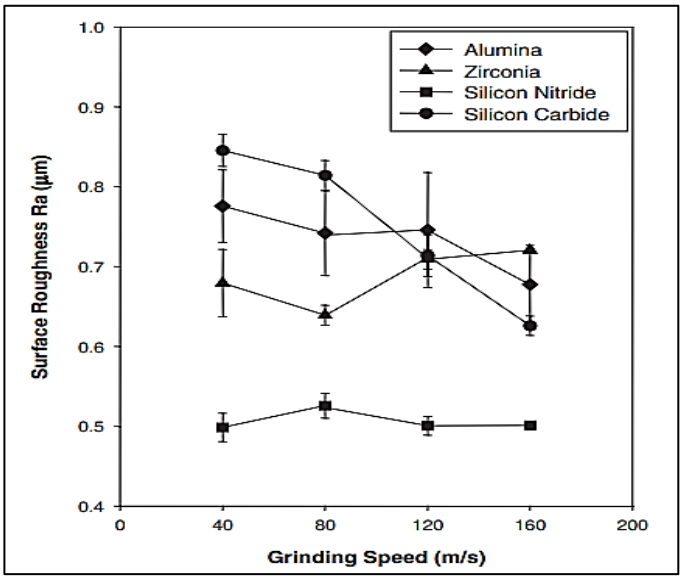


Figure 2.16 Surface roughness of the ceramics according to grinding speed [49]

The SEM images of the machined surfaces show that the material removal mechanism in ZrO_2 was in

ductile mode regardless of cutting speed (**Figure 2.17**). Brittle fractures were dominant on the SiC surface (**Figure 2.18**). Al_2O_3 was cut at low speed in brittle fracture mode, but at 160 m/s, a brittle-ductile transition occurred (**Figure 2.19**). The Si_3N_4 cutting mode was between semi-brittle and semi-ductile, as shown in **Figures 2.20**.

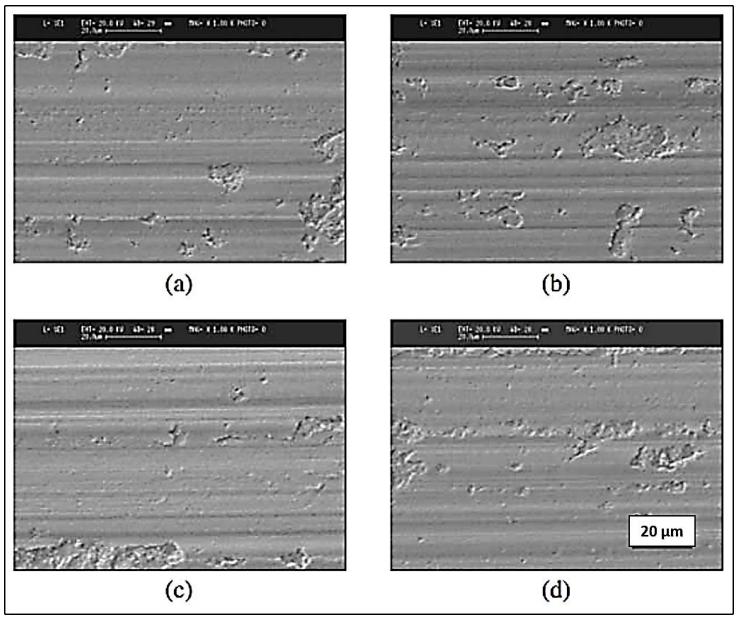


Figure 2.17 ZrO_2 ground surface at speeds of (a) 40 m/s, (b) 80 m/s, (c)120 m/s, and (d) 160 m/s [49]

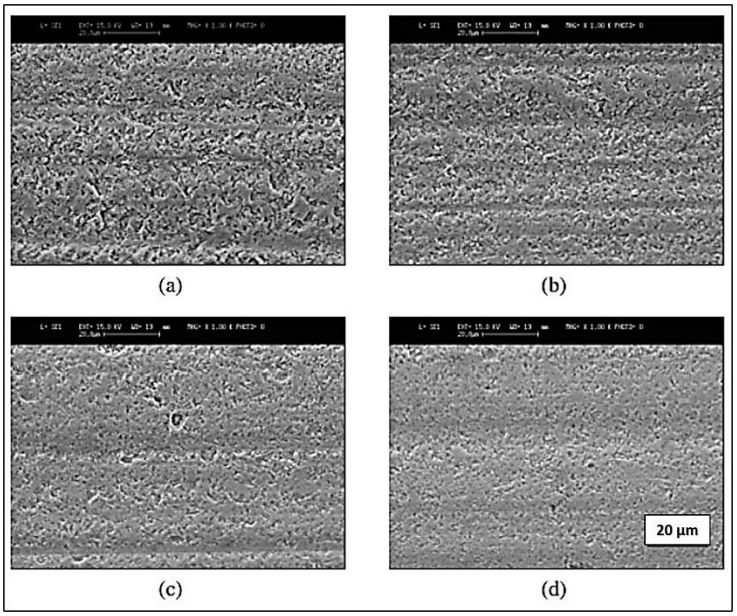


Figure 2.18 SiC ground surface at speeds of (a) 40 m/s, (b) 80 m/s, (c)120 m/s, and (d) 160 m/s [49]

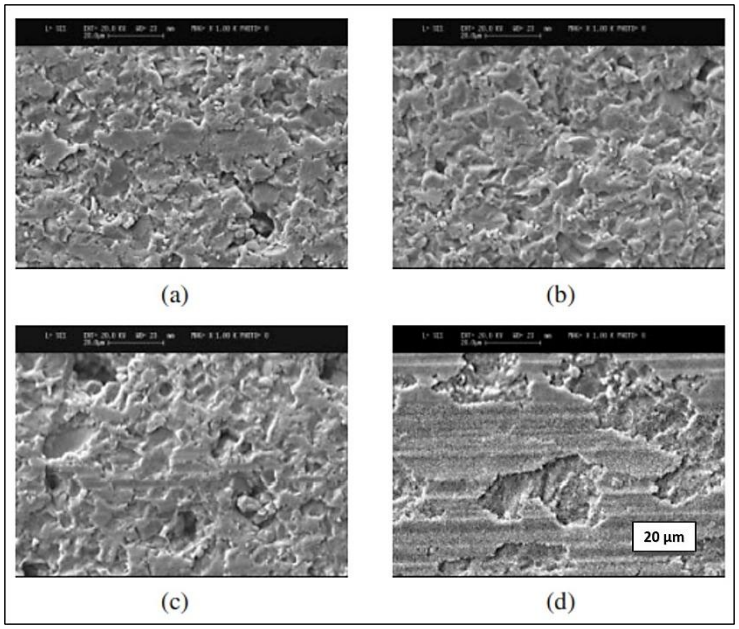


Figure 2.19 Al_2O_3 ground surface at speeds of (a) 40 m/s, (b) 80 m/s, (c)120 m/s, and (d) 160 m/s [49]

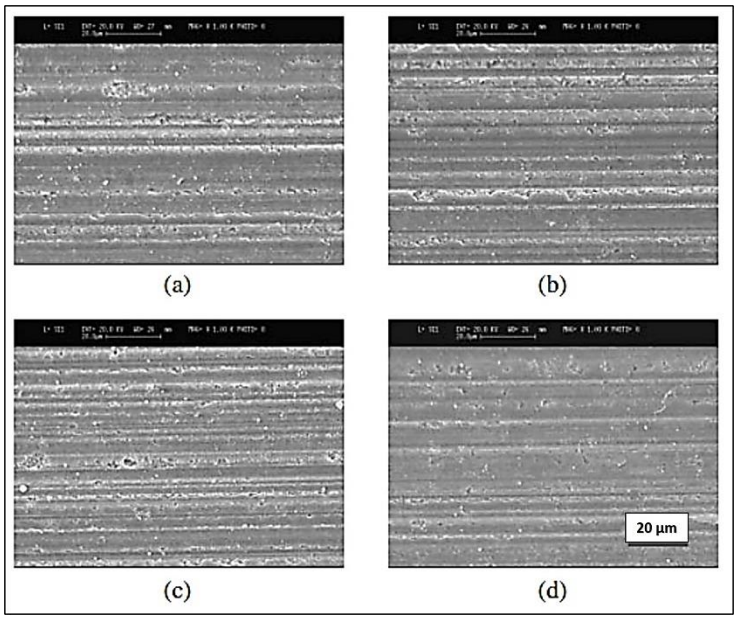


Figure 2.20 Si_3N_4 ground surface at speeds of (a) 40 m/s, (b) 80 m/s, (c)120 m/s, and (d) 160 m/s [49]

Chen [50] investigated the grinding of Al_2O_3, ZrO_2, and Si_3N_4 at high wheel speeds, as shown in **Table 2.2**. The ceramics were investigated using two diamond grit sizes, 30/35 and 50/60. The findings shows that the normal cutting force in both grit sizes was reduced by almost 30–75% as the wheel speed increased. The forces were highest in Si_3N_4, followed ZrO_2 and Al_2O_3. The forces

obtained using a wheel of grit 30/35 was lower than those obtained with a grit of 50/60, as shown in **Figure 2.21**.

Table 2.2 Grinding parameter levels [50]

Peripheral wheel speed V_s (m/s)	Depth of cut a_p (μm)	Workpiece velocity V_w (m/min)
30, 90, 150	30	0.6
	10	12
	20	6
	40	3

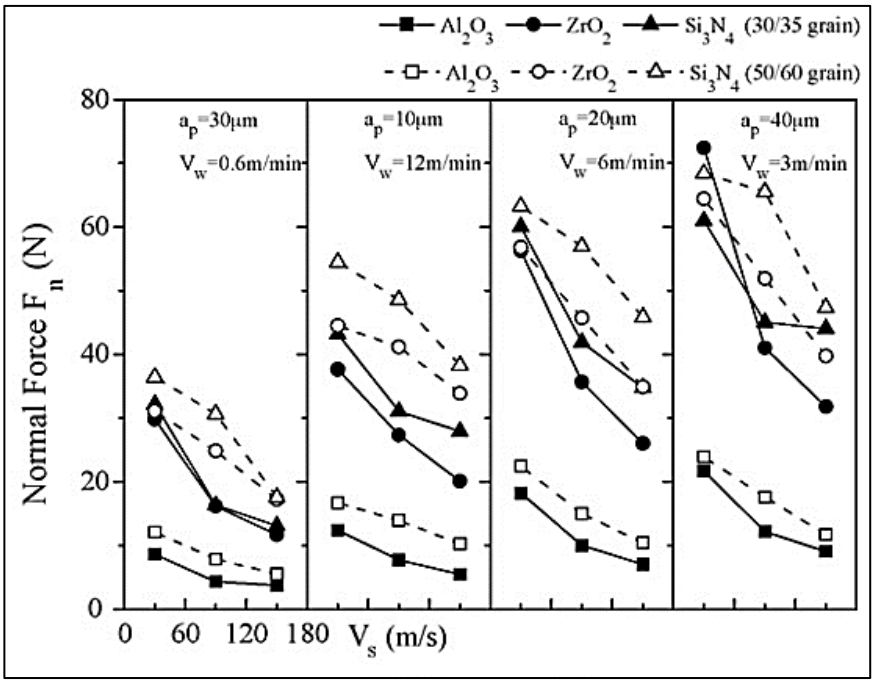


Figure 2.21 Normal grinding forces according to wheel speed [50]

The effects of wheel speed on ground surfaces are shown in **Figure 2.22**, where the surface roughness Ra obtained with a grit size of 30/35 decreased as the speed increased. The surface roughness obtained with a grit size of 50/60 did not exhibit significant changes except for silicon nitride, in which it decreased at higher wheel speeds. The surface roughness values obtained with a grit size of 50/60 was lower than that obtained with a grit size of 30/35. The micrograph analysis of ground surfaces revealed that the material removal mechanism in ZrO_2 was in ductile mode regardless of speed and grit size. In

alumina, the material removal mechanism was in brittle fracture mode regardless of grit size and wheel speed. The silicon nitride ground surface showed a brittle-ductile transition as the wheel speed increased with both grit sizes, as shown in **Figures 2.23** and **2.24**.

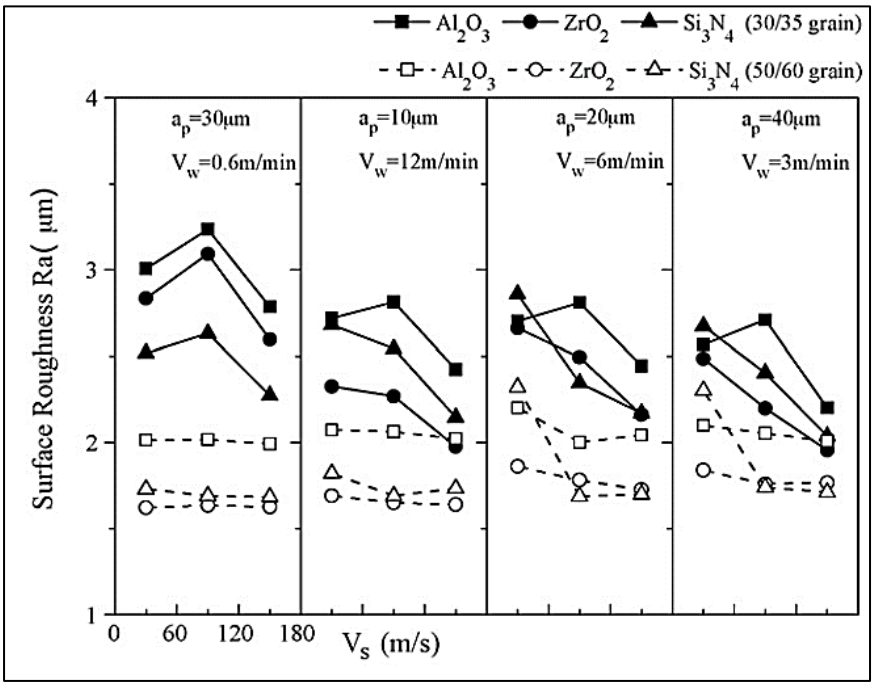


Figure 2.22 Surface roughness according to wheel speed [50]

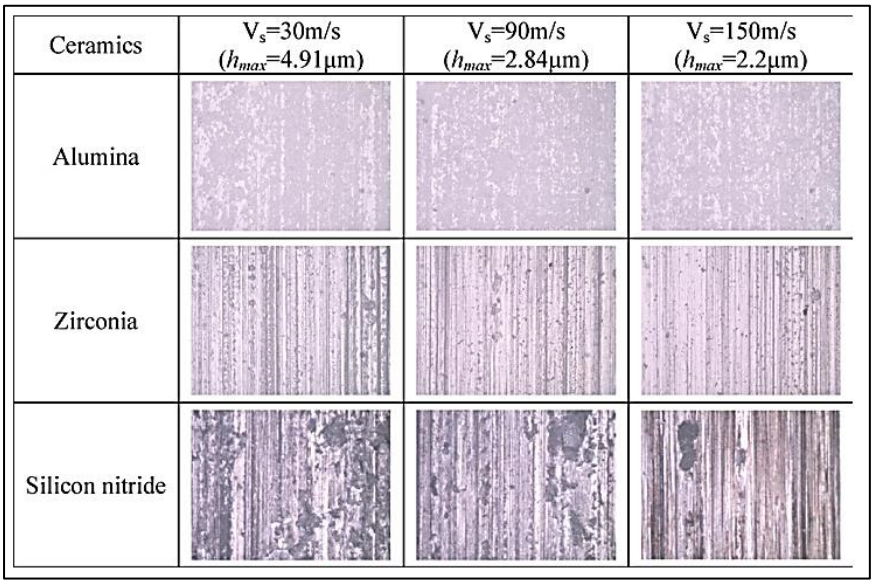


Figure 2.23 Ground surfaces of different ceramics at different wheel speeds (grit size of 35/35, cutting depth of 40 μm, and feed rate of 3 m/min) [50]

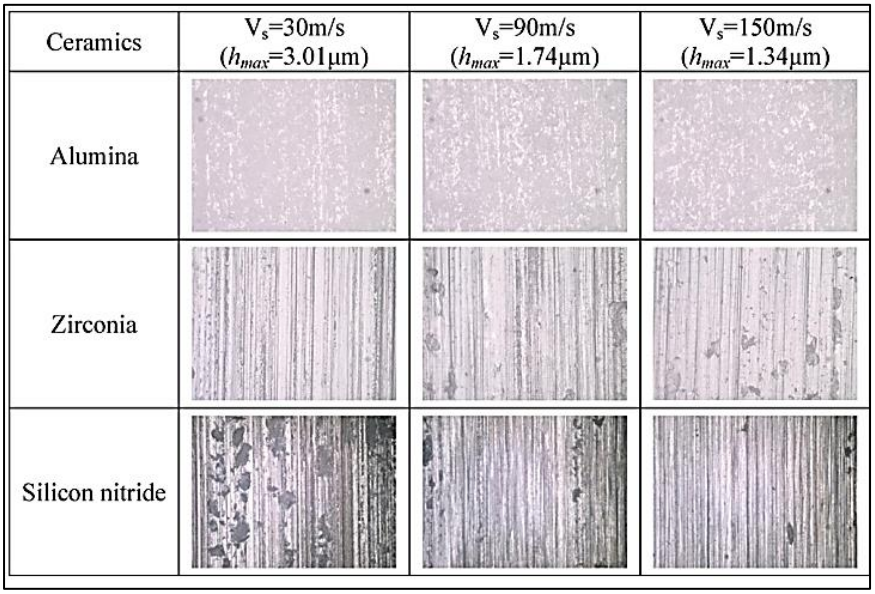


Figure 2.24 Ground surfaces of different ceramics at different wheel speeds (grit size of 50/60, cutting depth of 40 μm, and feed rate of 3 m/min) [50]

Ramesh [51] investigated the high-speed diamond grinding of ZrO_2, Al_2O_3, and SiC. The wheel speeds were 40, 80, 120, and 160 m/s, and the cutting depth range was 0.05–0.4 mm. The cutting forces decreased as the wheel speed increased in all ground ceramics. The surface roughness Ra improved from 0.8–1 μm to 0.5–0.8 μm when the speed increased from 40 m/s to 160 m/s. The material removal mechanism in ZrO_2 was in ductile flow, which is similar to that in metals. The Al_2O_3 surface texture showed a brittle-ductile transition when the wheel speed increased from 40 m/s to 160m/s. The SiC surface did not show any significant changes as the wheel speed increased, and the material removal was mainly in brittle fracture mode at all speeds.

A comparison between conventional and high-speed grinding was conducted by Yin et al. [52]. They investigated two materials, mono crystalline alumina and alumina-titania, with a wheel of 160-μm grit size and test speeds of 40 and 160 m/s, respectively. They found that the materials had similar micro-fracture mechanism. The surface roughness did not show any significant changes when the wheel speed increased. The increasing MRR in both grinding methods did not

affect the surface roughness. The increased MRR in conventional grinding resulted in grinding forces higher than those obtained from high-speed grinding at the same MRR increases.

The characteristics of the high-speed grinding and material removal mode with the sub-surface defects were investigated by Huang et al. [53]. The tested materials were yttria-partially-stabilised tetragonal ZrO_2, Al_2O_3, and alumina-titania. A diamond wheel grit size of 160μm was used; the machining speeds were 40, 80, 120, and160 m/s at a cutting depth range of 0.1–2 mm. Lateral cracking along the grain boundary was the mechanism of the cutting in alumina and alumina-titania, whereas both ductile-brittle fracture was observed in ZrO_2. The surface roughness improved at a feed rate of 500 mm/min at all test speeds when the cutting depth increased from 0.1 mm to 2 mm, but as a result, the tool life decreased significantly. This deeper cut did not affect the sub-surface defects in Al_2O_3 and alumina-titania but resulted in deeper surface damages in ZrO_2.

A similar study by Agarwal et al. investigated sub-surface and surface damages and the material removal mechanism in SiC, along with the related grinding characteristics [54]. They found that the material removal mechanism by grain dislodgment resulted in a reduction in grinding force and specific grinding energy.

The performance of Si_3N_4 when a resin bond diamond wheel was used was investigated by Hwang et al. [55], who focused on the effect of wheel speeds on the material removal mechanism at different grit sizes. At grit size of 160 μm, material was removed in brittle fracture mode, and the speed effect was insignificant. At a grit size of 20 μm, material was removed in ductile fracture mode, and the influence of speed on material removal was significant.

2.2.2.2 Ultrasonic Assisted Grinding

The limitations of the conventional grinding process especially with hard-to-cut and brittle materials have encouraged many studies over the last years to investigate the improvement that could be gained using UAG, sometimes called 'rotary ultrasonic machining', in terms of machining efficiency [56]. This new technique depends on the concept of adding high-frequency vibration with a small amplitude to the wheel/abrasive point or workpiece in conventional grinding. Many recorded works have applied this technique on several type of materials such as glass, metal alloy, composite materials, and advanced ceramics. All results obtained indicated that UAG improved the grinding efficiency in terms of reducing the grinding forces, surface roughness, dimension tolerance, surface/subsurface damages, wheel wear, and energy consumption, resulting in better cost efficiency and product quality [57-61].

Pei [28] investigated UAG to face mill magnesia-stabilised zirconia using a fractional factorial design. The tool used was conic in shape and covered with diamond from its conical surface to its bottom surfaces. The grit concentration was 100 by volume is shown in **Figure 2.25**. The cutting fluid was water, and the vibration amplitude was 23–33 μm, with a frequency of 20 kHz. The 5 two-level variables, namely speed, amplitude, feed rate, grit, cutting depth, and fractional factorial matrix of 16 tests, are shown in **Table 2.3**. The analysis was for four outputs of cutting forces, surface roughness, MRR, and material removal mechanism.

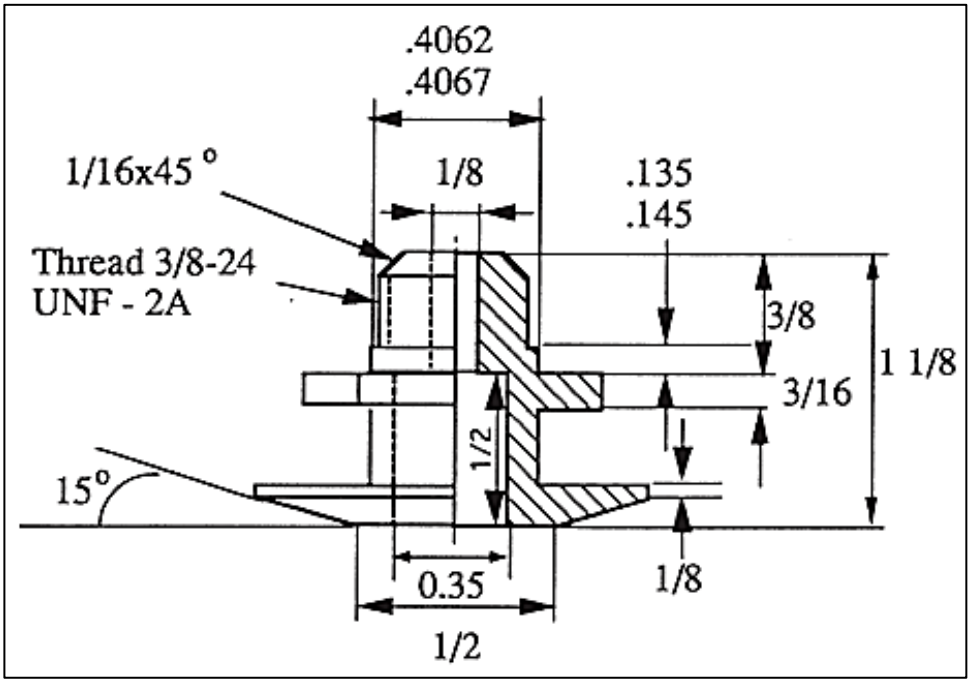


Figure 2.25 Conical abrasive tool [28]

Table 2.3 Machining parameter levels [28]

Test	Speed	Amplitude	Feedrate	Tool	DOC
1	−1	−1	−1	−1	1
2	1	−1	−1	−1	−1
3	−1	1	−1	−1	−1
4	1	1	−1	−1	1
5	−1	−1	1	−1	−1
6	1	−1	1	−1	1
7	−1	1	1	−1	1
8	1	1	1	−1	−1
9	−1	−1	−1	1	−1
10	1	−1	−1	1	1
11	−1	1	−1	1	1
12	1	1	−1	1	−1
13	−1	−1	1	1	1
14	1	−1	1	1	−1
15	−1	1	1	1	−1
16	1	1	1	1	1

Speed: + 1 = 60 rev/s (300 rpm);−1 = 16.7 rev/s (1000 rpm).
Amplitude: + 1 = 33 μm;−1 = 23 μm.
Feedrate: + 1 = 80 BLU/s;−1 = 40 BLU/s.
Tool: + 1 = 60/80;−1 = 170/200.
DOC: 1 = 1.10 mm;−1 = 0.05 mm.
Workpiece: magnesia stabilized zirconia.

Cutting Forces Analysis: The forces in the *y* and *z* directions were measured, but the maximum *F*z value was used to study the effects of other machining parameters on the cutting forces, as seen from the plots in **Figure 2.26**. The parameter with greatest effect was tool grain size. Finer grains resulted in higher cutting forces owing to the increasing efficient contact surface between the tool and workpiece. On other hand, the cutting forces increased as other parameters, including speed, amplitude, and cutting depth, increased. Regarding the effects of the two-factor interaction parameters on the cutting forces, the effect of vibration amplitude was most significant when it was used as a second-order interaction parameter but was not significant when it was used as a first-order interaction parameter.

Surface Roughness Ra: The results shown in **Figure 2.27** indicate that the main influencing parameters on the surface roughness values were grain size and spindle speed. The surface roughness values decreased as speed and grain increased. The coarse grain size with a higher spindle speed resulted in a higher ductile percentage. Therefore, to obtain a fine, good surface finish, the machining conditions must target surfaces with higher ductile percentages.

MRR Analysis: As shown in the results presented in **Figure 2.28**, MRR was only affected by feed rate and cutting depth. Other parameters, including speed, amplitude, and tool, showed no effects.

Cutting mode*:* The most influencing parameter on ductile percentage was grain size, and the ductile percentage increased as the speed and cutting depth increased. Unlike the conventional grinding process, the material removal mode tended to be more ductile when a tool with a large grain size was used, which might be due to the different machining mechanism used in this experiment, where the workpiece was fed in steps toward the tool while fed continually into

conventional grinding. For the two-factor interaction, the grinding tool type was the most influencing parameter.

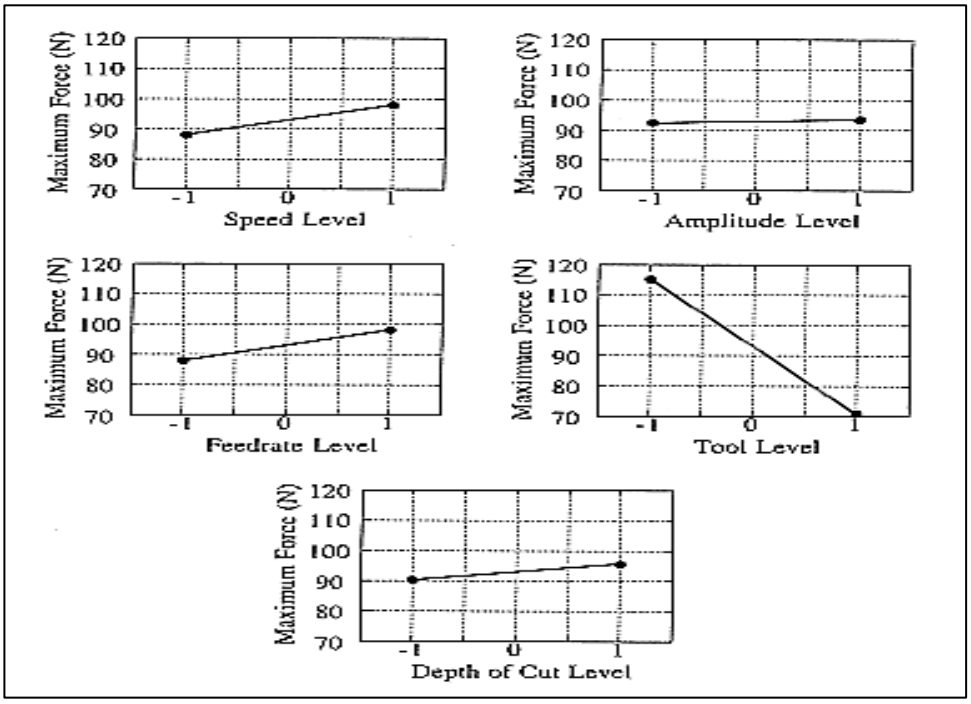


Figure 2.26 Main effects on the cutting forces [27]

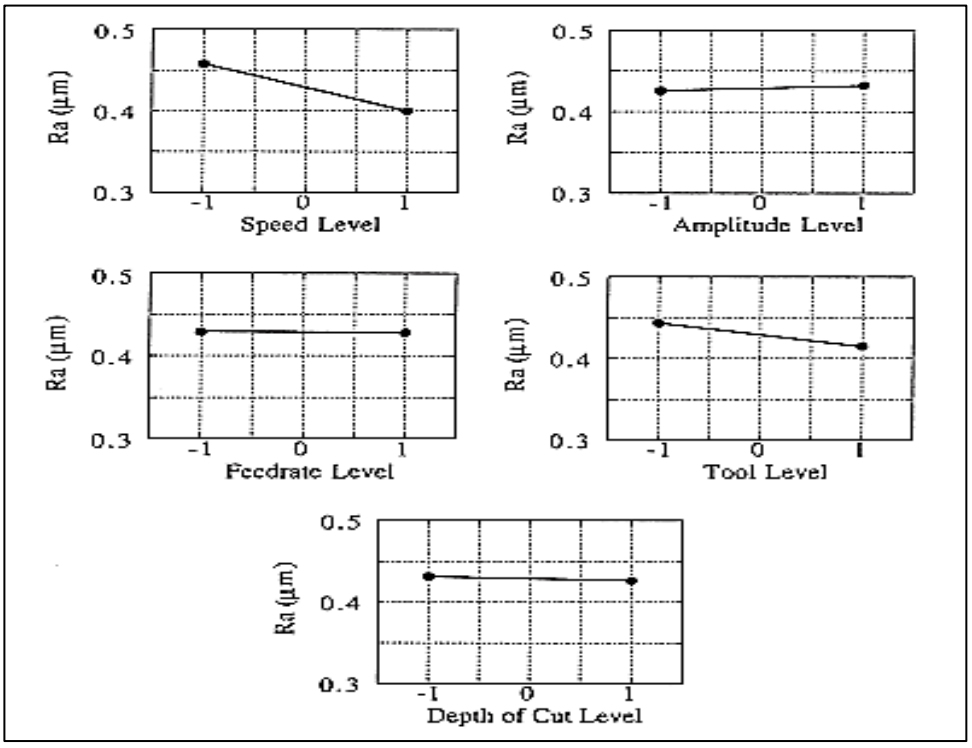


Figure 2.27 Main effects on the surface roughness [27]

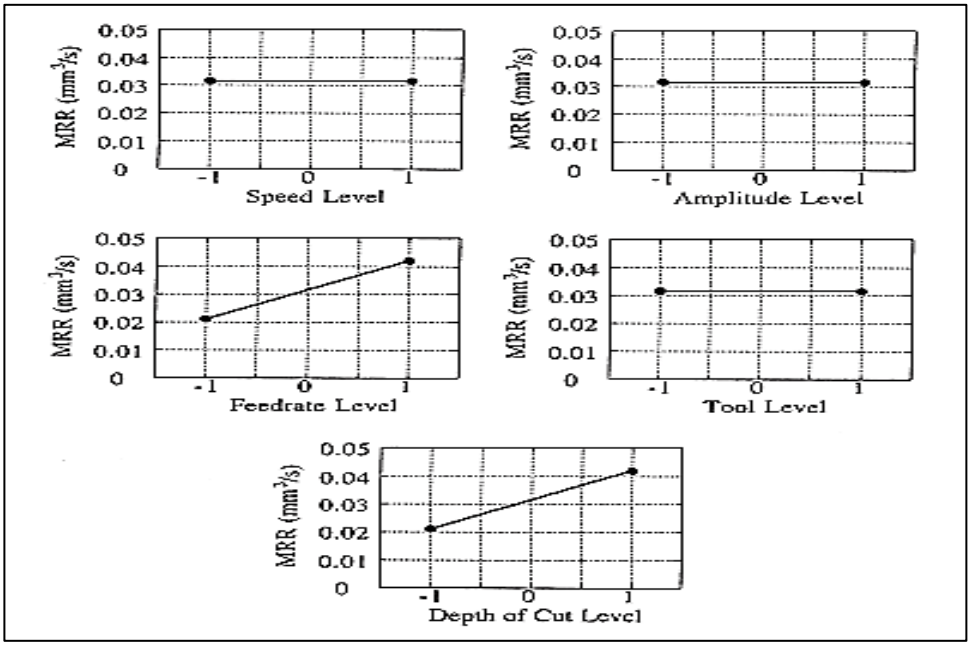


Figure 2.28 Main effects on MRR [27]

Another ceramic material, K9 optical glass, was investigated by Zhang et al. [30]. They used UAG to face mill the optical glass, as shown in **Figure 2.29**. The effects of vibration amplitude A, the speed, and the cutting depth on the cutting force were investigated at two cutting depth ranges, one higher and the other lower than the utilised US vibration amplitude (10 µm at 21 kHz). The results were compared with the cutting forces obtained with conventional diamond milling. The tool used in both experiments had an outer diameter of 7 mm, a wall thickness of 2 mm, and a grit size of D151.

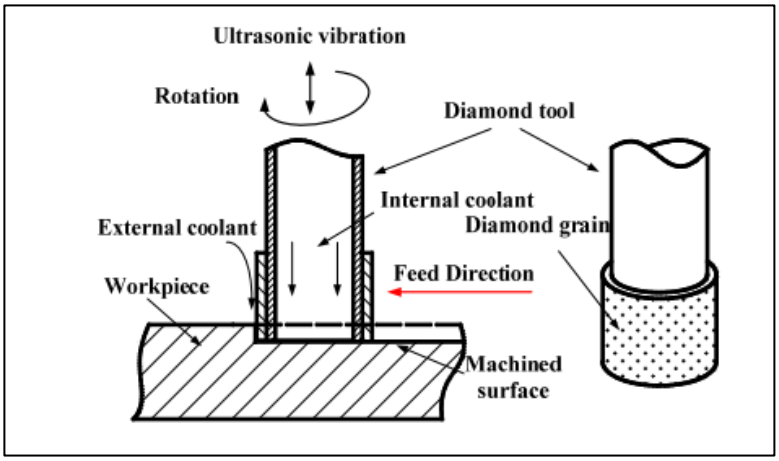


Figure 2.29 UAG setup of K9 optical glass machining [30]

Experiment 1

In experiment 1, the machining parameters were set at cutting depths lower than the vibration amplitude of 10 µm, as shown in **Table 2.4**. The results of the experiment are represented in **Figure 2.30**. The cutting forces were significantly decreased in UAG compared with the conventional diamond milling when the cutting depth was lower than the vibration amplitude. The cutting force decreased as the rotational speed increased but increased with the increasing feed rate and cutting depth.

Table 2.4 Experiment 1 parameters [30]

Process variable	*Unit*	*Value*
Spindle speed	r/min	1000, 3000, 6000
Feedrate	mm/min	100, 200, 400
Cutting depth	µm	3, 6, 9

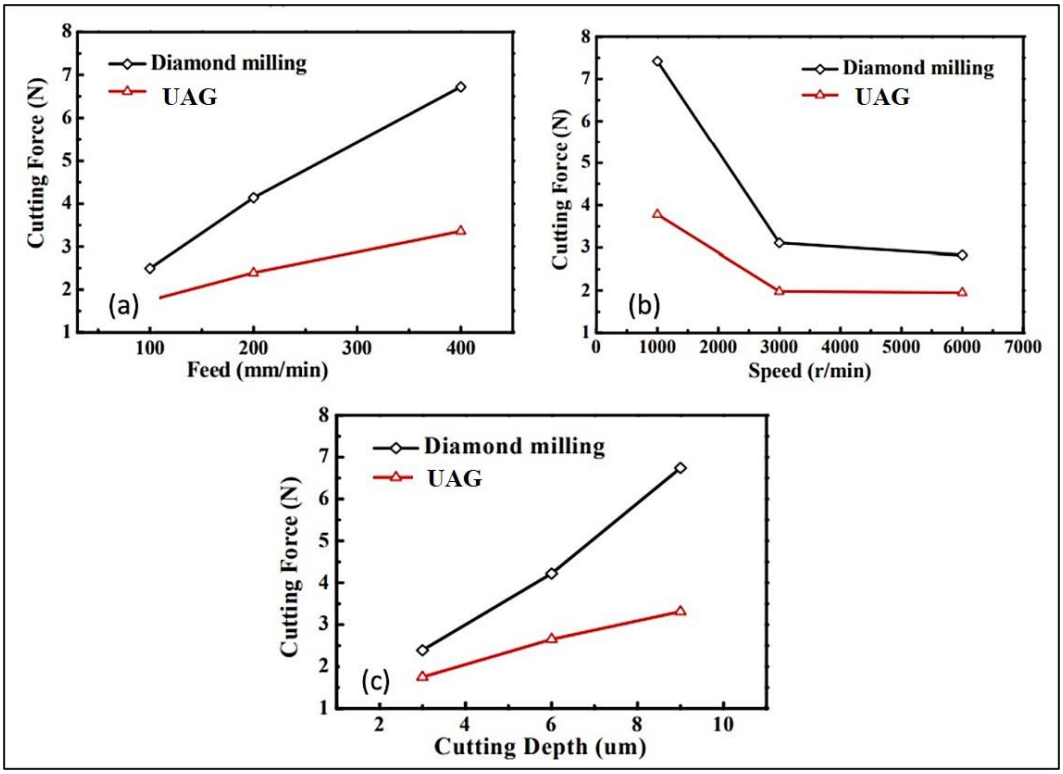


Figure 2.30 Effects of the variable parameters, (a) feed, (b) speed, and (c) cutting depth, on the cutting forces in conventional diamond milling compared with UAG at a cutting depth range of *A* = <10 µm [30]

The tool wear obtained from experiment 1 is shown in **Figure 2.31**, where (a) shows that the three types of tool wear, namely attrition, grain fracture, and bond fracture, were present at the end face of UAG, while bond and grain fractures and dislocation were present at the end face of the conventional diamond milling tool, as shown in **Figure 2.31 (b)**. In general, the diamond milling tool was damaged severely; a hole was created at the bottom face because of one of the grains was pulled off. Thus, UAG results in longer tool life and higher MRR if performed under the same cutting force as in diamond milling.

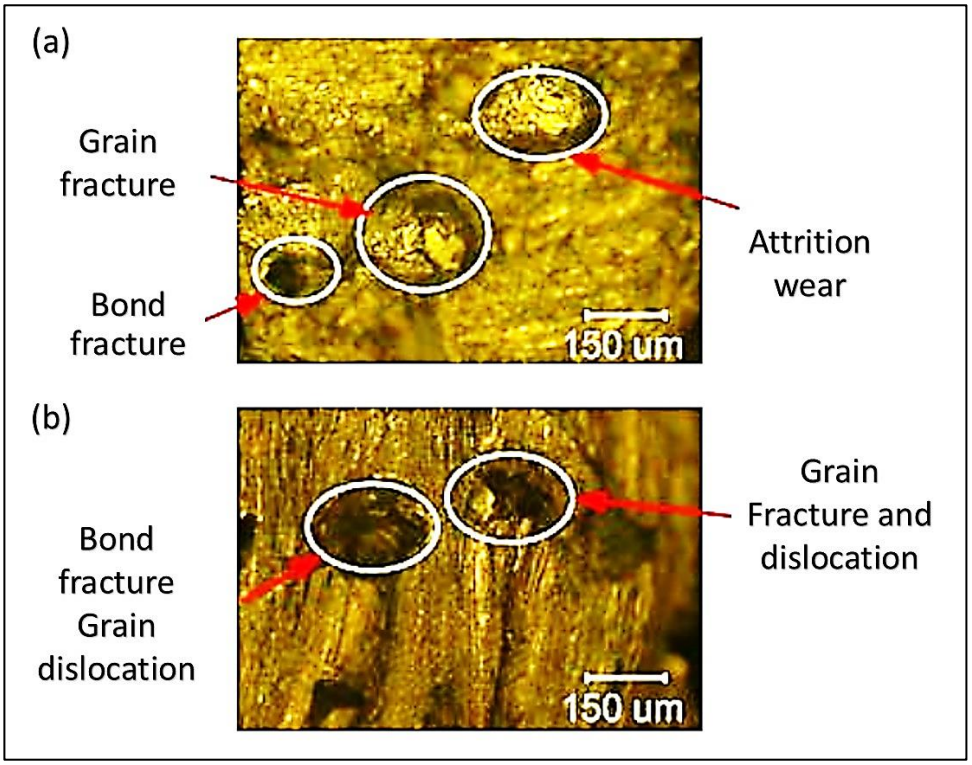


Figure 2.31 Tool wear in experiment 1, obtained with (a) UAG and (b) conventional milling [30]

Experiment 2

The machining parameters in experiment 2 are listed in **Table 2.5**. The tested cutting depth range was higher than the vibration amplitude of 10 µm. The results shown in **Figure 2.32** indicate that the reduction in cutting force was small. At some points, it could be greater than that in conventional diamond milling.

Table 2.5 Experiment 2 parameters [30]

Process variable	*Unit*	*Value*
Spindle speed	r/min	1000, 3000, 6000
Feedrate	mm/min	50, 100, 300
Cutting depth	µm	10, 20, 60

Thus, to obtain good diamond milling performance, the vibration amplitude of the US machine must be greater than the cutting depth. Another significant finding is that the depth of the surface damage with lateral cracks and the chipping size caused by UAG were less than those obtained with conventional diamond milling, The material removal mechanism was by brittle fractures in both the conventional and non-conventional methods.

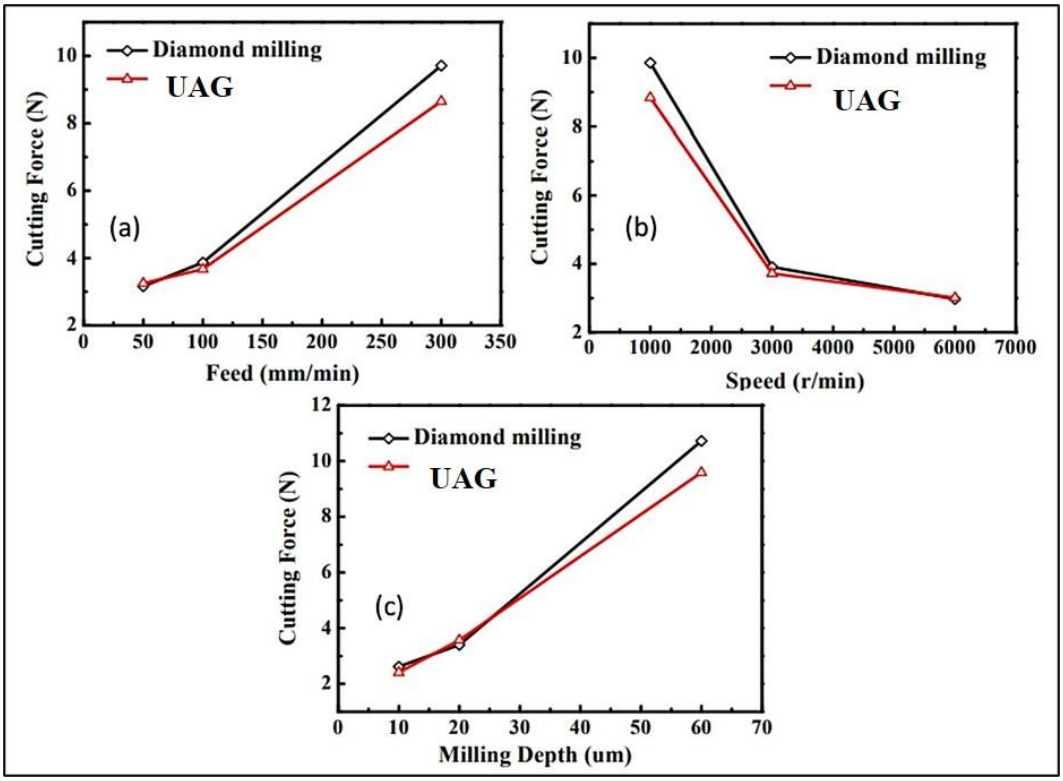


Figure 2.32 Effects of the variable parameters, (a) feed, (b) speed, and (c) cutting depth, on the cutting forces in conventional diamond milling compared with UAG at cutting depth range of *A* = >10 µm [30]

Optimisation of the operation parameter for zirconia face milling by UAG using three levels of the five-factor Taguchi L27 orthogonal array design was used by Abdo et al. [62]. The tool used had inner and outer diameters of 1.5 and 4 mm, respectively. The diamond grain size was 16.2 nm. The factor levels are listed in **Table 2.6**.

Table 2.6 Machining parameter levels [62]

Level	Spindle speed (rpm)	Feed rate (mm/min)	Vibration frequency (kHz)	Vibration power supply (%)*	Cutting depth (mm)
1	2000	50	20	50	0.025
2	2400	100	21.5	60	0.05
3	6000	150	23	70	0.075

The result of the analysis of variance (ANOVA) indicated the effects of the parameters on the cutting forces as follows: spindle speed (73%), feed rate (17%), amplitude (2.8 %), frequency (0.66%), and cutting depth (0.06%). The ANOVA of MRR revealed that only feed rate and cutting depth affected the MRR (both by 46%). The optimum machining parameters for the cutting forces were at the following conditions: N = 2000 rpm, F = 50 mm/min, cutting depth of 0.025 mm, frequency of 20 kHz, and amplitude of 50%. A minimum cutting force of 20.6 N was obtained. Moreover, the optimised parameters for the MRR conditions were as follows: N = 6000 rpm, F = 150 mm/min, cutting depth of 0.075 mm, frequency of 21 kHz, and amplitude of 50%, which obtained a minimum MRR of 0.307 mm^3/sec.

Abdo et al. [63] investigated the usefulness of the UAG method in the fabrication of micro-channels on ZrO_2 workpieces. A full factorial design of five factors, namely speed, feed, amplitude, frequency, and cutting depth, was used to analyse their effects on surface roughness

Ra, edge chipping, depth error, and width error. The five-factor levels are listed in **Table 2.7**. The tool used had a diameter of 0.5 mm, as shown in **Figure 2.33**.

Table 2.7 Machining parameter levels [63]

Parameter (unit) / levels	Lower level	Center point	Higher level
Cutting speed (S), rpm	3000	5000	7000
Feed rate (FR), mm/min	0.5	1	1.5
Depth of cut (DOC), mm	0.0125	0.025	0.0375
Amplitude (A), µm	5	20	35
Frequency (F), kHz	22	24	26



Figure 2.33 Cutting tool [63]

From 40 tests, the following optimal parameters were identified: F = 0.5 mm/min, cutting depth of 0.0125 mm, frequency of 26 kHz, N = 3000 rpm, and amplitude of 35 µm. These obtained the following values: Ra = 0.26 µm, edge chipping = 10.1 µm, depth error = 4.2%, and width error = 7.2%.

Moreover, Abdo et al. [64] investigated the effects of tool path and tool overlapping at several rates (0%, 5%, 10%, 15%, 20%, and 25%) of the tool diameter on the surface roughness, when machining a pocket in alumina (99.99%) using the UAG method. The tool used had outer and inner diameters of 2 and 1 mm respectively, with a diamond grain size of D46. The experimental setup is shown in **Figure 2.34.** The optimum machining parameters obtained were as follows: N = 8000 rpm, feed rate of 2 mm/min, cutting depth of 0.15 mm, frequency of 25 kHz, and amplitude of 5µm. A minimum Ra value of 0.155 µm and Rt value of 1.4 µm were obtained in a cutting tool path direction combining uni-directional and zigzag paths at a tool overlapping rate of 20%. Two tools were used in the experiment. The end-of-life criterion was reaching a 5%-dimensional error rate. The tool end face wear obtained is shown in **Figure 2.35**. The tool was worn out by bond fractures and the plastic deformation at the end face edges due to the high applied pressure. The SEM images of the machined pockets showed that a smoother surface with a ductile material removal mechanism could be obtained at higher tool overlapping rates of 20–25%, as shown in **Figure 2.36**.

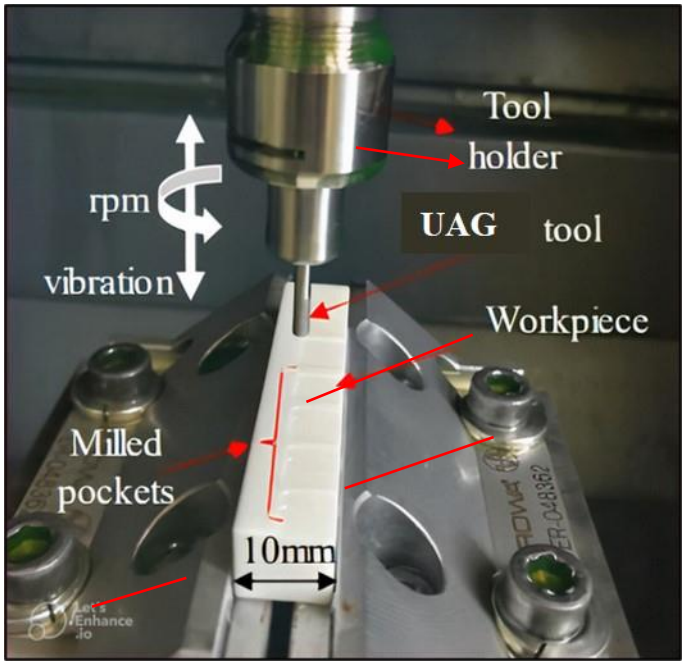


Figure 2.34 Experiment setup [64]

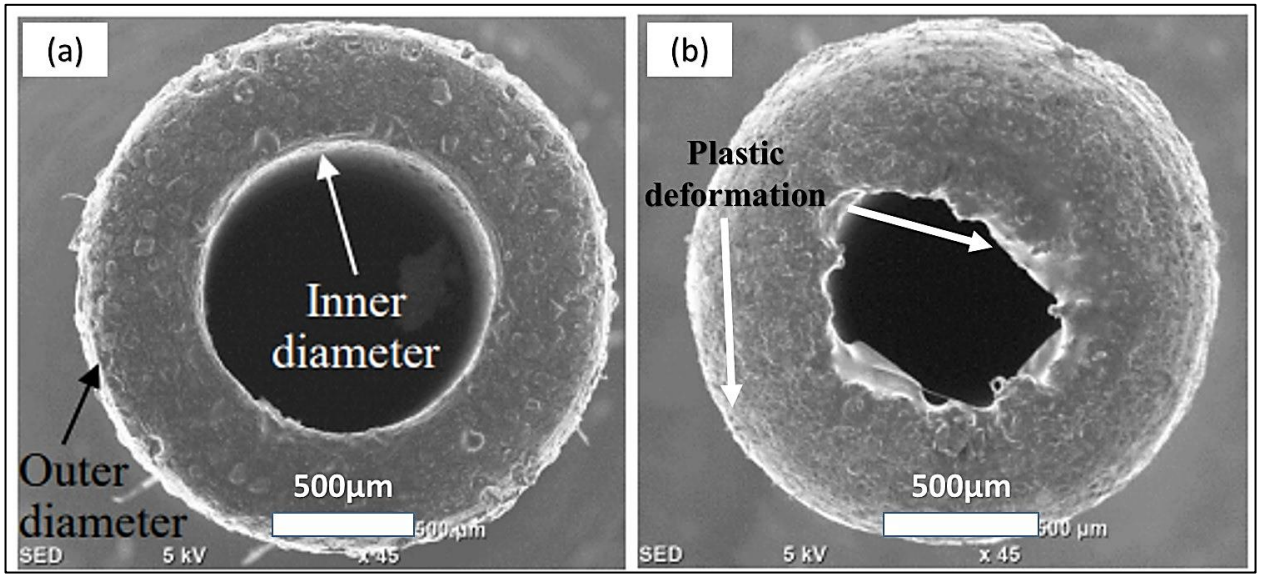


Figure 2.35 End face of (a) a new tool and (b) a worn tool after a dimensional error of 5% was reached [64]

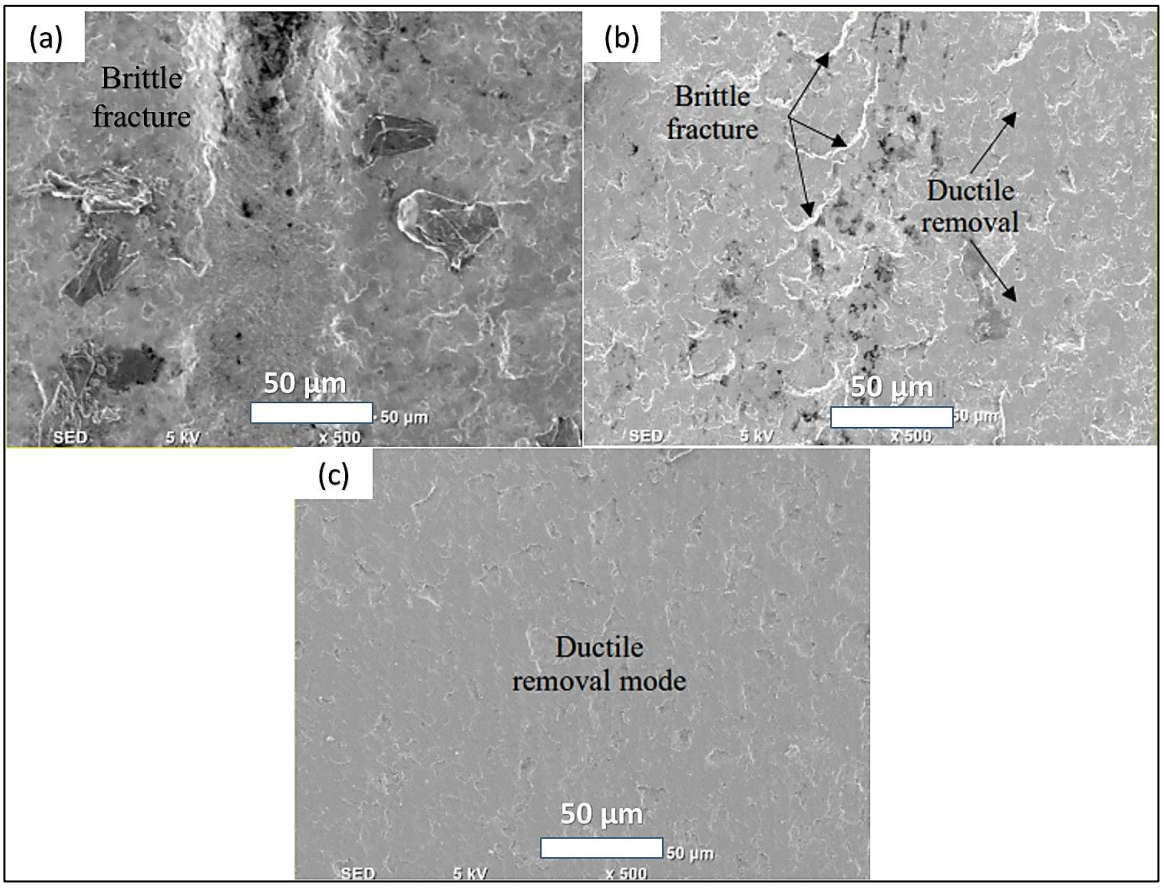


Figure 2.36 SEM image of the machined pockets at tool overlapping percentages of (a) 0%, (b) 10%, and (c) 20% [64]

Gong et al. [65] conducted comparisons between UAG of hard-brittle materials and conventional grinding. In their first experiment, they used K9 optical glass as the workpiece material, a diamond grinding tool with a 10-mm diameter, and water as cutting fluid. The machining cutting depth was 1 mm; stepover, 5 mm; speed, 4000 rpm; feed rate, 300 mm/min; and US amplitude, 4 µm at 20 kHz. The results showed that at the same machining conditions except that the vibration was turned off during conventional grinding, the tool wear in UAG showed less damage than that in conventional grinding.

In the second experiment, UAG was compared with high-speed machining (HSM). In UAG, an Al_2O_3 workpiece was used to machine a groove, whereas in HSM, a ferrite workpiece was used. The grinding tool used had a diameter of 0.3 mm. The machining parameters were set at several feed rates and cutting depths to investigate several MRR values. The results showed that a higher MRR was achieved with UAG when a deeper cut and lower feed rate were used, in contrast to the result of HSM for metals.

2.2.3 Summary

The Recent studies have investigated the cutting modes for hard and brittle materials when using an end mill and indicated that to achieve a smoother surface induced by the ductile cutting mode, the un-deformed chip thickness must be reduced to the value of the critical chip thickness, that must be smaller than material grains size [47]. However, over the last decades, knowledge has increased, producing new cutting tools such as cubic boron nitride (CBN), polycrystalline diamond (PCD), and diamond-coated tools, which have improved the conventional milling to cut hard-brittle materials such as advanced ceramics, titanium alloys, and glass in ductile or semi-ductile mode [37-41]. Moreover, it believed the use of ultrasonic vibration combined with

conventional milling or grinding is having the potentiality to improve the machinability of brittle and hard to cut materials.

Also, as Zhang et al. [30] mentioned the surface integrity of brittle materials has improved as the US amplitude was higher than cutting depth, but this is difficult to bee achieved in this project due to the low amplitude that produced from the used machine of rang 4 to 6 µm. The use of endmill to cut sintered advanced ceramics conventionally is rare due to the abrasive nature of these materials, that worn endmills fast.

However, the use of PCD and coated carbide cutters have shown good results as seen in Bian et al. [45,46] and Liu et al. [47] works. Liu has concluded that machining Al_2O_3 by CVD diamond coated cutter at MRR of 5-6 mm^3/min was possible. But it believed the utilized workpieces in this project could not be machined at MRR of 5-6 mm^3/min, because they are having hardness value greater than 1000 Knoop. Also, the effect of using cutting fluid in milling advanced ceramic was not clear, so it has been investigated.

It was obvious that there was no single study investigated the improvement that could be achieved when machining advanced ceramics by the combination of coated solid carbide end mills with US vibration. It believed that the potentiality is very high to increase the tool life, due to the decreases of cutting forces that produced from US vibration [30], as a result MRR could be increases. And the increment of MRR has direct influence on reducing the machining cost of advanced ceramics.

Benchmarking of the most used advanced ceramics in industry of ZrO_2, Al_2O_3, Si_3N_4, and SiC, when using coated solid carbide tools or diamond grinding points has never investigated before, which believed will help to provide a better understanding of how each ceramic properties, such as fracture toughness, hardness, and thermal conductivity will affect the tool life. So, it could be

good help for industry to tailor a designated tool to each ceramic material in terms of material and geometry of the tool, which will make advanced ceramics machining more efficient and effective. On following the research methodology of the project will be presented.

3. RESEARCH METHODOLOGY

In this chapter the project methodology, materials and tools, testing equipment, and measuring procedure will be presented. To achieve the main goal of the study in investigating advanced ceramic machinability, CVD diamond-coated end mills and diamond grinding points were used. The experimental work was divided into two phases. Each phase had four main stages, as shown in **Figure 3.1**. The research methodology depended mainly on benchmarking Al_2O_3, Si_3N_4, and SiC against ZrO_2, and the assessment criteria included tool wear, surface roughness, material removal mechanism, and cutting forces. Moreover, the effect of UAM were investigated and compared with the results obtained using conventional machining.

ZrO_2 was selected as the benchmarking material because of its good machinability compared to the other advanced ceramics. It also has the lowest hardness value (HV = 1200 kgf/mm^2), which significantly affects machinability. According to the literature review, ZrO_2 has a surface finish mainly obtained in ductile fracture cutting mode, which makes its machinability close to that of metals. In **phase 1**, 4-mm-diameter solid carbide CVD diamond-coated end mills were utilised. In **phase 1.A**, the machining of ZrO_2 was examined at different operation parameters. Two milling types, side and slot milling, were tested. The preferred milling type was selected on the basis of the best tool life.

In **phase 1.B**, the benchmarking of Al_2O_3, Si_3N_4, and SiC against ZrO_2 was performed using the parameters obtained in **phase 1.A**. Then, in **phase 1.C**, ZrO_2 was investigated using the UAM technique, where the same machining parameters selected in **phase 1.A** were used but with US vibration, high and low vibration amplitudes. In **phase 1.D**, the benchmarking of Al_2O_3, Si_3N_4, and SiC against ZrO_2 was performed using the UAM method with the preferred US amplitude obtained in **phase 1.C**. The benchmarking results were compared with those obtained with

conventional benchmarking to assess any improvement in machinability. **Phase 2** is almost a replication of **phase 1** except that the tool used was a single-layer electroplated diamond grinding point of 4-mm diameter and grit size of D126. The grinding point was used to machine slots on ceramic surfaces with the end face of the tool. This study will contribute more information about the practice of advanced ceramic machining to help and guide the industry in terms of the parameters that affect tooling performance, such as coating thickness, end-face profile geometry, diamond grit size, and bonding material. Moreover, the benchmarking approach differentiated the machinability of several advanced ceramics, which will provide better understanding of the influence of each ceramic properties on tool life performance in both conventional and non-conventional machining. On following section, the utilized tools and materials will be presented.

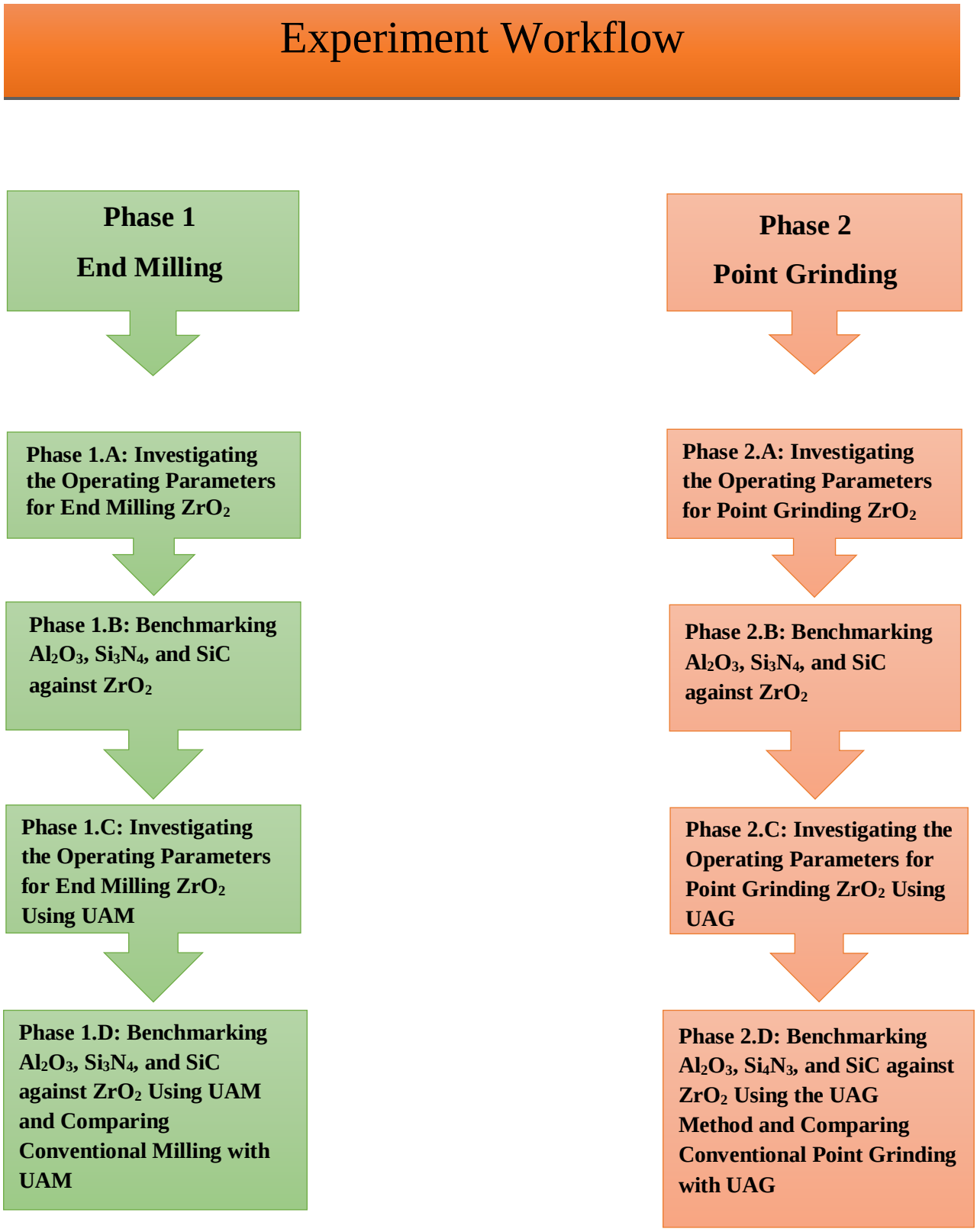


Figure 3.1 Project workflow

3.1 Materials and Tools

3.1.1 Workpieces

The four sintered advanced ceramics used as specimens were zirconia (ZrO_2), alumina (Al_2O_3), silicon nitride (Si_3N_4), and silicon carbide (SiC), manufactured by Goodfellow (**Figure 3.2**). The batch of workpieces have been ordered once, and two pieces of each ceramic have been used during the project. The mechanical properties of the sintered ceramics as provided by the manufacturer are shown in **Table 3.1**. It is noticeable that some of the advanced ceramics properties such as hardness and shear strength are having a range of values instead of one rigid number, and that refer to the non-uniformity of the ceramic microstructure that affected by the purity and sintering environment. Which made the same specimen sometimes exhibit variable hardness value at different locations.

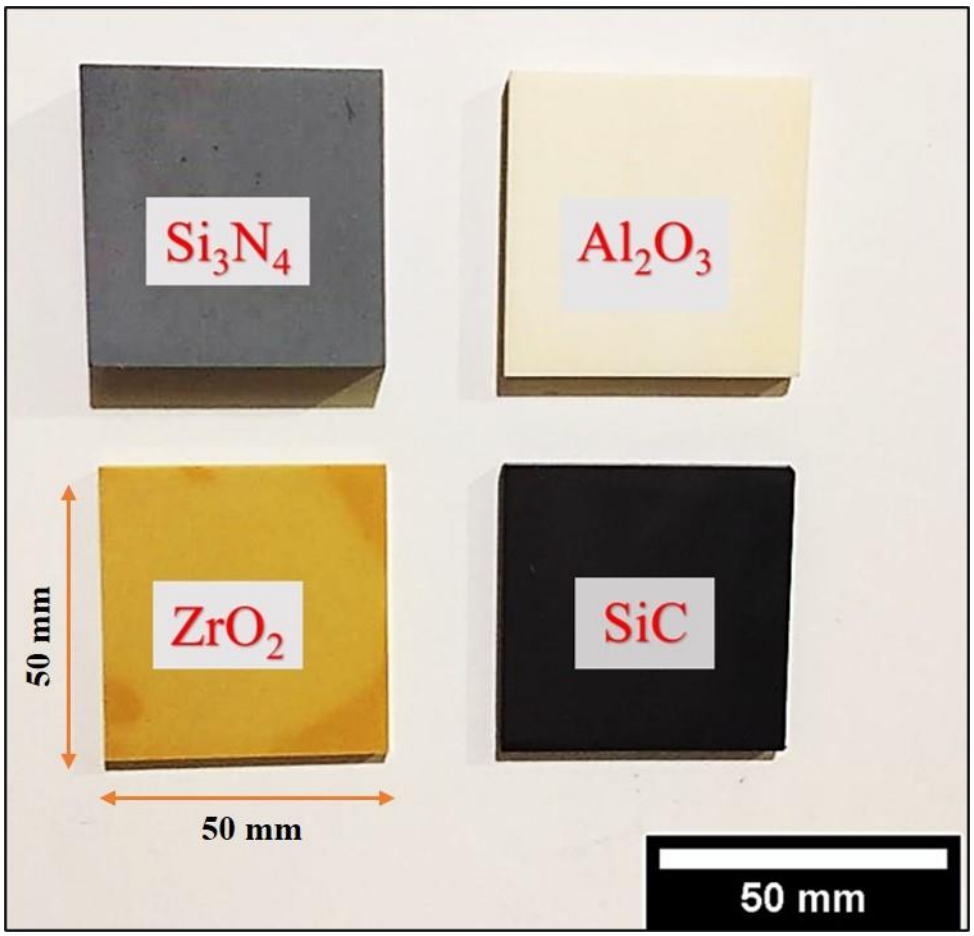


Figure 3.2 Sintered advanced ceramics used in the project

Table 3.1 The properties of the experimental ceramics with stainless steel 316

Material property	ZrO_2– stabilized with MgO	Al_2O_3– 99%	Si_3N_4– hot pressed	SiC
Hardness, Vickers (kgf/mm^2)	1200	1500–1650	1700–2200	2400–2800
Compressive strength (MPa)	1500–2000	2200–2600	2000–3500	1000–1700
Shear strength (MPa)	414	330	480–960	210–380
Tensile modulus (GPa)	200	300–400	280–310	200–500
Density (g/cm^3)	5.74	3.9	3.11	3.15
Melting point (°C)	-	2100	-	2650–2950
Thermal conductivity ($W\ m^{-1}\ K^{-1}$)	1.5–2.5	26–35	15–43	12
Upper continuous use temperature (°C)	1000	-	1100–1650	1500–1650
Workpiece dimensions (mm)	50 × 50 × 4	50 × 50 × 5	47 × 47 × 10	50 × 50 × 4

3.1.2 Cutting Tools

3.1.2.1 Phase 1, End Milling

Phase 1 was conducted using CVD diamond-coated carbide end mills manufactured by SECO Tools owing to their high hardness, strength, and chemical stability that could resist advanced ceramics. Using small-diameter end mills rather than a diamond grinding wheel could help increase the MRR in sintered ceramics. Complex shapes could also be produced. **Figure 3.3** and **Table 3.2** show the images and specifications of the end mills used in this study.

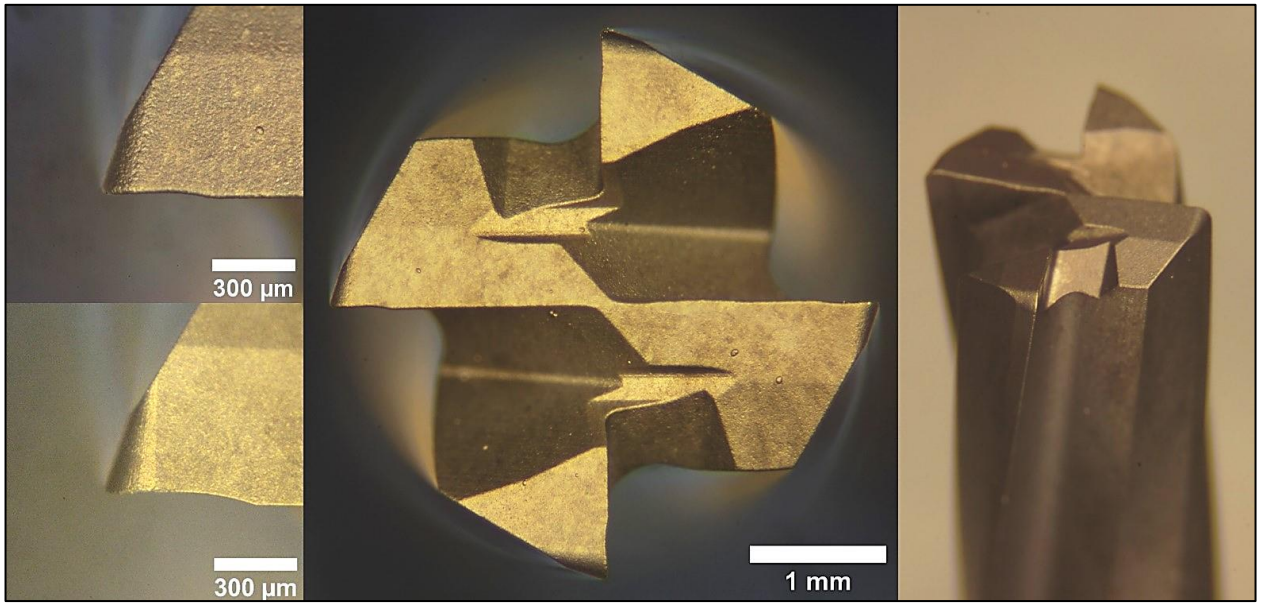


Figure 3.3 CVD diamond-coated end mill images (edge, end face, and side view)

Table 3.2 CVD diamond-coated end mill specifications

Description	Value
Cutting diameter	4.000 mm
Flute helix angle	10.0°
Peripheral cutting-edge count	4
Corner radius	0.20 mm
Cutting edge radius	20 µm
Net weight	0.012 kg
Coating type	DURA

The tool coating thickness was measured using an Alicona microscope, as shown in **Figure 3.4**. The diamond coating thickness was approximately 15 µm.

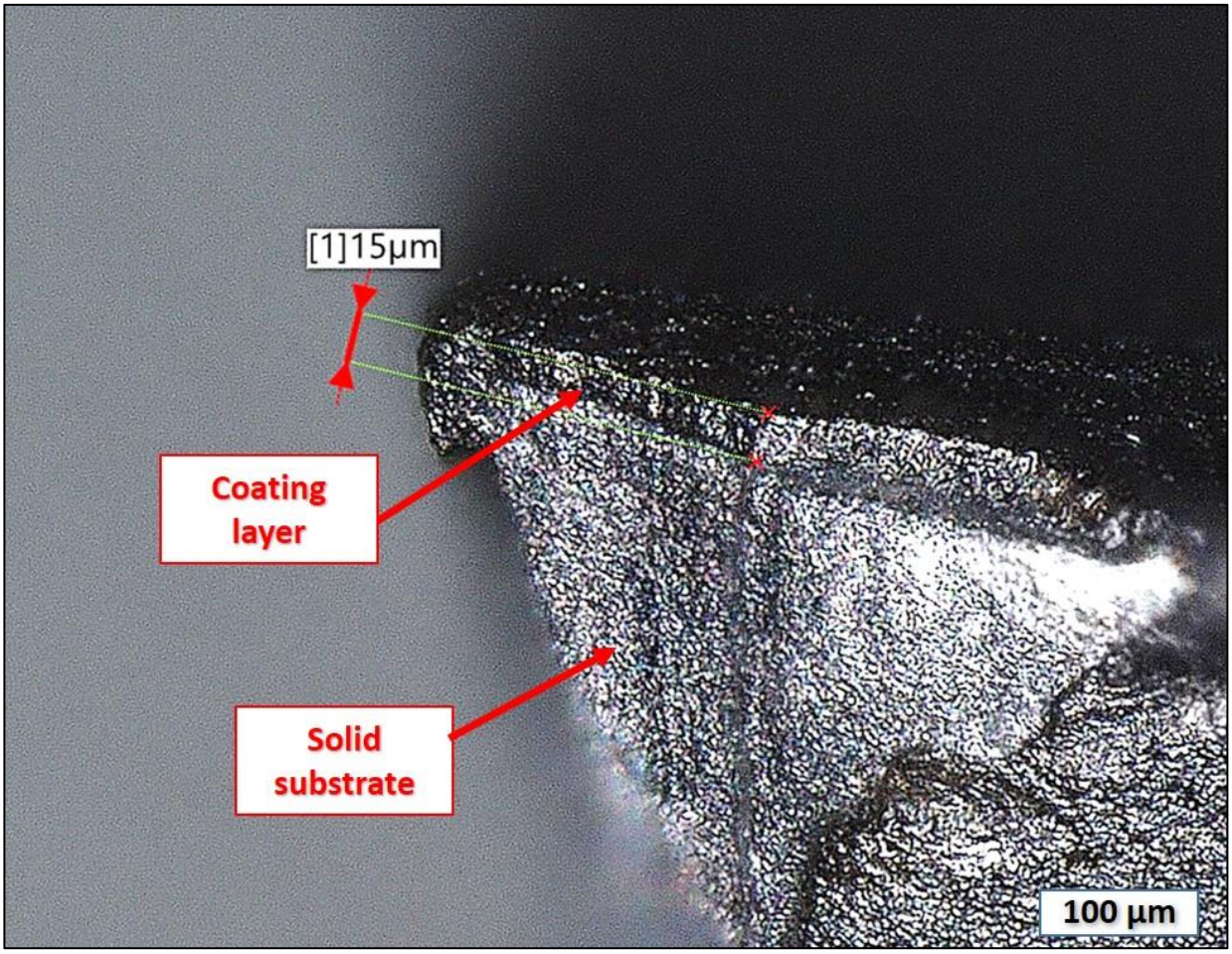


Figure 3.4 Thickness measurement of the CVD diamond coating

3.2.2.2 Phase 2, Point Grinding

Phase 2 was conducted using electroplated diamond grinding points (manufactured by KRASCO) with a diameter of 4 mm, grit size of D126, 3-mm-diameter steel shank, and 40-mm tool length, as shown in **Figure 3.5**. Diamond grinding points were used for advanced ceramics owing to their higher hardness and strength. Using small-diameter points rather than the conventional diamond grinding wheel allows for grinding more complex shapes. In addition, D126 size used in this project because they have the advantage of grain durability that can resist breaking down under high pressure. As the grains become finer, the force per particle increases; as a result, the grains become easier to break down.

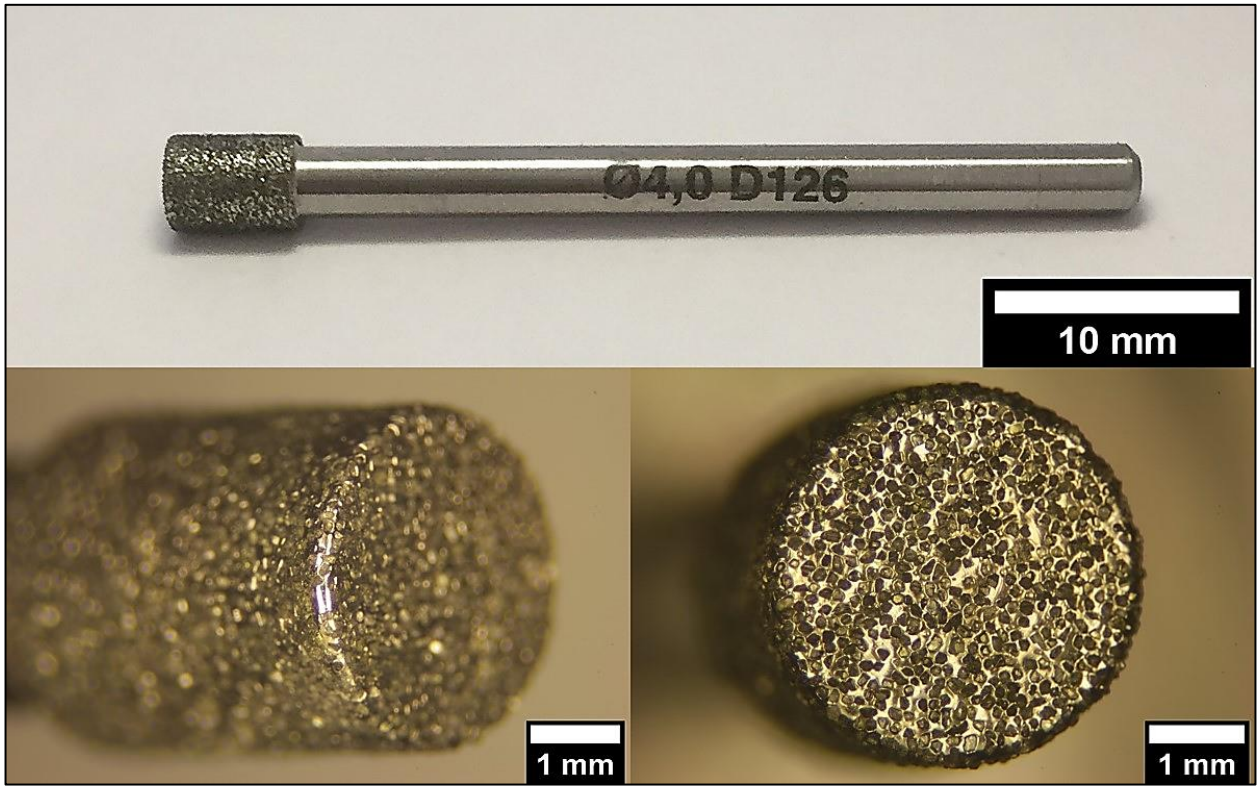


Figure 3.5 Electroplated diamond grinding point of D126 grit size: side and end views

3.1.3 Testing Equipment

The five-axis DMG Ultrasonic 20 Linear (**Figure 3.6**) was used to perform all project tests except for **phase 1.A** because the DMG machine arrived at the laboratory during the second year of the project. The technical characteristics of the CNC machine are listed in **Table 3.3**. All tests in **phase 1.A** were conducted using the three-axis CNC machine (model FX-5), manufactured by Matsuura (**Figure 3.7**), with a maximum spindle speed of 20,000/min. The cutting fluid used was from Quaker Houghton Hocut B795, which was maintained at a concentration of 10% vol, with two nozzles of flow rate of 4.5 L/min per nozzle.

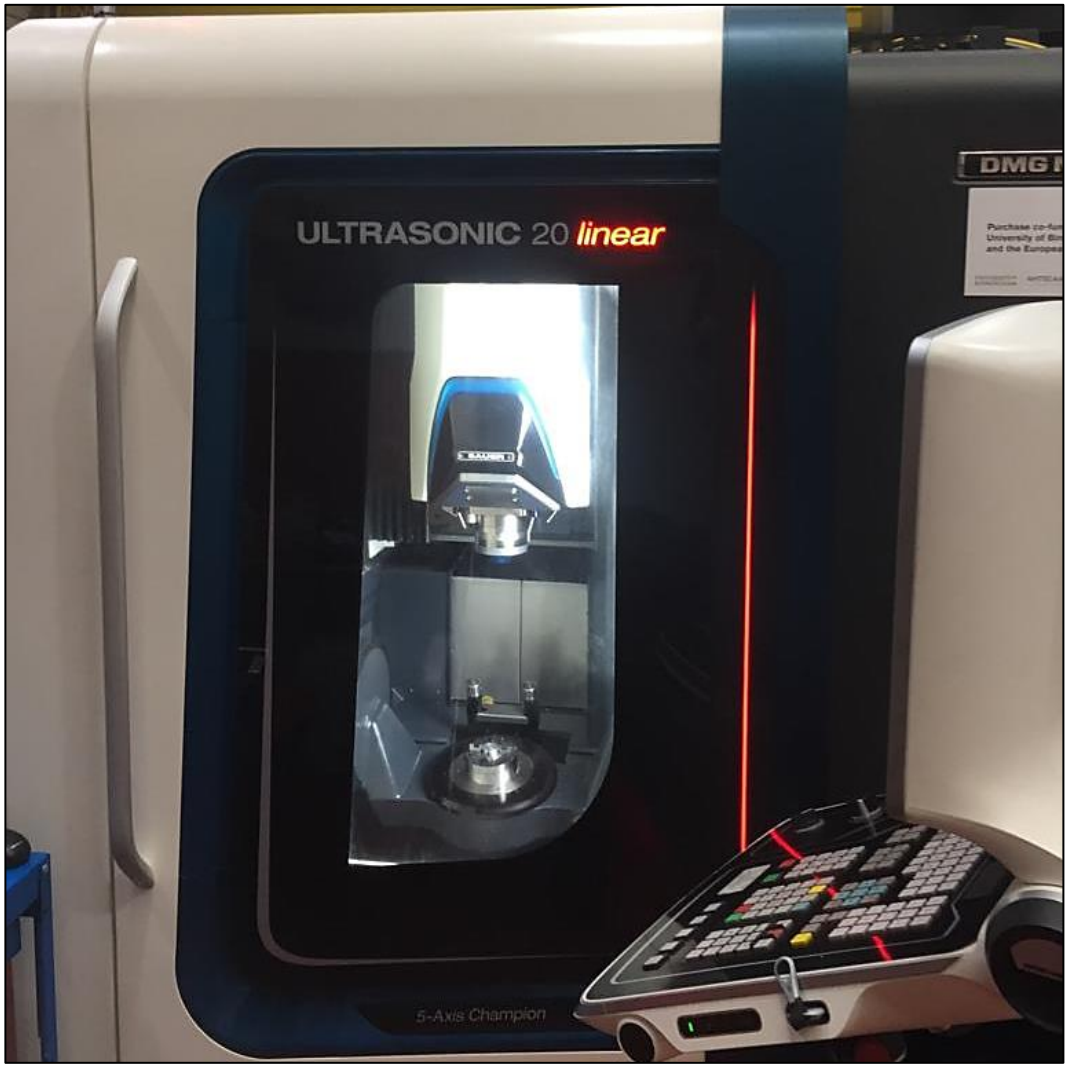


Figure 3.6 Five-axis DMG Ultrasonic 20 Linear

Table 3.3 Technical data of DMG Ultrasonic 20 Linear

Characteristic	Value
Number of axes	5
Traverse of *x*/*y*/*z*-axis	200/220/280 mm
Traverse of A and C axes	−30º to 130º and 360º
Position accuracy	<5 µm
Rapid traverse up to	40 m/min
Maximum speed	42000 rpm
Amplitude range	0–8 µm
Frequency range	18–48 kHz
Cutting fluid Hocut 795 B	Q = 4.5 L/min, 10% vol



Figure 3.7 Three-axis Matsuura FX-5 CNC machine

The cutting forces for all the tests were measured using a stationary dynamometer from Kistler type 9257A at sampling rate of 3000Hz, and the obtained signals were analysed using DynoWare. The surface roughness in **phase 1** was measured using an Alicona Infinite Focus microscope (**Figure 3.8a**) because of the narrow-machined surface width obtained from side milling. The surface roughness in **phase 2** was measured using a portable device (Surftest SJ-310) from Mitutoyo. The difference in surface roughness readings between two measuring devices was small as shown in **Figure 3.9.** Material removal mechanism imaging in the study was performed with an Alicona microscope at an original magnification of ×20. The tool wear observation in both end mills and grinding points was observed using an optical microscope, as shown in **Figure 3.8(b)**. Diamond coating thickness measurement and magnified worn cutting edges were imaged by Keyence digital microscope **Figure 3.8 (c).**

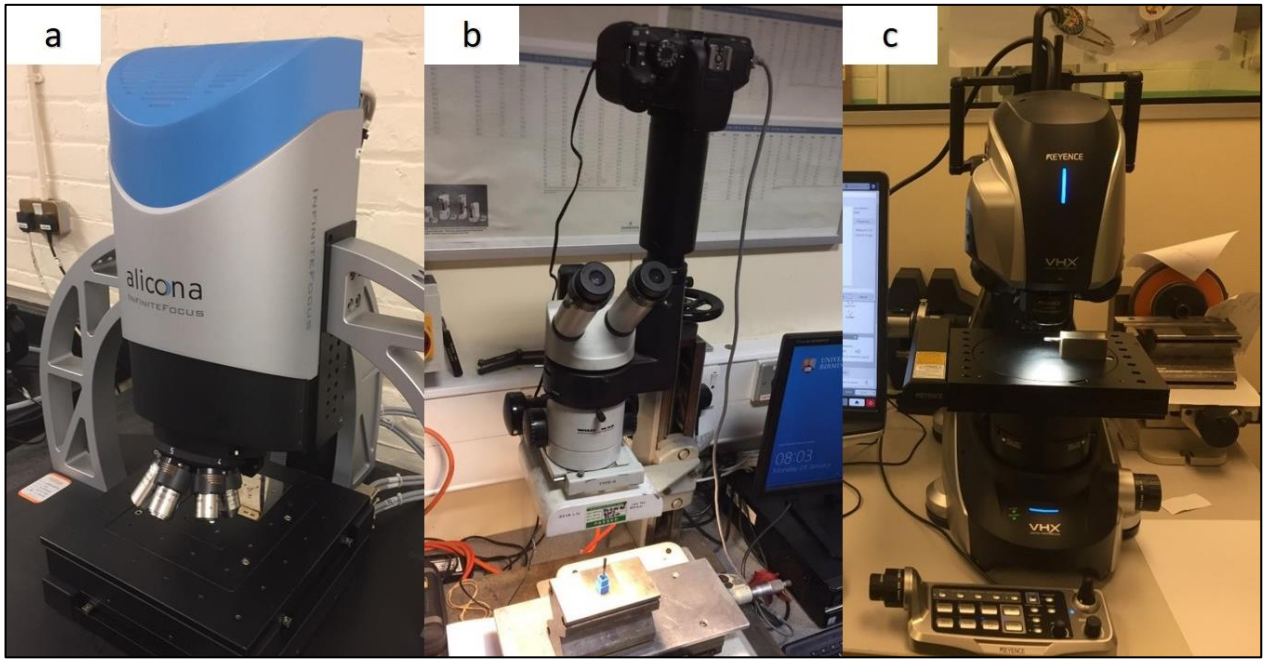


Figure 3.8 Microscopes used: (a) Alicona Infinite Focus microscope and (b) optical microscope for tool wear observation (c) Keyence digital microscope

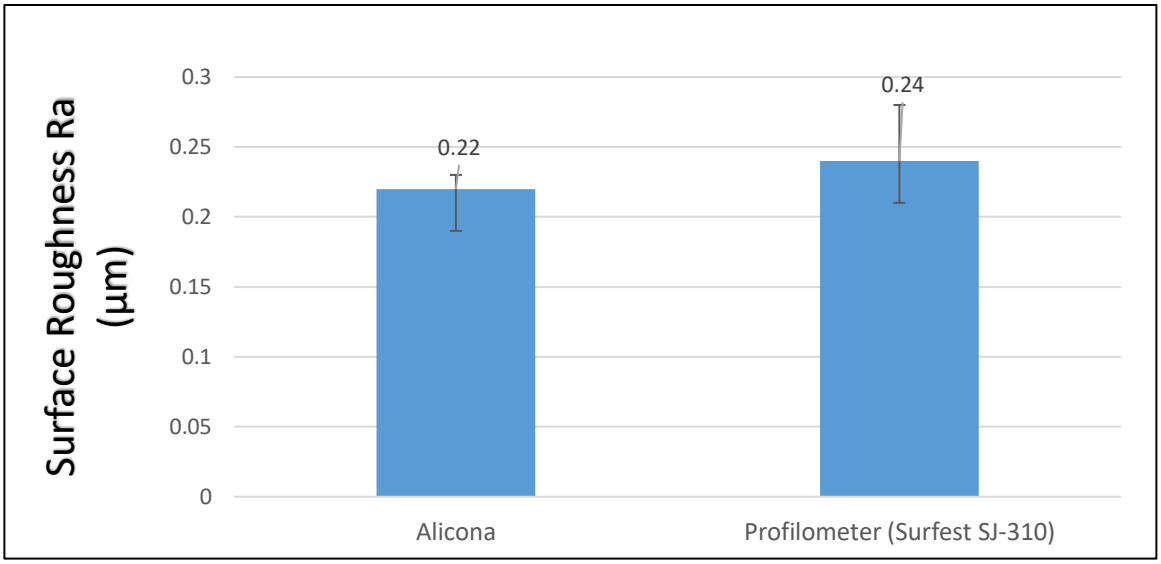


Figure 3.9 The surface roughness measurement variation between Alicona and stylus profilometer of Si_3N_4 sample that end milled at V=60 m/min, *fz* =0.5 µm/tooth, DOC=0.25 mm, and WOC=0.5 mm

3.2 Measuring Procedure

3.2.1 Phase 1, End Milling

a) Tool Wear/Life

The end-of-experiment criterion was reaching either the cutting distance of 2000 mm or the end of tool life. The evaluation standard of tool life was based on the ISO-8688-1 tool life criterion, where the tool is considered worn at average flank wear width of VB = 0.3 mm. Tool wear was checked after cutting 10 mm long for the first 50-mm cutting path and every 50 mm thereafter. All side milling tests were conducted in a standard manner, where the cutters rotate against the feed direction. Tools runout were controlled at 5-µm.

b) Surface Roughness

The average of three readings of the arithmetic Ra was measured at three locations (entrance-middle-end) along the last cutting pass, parallel to the feed direction, with a cut-off of 0.8 mm and an evaluation length of 4 mm. All readings were taken after the cutter's average flank wear reached VB = >0.3 mm. The machined surfaces were imaged at the end of each experiment using Alicona microscope at an original magnification of ×20 to investigate the material removal mechanism.

c) Cutting Forces

The average of six averages of the maximum peak-to-peak amplitudes were taken at six locations along the cutting path. Three readings were taken at each location. The measuring interval for one reading was 2 seconds, which represents 160 revolutions, to overcome the drifting issue, as shown in **Figure 3.10**.

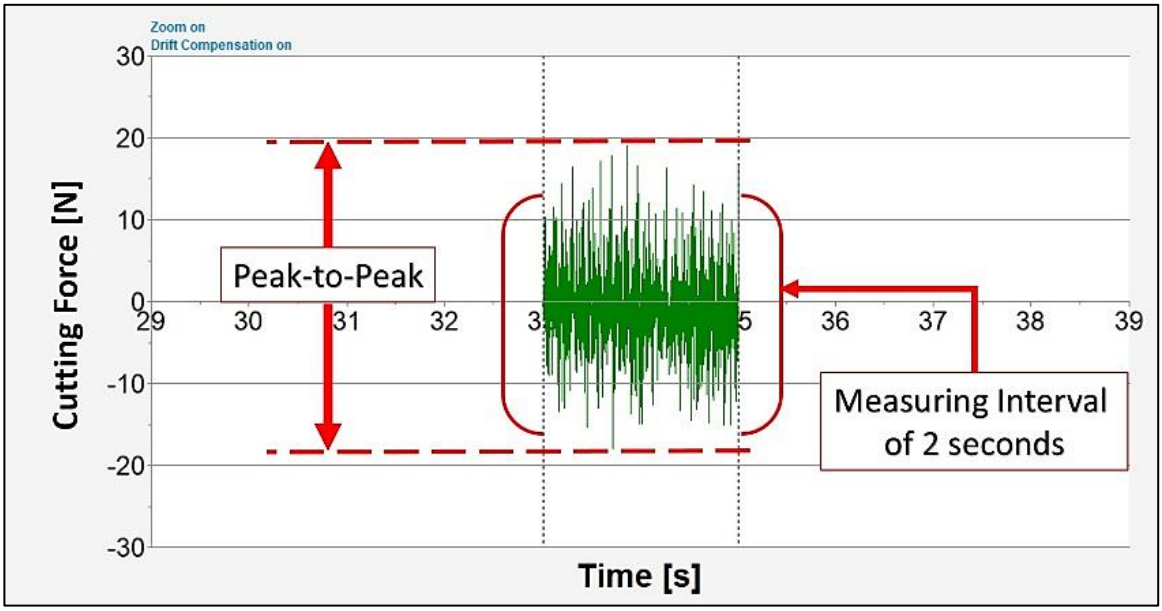


Figure 3.10 Example of one measurement of peak-to-peak value of approximately 38 N

3.2.2 Phase 2, Point Grinding

a) Tool Wear/Life

The end-of-experiment criterion was either the diamond grinding point machine a slot of 0.1-mm depth for 100 mm long, approximately 40 mm^3, or the tool's electroplated bond removed and worn. Diamond grain wear was observed on the optical microscope after every pass of 20 mm. All images of tool wear were taken at the end of each experiment.

b) Surface Roughness

The average of three readings of Ra at three locations (entrance-middle-end) on the last machining pass surface was taken parallel to the grinding feed direction. The machined surfaces were imaged at the end of each experiment using an Alicona microscope at an original magnification of ×20 to investigate the material removal mechanism.

c) Grinding Forces

The average of six averages of the maximum peak-to-peak amplitudes was taken at six locations along the grinding path. Three readings were taken at each location. The measuring interval for one reading was 2 seconds, as shown in **Figure 3.10**.

3.3 Experimental Procedure

3.3.1 Phase 1, End Milling

3.3.1.1 Phase 1.A: Investigating the Operating Parameters for End Milling ZrO_2

In **phase 1.A**, the machinability of ZrO_2 was investigated using the Matsuura FX-5 CNC machine at four sets of parameters. The four test sets are shown in **Table 3.4**, ordered according to their MRR values from high to low. The four combination sets can be divided into two milling types, slot milling, represented by tests 1 and 3, and side milling, represented by tests 2 and 4. Both types are illustrated in **Figure 3.11**. All tests were conducted at a cutting speed *V* of 60 m/min or spindle speed of 4777 rpm. The objectives in investigating the four sets were as follows: to obtain a machining parameter that will result in a reasonable tool life around 2000 mm that could be used for benchmarking in **phase1.B**; The effects of the cutting depth on slot milling and feed on side milling were also investigated.

Table 3.4 Machining parameter sets at cutting speed of 60 m/min (4777 rpm), (**phase1.A**)

Test No.	Feed rate, *f* (mm/rev)	Axial cutting depth, DOC (mm)	Radial cutting depth, WOC (mm)	MRR (mm^3/min)
1	0.002	0.12	4	4.58
2	0.004	0.25	0.5	2.38
3	0.002	0.06	4	2.29
4	0.002	0.25	0.5	1.19

The assessment criteria for **phase 1.A** were only tool life and surface roughness. All tests were conducted only once, and the preferred set for benchmarking was replicated for a confirmation run. The experimental setup is shown in **Figure 3.12**.

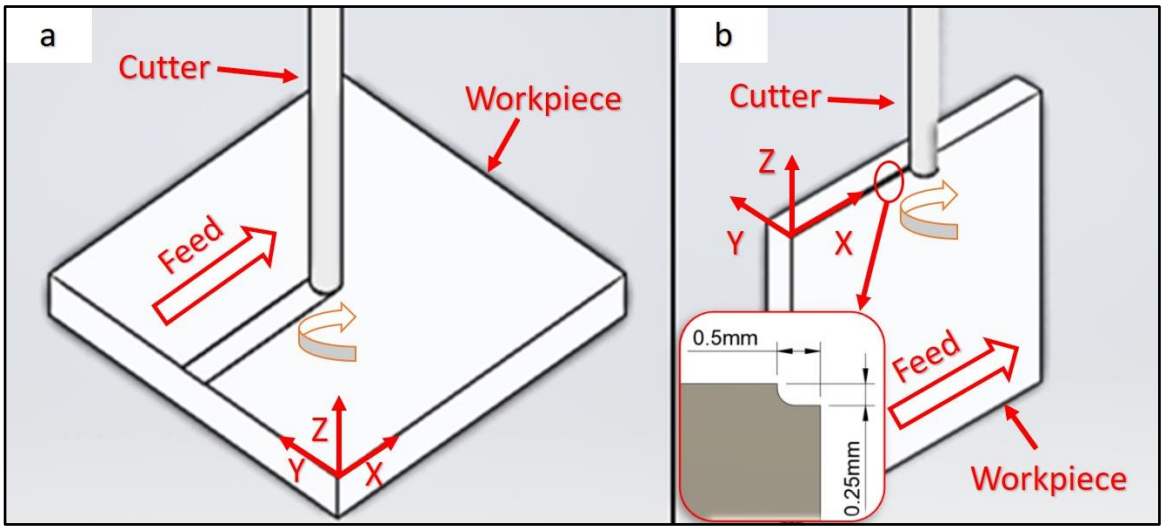


Figure 3.11 Schematic illustrating the milling process in (a) slot milling (tests 1 and 3) and (b) side milling (tests 2 and 4), (**phase 1.A**)

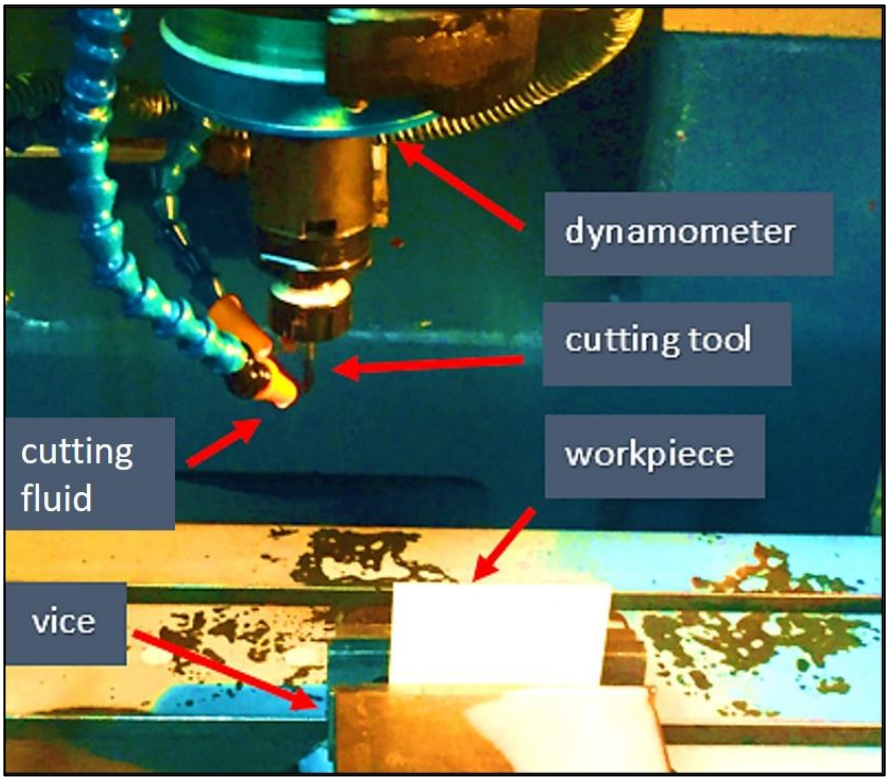


Figure 3.12 Experimental setup (**phase 1.A**)

3.3.1.2 Phase 1.B: Benchmarking Al_2O_3, Si_3N_4, and SiC against ZrO_2

In **phase 1.B**, the benchmarking of Al_2O_3, Si_3N_4, and SiC against ZrO_2 was performed on the basis of the results of **phase 1.A**. The most suitable machining parameters for benchmarking in side milling the four ceramics were as follows: axial cutting depth, 0.25 mm; radial cutting depth, 0.5 mm; feed rate, 9.55 mm/min; *f*z 0.5µm/tooth; spindle speed, 4777 rpm; and cutting speed *V*, 60 m/min. As discussed earlier, in **phase 1.A**, the selected parameter set resulted in the longest tool life (1800 mm) when milling ZrO_2. Thus, it will be more helpful to demonstrate the variation in the machinability of the four ceramics when using these parameters. The experimental setup and a schematic of machining process are shown in **Figure 3.13**.

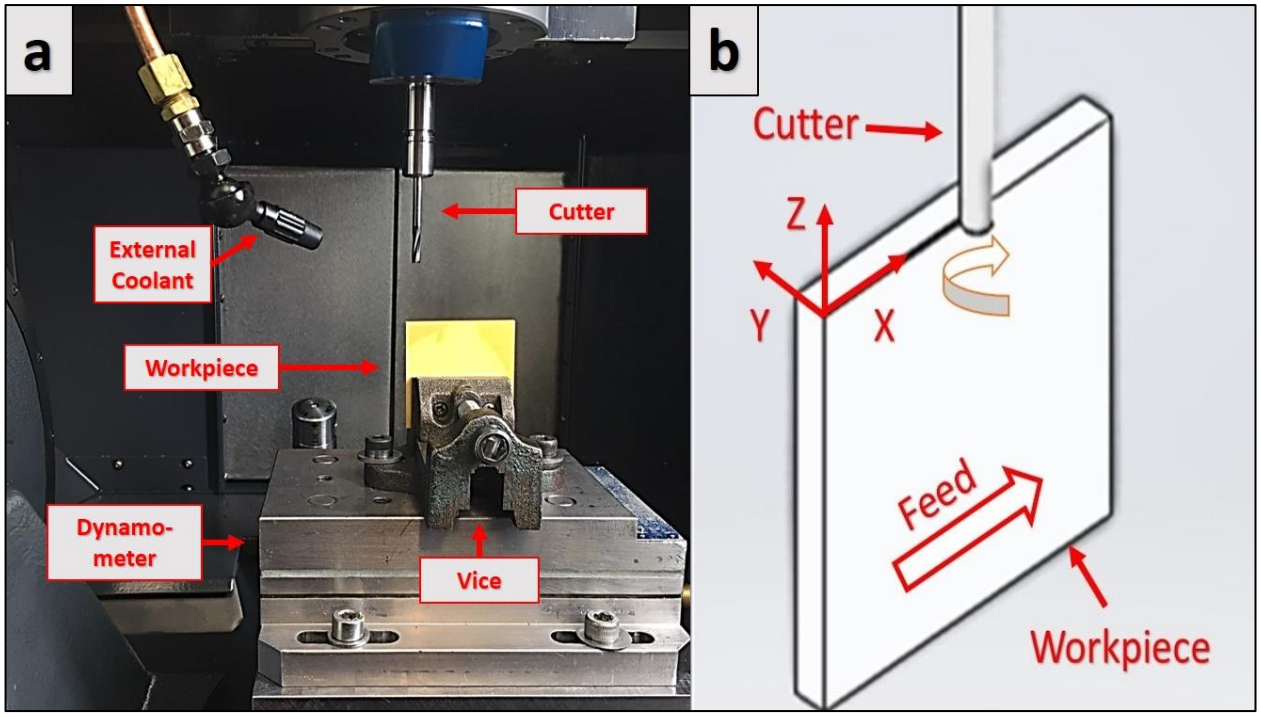


Figure 3.13 Illustration of (a) experimental setup, (b) machining process (**phase 1.B**)

3.3.1.3 Phase 1.C: Investigating the Operating Parameters for End Milling ZrO_2 Using UAM

On the basis of the results of **phase 1.A**, side milling ZrO_2 at a spindle speed of 4777 rpm (V = 60 m/min), feed rate of 9.5 mm/min (fz = 0.5 µm/tooth), axial cutting depth of 0.25 mm, and radial

cutting depth of 0.5 mm achieved a tool life of 1800 mm cutting length. The UAM was assessed using the same parameters but with US vibration. Two US vibration amplitude levels at a frequency of 33.5 kHz was investigated, at a low-level range of 0.5–2 µm and high-level range of 2–4 µm, as shown in **Table 3.5**. The amplitude measurement was performed before testing in the air with a laser scanner integrated into the CNC machine, as no method was available to measure US amplitude during machining. The machinability assessment included tool life, surface roughness, material removal mechanism, and cutting forces.

Table 3.5 Amplitude levels at a resonance frequency of 33.5 kHz (**phase 1.C**)

Parameter	Low	High
Amplitude range* (µm)	0.5–2	2–4
Power (W)	8–15	18–25

*Amplitude measured in the air.

During amplitude measurement, some degree of non-stability was observed in the US generator vibration. At the beginning of the measurement, the amplitude value increased up to 16 µm before it decreased to the setting value. The US generator started losing its amplitude after of machining of 50 mm, because of heating up. Also, it was difficult to know if the US generator is producing vibration while machining. Therefore, in this phase, each test was replicated twice to insure the consistency of results. The experimental setup and a schematic of machining process are shown in **Figure 3.14**.

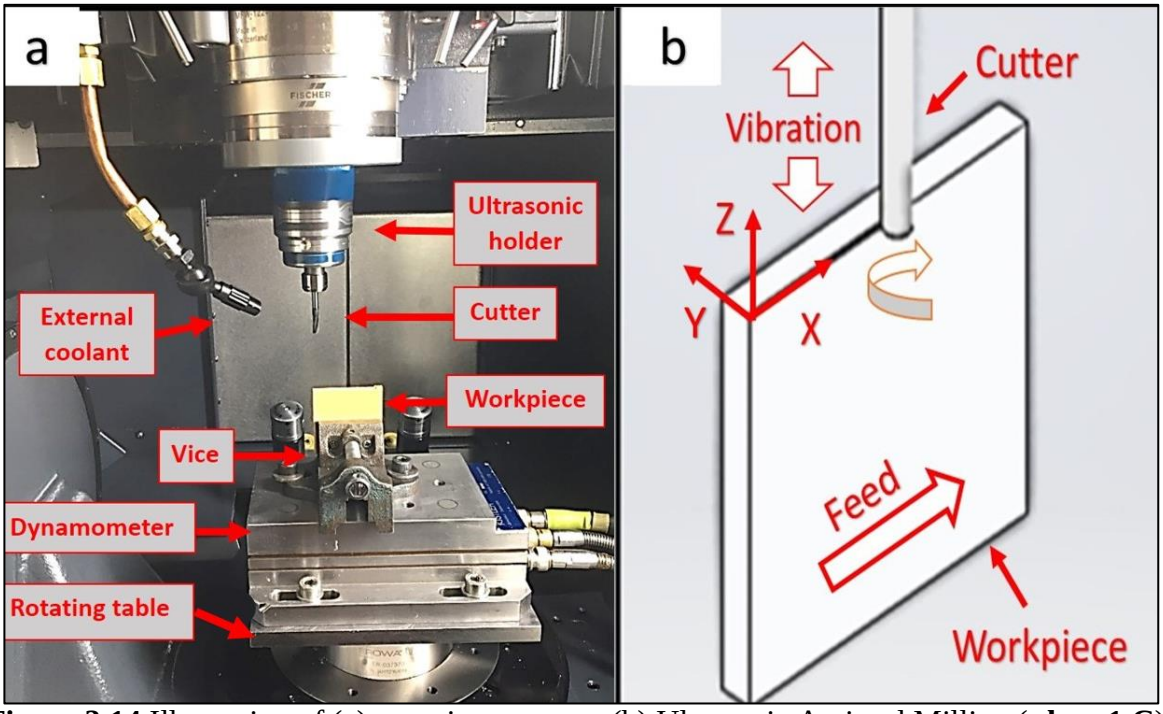


Figure 3.14 Illustration of (a) experiment setup, (b) Ultrasonic Assisted Milling (**phase1.C**)

3.3.1.4 Phase 1.D: Benchmarking Al_2O_3, Si_3N_4, and SiC against ZrO_2 Using UAM in Comparison with Conventional Milling

In this phase, Al_2O_3, Si_3N_4, and SiC were benchmarked against ZrO_2 at the low UAM parameters obtained in **phase 1.C**, where ZrO_2 had an amplitude range of 0.5–2 µm, frequency of 33,500 Hz, spindle speed of 4777 rpm (V = 60 m/min), feed rate of 9.5 mm/min (fz = 0.5 µm/tooth), axial cutting depth of 0.25 mm, radial cutting depth of 0.5 mm, and a tool life of 1300 mm, which is much better than the tool life of 150 mm obtained within the high US amplitude range of 2–4 µm. In terms of the surface roughness and cutting forces, better results were obtained at the low US amplitude, with an Ra value of 0.38 µm and F_Z value of 17.5 N, respectively, than at the high US amplitude, with an Ra value of 0.63 µm and F_Z of 79 N, respectively. Moreover, the results of UAM benchmarking were compared with those of conventional benchmarking to analyse the improvement that could be obtained using the UAM method. Each test in this phase was replicated

twice, and the best result was used for benchmarking. The experimental setup and a schematic of machining process are shown in **Figure 3.13** (**phase 1.C**).

3.3.2 Phase 2, Point Grinding

3.3.2.1 Phase 2.A: Investigating the Operating Parameters for Point Grinding ZrO_2

In **phase 2.A**, the machinability of ZrO_2 (HV = 1200 kgf/mm^2) was investigated using diamond grinding points, which were to be used as benchmarking points for the rest of ceramics in **phase 2.B** owing to the good machinability of ZrO_2. ZrO_2 was investigated at two levels of cutting speeds: at a high machining speed of 25000 rpm (V = 5 m/s) and feed rate of 5 mm/min and then at low machining speed of 5000 rpm (V = 1 m/s) and feed rate of 1 mm/min. Both tests were performed at the same feed per revolution (f = 0.2 µm/rev) and axial cutting depth of 0.1 mm. The parameter sets of the two tests are listed in **Table 4.3**. no replication conducted. The objectives for these two parameter sets were to investigate ceramic machining at a cutting speed of 5 m/s, which is used in point grinding hard metals, and to compare its effect on tool wear, surface finish, and cutting forces at a lower cutting speed of 1 m/s, which is used in ceramic machining, as reported in the literature, especially when the feed per revolution and axial cutting depth were maintained at the same value. Another objective was to obtain a machining parameter that will result in tool life at least of 100 mm that could be used in benchmarking in **phase 2.B**. The experimental setup and the illustration of the machined slots are shown in **Figure 3.15**.

Table 3.6 Machining parameters (**phase 2.A**)

Test	Feed rate (mm/min)	Feed/rev. f (µm/rev)	Spindle speed rpm	Cutting speed m/s	Cutting depth (mm)	MRR (mm^3/min)
High	5	0.2	25,000	5	0.1	2
Low	1	0.2	5000	1	0.1	0.4

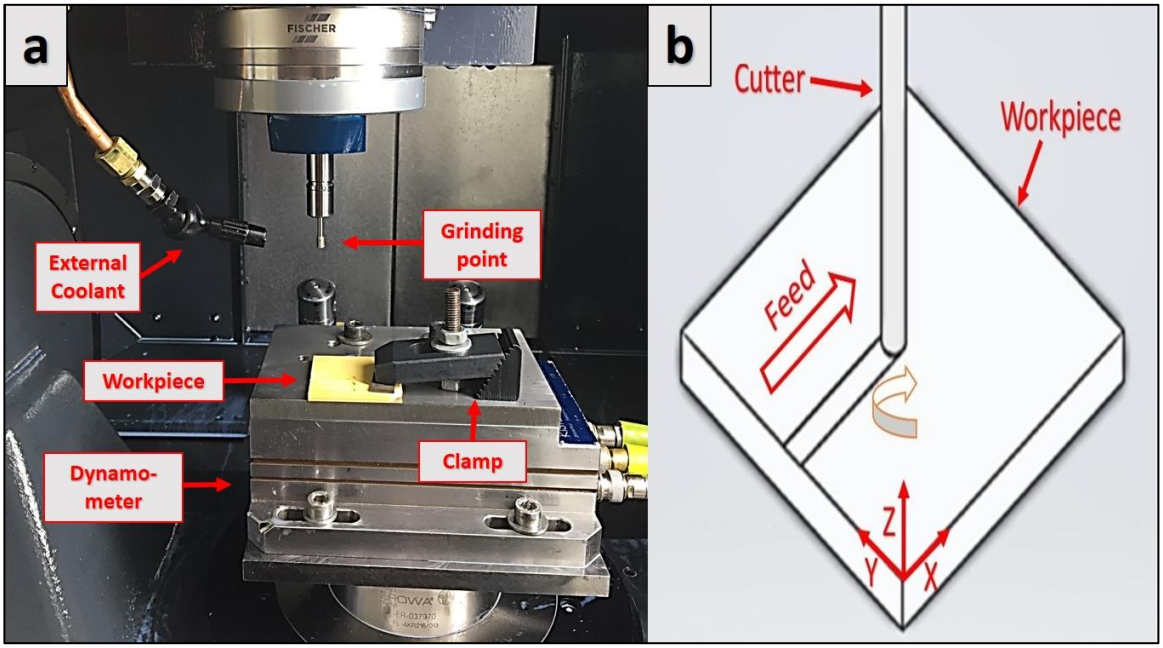


Figure 3.15 Illustration of (a) experimental setup, (b) machining process (**phase 2.A**)

3.3.2.2 Phase 2.B: Benchmarking Al_2O_3, Si_3N_4, and SiC against ZrO_2

In this phase**,** the benchmarking of Al_2O_3, Si_3N_4, and SiC against ZrO_2 were conducted on the basis of the results obtained in **phase 2.A**. Grinding ZrO_2 at a cutting speed of 1 m/s, feed rate of 1 mm/min, and axial cutting depth of 0.1 mm resulted in relatively less tool wear, good surface roughness Ra of 0.33 µm, and relatively low grinding forces. Therefore, it will be helpful to perform benchmarking at these parameters to demonstrate the variation in the machinability of the four utilised ceramics. The experimental setup and illustration of the machined slots are shown in **Figure 3.14, phase 2.A**.

3.3.2.3 Phase 2.C: Investigating the Operating Parameters for Point Grinding ZrO_2 Using UAG

On the basis of the finding obtained in **phase 2.A** that grinding ZrO_2 at a spindle speed of 5000 rpm (V = 1 m/s), feed rate of 1 mm/min (f = 0.2 µm/rev), and axial cutting depth of 0.1 mm obtained good tool life and surface roughness, UAG was investigated using the same parameters

but with US vibration. Low and high US vibration amplitudes at a resonance frequency of 29 kHz were used, as shown in **Table 3.7**. The experimental setup and illustration of the machined slots are shown in **Figure 3.16**.

Table 3.7 Amplitude levels at a resonance frequency of 29 kHz (**phase 2.C**)

Parameter	Low	High
Amplitude range* (µm)	1–2	5–6
Power (W)	15	21

*Amplitude measured in the air

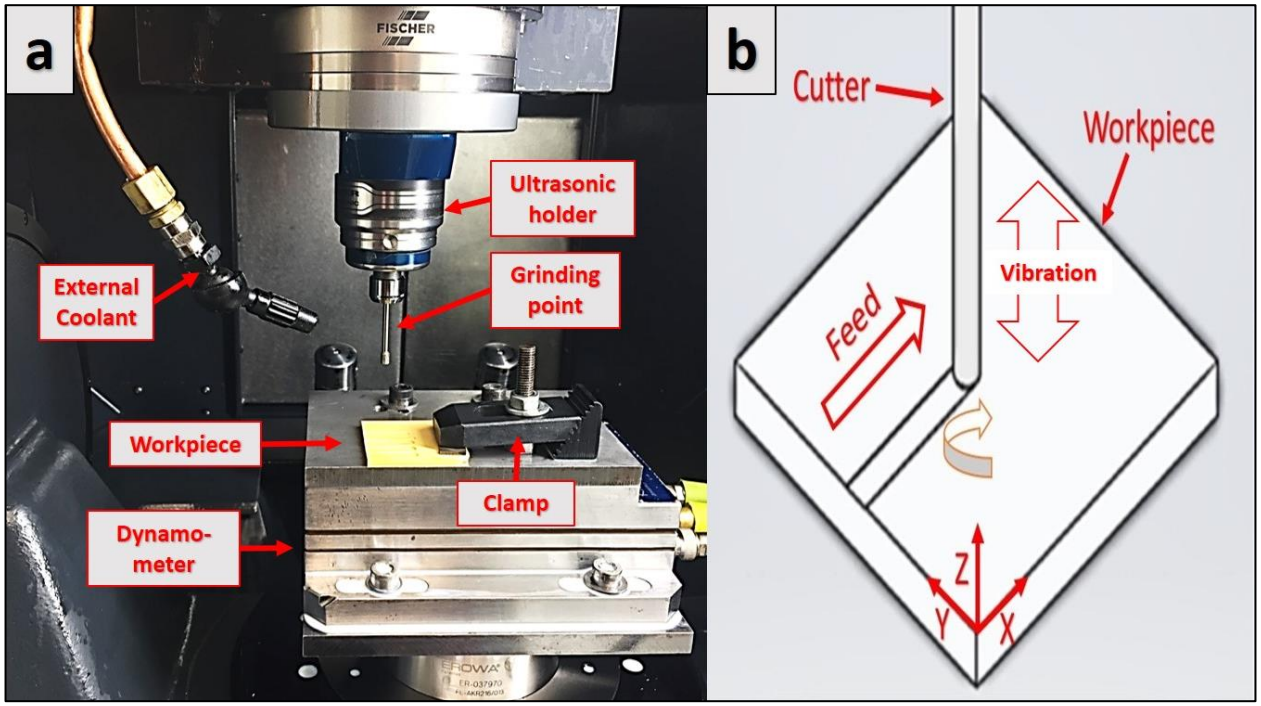


Figure 3.16 Illustration of (a) experimental setup, (b) Ultrasonic Assisted Grinding (phase 2.C)

3.3.2.4 Phase 2.D: Benchmarking Al_2O_3, Si_4N_3, and SiC against ZrO_2 Using the UAG Method and Comparing Conventional Point Grinding with UAG

In this phase**,** the benchmarking of Al_2O_3, Si_3N_4, and SiC against ZrO_2 was conducted on the basis of the results obtained in **phase 2.C**. Grinding ZrO_2 using the UAG method at a cutting speed of 1

m/s, feed rate of 1 mm/min, and axial cutting depth of 0.1 mm resulted in relatively less tool wear at the US vibration amplitude range of 1–2 µm than at the higher US vibration amplitude range of 5–6 µm and lower grinding forces. Therefore, benchmarking at these parameters is useful for demonstrating the variation in the machinability of the four utilised ceramics when UAG is applied. Moreover, the UAG benchmarking results were compared with the conventional benchmarking results in **phase 2.B** to analyse if any improvement has obtained. The experimental setup and illustration of the machined slots are shown in **Figure 3.15**.

3.3.3 Testing Statistics

The summary of all tests and replications number that conducted for the project are shown in **Table 3.8.** Where 28 tests conducted for phase 1 and 10 for phase 2, in total of 38 tests.

Table 3.8. Summary of project's testing number

	Number of Tests	Replication	Number of Replication Tests	Total Number of Tests	Notes
Phase 1. A	**4**	**-**	**1**	**5**	**Only one test has been replicated**
Phase 1. B	**4**	**1**	**4**	**8**	
Phase 1. C	**2**	**2**	**4**	**6**	
Phase 1. D	**3**	**2**	**6**	**9**	
Phase 2. A	**2**	**0**	**0**	**2**	
Phase 2. B	**3**	**0**	**0**	**3**	
Phase 2. C	**2**	**0**	**0**	**2**	
Phase 2. D	**3**	**0**	**0**	**3**	
Total	**23**	**-**	**15**	**38**	

On following two chapters the results of 38 conducted tests have been discussed. Where diamond coated end mills and diamond grinding points have machined the four common advanced ceramics of ZrO_2, Al_2O_3, Si_3N_4, and SiC conventionally and by ultrasonic assisted machining, besides benchmarking. Where the observations were focused on tool life and wear, surface roughness, and cutting forces.

4. RESULTS AND DISCUSSION: PHASE 1, END MILLING

The objective of this chapter is to investigate the machining parameters for the use of diamond-coated end mills on ZrO2 with a 4-mm-diameter tool. And benchmark Al_2O_3, Si_3N_4, and SiC against ZrO_2 for the use of diamond-coated end mills conventionally. The assessment criteria included tool wear, surface roughness, material removal mechanism, and cutting forces. Moreover, to investigate the improvement in advanced ceramics machinability when UAM used.

4.1 The Effect of Cutting Fluid on Tool Life

No clear report from the literature was found about the effect of the cutting fluid when using diamond-coated tools for machining advanced ceramic materials. It was important to investigate the effect of the cutting fluid on tool life before conducting an extensive experimental work. In Liu and Camfield's [45] experiment, the workpiece used was Al_2O_3 of 99% purity, with a hardness value of HK = 1000 kgf/mm^2 (Knoop scale). It was machined in a dry environment. In the work of Bian et al. [43], the experiment was conducted against ZrO_2 in a conventional flood environment.

Therefore, two 4-mm-diameter ball-nose end mills with CVD diamond coating (DURA) were tested to cut two slots on 99% purity alumina with an HV of 1500–1650 kgf/mm^2. The first tool was used in a dry environment, whereas the second tool was used a cutting fluid of Hocut B795 at 10% vol concentration at a flow rate of 4.5 L/min. The machining parameters were a feed rate of fz =0.5µm/ tooth, spindle speed of 3183 rpm, maximum cutting speed of 10.95 m/min, and cutting depth of 0.1 mm.

The results showed the superior performance of the cutter that machined in a wet environment. In dry machining, the diamond coating was delaminated at a wide area on the flank face, and the solid carbide substrate was exposed, with a flank wear of VB > 0.3 mm just after 20 mm of

cutting length (**Figure 4.1a**). In the wet environment, the tool flank wear almost reached a VB of 0.016 mm after reaching a cutting length of 50 mm, as shown in **Figure 4.1(b)**.

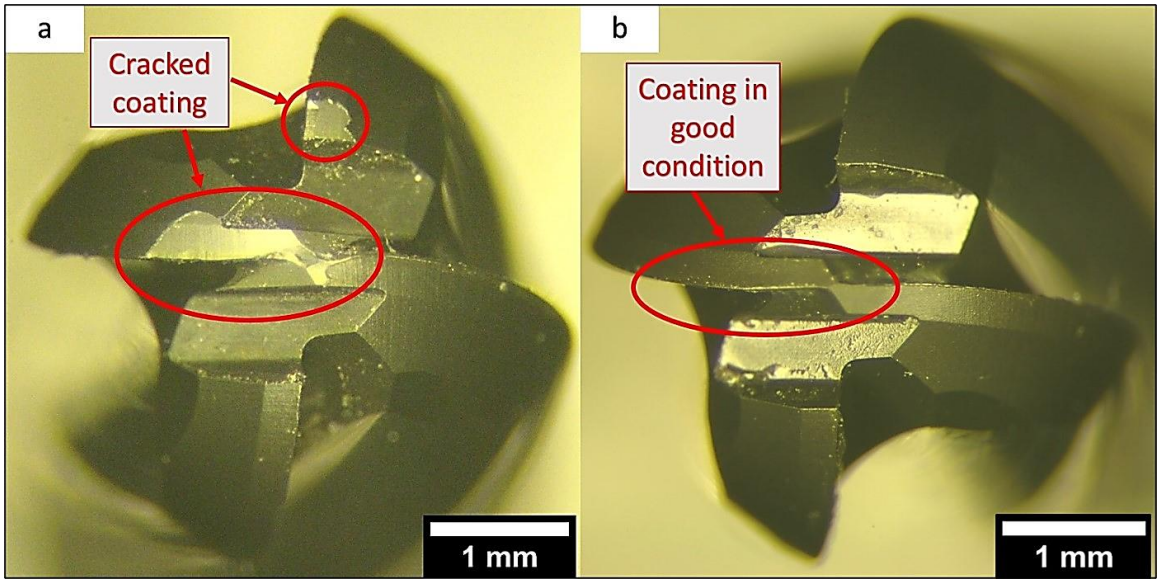


Figure 4.1 Tool wear in ball-nose end mills of (a) VB > 0.3 mm in a dry environment after cutting 20 mm and (b) VB of 0.016 mm in a wet environment after cutting 50 mm

4.2 Phase 1.A: Investigating the Operating Parameters for End Milling ZrO_2

a) Tool Life Analysis

Tool life is generally considered one of the most important factors in machinability evaluation because the cost of machining is significantly affected by the number of cutting tools used during machining. **Figure 4.2** shows the tool flank wear according to the cutting length of the four CVD diamond-coated end mills used to machine ZrO_2. The tool wear according to the cutting time is shown in **Figure 4.3**, where test 1 took 1 min; test 2, 5.2 min; and test 3, 3.1 min. The longest cutting time, which was more than 3 h was in test 4, and test 4 confirmation took 167.5 min.

The results show the outstanding performance of the test 4 cutter (fz = 0.5µm/tooth, V = 60 m/min, axial depth = 0.5 mm, and radial depth = 0.25 mm), which cut a length of 1800 mm. This cutting length is almost 15 times the total cutting length of the rest of the cutters, with the test 1

cutter cutting almost 10 mm and the test 2 and 3 cutters cutting approximately 100 and 30 mm, respectively.

The slot milling trends (tests 1 and 3) showed a similar behaviour, where the wear was rapid and sudden compared to side milling, due to higher uncut chip thickness that equal to the feed per reviolation of 0.002 mm, beside the longer cutting path for the cutting edges that cut for half circle which increases the generated heat and resulting in faster wear rate. The effect of the axial cutting depth was noticeable; as the depth decreased from 0.12 mm in test 1 to 0.6 mm in test 3, the cutting length in test 3 almost tripled. Due to the reduction in cutting forces that. On the other hand, side milling (tests 2 and 4), the influence of the feed rate or feed per revolution *fz* on the tool life was noticeable; as the *fz* decreased from 1 µm/tooth in test 4 to 0.5 µm/tooth in test 2, the maximum uncut chip thickness decreases from 0.0026 mm to 0.0013 mm, as calculated from engagement angle **ψ, Figure 4.4**, where uncut chip thickness = ***f sin (ψ).*** Thus, as a result cutting forces decreased and the tool life increased by 22.5 times, from a cutting length of 80 mm to 1800 mm.

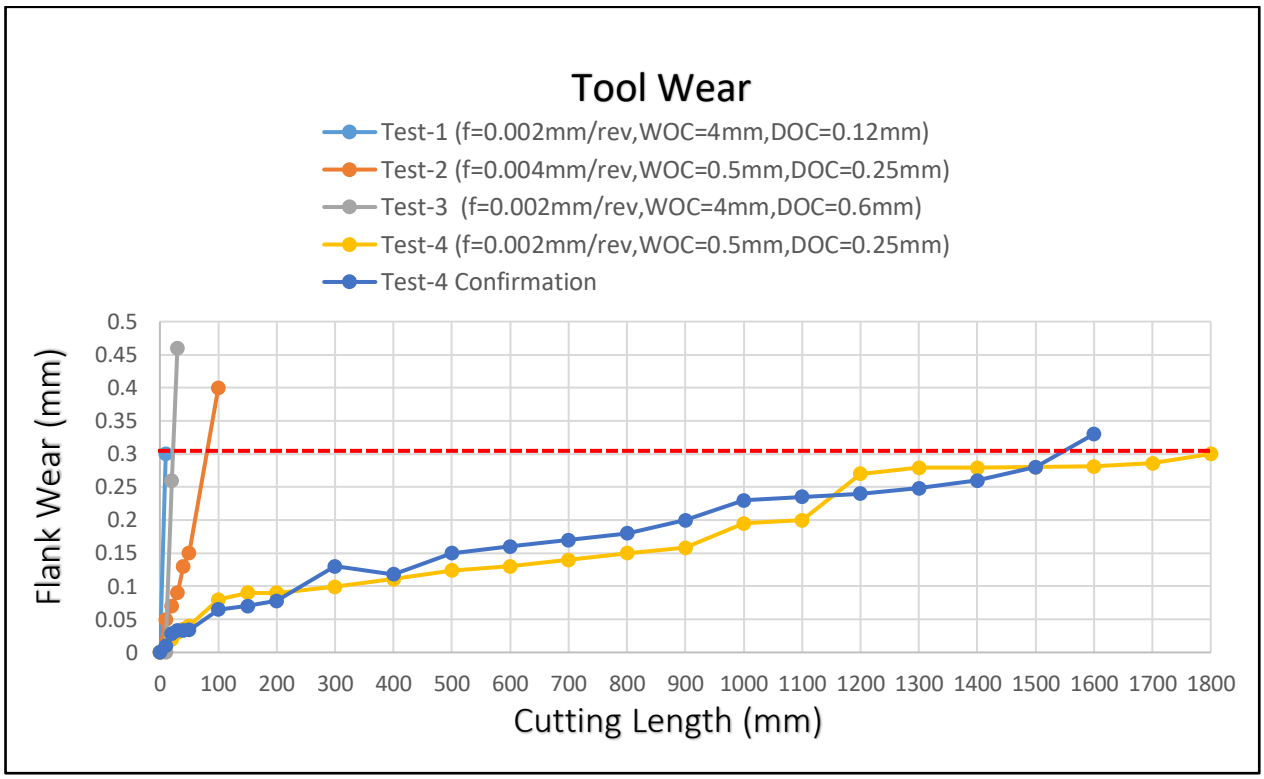


Figure 4.2 Tool flank wear according to cutting length (**phase 1.A**)

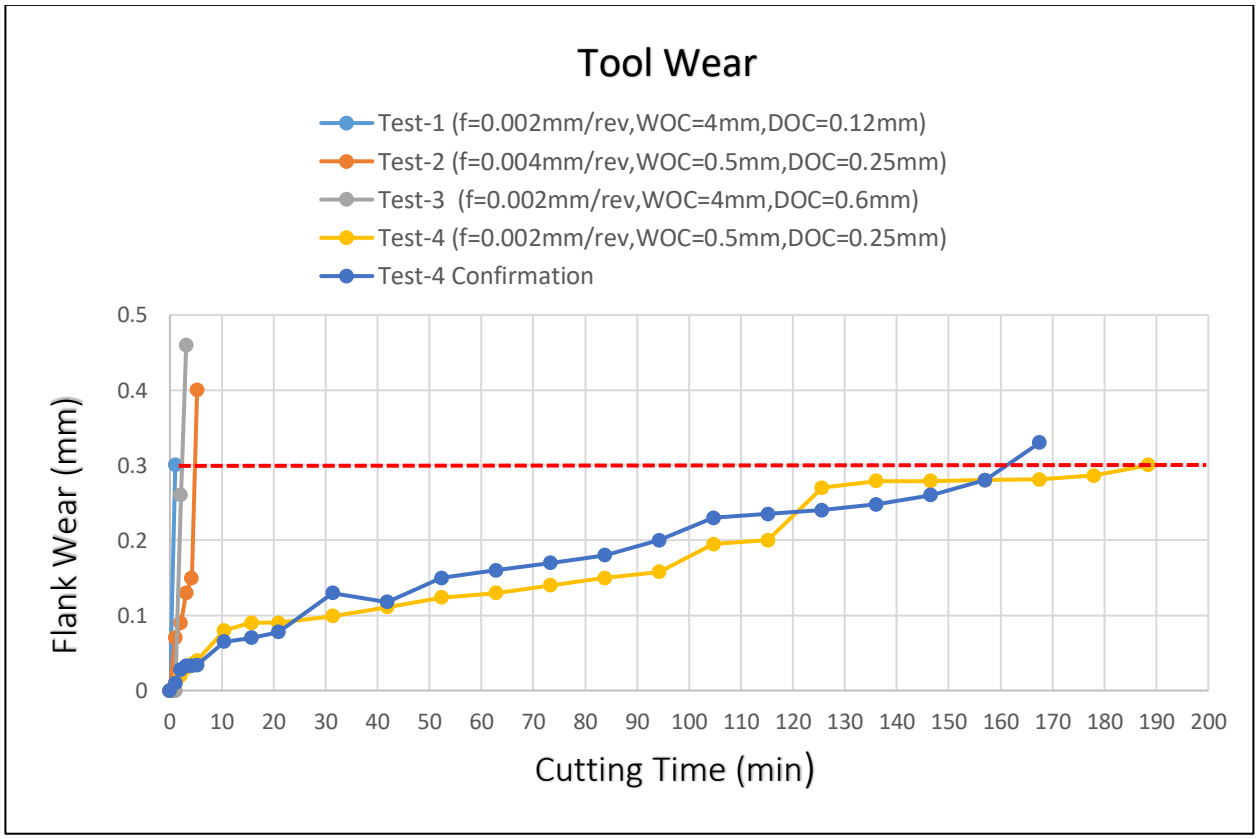


Figure 4.3 Tool flank wear according to cutting time (**phase 1.A**)

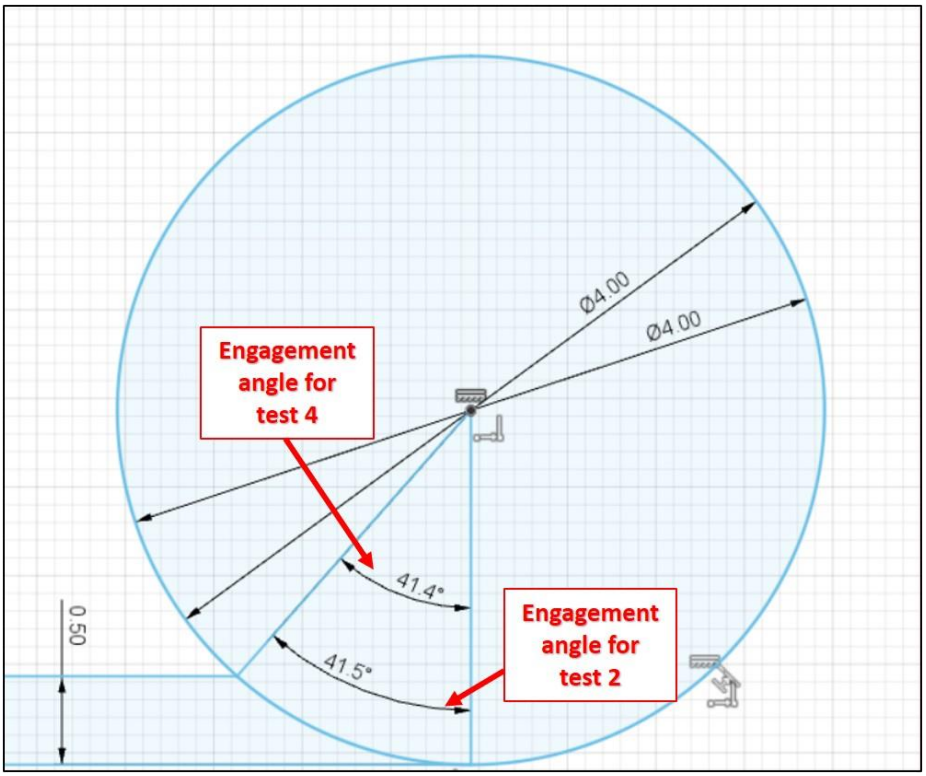


Figure 4.4 Illustration of engagement angles for test 2 & 4

Tool flank wear images of the cutters used are shown in **Figures 4.5** to **4.8**. **Figure 4.5** shows the worn flank face of Test 1. The wear was so severe that the diamond coating on the flank face was cracked and that on the four edges of the tool were removed, and all four cutting edges were worn. Besides a large fragment of solid carbide substrate was removed from edge 2. The tool wear of Test 2, is shown in **Figure 4.6**. All four edges were worn, with edges 1 and 2 having more exposed areas of substrate because of coating delamination. It is believed that the coating bonding varies between edges; therefore, some edges have barer areas of substrate than others.

The tool wear of Test 3, is shown in **Figure 4.7**. On edge 1, the coated layer was removed, and the tip showed minor chipping. Edge 2 was in good condition, whereas edges 3 and 4 had cracked coating and worn tips. However, the tool wear in Test 3 was less than that in cutter 1, which indicates the effect of decreasing the cutting depth from 0.12 mm to 0.06 mm on tool wear. **Figure 4.8** shows the flank wear of Test 4. The wear by abrasion was dominant in all four cutter edges, with smoother rounded edges. Which is unlike the wear in the previous three cutters,

indicating the lower cutting forces. The comparison between Test 4 (f = 0.5 µm/tooth) and cutter 2 (f = 1 µm/tooth) showed the significant influence of feed and the uncut chip thickness reduction on flank wear. It believed the slotting cutters exhibited worse worn flank face due to higher generated heat that related to longer engagement time between tool and workpiece when the tool cut in full diameter. Moreover, some of the obtained tool wear patterns such as coating delamination was similar to what observed by Bian [46] that machined sintered zirconia by diamond coated endmill.

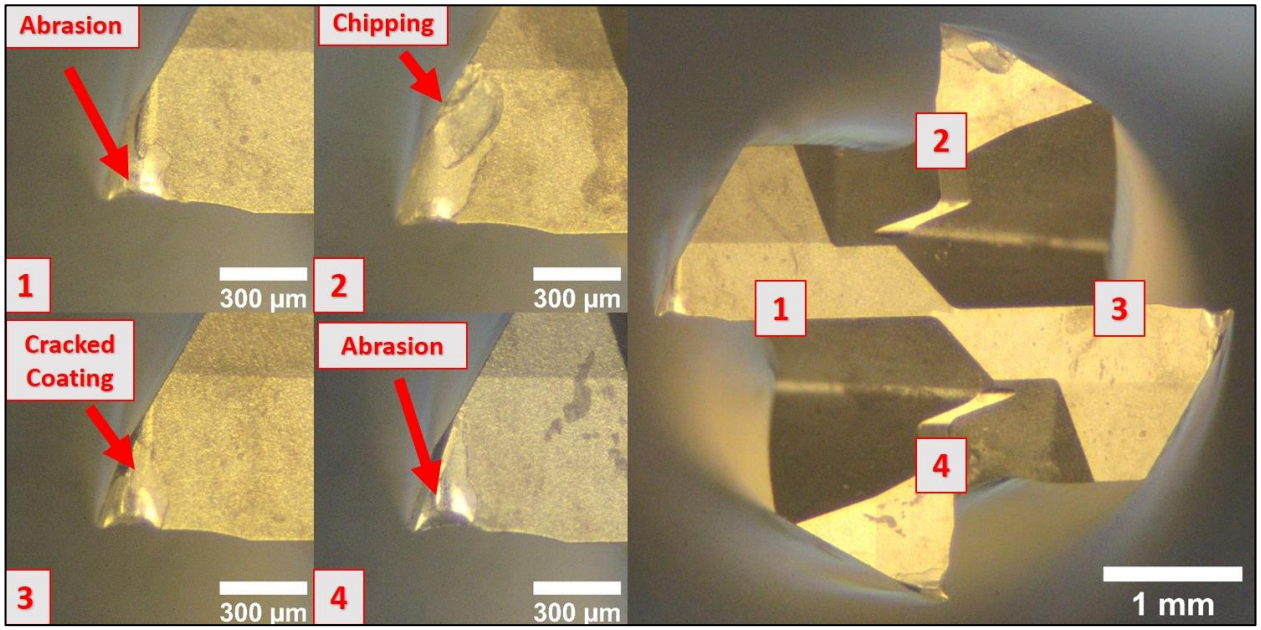


Figure 4.5 Tool flank wear of Test 1 after cutting 10 mm at V = 60 m/min, fz = 0.5 µm/tooth, WOC = 4 mm, and DOC = 0.12 mm (**phase 1.A**)

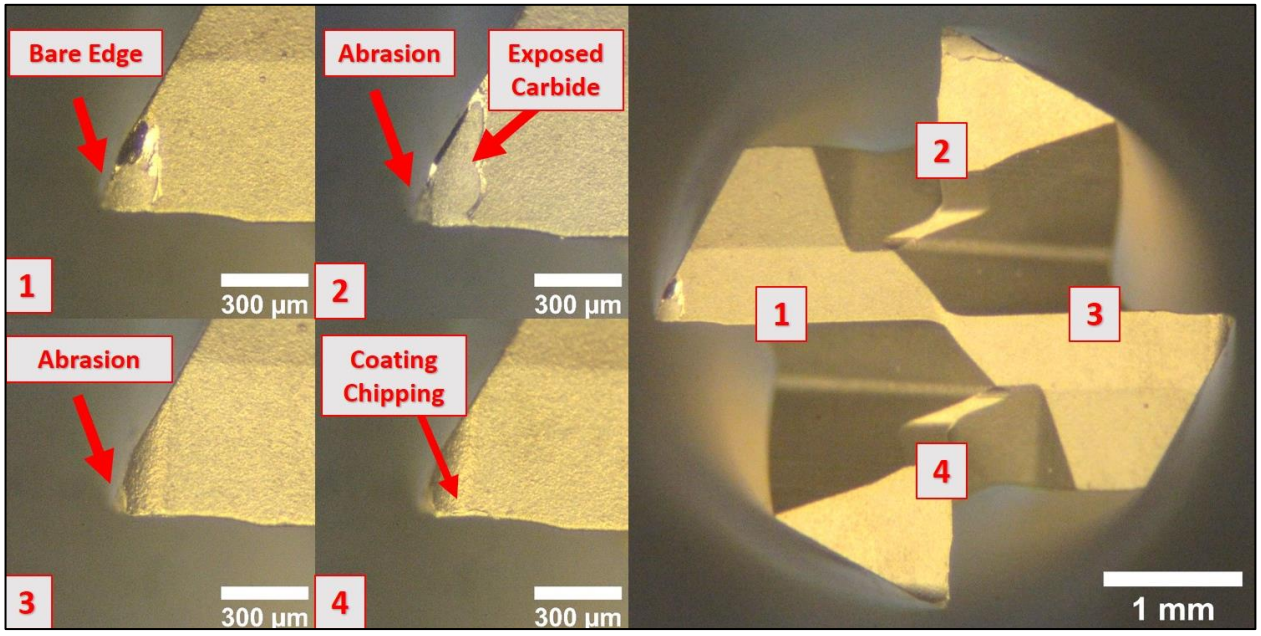


Figure 4.6 Tool flank wear of Test 2 after cutting 80 mm at V = 60 m/min, fz = 0.5 µm/tooth, WOC = 0.5 mm, and DOC = 0.25 mm (**phase 1.A**)

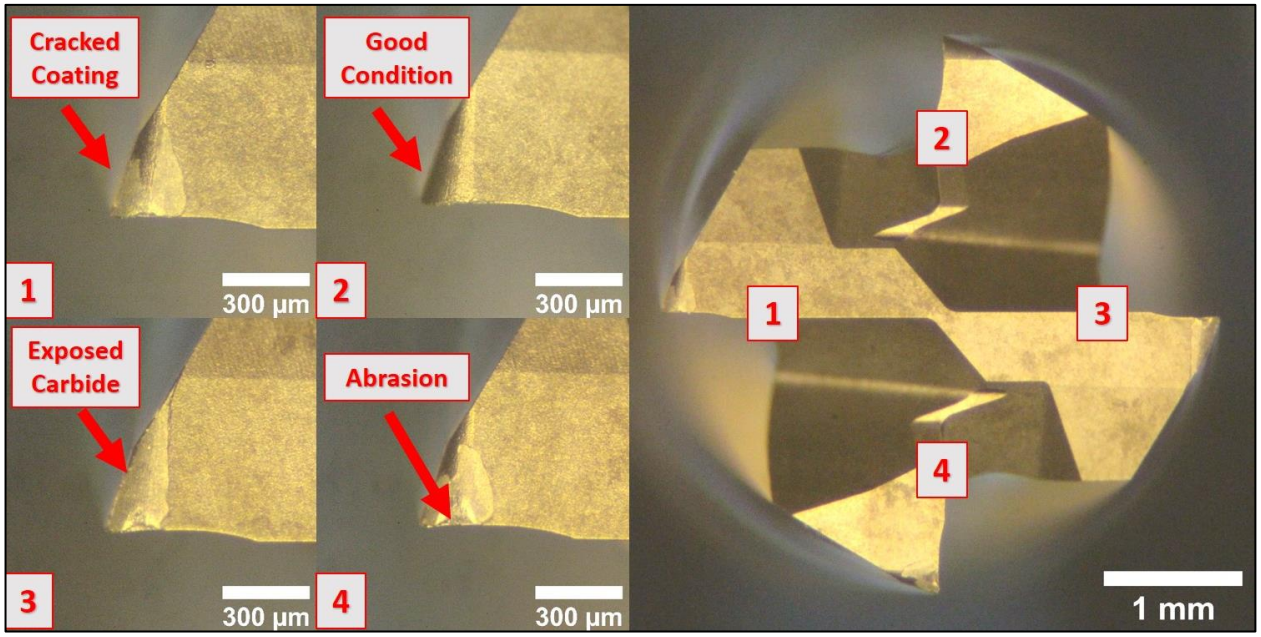


Figure 4.7 Tool flank wear of Test 3 after cutting 30 mm at V = 60 m/min, fz = 0.5 µm/tooth, WOC = 4 mm, and DOC = 0.06 mm (**phase 1.A**)

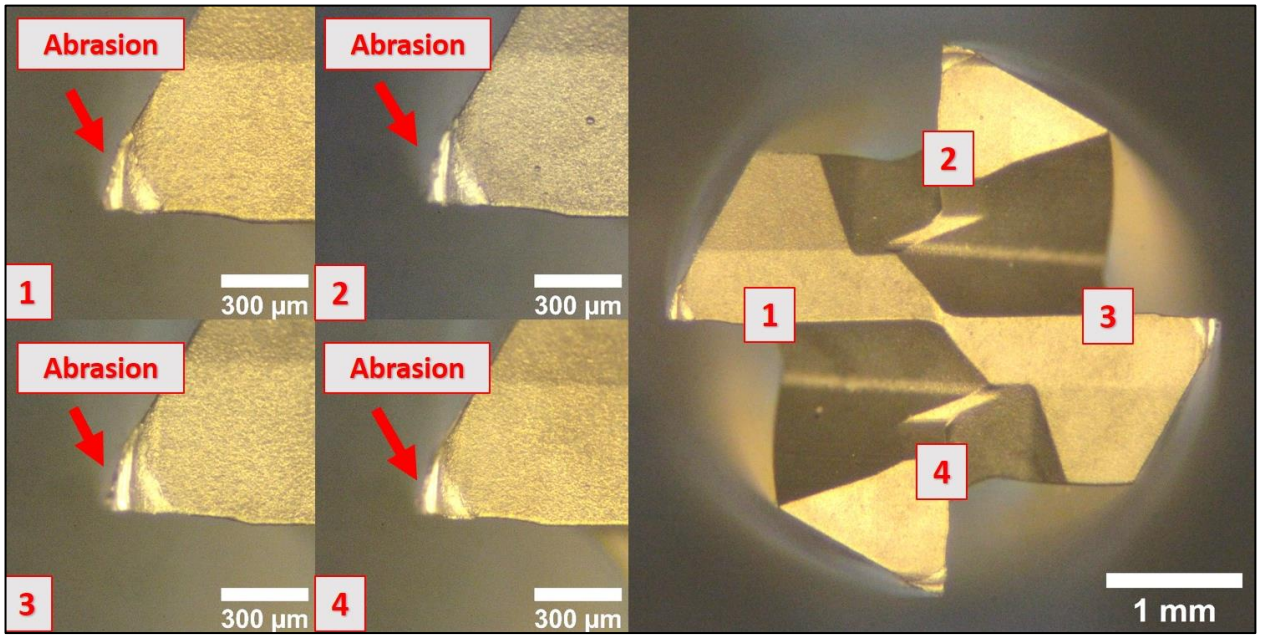


Figure 4.8 Tool flank wear of Test 4 after cutting 1800 mm at V = 60 m/min, fz = 0.5 µm/tooth, WOC = 0.5 mm, and DOC = 0.25 mm (**phase 1.A**)

b) Surface Roughness Analysis

The Ra values of the four machining conditions are shown in **Figure 4.9**, with error bars. The surface roughness after slot milling in tests 1 and 3 were similar, with Ra values of 0.18 and 0.14 µm, respectively. This indicates that the effect of reducing the cutting depth from 0.12 mm in test 1 to 0.06 mm in test 3 was insignificant when the depth of cut difference is small. For side milling the increase in feed fz from 0.5 µm/tooth to 1 µm/tooth resulted in a significant increase in surface roughness from 0.29 in test 2 to 0.64 µm in test 4, indicating an almost 100% increment, due to what known as feed marks that increases as feed increase and resulting in higher surface roughness, besides the higher chip thickness increases the forces in Test 2 that worn the tool faster and removed diamond coating and resulting in poorer surface finish. When comparing between slotting and side milling in Test 2 and Test 3 especially, both having close MRR value. Noticeably Test 3 has lower Ra, which believed due to its lower depth of cut that reduces cutting forces.

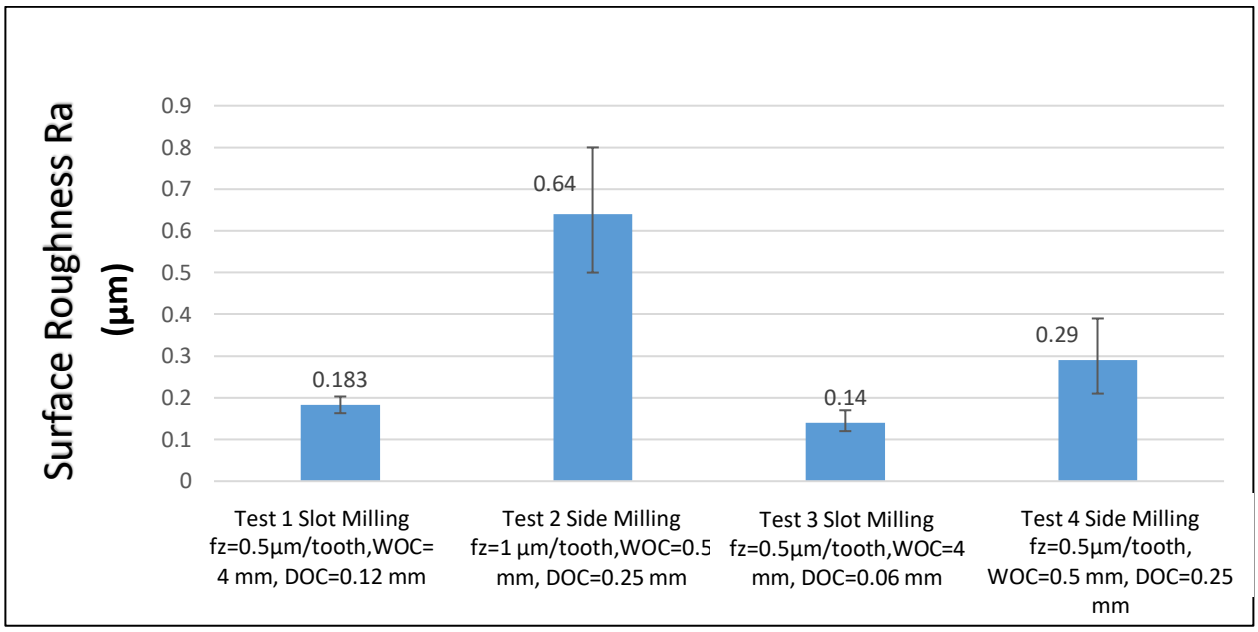


Figure 4.9 Average surface roughness Ra of ZrO_2 obtained under conventional machining conditions (**phase 1.A**)

4.3 Phase 1.B: Benchmarking Al_2O_3, Si_3N_4, and SiC against ZrO_2

a) Tool Life Analysis

The behaviours of the CVD diamond-coated end mills toward the four ceramics (ZrO_2, Al_2O_3, Si_3N_4, and SiC) and the corresponding cutting times are shown in **Figures 4.10**. Among the four ceramics, ZrO_2 (HV = 1200 kgf/mm^2) showed outstanding machinability, where the cutter machined a length of 1500 mm, at first run removing material volume of 187 mm^3 in 157 min. The cutter flank wear started to occur just after cutting 20 mm and increased gradually until the flank wear reached a VB value of >0.3. In replication the cutter machined for 1300 mm in 137 min. Al_2O_3 showed a much lower tool life due to its higher hardness of HV = 1500–1650 kgf/mm^2, where the cutter in first run cut for 100 mm, removing a material volume of 12 mm^3 in 10 min, The cutter showed a linear flank wear until reaching a cutting length of 50 mm. The wear crossed over 0.3 mm rapidly at 100 mm. In replication the cutter cut for 50 mm in 5 min. By comparing this short tool life at the low MRR of 1.19 mm^3/min to that machined by Liu [47] by

similar diamond coating cutters at 5-6 mm^3/min, it indicating that this variation in the machinability could only be attributed to the difference in hardness value of his workpiece of 1080 HV. The Si_3N_4 exhibited a tool life almost similar to that of Al_2O_3. This could be explained by the hardness value of Si_3N_4 (HV = 1700–2200 kgf/mm^2), which was close to the hardness range value of Al_2O_3. The cutter cut 40 mm, removing a material volume of 5 mm^3 in 4 min. In replication it cut for 20 mm in 2 min. SiC showed the lowest tool life, where the cutter worn from the first 10 mm, in both runs removing only 1.25 mm^3 of material volume in 1 minute. This could be explained by its highest hardness value of HV = 2400–2800 kgf/mm^2.

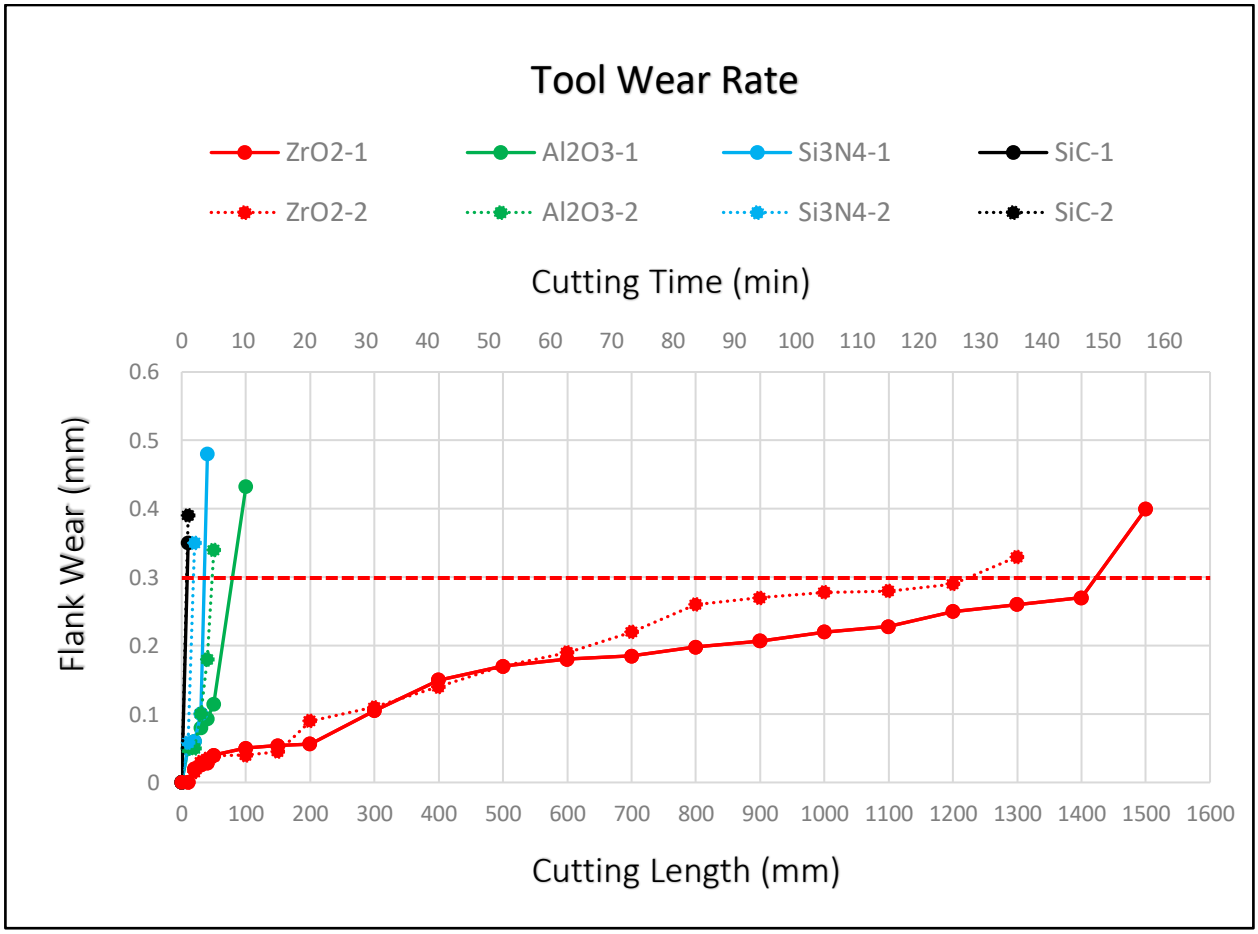


Figure 4.10 Tool flank wear according to cutting length & time (**phase 1.B**)

The tool flank wear of the four cutters is shown in **Figures 4.11** to **4.15**. All images were captured at the end of life of the cutters. **Figure 4.11** shows the flank wear of the ZrO_2 cutter after cutting 1500 mm, indicating the longest tool life. All four edges were affected by abrasion wear, and one edge (edge 2) also showed coating removal that exposed the carbide substrate. This could explain why the tool life showed a rapidly increasing trend at the end of life. Moreover, compared with the tool life of the ZrO_2 cutter in **phase 1.A**, which was performed with Fx-5 CNC, the cutter had a longer life of 1800 mm, demonstrating the effect of each CNC vibration, fixture, workpiece alignment accuracy on the machining results.

The flank wear of the Al_2O_3 cutter after cutting 100 mm is shown in **Figure 4.12**, where all the edges of the tool were worn, and the coating layer surrounding the worn area was removed, exposing large areas of solid carbide substrate. The tool flank wear of the Si_3N_4 cutter after cutting 40 mm is shown in **Figure 4.13**. All the tips of the tool had worn. A large layer of the coating of edge 4 was removed, which was the reason for the rapid end of the tool's life. The wear of the Al_2O_3 cutter, which had low hardness, was higher than that of Si_3N_4. This difference between the two cutters was due to the difference in wear observation periods. The Al_2O_3 cutter machined a length of 50 mm without meeting the end-of-life criteria, so the next observation was made at 100 mm, machining more than 50 mm without observation. However, the Si3N4 cutter machined only 40 mm, so the cutter was checked every 10 mm. The shortest tool life was obtained by the SiC cutter, whose flank wear is shown in **Figure 4.14**. The cutter cut only 10 mm, and the resulting wear was so severe that all four edges were worn and some coating was removed from the areas surrounding the worn tips. This poor performance by the cutter could be related to the high hardness of SiC (HV = 2400–2800 kgf/mm^2). A close-up image of the worn edges by the four cutters is shown in **Figure 4.15,** noticeably ZrO_2 has produced smoother

rounded wear line at the cutter edge and the coating layer has limited delamination spot around worn edge as shown in **Figure 4.15 (a)**. The worn edges of Al_2O_3 and Si_3N_4 cutters were showing similar wear patterns, where traces of abrasion could be seen at their tips with fracture or detached coating layers around, **Figure 4.15 (b) & (c).** SiC cutter has shown the worst worn edges where it could be seen that the most removed material from the tool has done by cutting SiC **Figure 4.15 (d).**

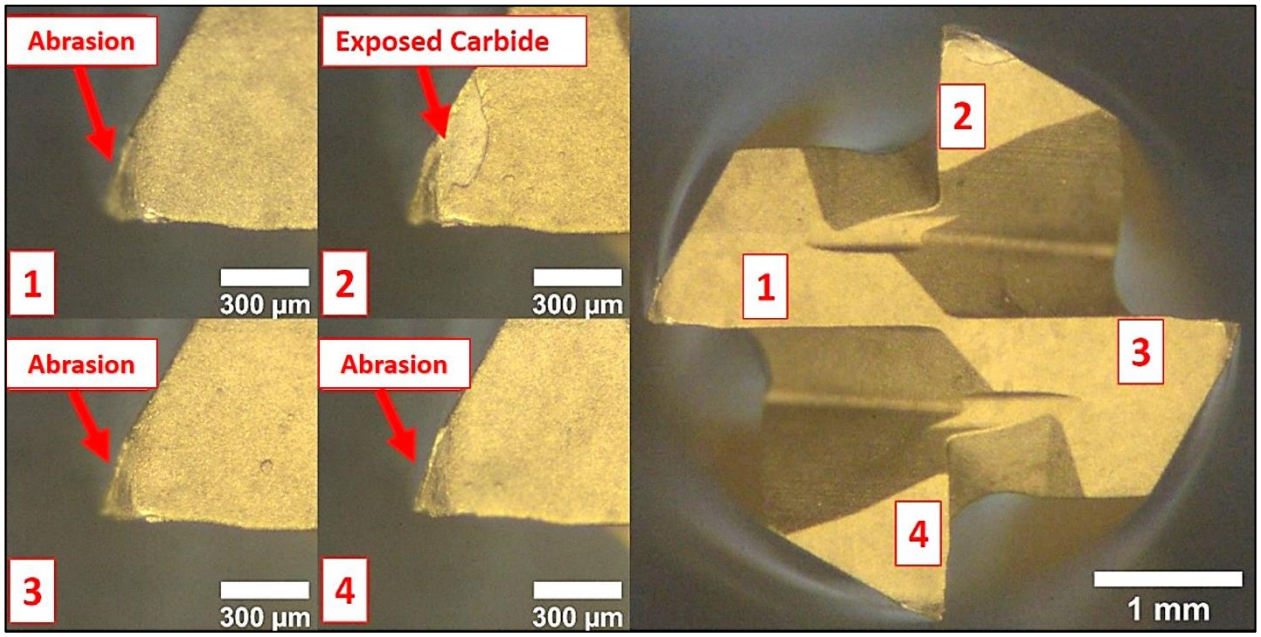


Figure 4.11 Tool flank wear of the cutter of ZrO_2 after cutting 1500 mm at V = 60 m/min fz = 0.5 µm/tooth, WOC = 0.5 mm, and DOC = 0.25 mm (**phase 1.B**)

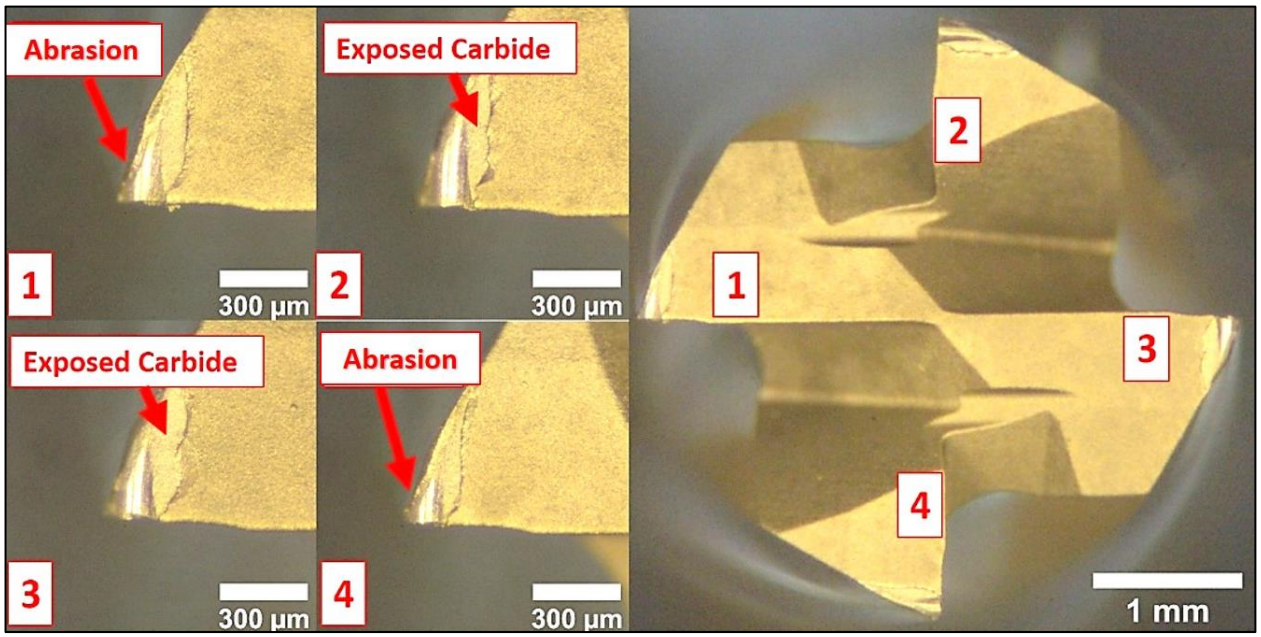


Figure 4.12 Tool flank wear of the cutter of Al_2O_3 after cutting 100 mm at V = 60 m/min, fz = 0.5 µm/tooth, WOC = 0.5 mm, and DOC = 0.25 mm (**phase 1.B**)

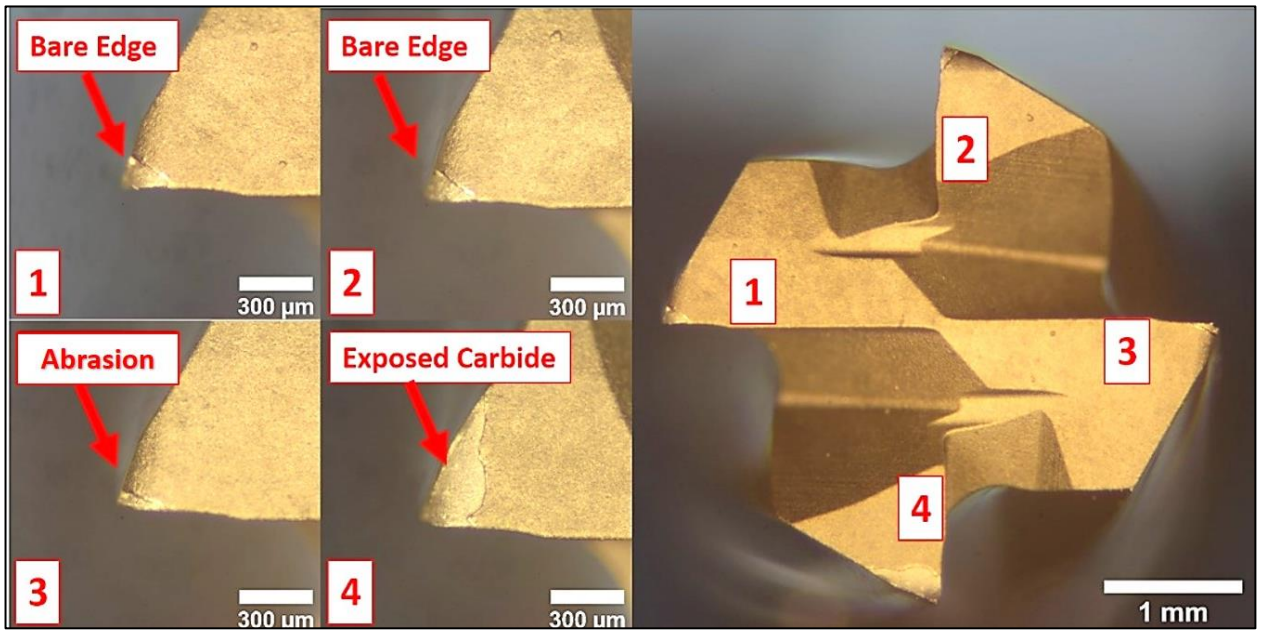


Figure 4.13 Tool flank wear of the cutter of Si_3N_4 after cutting 40 mm at V = 60 m/min, fz = 0.5 µm/tooth, WOC = 0.5 mm, and DOC = 0.25 mm (**phase 1.B**)

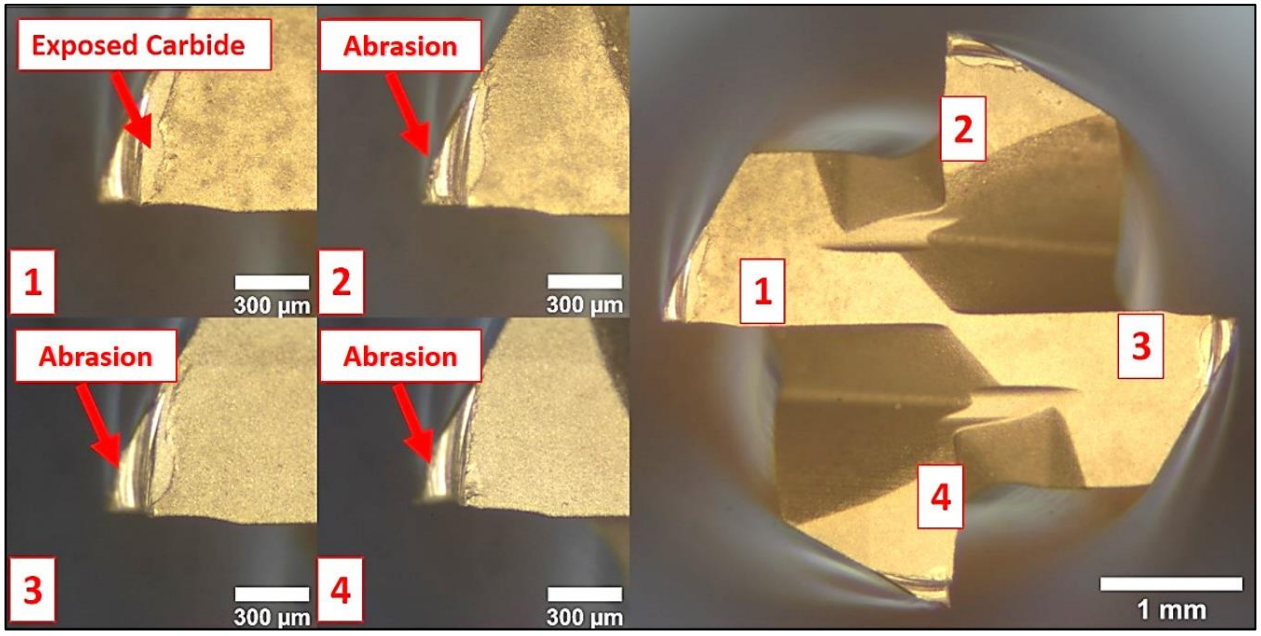


Figure 4.14 Tool flank wear of the cutter of SiC after cutting 10 mm at V = 60 m/min fz = 0.5 µm/tooth, WOC = 0.5 mm, and DOC = 0.25 mm (**phase 1.B**)

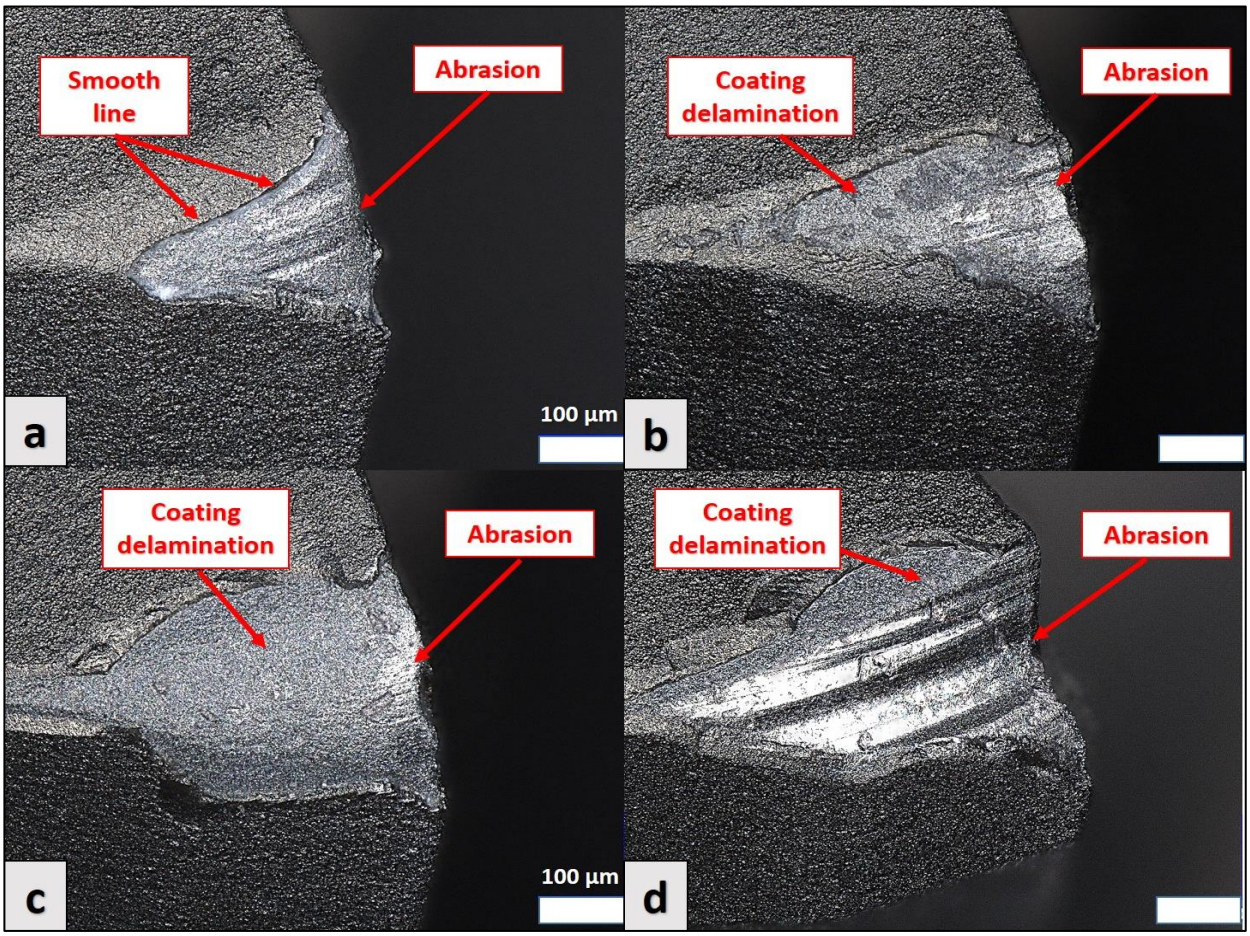


Figure 4.15 Tool wear at the cutting edge of the cutters of (a) ZrO_2, (b) Al_2O_3, (c) Si_3N_4, (d) SiC by conventional machining **(phase 1.B)**

b) Surface Roughness Analysis

The average surface roughness Ra values of the four machined ceramics are shown in **Figure 4.16**, with error bars. The **oxide** ceramics had obtained higher average surface roughness values than the **non-oxide** ceramics, where ZrO_2 and Al_2O_3 obtained Ra values of 0.33 and 0.47 µm, respectively. The non-oxides ceramics, Si_3N_4 and SiC, obtained Ra values of 0.24 and 0.28 µm, respectively. Generally surface roughness is affected by several factors, cutter material and geometry, cutting fluid and applying method, the machined material properties, and the machining parameters. In benchmarking study, the only factor that varying the surface roughness value is the workpiece properties, since the other machining variables of tool, cutting fluid, and machining parameters were similar. According to some studies, materials could be machined in the ductile cutting mode, which enhances surface integrity, only if the cutting was performed at a small cutting scale close to or below the grain size of the material. In this experiment, the chip thickness was at 0.3 µm, which is equal to or smaller than the grain sizes of all the machined ceramics in this study, which ranged from 2 to 10 µm, similar to those reported in previous studies [13,66,67].

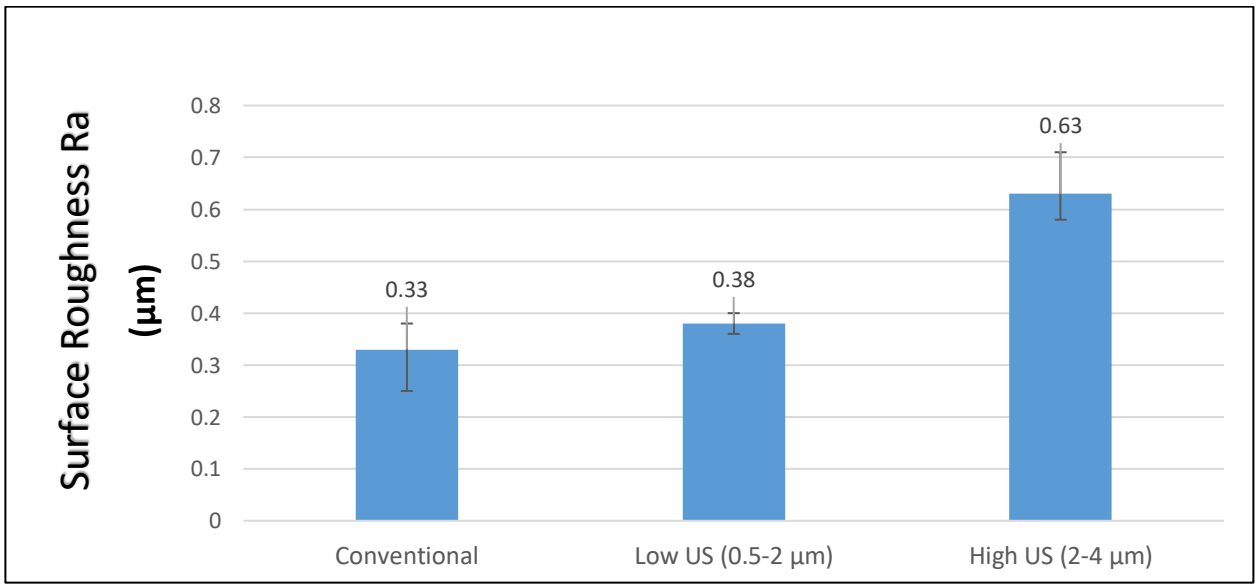


Figure 4.16 Average surface roughness Ra of ZrO_2, Al_2O_3, Si_3N_4, and SiC obtained by conventional milling (**phase 1.B**)

The machined surfaces of the ceramics were observed using the Alicona microscope at the end of each test and the end of life of the tool, as shown in **Figure 4.17**, to investigate the material removal mechanism. It is common in hard and brittle material machining to cut in brittle mode, which affects the capability of the material to withstand loading and unloading cycles due to the subsurface cracks caused by brittle fractures. Therefore, cutting ceramics in ductile mode is mostly preferred to improve material toughness by reducing the number of subsurface cracks that lead to material failure. The plastic flow mode ductile cutting mode will suppress crack propagation.

The ZrO_2 surface shown in **Figure 4.17(a)** was machined mostly in ductile cutting mode. It shows a wide flat bright area reflecting the microscope light. Traces of scratches of the edges of the tool can be seen forming a continuous line on the surface. Brittle fractures can be observed as black areas or voids that scatter microscope light. The exhibited plasticity of ZrO_2 could be explained by its relatively low hardness (HV = 1200 kgf/mm^2) and high fracture toughness (6–9 MPa $M^{1/2}$) that enable it to resist crack propagation due to the tetragonal-monoclinic grain transformation at the tips of the cracks that toughened the workpiece. This result is consistent with the finding of some studies that ZrO_2 ground using a diamond grinding wheel and obtained a surface finish dominated by ductile fractures, making ZrO_2 machining similar to that of metals [51]. Unlike ZrO_2, Al_2O_3 showed more surfaces dominated by brittle fractures than surfaces dominated by ductile fractures, as shown in **Figure 4.17(b)**, where a scattered white dot can be seen, representing plastic deformation as bright islands on the surfaces. The machined surfaces of Si_3N_4 and SiC are shown in **Figure 4.17(c) and (d)**. Both could be considered brittle surfaces because of their high percentages of brittle spots on their surfaces. The obtained machined surfaces were similar to that obtained by Yin [49].

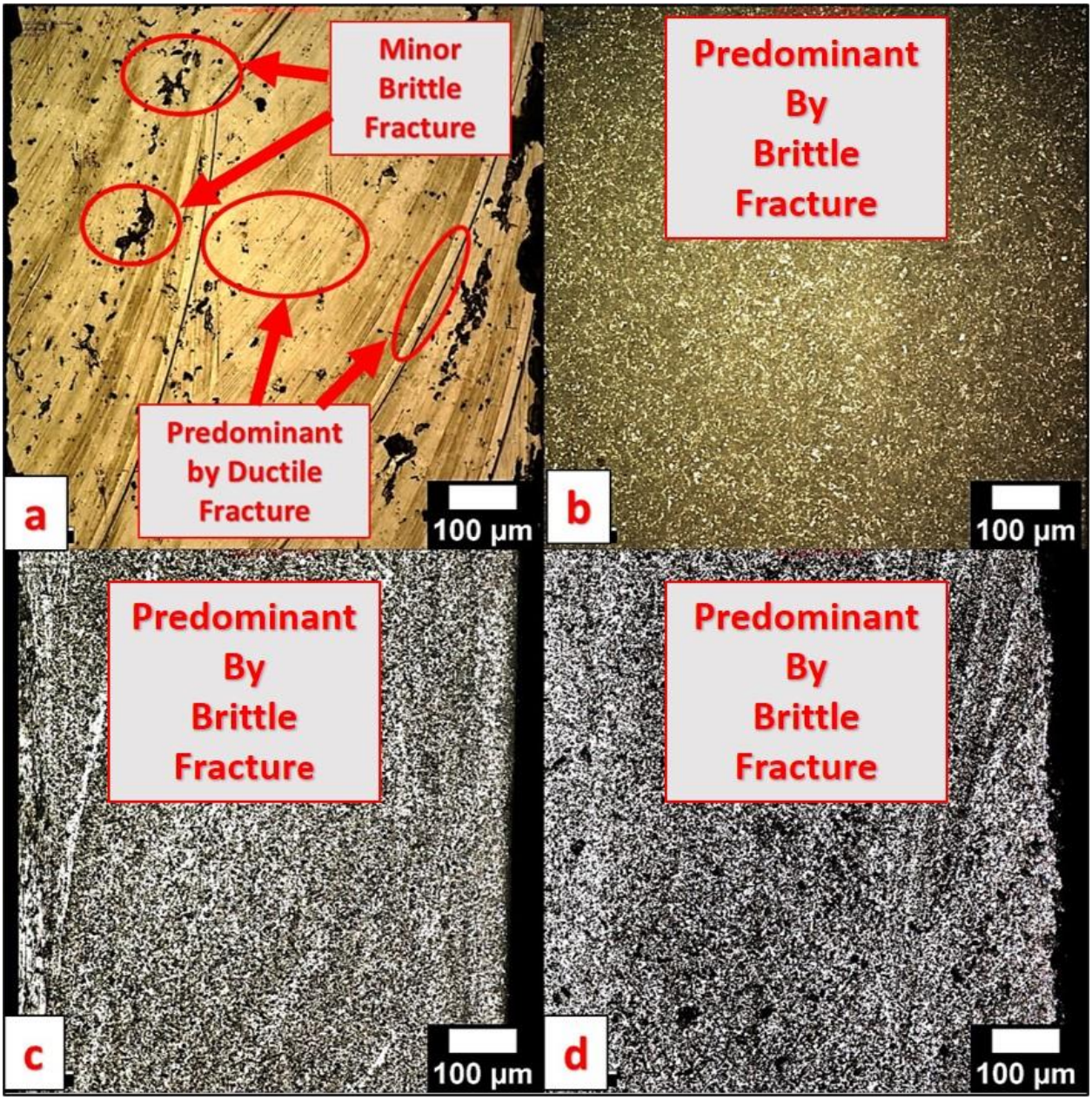


Figure 4.17 Microscopic images of the machined surfaces of (a) ZrO_2, (b) Al_2O_3, (c) Si_3N_4, and (d) SiC (**phase 1.B**)

c) Cutting Forces Analysis

The resulting average cutting forces are shown in **Figure 4.18**, with error bars. The force signals obtained from DynoWare are shown in **Appendix A.1(a)**. ZrO_2 had the lowest hardness (HV = 1200 kgf/mm^2) and the lowest cutting forces of F_X = 30 N, F_Y = 34 N, and F_Z = 22 N. As the hardness of Al_2O_3 (HV = 1500–1650 kgf/mm^2) and Si_3N_4 (HV = 1700–2200 kgf/mm^2) increased,

the forces increased to F_X = 35 N, F_Y = 33 N, and F_Z = 36 N, and F_X = 55 N, F_Y = 58 N, and F_Z = 51 N, respectively. The highest cutting forces were obtained by SiC, which had the highest hardness value among the four workpieces (HV = 2400–2800 kgf/mm^2), with F_X = 74 N, F_Y = 66 N, and F_Z = 65 N. The effects of the cutting forces on tool life and wear were obvious; as the forces increased, the tool life decreased. The forces in the *z*-axis were mainly responsible for flank wear, as the normal force increases on the tool flank face the friction force between the workpiece and flank face will increases.

The ZrO_2 cutter, which cut for longest life of 1500 mm, obtained the lowest F_Z value of 22 N. The edges of the tool did not show any chipping, and the tool was mainly worn by abrasion, as shown in **Figure 4.15 (a)**. On the other hand, as the cutting force F_Z values in the *z*-axis increased linearly to 36, 51, and 65 N for in Al_2O_3, Si_3N_4, and SiC, respectively, the tool lives decreased linearly to 100, 40, and 10 mm, respectively. The tool wear of all three cutters was caused by the chipping or fractured coating layers and abrasion of the edges, as shown in **Figures 4.15 (b), (c)** and **(d)**. Moreover, all cutters showed fluctuations in the cutting forces at some point during cutting, which were believed caused by the non-uniformity of the hardness of the ceramic workpieces, worn flank face, the irregular discontinuous chips that could be jammed in cutting zone while machining progress.

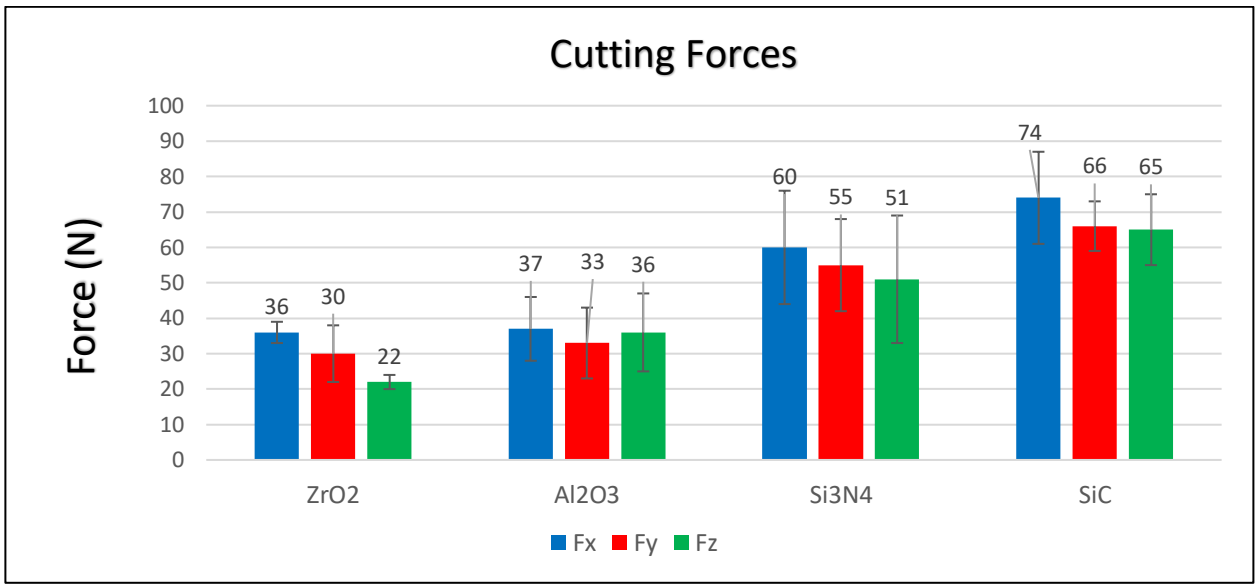


Figure 4.18 Average maximum absolute peak-to-peak cutting forces of the conventionally machined ZrO_2, Al_2O_3, Si_3N_4, and SiC (**phase 1.B**)

4.4 Phase 1.C: Investigating the Operating Parameters for End Milling ZrO_2 Using UAM

a) Tool Life Analysis

ZrO_2 workpiece machined at two US vibration amplitude levels: low (0.5–2 µm) and high (2–4 µm). The amplitude measurement was performed in open air before the tool touched the workpiece. Because there is no way to insure if the US holder is generating any vibration during the machining. The tool frequency was set at 33.5 kHz, and the tool was calibrated after every couple of passes to ensure the stability of the amplitude level, as the resonance frequency is sensitive to the tool weight, and overhang length, which could change after machining one pass, especially in the case of machining hard-to-cut materials such as ZrO_2.

The tool wear trends at the two levels were compared with the conventional trend in **phase 1.B**, as shown in **Figures 4.19**. From the three runs of high amplitude the longest obtained tool life was of 150 mm in 15.7 min. For low US amplitude range of 0.5–2 µm the longest obtained tool life out of three runs was 1300 mm in 136 min. Noticeably the second run was close to first run

with 1200 mm, but the third one was 200 mm, and that due to instability of US holder that sometimes being highly fluctuated. From **phase 1.B** the longest tool life obtained at the zero-amplitude level or with the conventional milling tool that cut 1500 mm in 157.8 min, which is approximately 10 times longer than that obtained at the high US level.

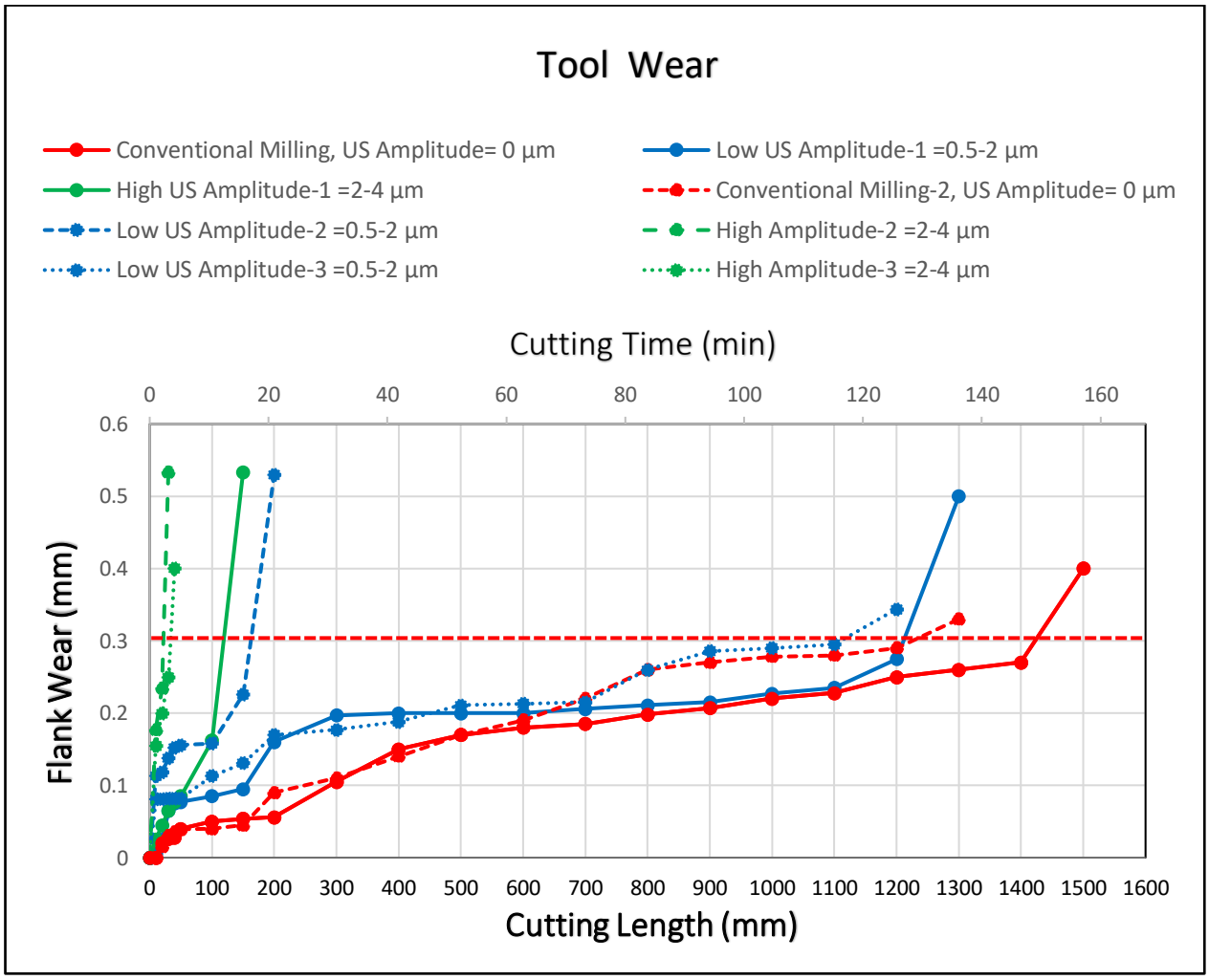


Figure 4.19 Tool flank wear according to cutting length & time (**phase 1.C**)

The flank wear of the conventional milling tool is shown in **Figure 4.11**. As discussed earlier, in **phase 1.B**, the tool showed a large area of delaminated coating in one of its teeth, exposing the solid carbide substrate clearly. Most wear in all tooth tips was caused by abrasion, as traces of scratching trace could be observed on all of them.

The flank wear of the cutter with a low US amplitude range (0.5–2 μm) is shown in **Figure 4.20**. Tips 3 and 4 showed large areas of coating delamination, mainly caused by the hammering movement of the US vibration in the vertical axis, which weakened the bonding force between the solid substrate and diamond coating. Tool tips showed abrasion wear at all its edges, reflecting the effect of the high hardness of the machined material. The cutter with high level of amplitude (2–4 μm) showed severe tool flank wear, as shown in **Figure 4.21**. The four tips were chipped, due to what believed the higher hammering that fractured the tip by mechanical fracture. Also, the diamond coating was delaminated exposing more area of solid substrate compared to the low US level.

The effect of the US hammering is clearly depicted in **Figures 4.20** and **4.21**. The vibration represented in the *z*-axis caused an intermit contact between the tool tip and workpiece, produced a hammering movement that resulted in the localised cracking of the diamond coating, as seen in the low-amplitude cutter. However, as the vibration amplitude increased, the effect of hammering increased and resulted in more cracking and chipping of the tips, and larger areas of the diamond coating removed.

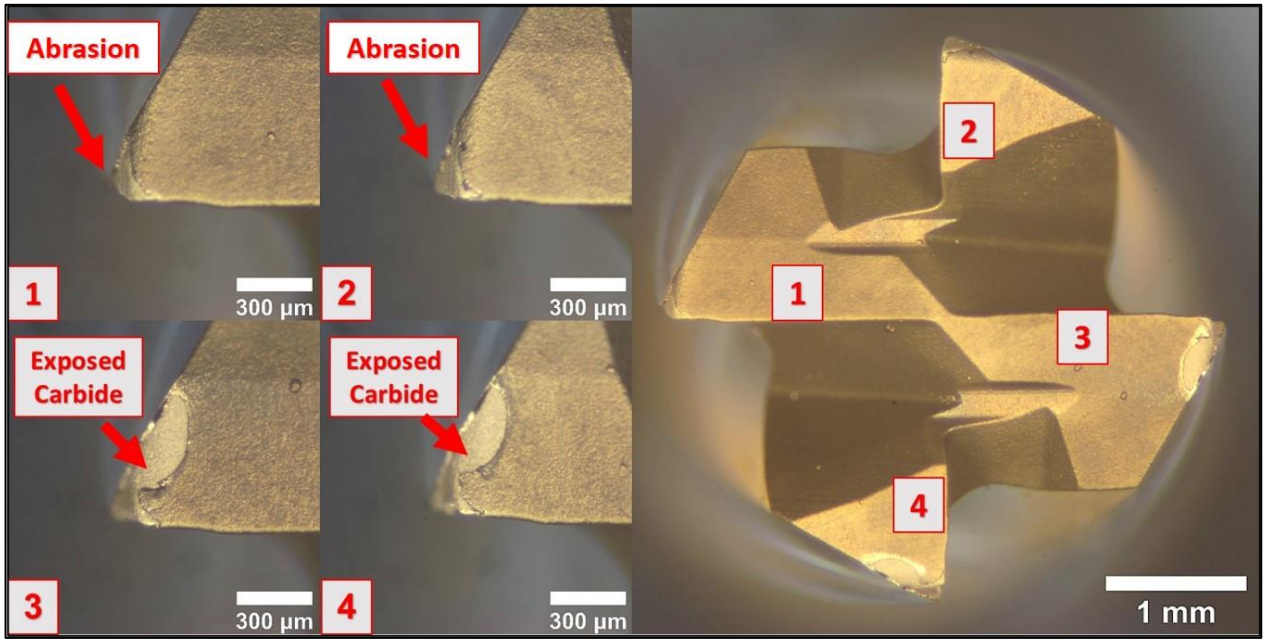


Figure 4.20 Tool flank wear of the cutter with low US amplitude (0.5–2 µm) after cutting 1200 mm (**phase 1.C**)

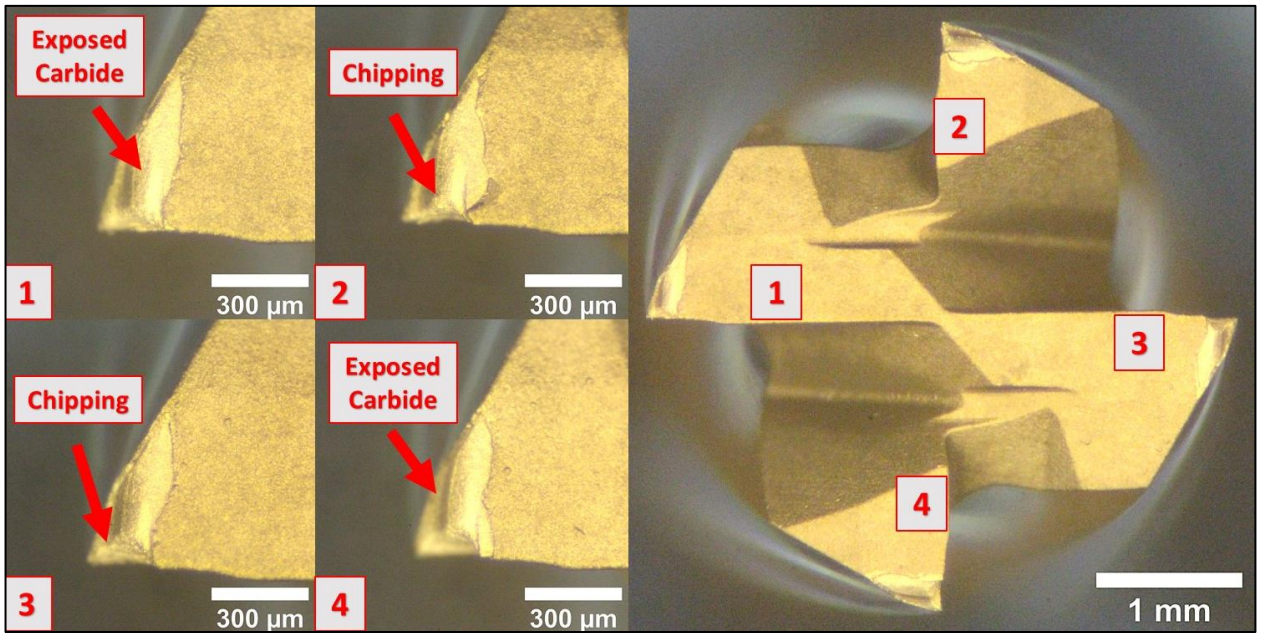


Figure 4.21 Tool flank wear of the cutter with a high US amplitude (2–4 µm) after cutting 150 mm (**phase 1.C**)

b) Surface Roughness Analysis

The average of surface roughness Ra values of the three machining conditions are shown in **Figure 4.22**, with error bars. The conventional machining of 0-µm amplitude obtained an Ra value of 0.33 µm. The low and high US vibration amplitudes obtained Ra values of 0. 38 and

0.63 µm, respectively. As the US amplitude increased from 0 µm to within the low US amplitude of 0.5–2 µm, the Ra did not change significantly. However, as the amplitude increased from 0 µm to within the range of 2–4 µm, the Ra value increased by almost 90%. The machined surfaces imaged with Alicona microscope at magnification of ×20 is shown in **Figure 4.23**. Conventional machining without US vibration obtained better surface finish than UAM. The cutting mode was dominated by ductile fracture mechanism, as shown in **Figure 4.23(a)**.

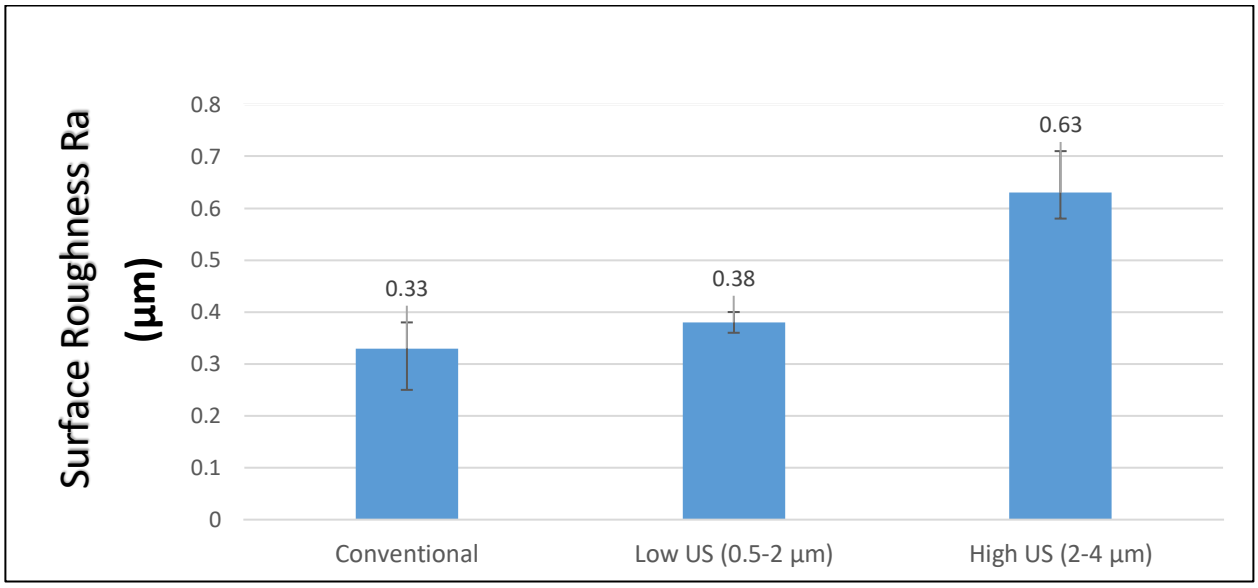


Figure 4.22 Average surface roughness Ra at the conventional, low, and high US amplitudes obtained with ZrO_2 machining by UAM (**phase 1.C**)

While, the machined surfaces obtained with UAM (**Figure 4.23 b and c**) clearly showed that the main material removal mechanism was by brittle fracture. This might be due to multiple factors. The first one is the material removal mechanism, where in UAM depends mainly on the hammering effect, which creates more cracks on the surface than conventional brittle cutting of hard material, and relies on cracks propagation to remove the material. In conventional machining, material is removed mainly by the progressive movement of the cutting edge toward the material till the cracks initiated at the tool tip, and then the chips formed. The second reason

is that the heat generated in the contact zone that softens the material is higher in conventional machining than in UAM [68], so the surface is cut in ductile mode.

The tool tip used in conventional machining has a higher chip load and longer friction time with the surface, whereas the intermitted movement in US machining reduces the chip load and allows more cutting fluid to flow through the contact zone. The third reason is that the tool wear in UAM causes faster loss of diamond coating due to the US hammering movement; thus, the cutting process by the bare solid carbide substrate mostly results in poor surface finish as the US amplitude increases.

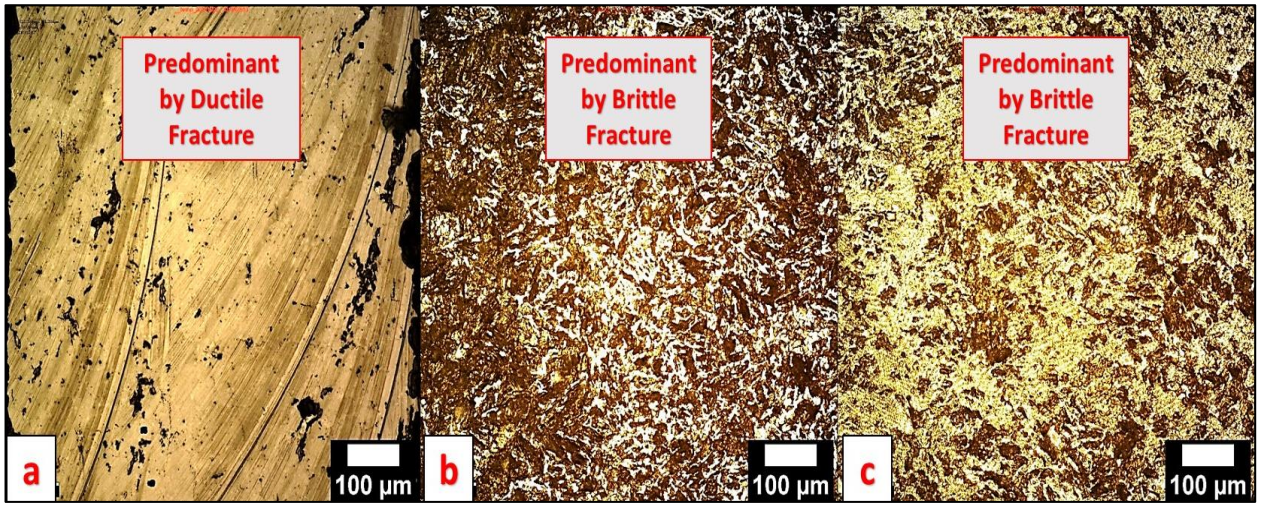


Figure 4.23 Microscopic images of ZrO_2 surfaces machined by (a) conventional milling (vibration amplitude = 0 µm), (b) a cutter with low US vibration amplitude (0.5 –2 µm), and (c) a cutter with high US vibration amplitude (2–4 µm), (**phase 1.C**)

c) Cutting Forces Analysis

The obtained cutting forces of the three machining conditions at the conventional, low, and high US amplitudes are shown in **Figure 4.24**. The conventional milling with a tool life of 1500 mm obtained average cutting forces of F_X = 36 N, F_Y = 30 N, and F_Z = 22 N. The cutter with low US vibration (amplitude = 0.5–2 µm) and a tool life of 1300 mm obtained cutting forces of F_X = 13 N, F_Y = 8.4 N, and F_Z = 17.5 N. The cutter with high US vibration (amplitude = 2–4 µm) and

tool life of 150 mm obtained cutting forces of F_X = 45.8 N, F_Y = 37 N, and F_Z = 79 N. The cutting forces of UAM, represented in the *z*-axis, are higher than those in the *x*- and *y*-axes.

The obtained cutting forces were significantly reduced as the US vibration was activated at the low amplitude range (0.5–2 µm). The F_X, F_Y, and F_Z values were reduced by 63%, 72%, and 20%, respectively, compared with those in conventional machining. However, as the US amplitude increased to within the high range (2–4 µm), the forces increased significantly by 27%, 23%, and 250% for the F_X, F_Y, and F_Z values, respectively.

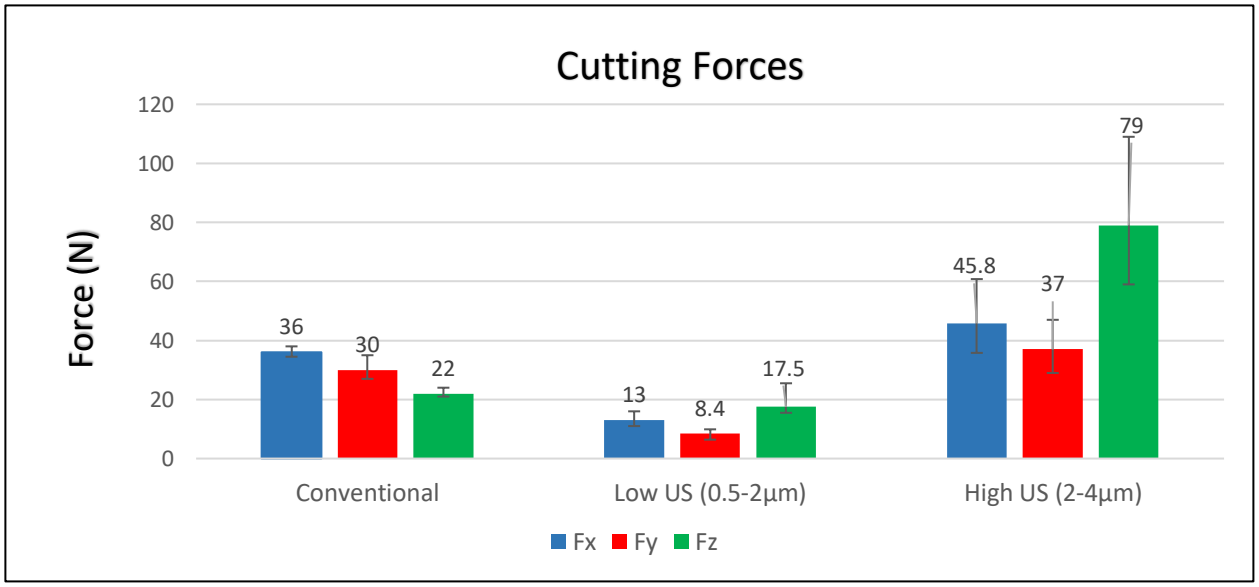


Figure 4.24 Average maximum absolute peak-to-peak cutting forces of the conventional, low-amplitude US, and high-amplitude US machining of ZrO_2 (**phase 1.C**)

Based on the results it is believed that utilized diamond coated end mill had an optimum US amplitude value that could withstand and will reduce the cutting forces till certain level. However, as the US amplitude increases the cutting forces in the *z*-axis increases significantly because of the increased hammering that resulted in intensive stresses and shocks that chipped of the tool edges, as shown in **Figure 4.21**, thus the cutting will be conducted with dull non sharp edge that will increases the cutting forces and surface roughness eventually.

4.5 Phase 1.D: Benchmarking Al_2O_3, Si_3N_4, and SiC against ZrO_2 Using UAM in Comparison with Conventional Milling

a) Tool Life Analysis

The tool wear trends obtained from conventional and UAM benchmarking are shown in **Figures 4.25** and **4.26**. The obtained tool wear trends by UAM are shown in **Figure 4.25**, it was noticed that out of three tests for Al_2O_3 machining, two have cut till reach 2000 mm while one cut only for 100 mm which was similar to that of conventional machining. This high variation in tool life due to the instability in US holder that sometimes stop producing vibration during the machining. For Si_3N_4 the variation in testing also was noticeable where it obtained 20, 30, and 50 mm tool life. Also, in SiC machining that obtained tool lives of 10, 50, and 100 mm.

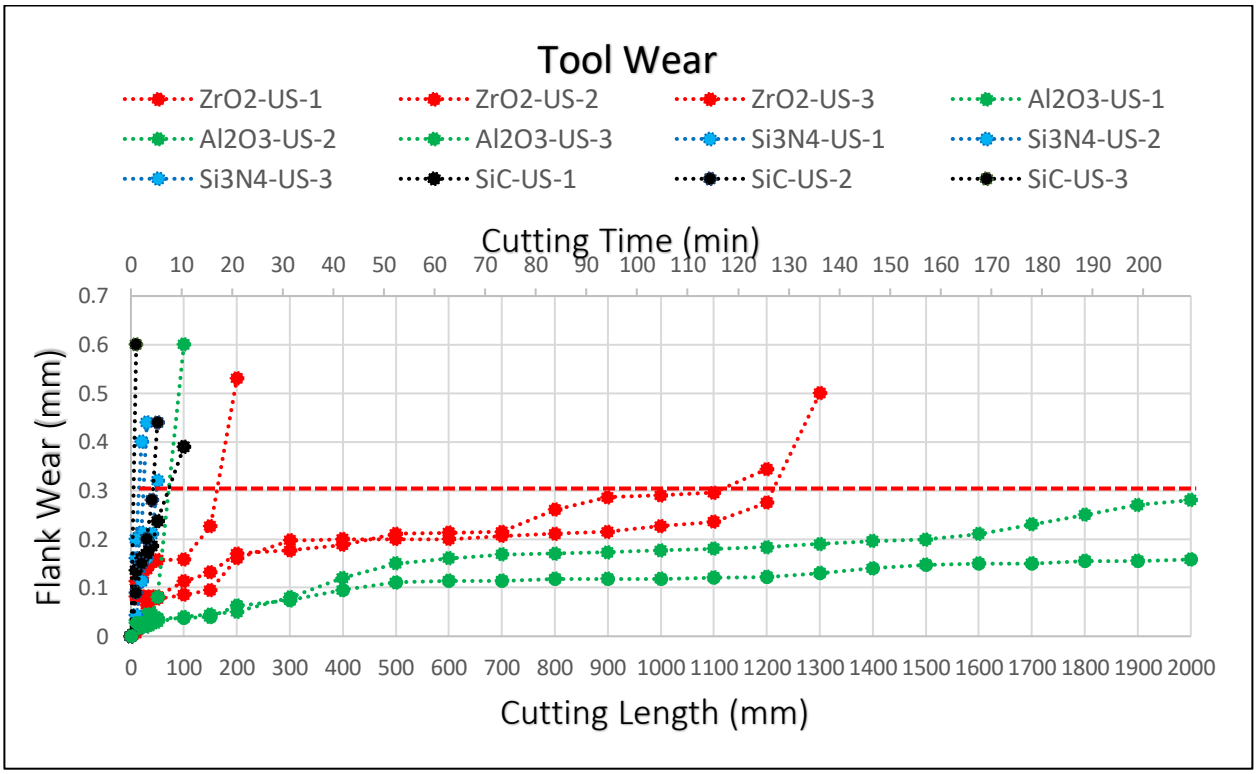


Figure 4.25 Tool flank wear trends according to the cutting length & time of ZrO_2, Al_2O_3, Si_3N_4, and SiC by UAM (**phase 1.D**)

In **Figure 4.26** the best obtained trends by UAM have benchmarked, because it difficult to benchmark 12 flank face or 12 surface roughness neither possible to have an average of suspicious results like the 100 mm that obtained by Al_2O_3 due to US holder instability, represented by solid

lines in the figure which indicate that the cutter of Al_2O_3 had the longest tool life of 2000 mm cutting length achieved at a cutting time of 209 min, followed by the cutter of ZrO_2, with a tool life of 1300 mm or 136 min, and the cutter of SiC, with a tool life of 100 mm or 10 min. The Si_3N_4 cutter had the shortest tool life of 50 mm or 5 min. When the advanced ceramics were machined using UAM, the relationship between ceramic hardness and tool life was not directly proportional, unlike that in the conventional machining in **phase 1.B**. In UAM, the Al_2O_3 cutter obtained the longest tool life even though Al_2O_3 does not have the lowest hardness value among the four ceramics. The Si_3N_4 cutter had the shortest tool life even though it does not have the highest hardness value. Obviously, this change in tool life behaviour according to hardness was due to the change in the material machining mechanism of progress of cutting-edge toward material to penetrate till the compression at the tool tip initiate the crack that propagate forming the chips, even before a shear plane forming, to machining by UAM the hammering or US vibration that initiated cracks on material surface, so as the tool tip progress into the material, lower forces are needed to form the chips and the resistance of material surface for penetration reduced, or in another word the resistance of surface hardness against tool tip reduced.

Thus, it is believed that the effect of fracture toughness of the ceramics has been increased on the machining process. Where in conventional machining the tool tip is facing a resistance during penetration the surface of the workpiece, that initiate the crack of forming chips. But, in UAM machining the cracks are already ahead tool tips existed and the most machining forces were to overcome the fracture toughness of the workpiece.

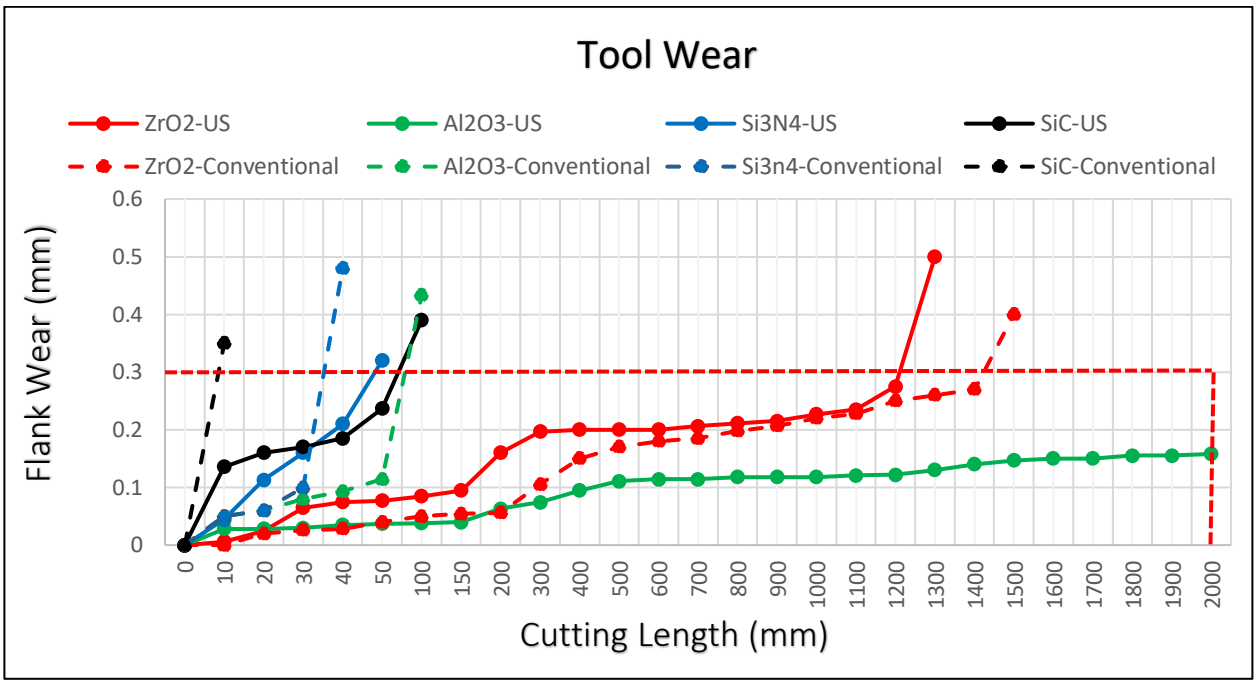


Figure 4.26 Tool flank wear trends according to the cutting length & time of ZrO_2, Al_2O_3, Si_3N_4, and SiC by conventional machining and UAM (**phase 1.D**)

The tool life of the cutter of Al_2O_3 improved from 100 mm in conventional milling to 2000 mm in UAM, which indicates 1900% improvement. The tool lives of the cutters of Si_3N_4 and SiC improved from 40 and 10 mm in conventional milling to 50 and 100 mm, respectively, which indicate improvements of 25% and 900%, respectively. However, the cutter of ZrO_2 did not show any improvement which might due to thermal softening, as it showed the lowest thermal conductivity (1.5–2.5 W m^{-1} K^{-1}) among the four ceramics, it will be discussed in cutting forces section.

The tool flank wear of the four cutters used in UAM at US amplitudes of 0.5–2 µm are shown in **Figures 4.20**, **4.27**, **4.28**, **4.29** and **4.30**. The tool flank wear of the cutter of ZrO_2 was discussed earlier in **phase 1.C**. The tool flank wear of the cutter of Al_2O_3 after cutting 2000 mm and meeting the end-of-test criterion is shown in **Figure 4.27 & 30 (b)**. The wear was mainly due to coating fracture, as traces of abrasion at the four tips could be observed. Compared with the flank wear of

the conventional milling cutter of Al_2O_3 (**phase 1.B**), the flank wear of the UAM cutter was less in worn area, which indicates the lower cutting forces.

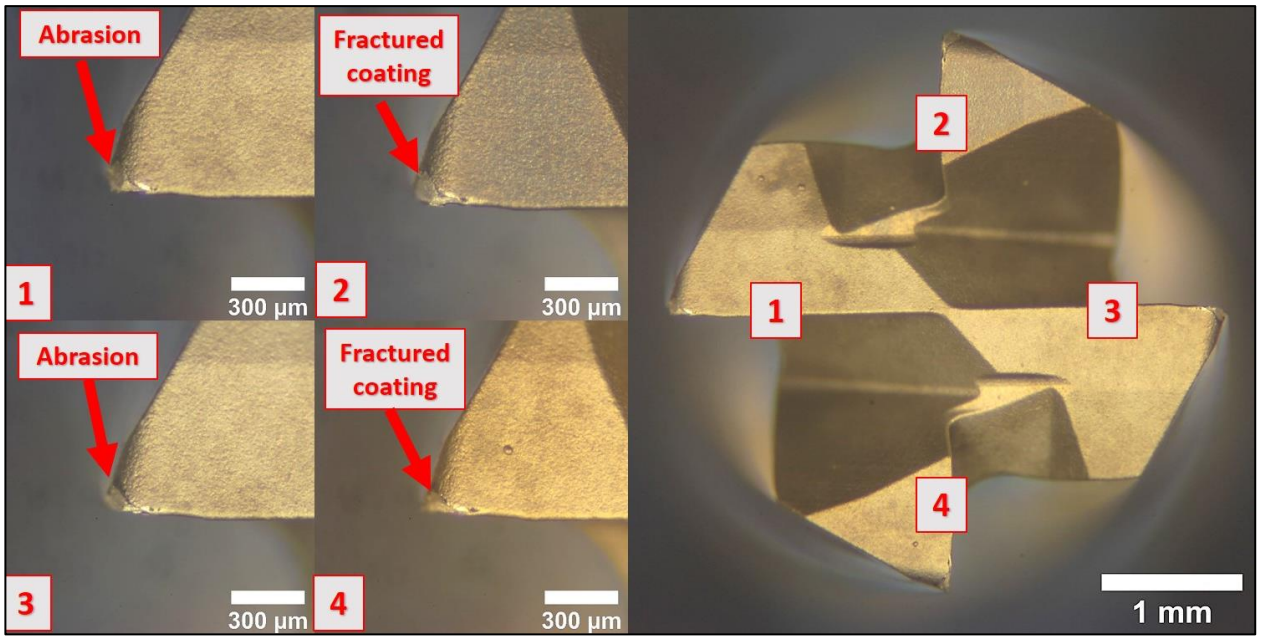


Figure 4.27 Tool flank wear of the cutter of Al_2O_3 at US amplitudes of 0.5–2 µm after cutting 2000 mm (**phase 1.D**)

The tool flank wear of the cutter of Si_3N_4 in UAM after cutting 50 mm and meeting the end-of-test criterion by reaching the average flank wear of 0.3 mm is shown in **Figure 4.28 & 30 (c)**. The cutter flank wear was due to coating fracture. All four tips had chipped coating and edge 3 showed chipped tip. Compared with the conventional Si_3N_4 cutter (**phase 1.B**) showed similar flank wear, except for the large delaminated area in one of the edges of the conventional cutter due to the higher cutting force and higher heat in the contact zone. The flank wear of the cutter of SiC used in UAM, which reached end of life at 100 mm, is shown in **Figure 4.29 & 30 (d)**. All four tips showed wear by abrasion, no coating delamination or chipping observed . Compared with the conventional cutter used to machine SiC, shown in (**phase 1.B**). The effect of US hammering at low amplitude obviously reduced the cutting forces, where it could be seen lesser volume of the cutter material has removed by UAM.

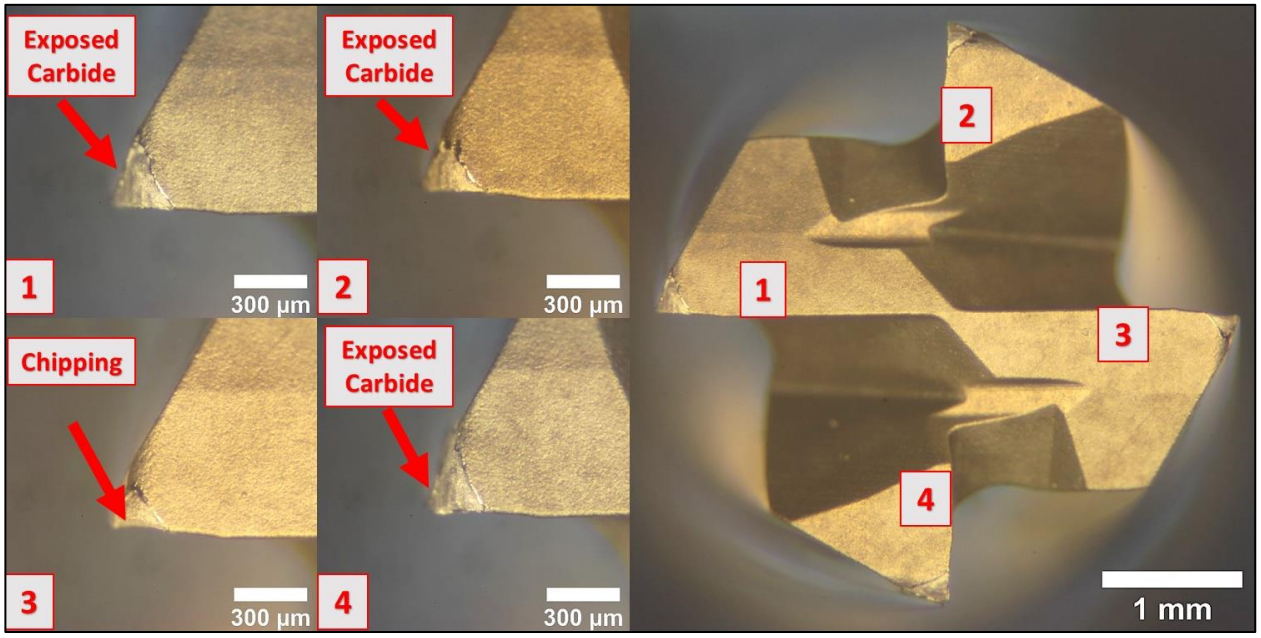


Figure 4.28 Tool flank wear of the cutter of Si_3N_4 at US amplitudes of 0.5–2 µm after cutting 50 mm (**phase 1.D**)

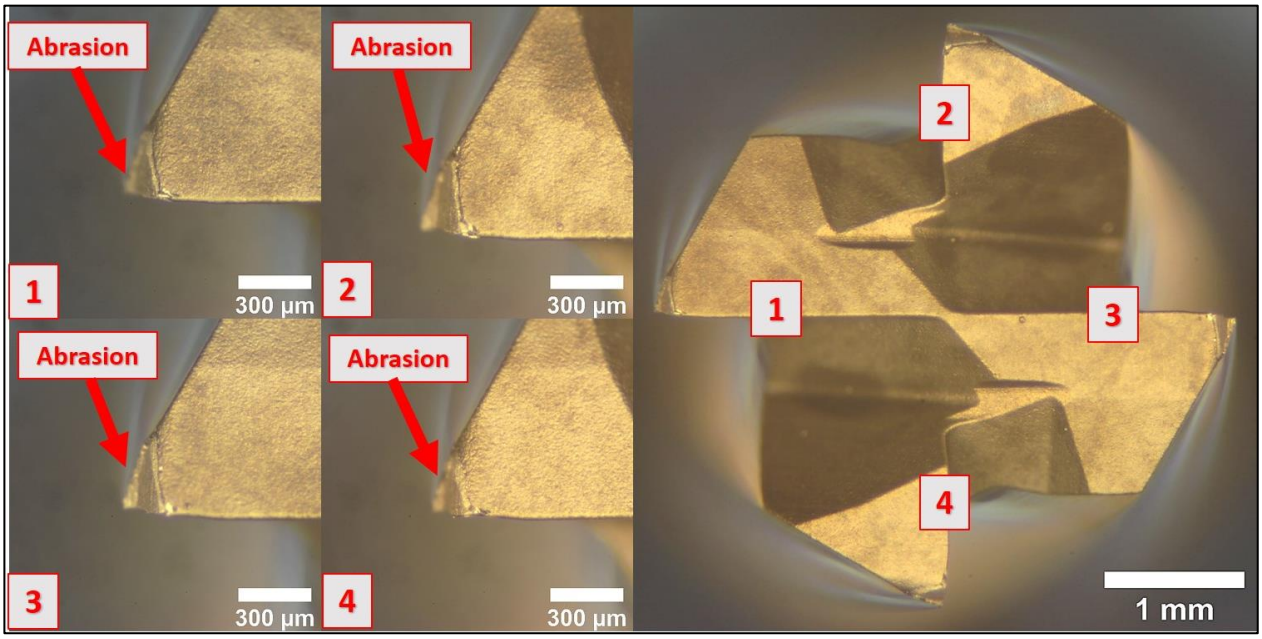


Figure 4.29 Tool flank wear of the cutter of SiC at US amplitudes of 0.5–2 µm after cutting 100 mm (**phase 1.D**)

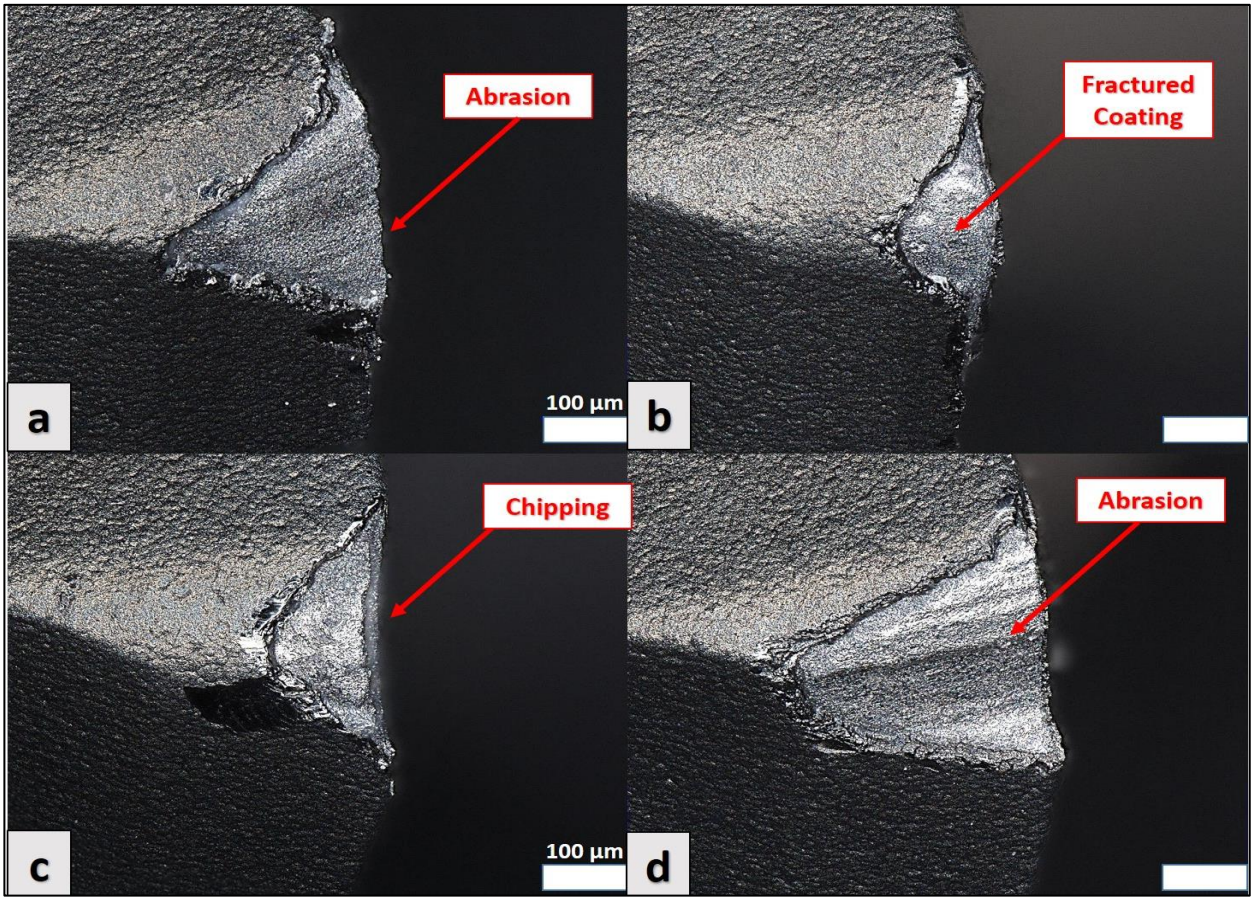


Figure 4.30 Tool wear at the cutting edge of the cutters of (a) ZrO_2, (b) Al_2O_3, (c) Si_3N_4, (d) SiC by UAM **(phase 1.D**)

b) Surface Roughness Analysis

The average surface roughness Ra values of the four ceramics machined using UAM and the conventional method are shown in **Figure 4.31**, with error bars. The Ra values obtained with UAM for ZrO_2, Al_2O_3, Si_3N_4, and SiC were 0.38, 0.5, 0.26, and 0.24 µm, respectively. They were close to those obtained using conventional machining, which were 0.33, 0.47, 0.24, and 0.28 µm, respectively. The similarity in Ra values between conventional machining and UAM was due to the relatively small US vibration amplitude used (0.5–2 µm). Because as obtained in **phase 1.C** as the US amplitude increases the higher radial and lateral crack length will be induced which will increases Ra value, besides the chipped tool tips that resulted at high amplitude also will increases the Ra value from cutting with dull edges.

The microscopic images of the four ceramics machined using UAM are shown in **Figure 4.32**. By comparing UAM with the conventional machining shown in **Figure 4.17**, the effect of US vibration on ZrO_2 became apparent. **Figure 4.32 (a)** shows that the fractures on the ZrO_2 surface changed from being dominantly ductile in conventional machining to dominantly brittle in UAM. For Al_2O_3, the surface machined using UAM showed more brittle fracture spots than the surface machined using the conventional method. Both surfaces were dominated by brittle fractures, and the effect of US vibration at the amplitude of 0.5–2 µm could be considered insignificant (**Figure 4.32 b**).

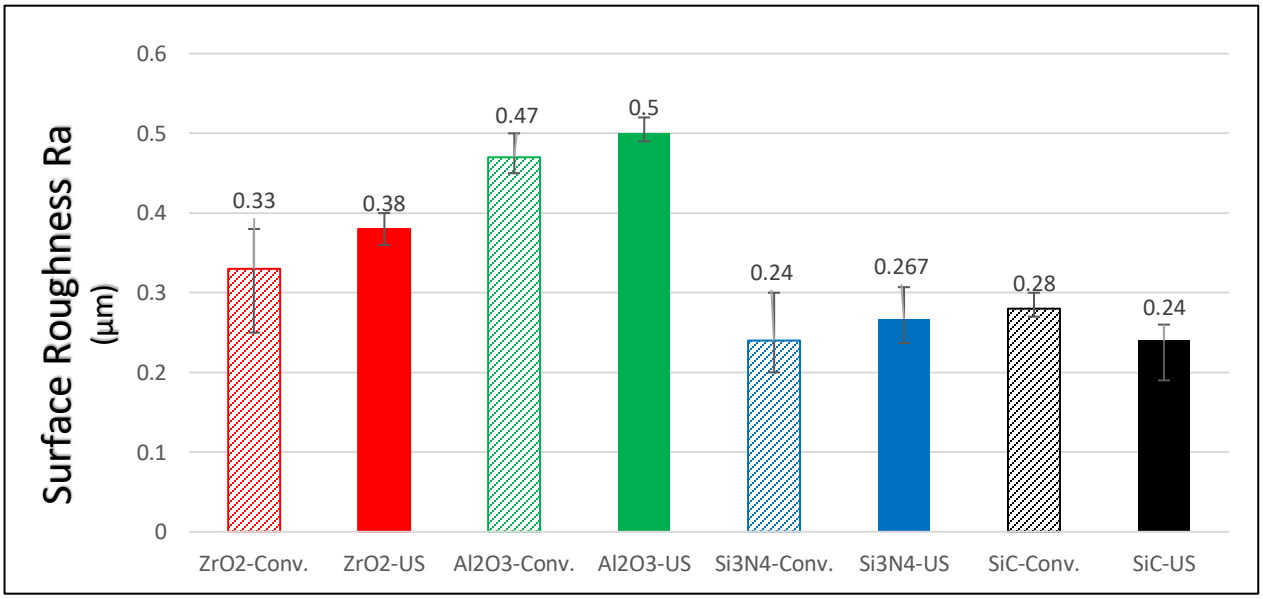


Figure 4.31 Average surface roughness Ra values of ZrO_2, Al_2O_3, Si_3N_4, and SiC obtained using conventional machining and UAM (**phase 1.D**)

The non-oxide ceramics of Si_3N_4 and SiC (**Figures 4.32 c and d**) showed similar brittle surfaces obtained using UAM, which were also similar to the surfaces machined using conventional machining, where the machined surfaces showed almost equal areas of brittle and ductile fractures.

It was clear that ZrO_2 was the most affected by the material removal mechanism of US vibration, showing a change in surface from being dominated by ductile fractures to being dominated by brittle fractures. Due to the changing in material removing mechanism, in conventional machining it believed the self-toughening mechanism that ZrO_2 exhibited by supressing cracks propagation has made the chip formation conducted by shearing mainly, where material layers slip plastically to form chips similar to that in metal machining. However, when UAM applied the hammering of US had initiated cracks ahead tool tip that had deeper cracks length where the self-toughening mechanism no longer able to suppress, thus the material removed by crack propagation mainly.

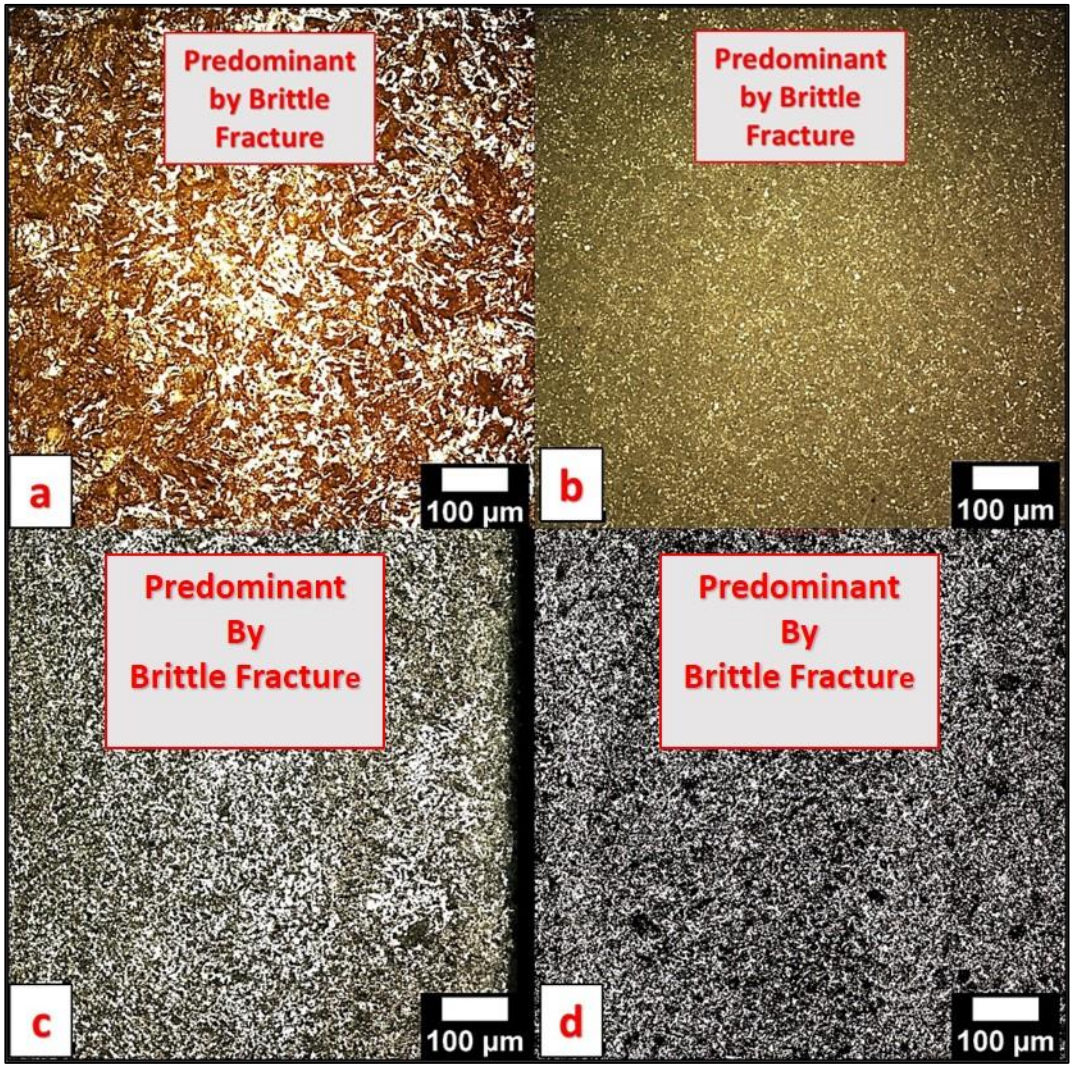


Figure 4.32 Microscopic images of surfaces machined using UAM at US amplitudes of 0.5–2 µm: (a) ZrO_2, (b) Al_2O_3, (c) Si_3N_4, and (d) SiC (**phase 1.D**)

c) Cutting Forces Analysis

The cutting forces obtained using UAM and conventional machining are shown in **Figure 4.33**. The force signals obtained using DynoWare are shown in **Appendix A.1(b)**. The following are the tool lives and cutting forces achieved by the ceramic cutters, respectively: ZrO_2, 1300 mm and F_X = 13 N, F_Y = 8.4 N, and F_Z = 17.5 N; Al_2O_3, 2000 mm and F_X = 10.6 N, F_Y = 7.8 N, and F_Z = 19.6 N; Si_3N_4, 50 mm and F_X = 24.6 N, F_Y = 14.9 N, and F_Z = 50 N; and SiC, 100 mm and F_X = 12.2 N, F_Y = 9.6, and F_Z = 14 N. The forces obtained show significant decreases in cutting forces due to the effect of US vibration compared with those obtained using conventional machining in **phase 1.B**. The influence of ceramic hardness was no longer directly proportional to the cutting forces, as the hardest ceramic (SiC; HV = 2400–2800 kgf/mm^2) obtained the lowest F_Z value (14 N). The tool lives of the four cutters were no longer directly proportional to the cutting forces, where the ZrO_2 cutter had a cutting length of 1300 mm and F_Z value of 17.5 N, whereas the cutter of Al_2O_3 had a cutting length of 2000 mm and F_Z value of 19.6 N. This is believed to be due to two main causes.

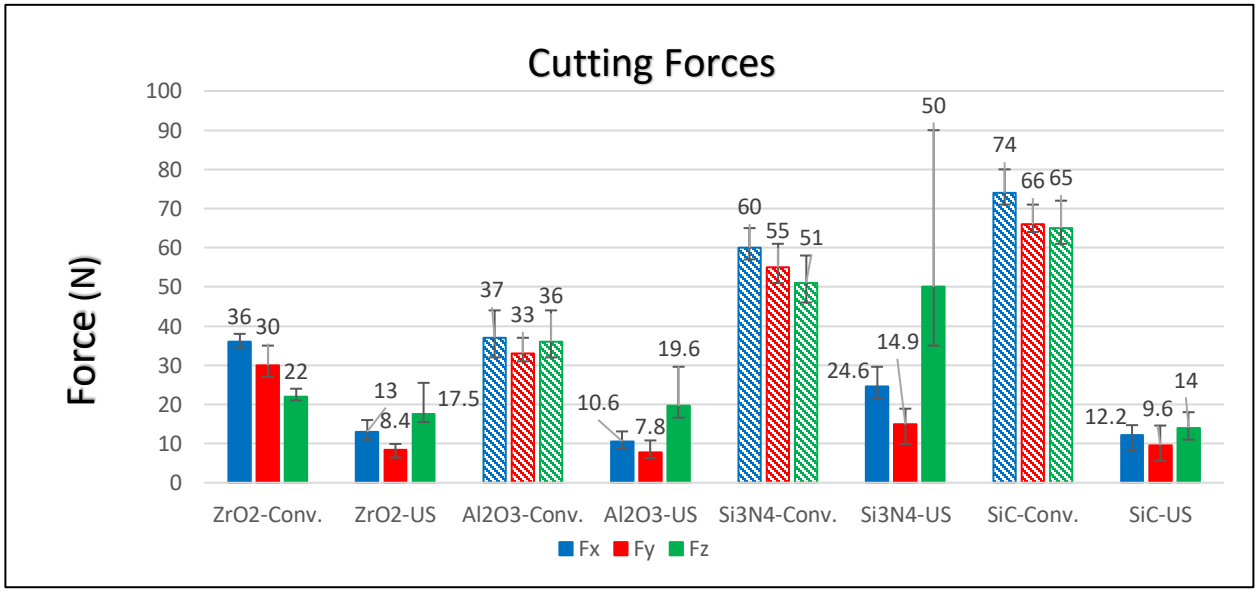


Figure 4.33 Average maximum absolute peak-to-peak cutting forces of ZrO_2, Al_2O_3, Si_3N_4, and SiC using conventional machining and UAM (**phase 1.D**)

First, because of the intermitted contact between the cutter and the workpiece due to US vibration reduced the friction time, resulting in decreased cutting forces. Moreover, the amount of cutting fluid flow into the contact zone increased because of the intermitted contact, removing the debris and swarf more efficiently. Second is the cutting mechanism that changed from cutting in conventional machining to hammering in UAM. In conventional machining, the cutting forces were affected mainly by hardness, which resists the penetration of the cutter's edge. In UAM, the cutting forces are affected mainly by fracture toughness, which resists the propagation of the cracks created by US hammering.

Therefore, when comparing the non-oxide ceramic cutters, Si_3N_4 (HV = 1700–2200 kgf/mm^2) and SiC (HV = 2400–2800 kgf/mm^2), in conventional machining, it was found that the Si_3N_4 cutter had a tool life of 40 mm, with an *F* value of 96 N, whereas the SiC cutter had a tool life of 10 mm, with an *F* value of 118 N. However, with the UAM method, the SiC cutter reached a tool life of 100 mm, with an *F* value of 20 N, which is better than that achieved with the Si_3N_4 cutter of 50 mm, with an *F* value of 57 N. This is believed to be due to several factors. The main reason is the reduction in cutting forces, which were affected mainly by their fracture toughness. The fracture toughness of Si_3N_4 and SiC were 5–8 MPam½ and 2–4 MPam½, respectively.

Moreover, when comparing the tool life of the oxide ceramic cutters, ZrO_2 (HV = 1200 kgf/mm^2) and Al_2O_3 (1500–1650 kgf/mm^2), in conventional machining, it was found that the ZrO_2 cutter reached a tool life of 1500 mm, with an *F* value of 51 N, whereas the Al_2O_3 cutter obtained a tool life of 100 mm, with an *F* value of 61 N. However, by using the UAM method, the cutter of Al_2O_3 obtained a tool life of 2000 mm, with an even higher *F* value of 23 N, which is longer than that of the cutter of ZrO_2 (1300 mm, *F* = 23 N). This might happen due to the higher heat generated in the cutting zone due to UAM hammering that absorbed by the ZrO_2 workpiece, which weakened the

bonding force of the diamond coating. ZrO_2 has a very low thermal conductivity coefficient of 1.5–2.5 W m^{-1} K^{-1} compared with Al_2O_3 (26–35 W m^{-1} K^{-1}). Thus, the heat generated by UAM in the contact zone of ZrO_2 did not spread or was not transferred to the surrounding areas with higher efficiency rates, which might have resulted in higher thermal softening proportional to the US vibrational.

Another important finding is that when comparing the oxide ceramics with lower hardness values with the non-oxide ceramics with higher hardness values, it was found that the tool life of the non-oxide ceramics in UAM did not exceed that of the oxides. Owing to the large difference in hardness value, the UAM method still could not overcome. By contrast, the differences in hardness between ZrO_2 and Al_2O_3, and between Si_3N_4 and SiC were relatively small. This indicates that the hardness value affects the tool life even when the forces are reduced, as observed from the tool life of the SiC cutter of 100 mm at an F_Z value of 14 N compared with the tool life of ZrO_2 of 1300 mm at an F_Z value of 17.5 N.

The percentage of reduction in cutting forces was proportional to the fracture toughness value, where the reduction in F value was significantly higher in SiC and Al_2O_3 than in ZrO_2 and Si_3N_4. The highest reduction was obtained by SiC (fracture toughness = 2–4 MPam½) from 118 N to 20 N, which is a decrease of 82%, followed by Al_2O_3 (fracture toughness = 2.5–4 MPam½), which was reduced from 61 N to 23 N (a decrease of 62%) and ZrO_2(fracture toughness = 6–9 MPam½), which was reduced from 51 N to 23 N (a decrease of 54%). In Si_3N_4 (fracture toughness = 5–8 MPam½), which was reduced from 96 N to 57 N (a decrease of 40%).

However, the effect of the cutting forces obtained with UAM on the observed tool flank wear was consistent among the four cutters. When comparing the **Figure 4.15** of conventional to **Figure 4.30** of UAM it could be seen clearly that tool wear severity was much lower by UAM.

Thus, it can be concluded that US vibration significantly reduced the cutting forces. These reductions played an important role in improving the machinability of Al_2O_3. SiC showed good improvement, Si_3N_4 showed limited enhancement, and ZrO_2 unexpectedly showed a drawback, which could be overcome by enhancing the CVD diamond coating properties.

4.6 Summary of Results

The following **Table 4.1** is summarizing the obtained technical results of **Phase 1**, where it shows the improvement by UAM in the tool lives of three of advanced ceramics cutters, and the reduction in the cutting forces that took place in all tested ceramics. The surface roughness Ra values were almost at the same range in Conventional and UAM.

Table 4.1 Summary of the technical results of Phase 1

Material	**Conventional End Milling**			**UAM**		
	Average Tool life (min)	Surface Roughness Ra (µm)	Cutting Force (N)	Average Tool life (min)	Surface Roughness Ra (µm)	Cutting Force (N)
ZrO_2	146.5	0.33	51	94.2	0.38	23
Al_2O_3	7.8	0.47	61	142.8	0.5	23
Si_3N_4	3	0.24	96	3.4	0.26	57
SiC	1	0.28	118	5.5	0.24	20

5. RESULTS AND DISCUSSION: PHASE 2, POINT GRINDING

The objective of this chapter is to Investigate the effect of using electroplated diamond grinding points with a small diameter (4 mm) on ZrO_2 at a relatively high cutting speed. And benchmark Al_2O_3, Si_3N_4, and SiC against ZrO_2 for the use of diamond grinding points conventionally. The assessment criteria include tool wear, surface roughness, material removal mechanism, and cutting forces. Also, to investigate the improvements that can be achieved using non-conventional methods of UAG.

5.1 Phase 2.A: Investigating the Operating Parameters for Point Grinding ZrO_2

a) Tool Wear Analysis

The resulting tool wear at both grinding points is shown in **Figures 5.1** and **5.2**. The figures show the tools before and after machining. The high-level tool (**Figure 5.1**) that machined at a cutting speed of 5 m/s and feed rate of 5 mm/min, f = 0.2µm/rev, was severely worn just after one pass of 20 mm. The electroplated bond cracked and was worn fast at the circumference, and part of the slot was rubbed by the bare shank material. Traces of diamond grains worn by abrasion were observed. The centre area of the end face remained in good condition. The low-level tool (**Figure 5.2**) that machined at a V value of 1 m/s and feed rate of 1 mm/min, f = 0.2µm/rev, showed less wear even after cutting 100 mm or 40 mm^3. Some abrasion wear could be observed on some grains at the edge of the tool, and some grains were fractured, producing sharper angles. Some grains were good condition without any trace of wear. Moreover, the electroplated bond was in good condition, shining without any scratches. The higher cutting speed of 5 m/s at a MRR of 2 mm^3/min resulted in higher grinding energy, which weakened the electroplated bond adhesion force because of the higher heat and force, resulting faster tool wear.

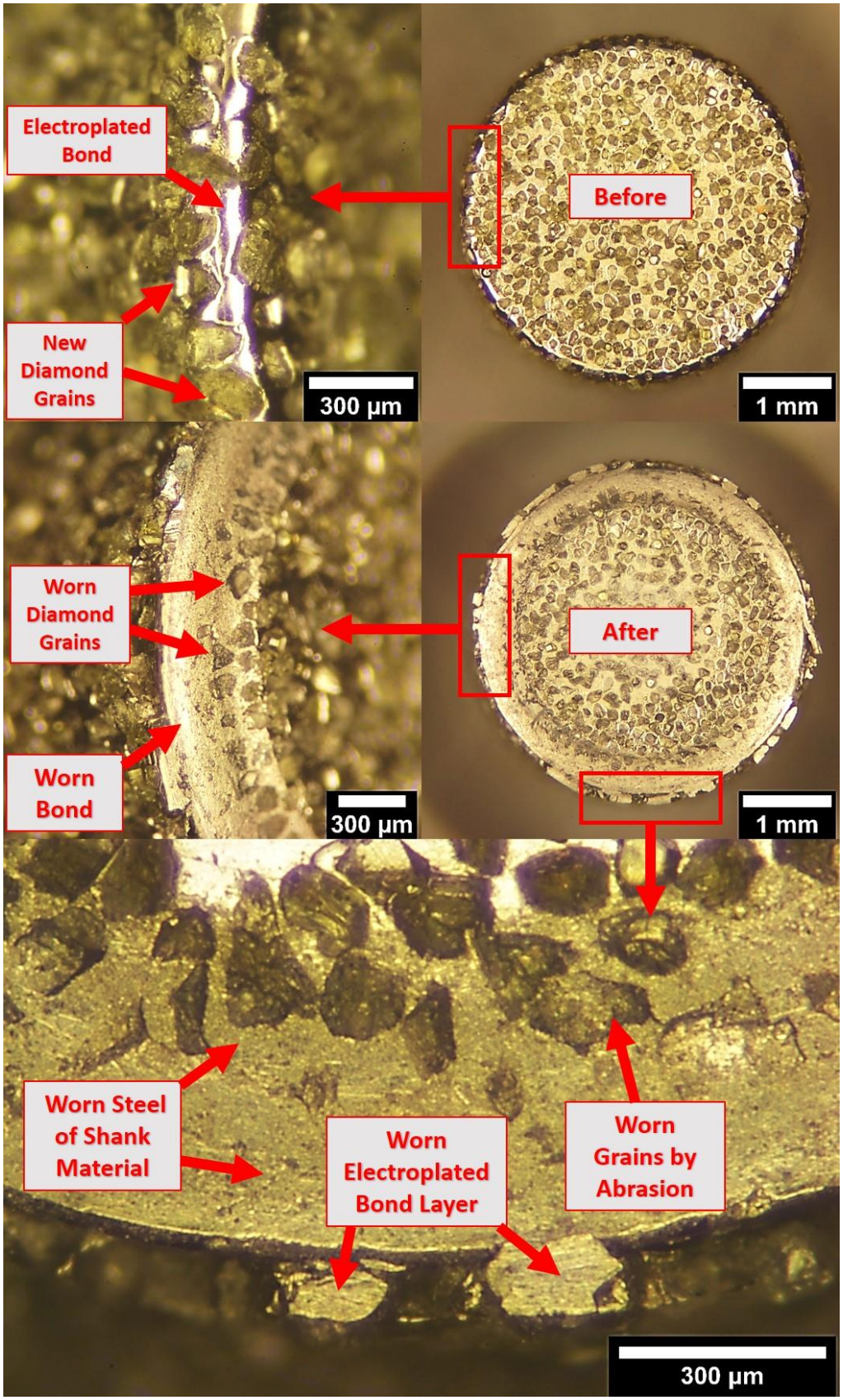


Figure 5.1 Tool wear at a speed of 5 m/s and feed of f = 0.2µm/rev after grinding for 20 mm (**phase 2.A**)

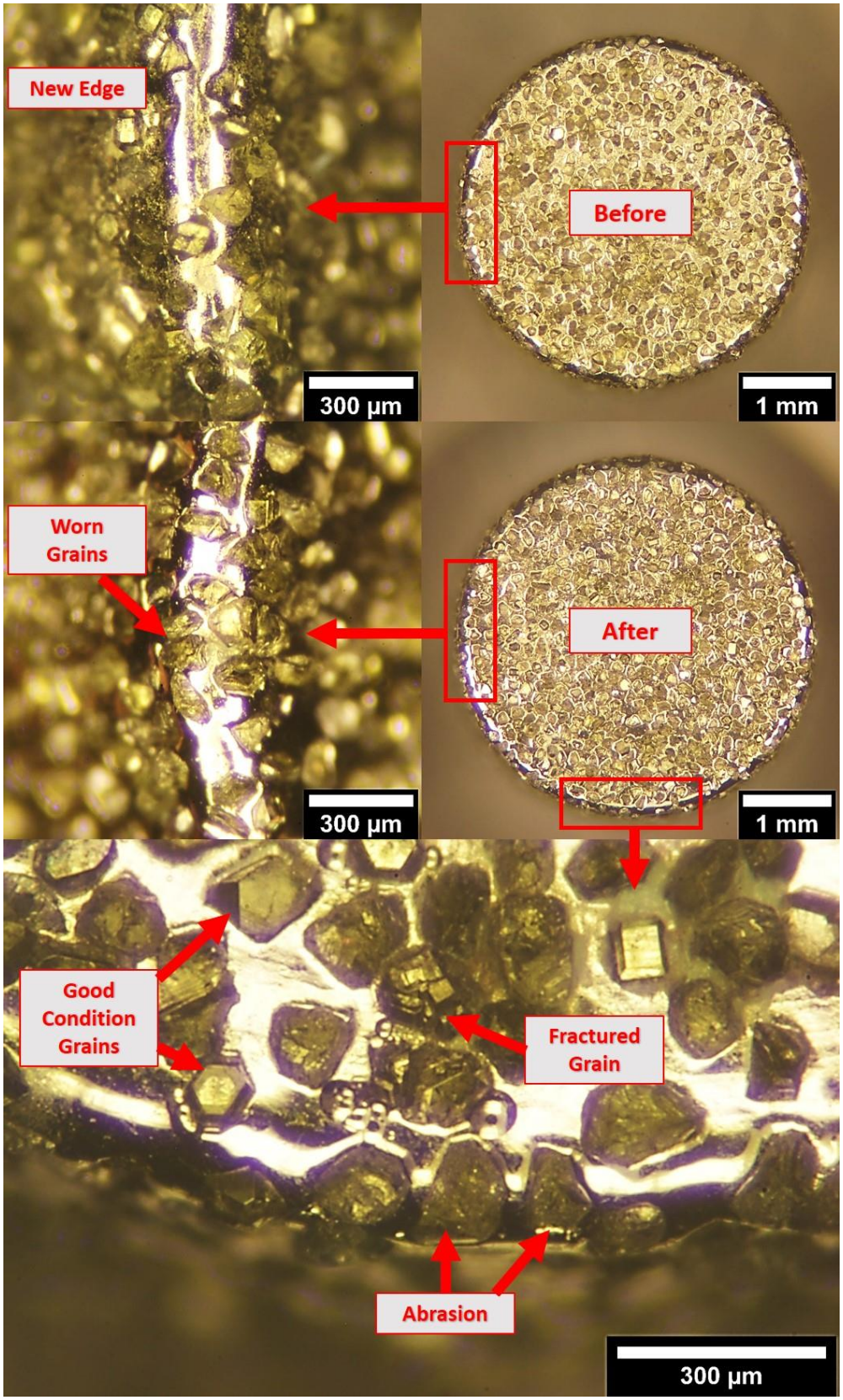


Figure 5.2 Tool wear at a speed of 1 m/s and feed of f = 0.2µm/rev after grinding for 100 mm (**phase 2.A**)

b) Surface Roughness Analysis

The Ra values obtained in the two grinding conditions are shown in **Figure 5.3**. The high-level speed of 5 m/s and feed of f = 0.2µm/rev obtained an Ra value of 0.79 µm, with high reading variation. The low-level speed of 1 m/s and feed of f = 0.2 µm/rev obtained an Ra value of 0.33µm.

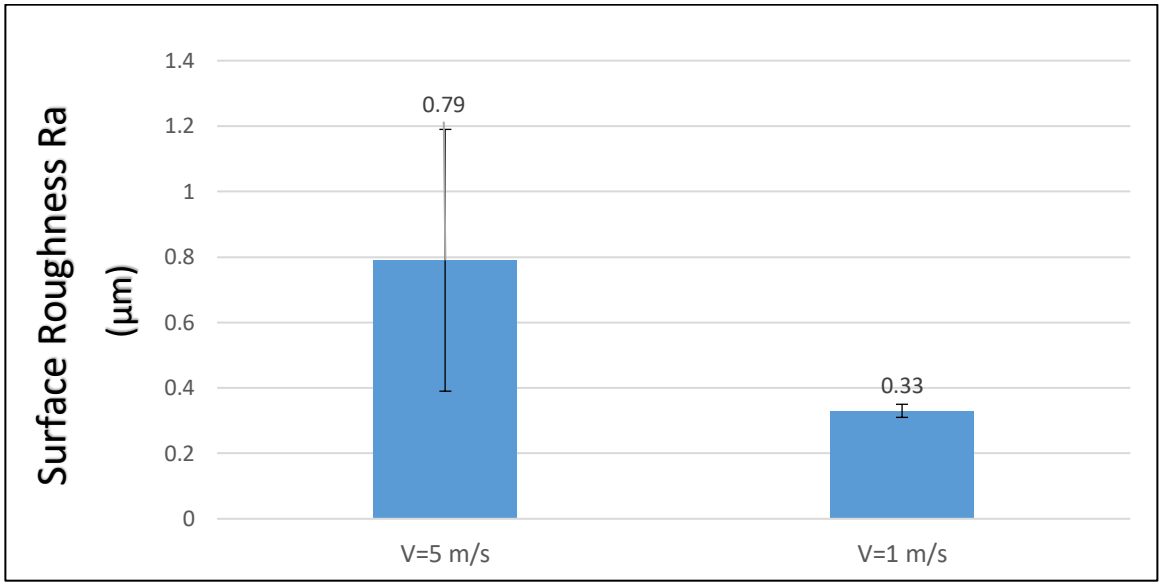


Figure 5.3 Average surface roughness Ra of ZrO_2 obtained using conventional point grinding at a high-speed V = 5 m/s and low speed V = 1 m/s (**phase 2.A**)

Microscopic images of the machined surfaces are shown in **Figure 5.4**. The material removal mechanism of the high-level surface was dominated by ductile fractures, as shown in **Figure 5.4(a)**, where the plastic flow of the material could be observed on machined surfaces as arc patterns distributed all over the surface. The low-level surface was obtained by a material removal mechanism dominated by brittle fractures, as shown in **Figure 5.4 (b)**. Cutting with a worn tool at high-level parameters, believed caused the ductile fractures mode. The high heat generated at higher speed might soften the material. Besides, the relatively positive rake angle of the bare shank metal edge that cut the ZrO_2 will eventually result in plastic flow. However, the ductile cutting mode does not guarantee a good surface roughness, as a higher Ra value was

obtained with a high-level tool. It believed the machined surface has higher asperities at the edges of arc patterns due to plastic deformation, or due to the folded asperities as found in Ramesh work [51].

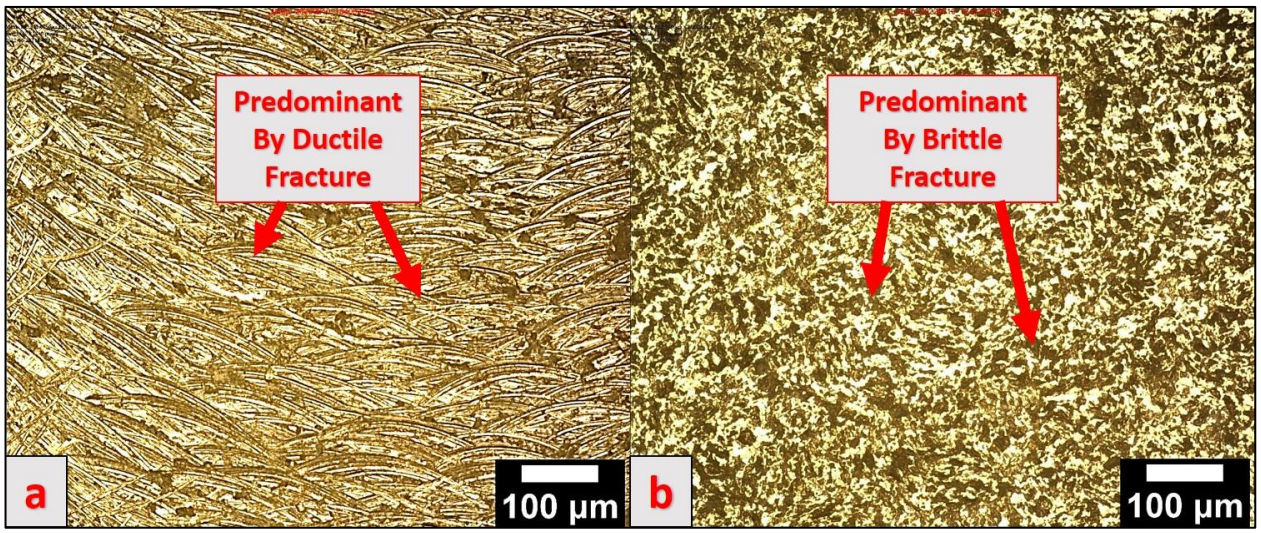


Figure 5.4 Microscopic images of the ZrO_2 surfaces machined by the grinding point at (a) V = 5 m/s and feed f = 0.2µm/rev, and (b) V = 1 m/s and feed f = 0.2µm/rev (**phase 2.A**)

c) Grinding Forces Analysis

The grinding force averages obtained in the two machining conditions are shown in **Figure 5.5**, with error bars. The effects of higher speed on the grinding forces were obvious, where machining at V = 5 m/s obtained forces of F_X = 212 N, F_Y = 194 N, and F_Y = 233 N, which were higher by almost four times those obtained with machining at a lower speed. The effects of the high forces obtained could be observed on the tool wear in **Figure 5.1**, which could not machine more than one pass of 20 mm. At a lower speed of 1 m/s, the obtained grinding forces were reduced to F_X = 70 N, F_Y = 47 N, and F_Z = 67 N, which were reflected on the good condition of the many diamond grains at the cutting edge of the grinding point (**Figure 5.2**) even after grinding 100 mm. The force fluctuation at the cutting speed of 5 m/s was higher owing to the eroded electroplated bond that worn out as the machining progressed, and the grinding point

started grinding with the bare shank metal. The force fluctuation at a cutting speed of 1 m/s was much lower and steadier during the whole cutting path of 100 mm.

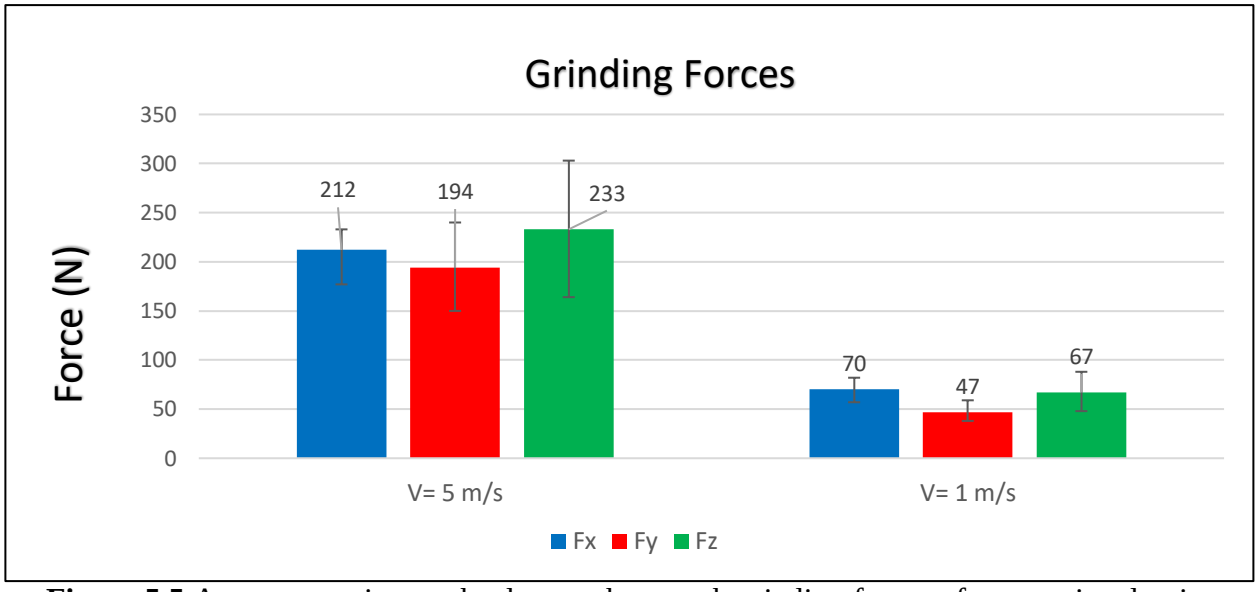


Figure 5.5 Average maximum absolute peak-to-peak grinding forces of conventional point grinding of ZrO_2 at a high speed of V = 5 m/s and low speed of V = 1 m/s (**phase 2.A**)

5.2 Phase 2.B: Benchmarking Al_2O_3, Si_3N_4, and SiC against ZrO_2

a) Tool Wear Analysis

The tool wear of the grinding points that ground ZrO_2, Al_2O_3, Si_3N_4, and SiC are shown in **Figures 5.2**, **5.6**, **5.7**, and **5.8**, respectively. All images of tool wear were taken after each point ground a slot 0.1 mm deep and 100 mm long. This removed approximately 40 mm^3 of material volume in a grinding time of 100 min. The tools diameters were measured five times at different locations, before and after slots machining. It found that there was no significant change in measurements, both readings of before and after were having the same error by using the optical microscope. Thus, the tool wear evaluation based on the microscopic observation basically, and later supported by grinding forces values.

The diamond grains at the circumference edge of all utilised points showed abrasion wear because the grinding was mainly performed by the edge grains. Several fractured grains were also found. However, the grains most affected by abrasion were found at the Si_3N_4, ZrO_2, and Al_2O_3 points, where the tools were grinding so close from the electroplated bond. The SiC point showed grains less worn edge, with more grains resharpen by fracture. Moreover, none of the utilised points showed worn, fractured, or even scratched bonds. Also, no trace of grain dislocation was found at any grinding points. This indicates the high strength of the utilised electroplated bond, especially the ground ceramics with high hardness up to 2800 kgf/mm^2.

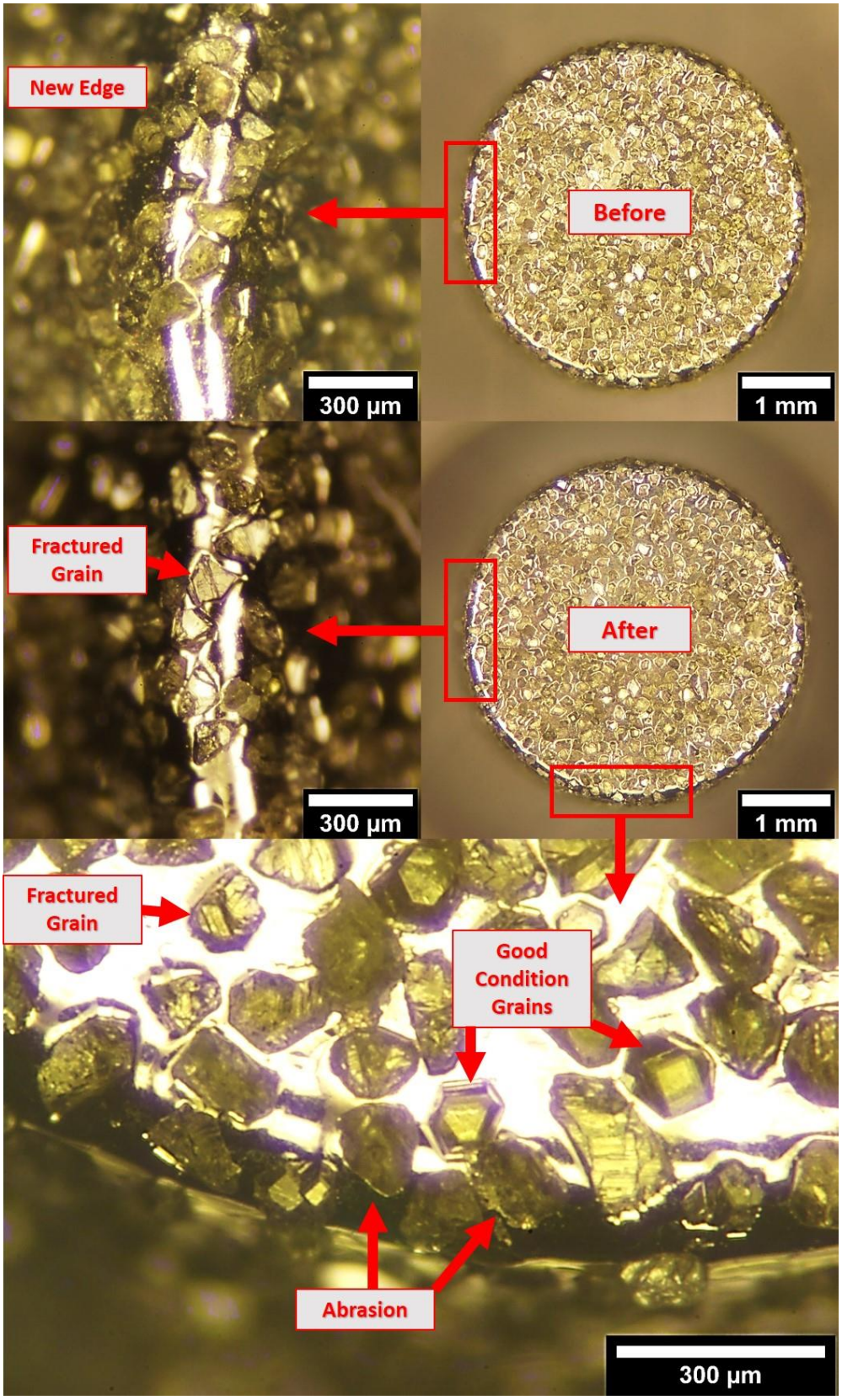


Figure 5.6 Tool wear of the Al_2O_3 grinding point after grinding 100 mm (**phase 2.B**)

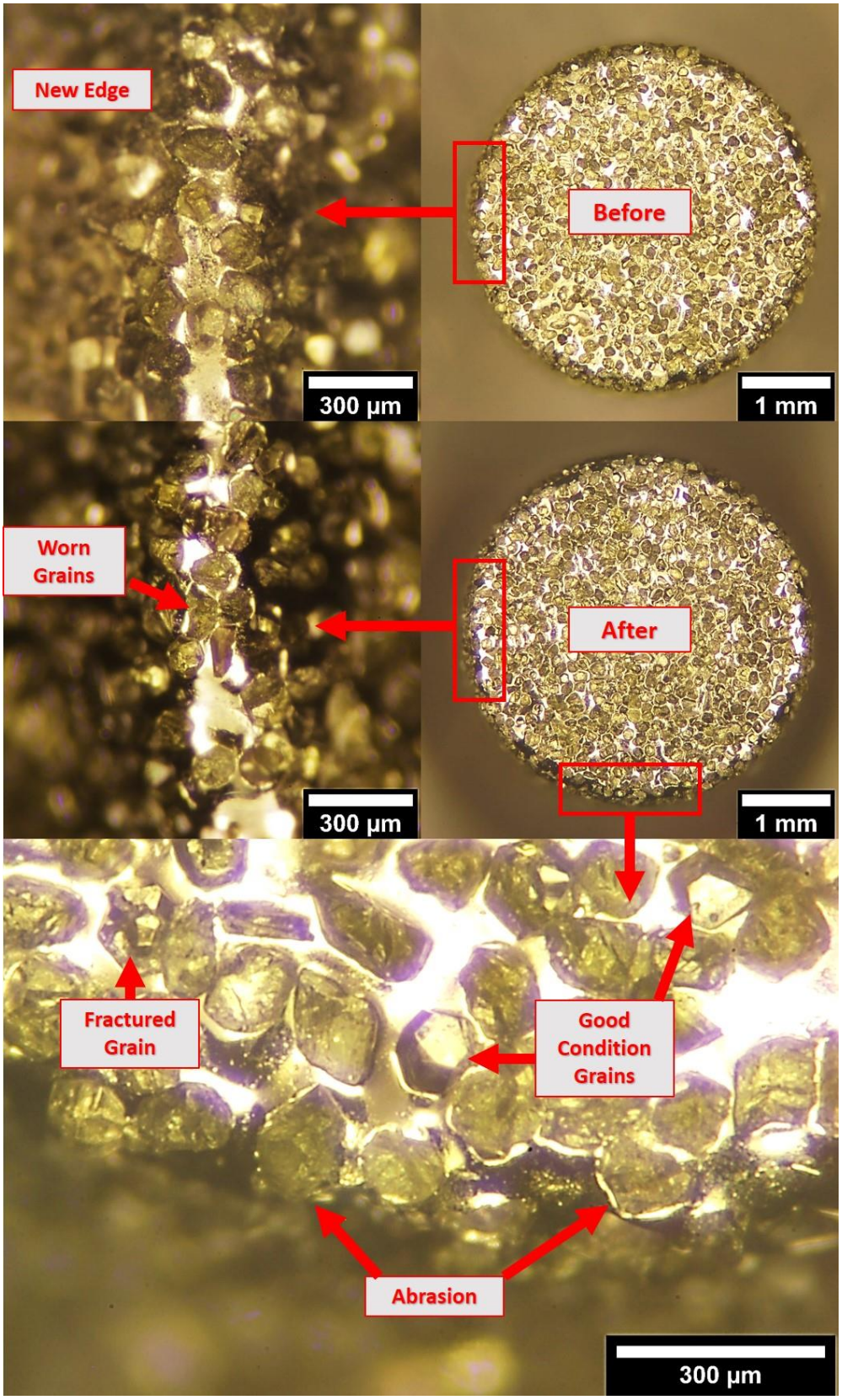


Figure 5.7 Tool wear of the Si_3N_4 grinding point after grinding 100 mm (**phase 2.B**)

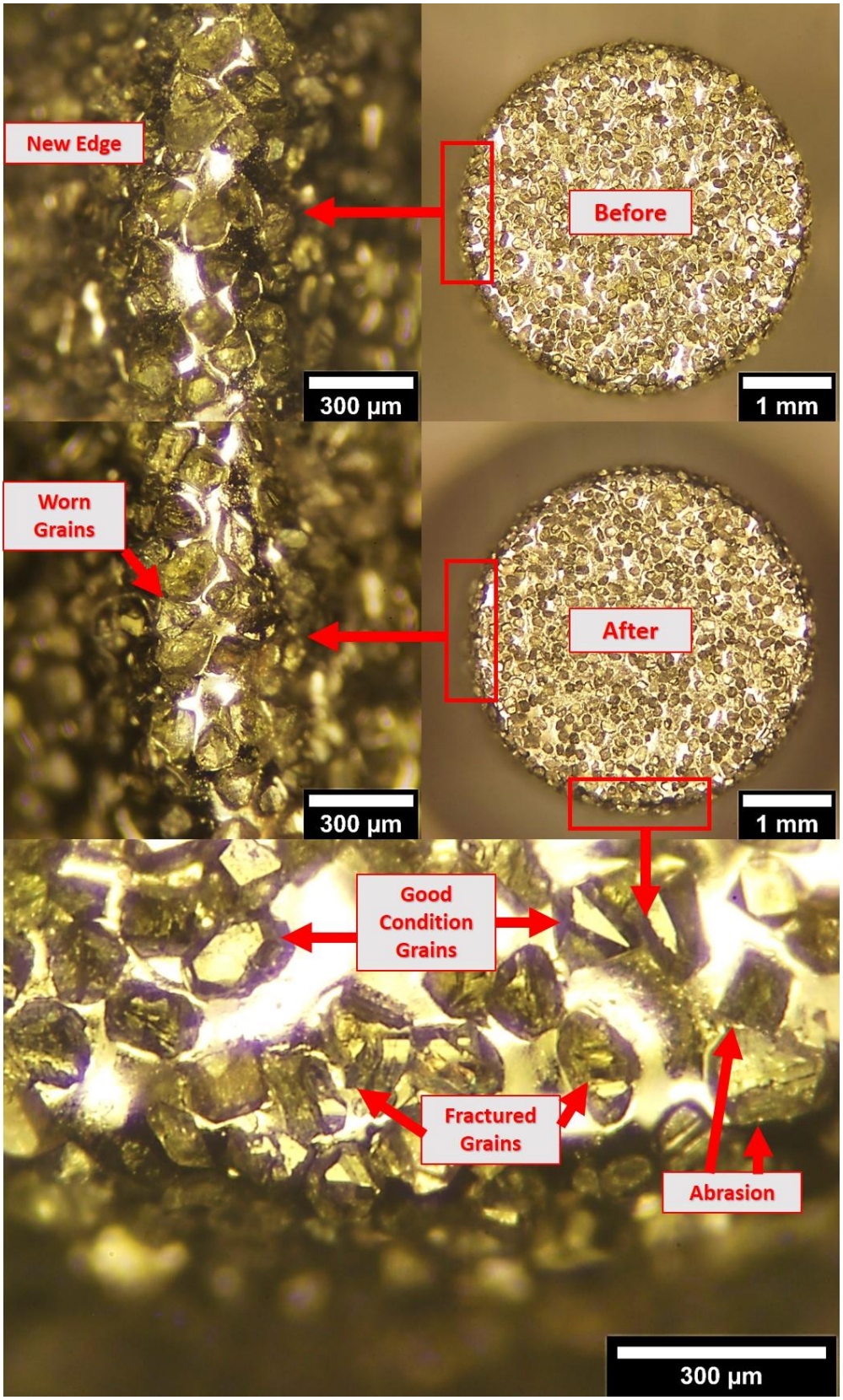


Figure 5.8 Tool wear of the SiC grinding point after grinding 100 mm (**phase 2.B**)

b) Surface Roughness Analysis

The Ra values obtained by the four ground ceramics are shown in **Figure 5.9**. ZrO_2, Al_2O_3, Si_3N_4, and SiC obtained Ra values of 0.33, 0.52, 0.16, and 0.08 µm, respectively. The results were similar to the surface roughness results obtained in **phase 1.A** of end milling, where the non-oxide ceramics obtained lower Ra values than the oxide ceramics.

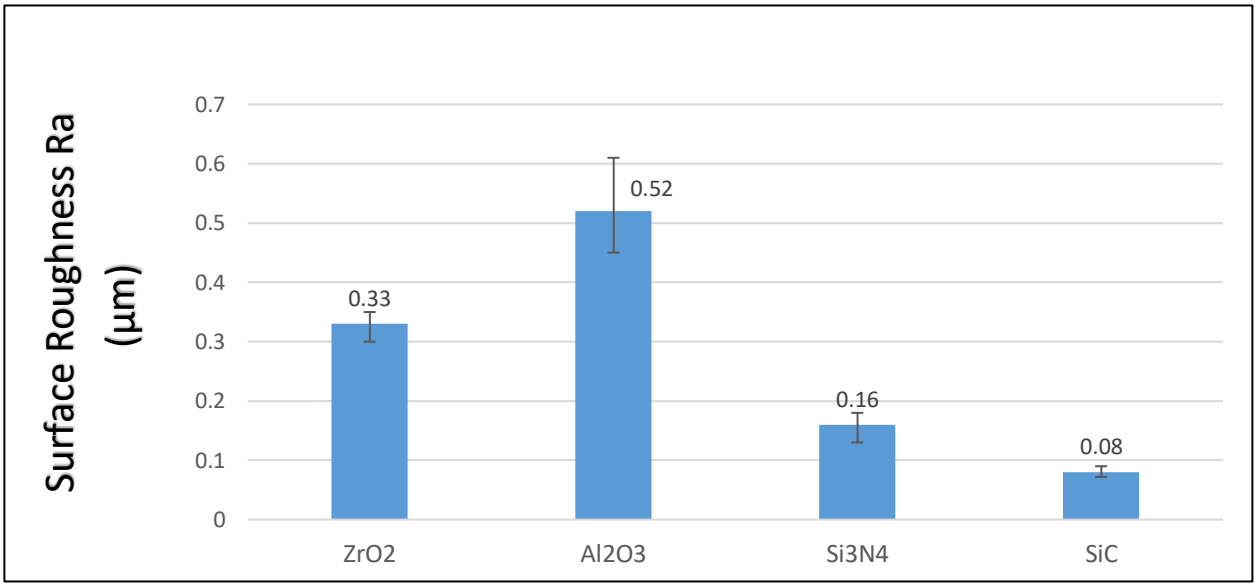


Figure 5.9 Average surface roughness Ra of ZrO_2, Al_2O_3, Si_3N_4, and SiC machined using conventional grinding points (**phase 2.B**)

The microscopic images of the machined surfaces are shown in **Figure 5.10**. In general, all machined surfaces exhibit a material removal mechanism by brittle fractures. However, some surfaces have more ductile spots than others. ZrO_2 (**Figure 5.10 a**) obtained larger ductile regions than the rest of the ceramics. The Al_2O_3 surface (**Figure 5.10 b**) showed more brittle regions than ductile regions, as evidenced by the higher number of dark regions. On the Si_3N_4 (**Figure 5.10 c**) and SiC surfaces (**Figure 5.10 d**), a balanced percentage could be observed between the ductile and brittle regions. Both surfaces had fewer ductile spots than the ZrO_2 surface and more ductile spots than Al_2O_3.

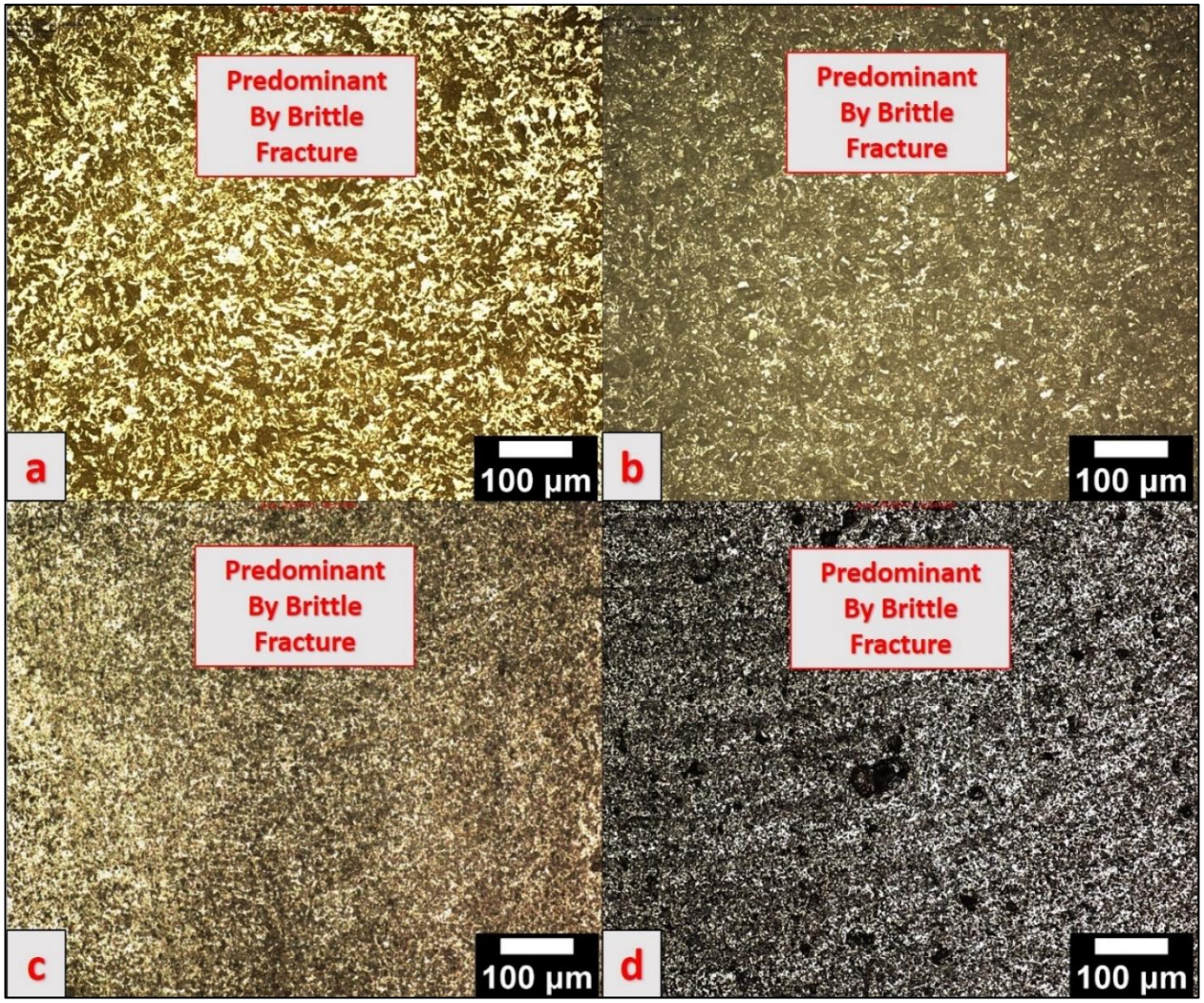


Figure 5.10 Microscopic images of (a) ZrO_2, (b) Al_2O_3, (c) Si_3N_4, and (d) SiC ground using conventional grinding points at V = 1 m/s and f = 0.2µm/rev (**phase 2.B**)

c) Grinding Forces Analysis

The average grinding forces obtained are shown in **Figure 5.11**. The force signals obtained using DynoWare are shown in **Appendix A.2(a)**, where ZrO_2 obtained forces of F_X = 70 N, F_Y = 47 N, and F_Z = 67 N. Al_2O_3 obtained forces of F_X = 34 N, F_Y = 25 N, and F_Z = 47 N. The highest forces were obtained by Si_3N_4, where F_X = 226 N, F_Y = 178 N, and F_Z = 180 N. The lowest cutting forces were obtained by SiC, which had the highest hardness value, where F_X = 19 N, F_Y = 14 N, and F_Z = 21 N. The effects of these low forces were noticeable on the SiC grinding point diamond grains, which exhibited the lowest wear among the four tools (**Figure 5.8**).

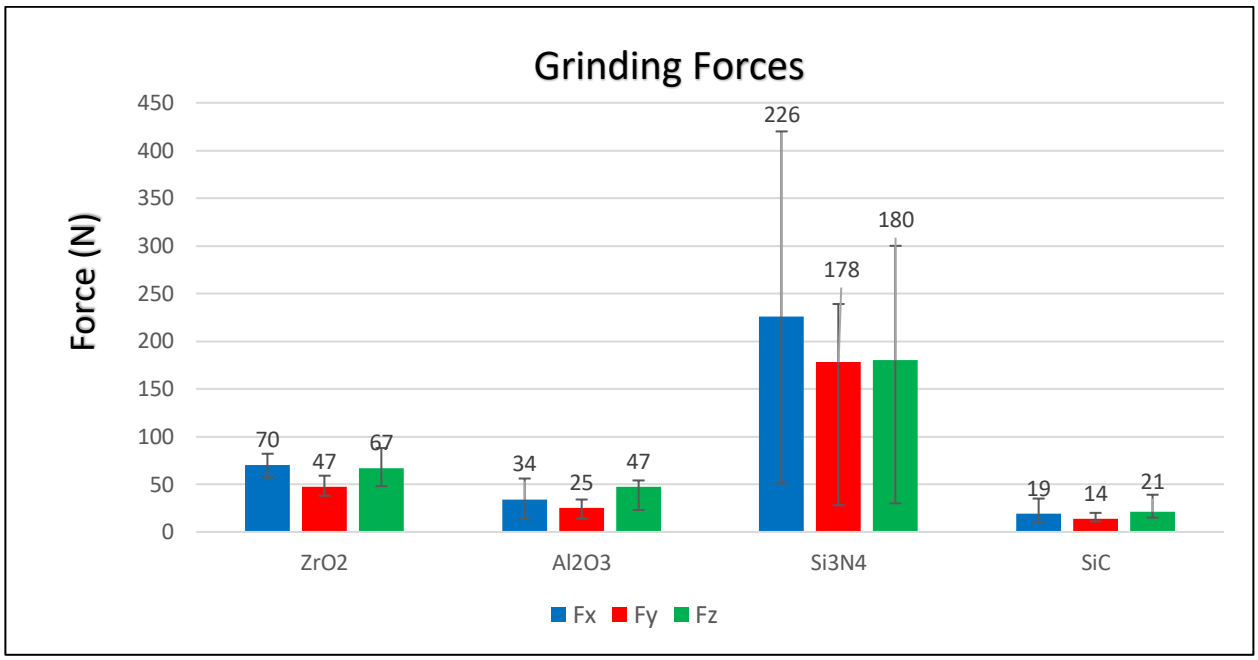


Figure 5.11 Average maximum absolute peak-to-peak grinding forces of conventional point grinding of ZrO_2, Al_2O_3, Si_3N_4, and SiC at V = 5 m/s and V = 1 m/s (**phase 2.B**)

The influence of ceramic hardness on the cutting forces when a grinding point was utilised was reduced. Other properties such as fracture toughness had more influence on the material removal process. Owing to the variations in geometry, height, and rake angle of the diamond grains, point grinding machining had the same influence as UAM. As shown in **Figure 5.12**, some grains had lower heights and negative rake angles. When rubbed on the workpiece, they produce a hammering effect that creates surface cracks. As higher and sharper grains contact the workpiece, the scratching of the material will be performed at lower forces due to the crack's propagation.

The cutting forces obtained in **phase 1** of end milling support this analysis, where in **phase 1.A**, the cutting forces increased as the hardness of the ceramics increased. The high-to-low order were SiC, Si_3N_4, Al_2O_3, and ZrO_2. The conventional machining had no hammering movement during material removal. However, when hammering movement was involved in the machining, as in **phase1.B**, the order of cutting forces of the four ceramics from high to low was almost similar to that obtained in this phase (**phase 2.B**).

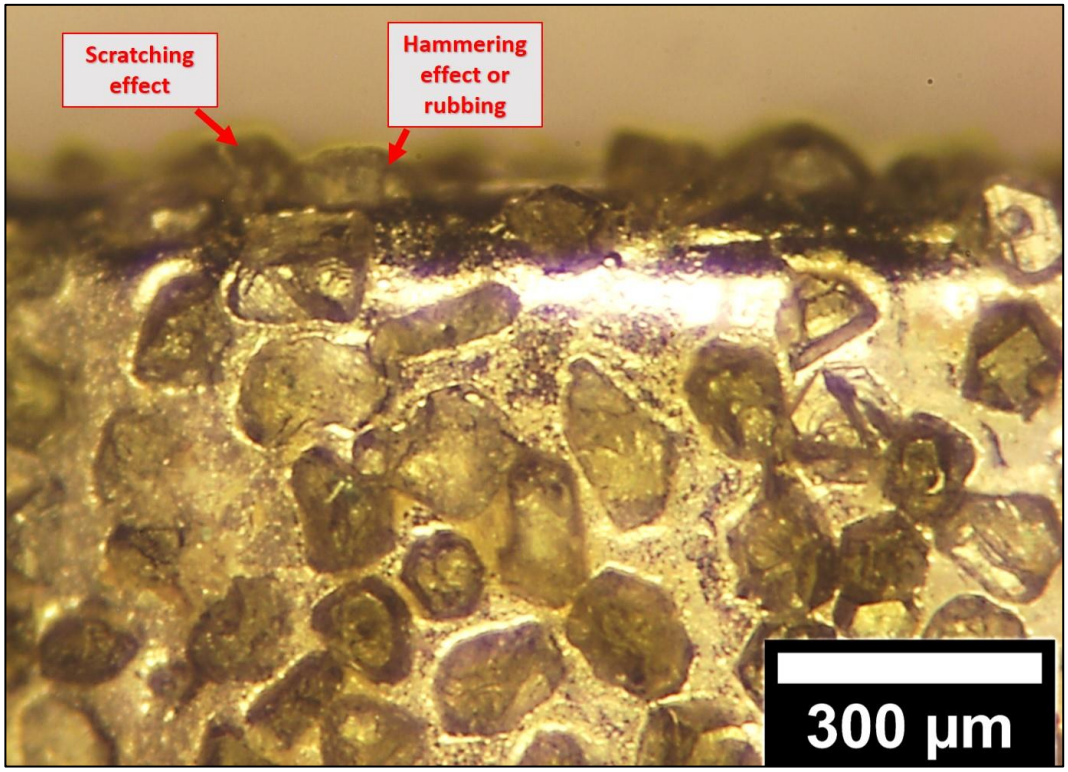


Figure 5.12 Side view of the utilised grinding point showing the effects of the geometry of the grains on material removal (**phase 2.B**)

It believed when hammering movement was involved in the machining of ceramics, fracture toughness became the most influencing properties on the machining forces. As the hammering produces cracks and if the material exhibits low resistance against crack propagation, the material cutting forces will be lower regardless of the ceramic hardness value. This is a noticeable behaviour of SiC. The fracture toughness of Si_3N_4, ZrO_2, Al_2O_3, and SiC were 5–8, 6–9, 2.5–4.5, and 2.5–4 MPam½, respectively. Their shear strengths were 480–960, 414, 330, and 210–380 MPa, respectively.

5.3 Phase 2.C: Investigating the Operating Parameters for Point Grinding ZrO_2 Using UAG

a) Tool Wear Analysis

The images of tool wear at high and low US amplitudes are shown in **Figures 5.13** and **5.14**, respectively. At a high US amplitude of 5–6 µm (**Figure 5.13**), the effect of US vibration was

noticeable, where the hammering movement in the *z*-axis caused a fracture at the bond on one side, and a fragment of the bond was removed. The diamonds grains around the grinding edge were eroded faster owing to the vibration. This led to a direct contact between the workpiece and the bond, abrasion on the diamond grains was observed.

On the other hand, as the US amplitude was reduced to 1–2 µm, the tool had much less fractured grains, more grains in good condition, and no fractured bond, as shown in **Figure 5.14**. However, a bond worn by abrasion around the tool edge was observed, which was due to the eroded grains, which underwent wear until their heights reached the bond surface level. The diamond grains were significantly affected by the hammering movement at both US levels because of the mechanism of the applied forces on the grains, which wore out the diamond grains mainly by mechanical fracture.

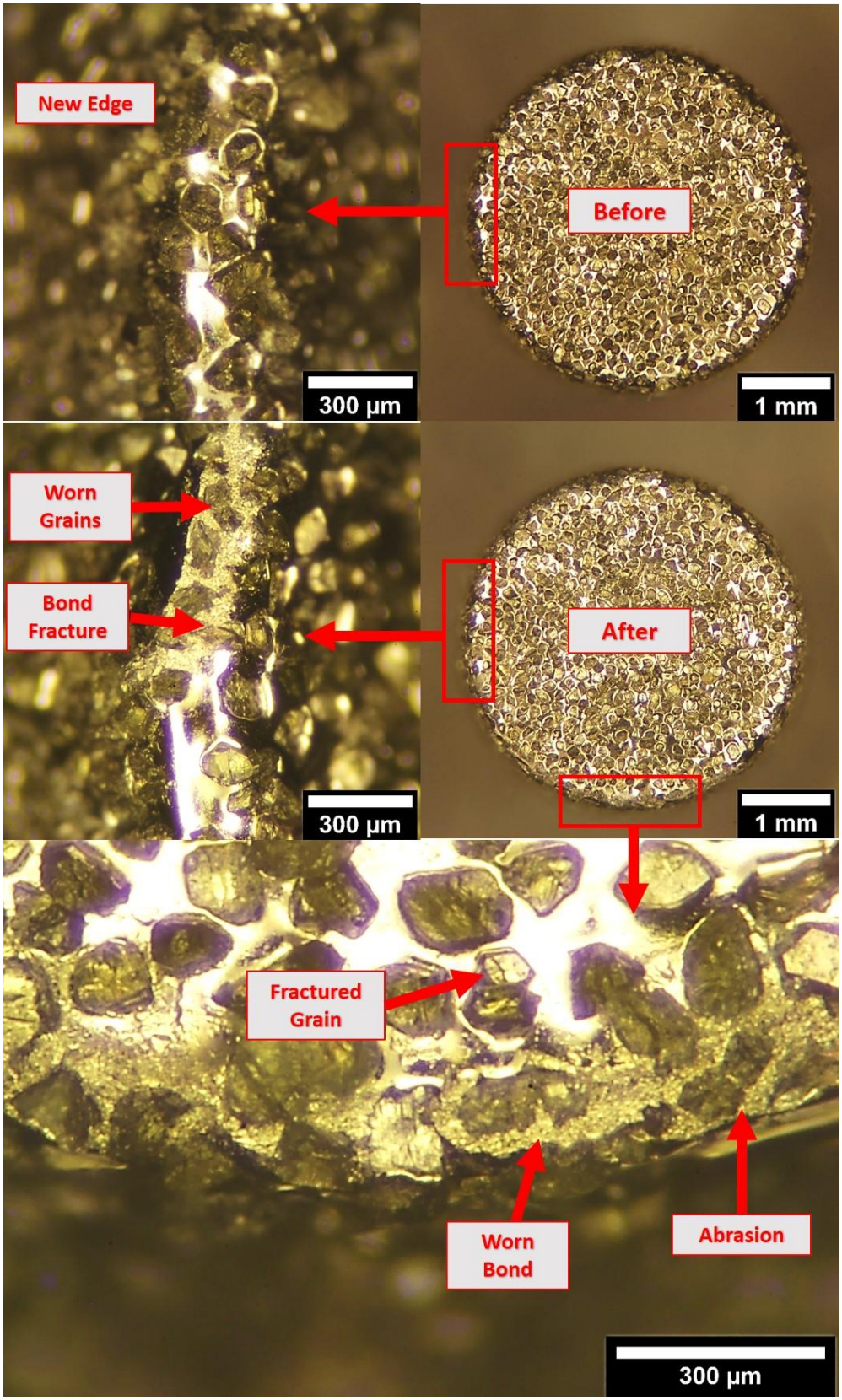


Figure 5.13 Tool wear of the ZrO_2 grinding point after grinding 100 mm at high US amplitudes of 5–6 µm, V = 1 m/s, and f = 0.2µm/rev (**phase 2.C**)

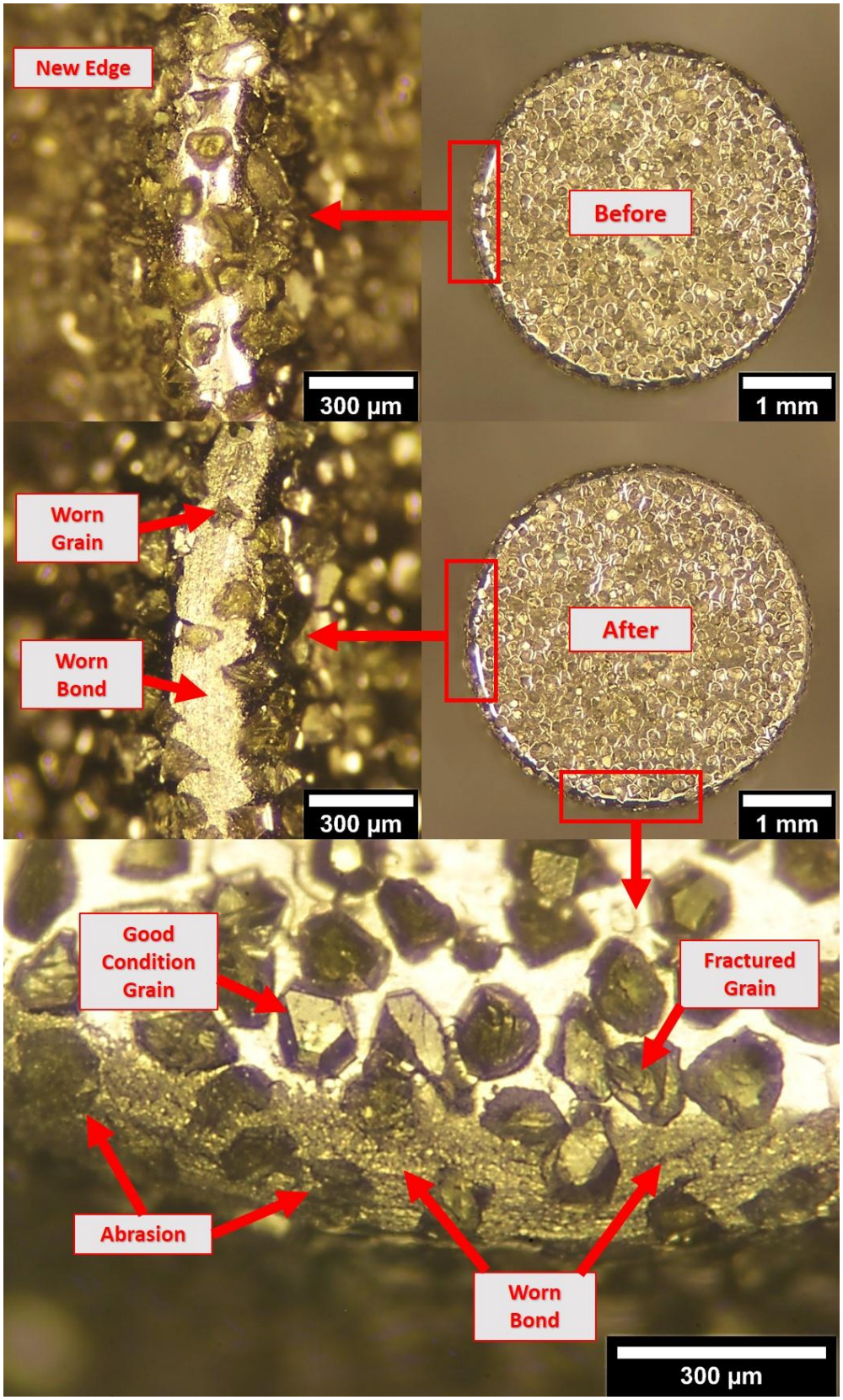


Figure 5.14 Tool wear of the ZrO_2 grinding point after grinding 100 mm at low US amplitudes of 1–2 µm, V = 1 m/s, and f = 0.2µm/rev (**phase 2.C**)

b) Surface Roughness Analysis

The obtained Ra values at the two US amplitude levels are shown in **Figure 5.15**. The surface roughness Ra at the high US amplitude of 5–6 µm obtained an Ra value of 0.43 µm. At the low US amplitude of 1–2 µm, an Ra value of 0.58 µm was obtained, with higher reading variation, which was unexpectedly higher than the high-level Ra.

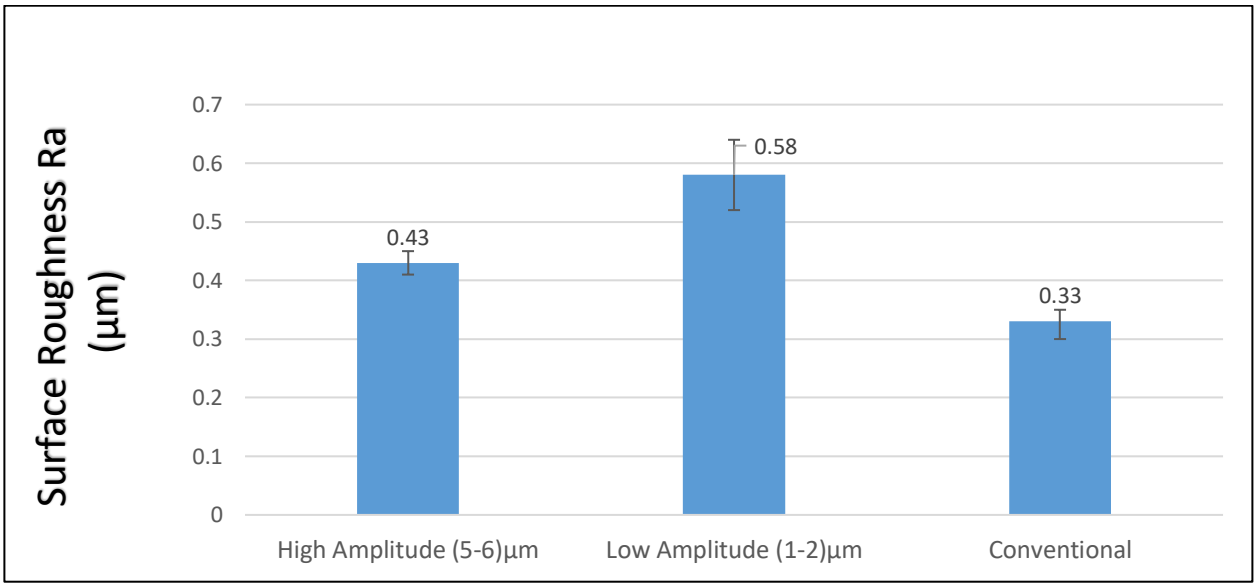


Figure 5.15 Average surface roughness Ra of ZrO_2 obtained using UAG at high, low US amplitudes of 5–6 µm and 1–2 µm, respectively and conventional (**phase 2.C**)

The surface roughness results could be explained by the microscopic images of the machined surfaces shown in **Figure 5.16**, where both surfaces were machined mostly in brittle fractures. However, the low-level surface showed more plastic flow spots that were larger than those obtained for the high-level surface. At lower vibration amplitudes, the potential of ductile material removal is higher because of the higher possibility of material removal by cutting at a critical depth as Zhang et al. [28] mentioned. Plastic flow spots have higher or folded asperities at their edges because of the larger plastic deformation area of the material that will elongate the asperity height and fold it, Ramesh [49], which believed results in higher Ra values.

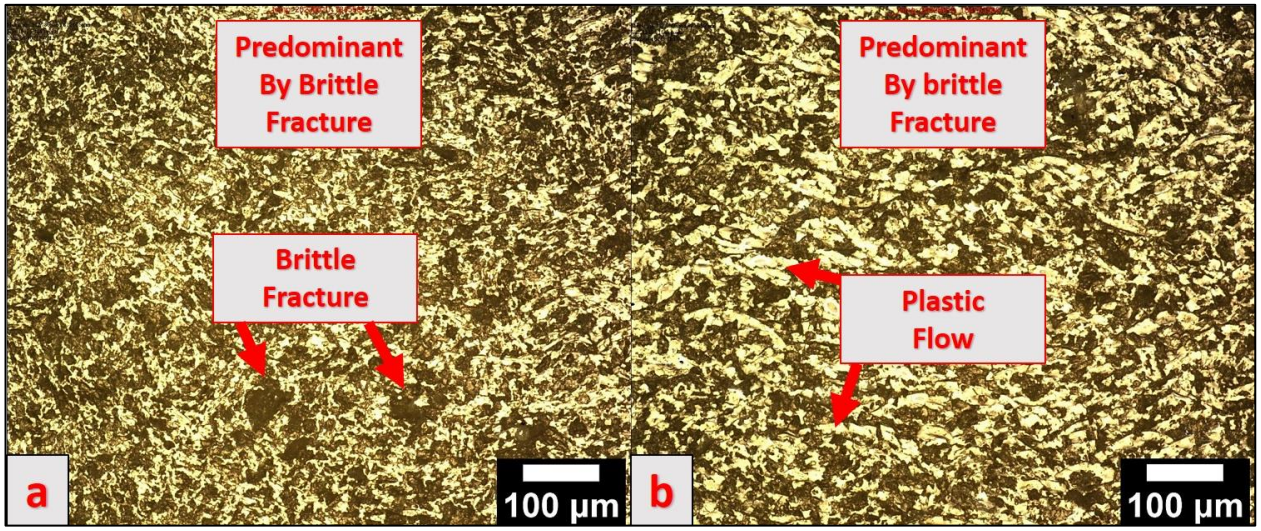


Figure 5.16 Microscopic images of ZrO_2 ground using UAG at (a) high US amplitudes of 5–6 µm and (b) low US amplitude of 1–2 µm (**phase 2.C**)

c) Grinding Forces Analysis

The resulting average grinding forces are shown in **Figure 5.17**. The grinding forces obtained at high-level amplitudes were F_X = 79 N, F_Y = 22 N, and F_Z = 39 N, whereas those obtained at low-level amplitudes were F_X = 65 N, F_Y = 19 N, and F_Z = 33 N. The grinding forces decreased as the US vibration decreased from 5–6 µm to 1–2 µm, which indicates that the optimum US amplitude for machining ceramics using this tool is higher than 2 µm and lower than 5 µm. In **phase 2.B**, the grinding forces in conventional grinding at 0-µm US amplitude obtained forces of F_X = 70 N, F_Y = 47 N, and F_Z = 67 N, which were higher than the low-level grinding forces. Moreover, the effect of high-level forces on tool, has fractured a fragment of the electroplated bond owing to mechanical stresses (**Figure 5.13**), which is unlike the tool wear at low amplitude levels (**Figure 5.14**) that exhibited much lower wear.

Another important finding is that in conventional grinding, the forces were higher than those obtained at low amplitude levels, but the tool wear (**Figure 5.2**) was much less severe, where the electroplated bond was in good condition without scratches. Even the hammering movement in the *z*-axis reduced the grinding forces, the increasing stresses have eroded the diamond grains

faster under US vibration even if the applied grinding forces were lower. This indicates that tool wear is more sensitive towards the type of grinding force applied (whether applied gradually or by hammering) than to the value of absolute magnitude of the forces.

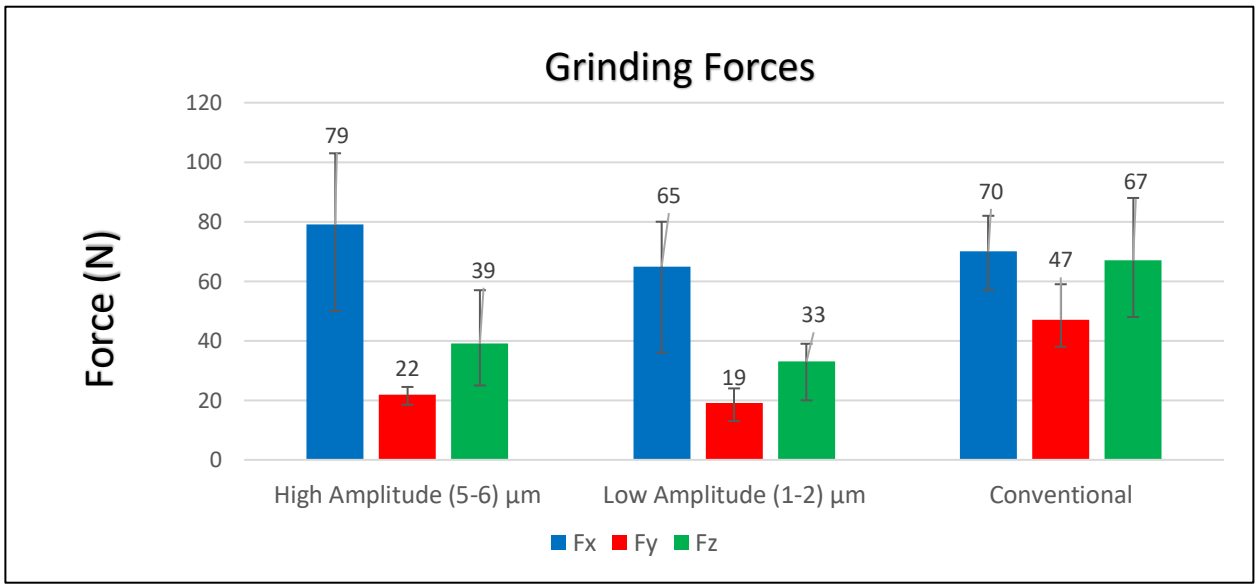


Figure 5.17 Average maximum absolute peak-to-peak grinding forces of UAG for ZrO_2 using a grinding point at high and low US amplitudes of 5–6 µm and 1–2 µm, respectively and Conventional (**phase 2.C**)

5.4 Phase 2.D: Benchmarking Al_2O_3, Si_4N_3, and SiC against ZrO_2 Using the UAG Method and Comparing Conventional Point Grinding with UAG

a) Tool Wear Analysis

The tool wear of the grinding points that ground ZrO_2, Al_2O_3, Si_3N_4, and SiC are shown in **Figures 5.14**, **5.18**, **5.19**, and **5.20**, respectively. All the tools utilised showed worn electroplated bond, fractured grains, and flat grains worn by attrition. However, the most severe tool wear was observed in the Si_3N_4 tool, which showed more worn area at the bond. This was followed by the ZrO_2 and Al_2O_3 tools. The SiC tool showed the least tool wear, having only minimum wear of the bond area, where the worn bond was observed at a limited spot on the tool circumference edge.

By comparing the tool wear obtained by UAG with that obtained using the conventional grinding points in **phase 2.B**, it was clearly found that the UAG wore out the tools faster where no bond wear by the conventional method was observed on any tools. In UAG, the US hammering movement increased the grains wear rate by fractures, eventually causing the tools to grind with the electroplated bond.

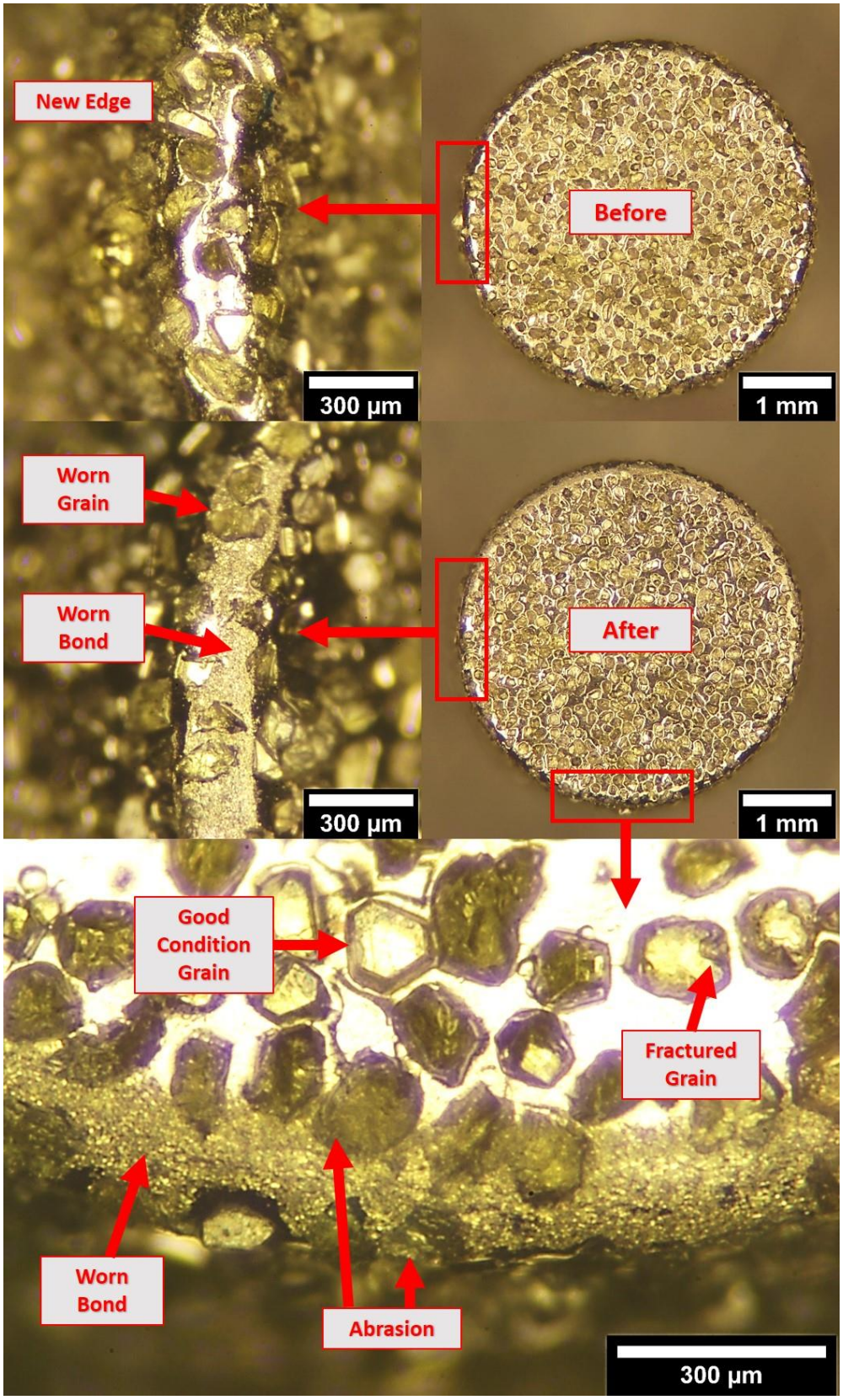


Figure 5.18 Tool wear of the Al_2O_3 grinding point after grinding 100 mm at US amplitudes of 1–2 µm, V = 1 m/s, and f = 0.2µm/rev (**phase 2.D**)

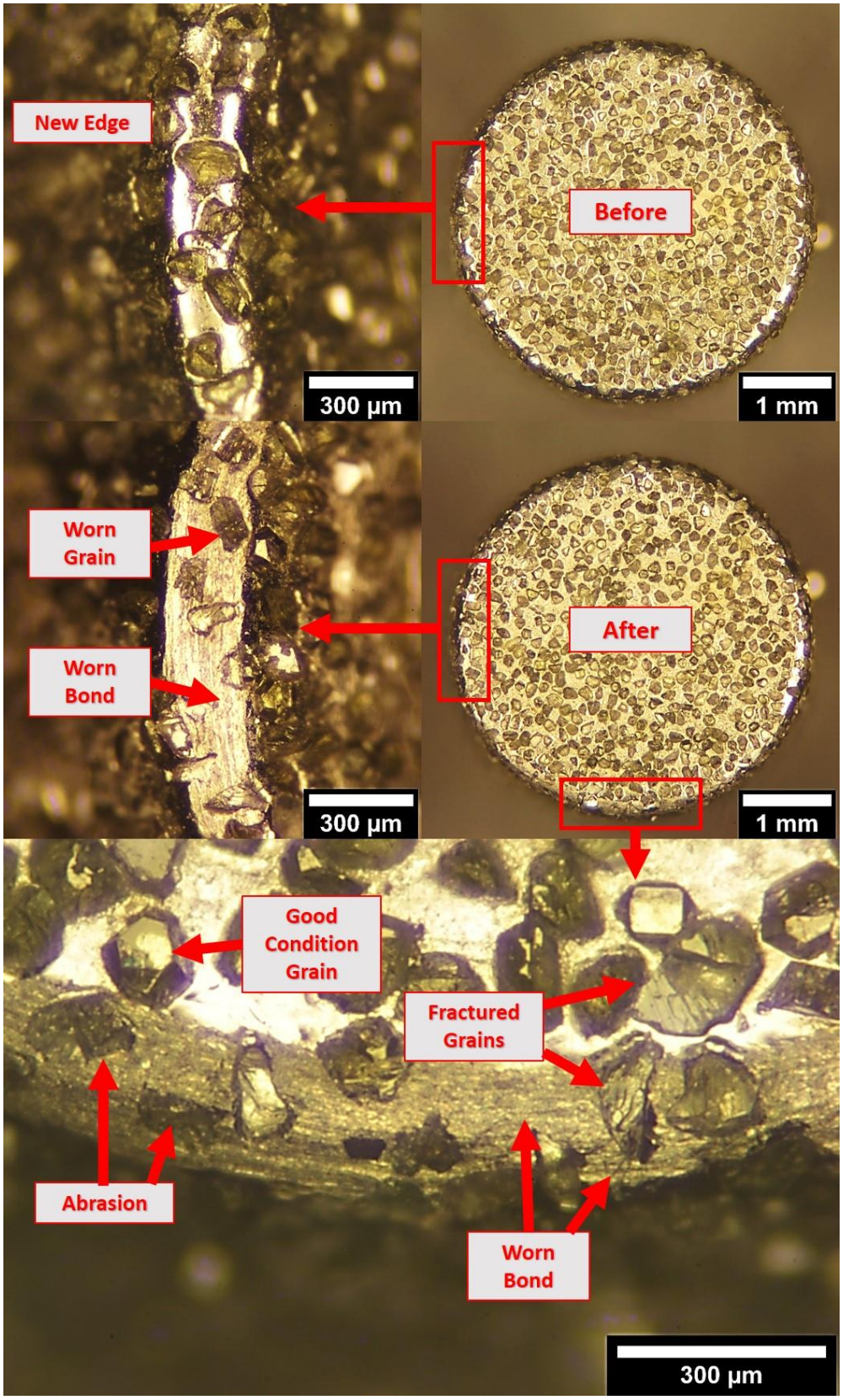


Figure 5.19 Tool wear of Si_3N_4 grinding point after grinding for 100 mm, at US amplitude of (1-2) µm, V= 1 m/s, and *f* = 0.2µm/rev (**phase 2.D**)

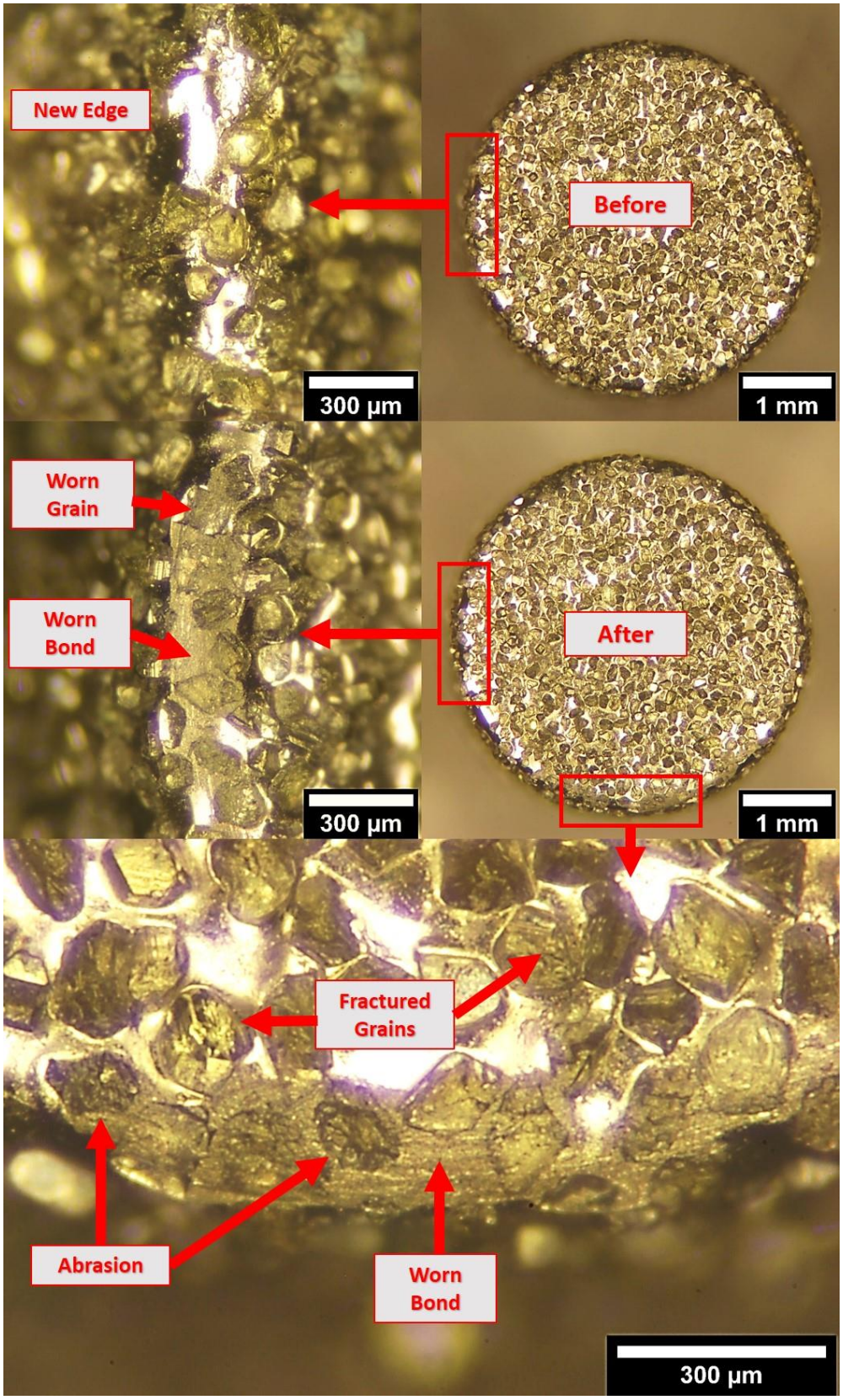


Figure 5.20 Tool wear of the SiC grinding point after grinding 100 mm at US amplitudes of 1–2 µm, V = 1 m/s, and f = 0.2µm/rev (**phase 2.D**)

c) Surface Roughness Analysis

The Ra values of the four ceramics machined using UAG and those obtained earlier from the conventional grinding points in **phase 2.B** are shown in **Figure 5.21**. The surface roughness Ra obtained using UAG had the same order of Ra values obtained using the conventional method, where the highest Ra obtained by Al_2O_3 (0.63 µm), followed by ZrO_2 (0.58 µm), Si_3N_4 (0.17 µm), and SiC (0.07 µm).

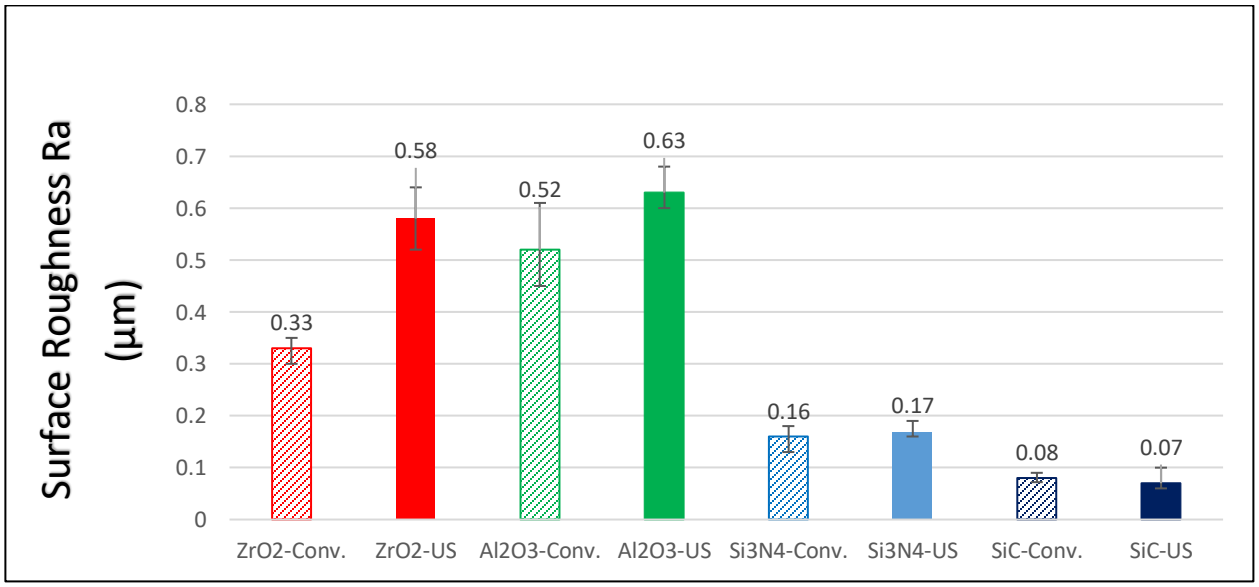


Figure 5.21 Average surface roughness Ra of ZrO_2, Al_2O_3, Si_3N_4, and SiC machined using the conventional grinding points and UAG (**phase 2.D**)

All the machined surfaces of the four ceramics showed a predominant material removal mechanism by brittle fractures, **Figure 5.22**. However, some ceramics had more ductile or plastic flow than other. The ZrO_2 surface (**Figure 5.22 a**) showed several spots with relatively larger areas of plastic flow, besides relatively larger brittle fracture areas, caused by US hammering compared with the conventionally ground surface shown in **Figure 5.10 (a)**.

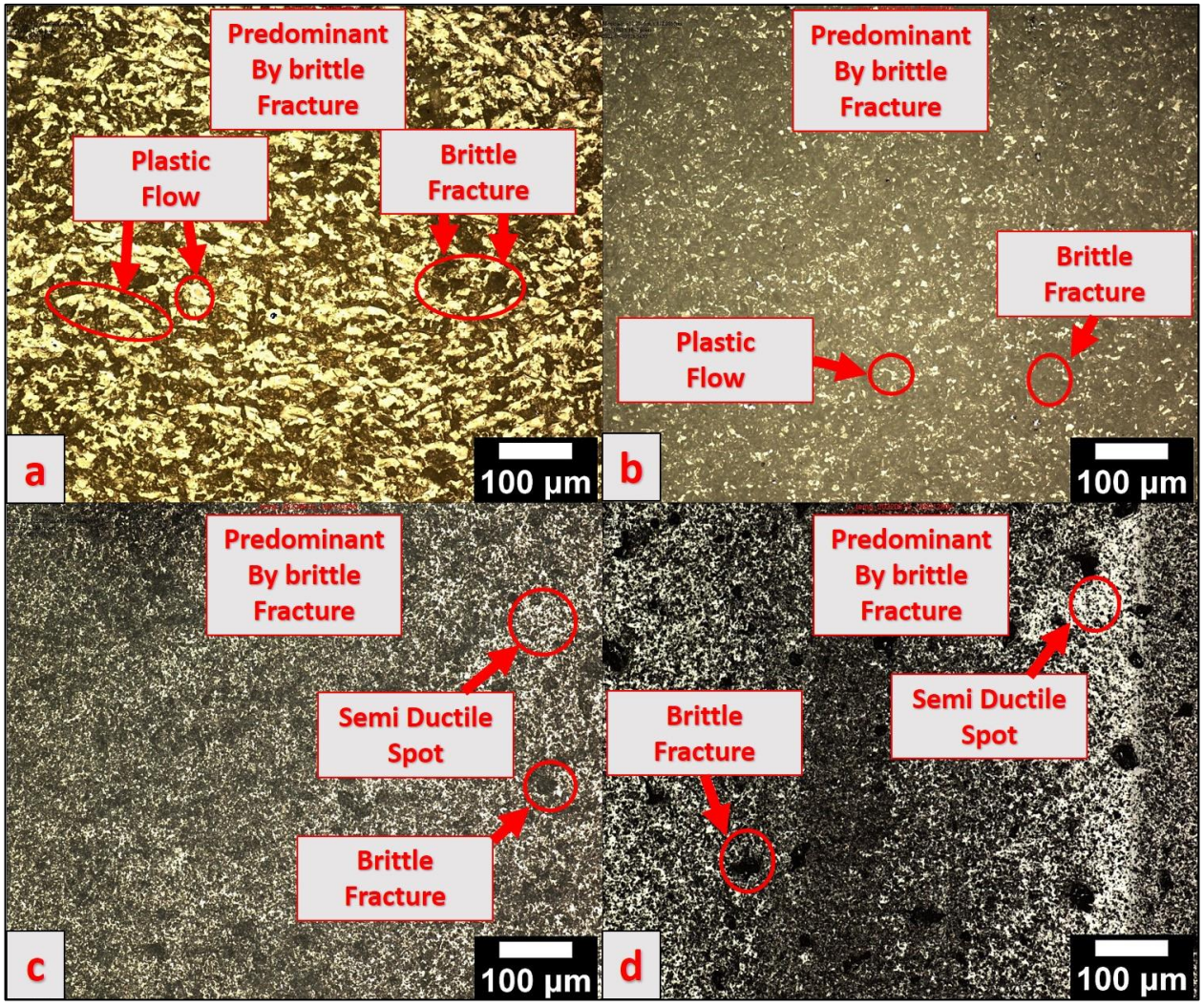


Figure 5.22 Microscopic images of the surfaces machined using UAG at US amplitudes of 1–2 µm: (a) ZrO_2, (b) Al_2O_3, (c) Si_3N_4, and (d) SiC (**phase 2.D**)

On the Al_2O_3 surface (**Figure 5.22 b**), the area occupied by brittle fractures was much larger than that that occupied by brittle fractures obtained using conventional grinding (**Figure 5.10 b**). In addition, the plastic flow areas were smaller and fewer. The Si_3N_4 and SiC surfaces shown in **Figure 5.22 (c)** and **(d)** had similar material removal mechanisms. In general, they are dominated by brittle fractures, but large areas of semi-ductile spots appear as white areas with dark dots. The white area is plastic flow, and the dark spots are brittle fractures. This behaviour of non-oxide ceramics, which had lower ductility than ZrO_2 and higher ductility than Al_2O_3, might be the reason for the stability in their Ra values when they were machined conventionally, as shown in **Figure 5.10 (c)** and **(d),** or by UAG.

d) Grinding Forces Analysis

The average grinding forces obtained using UAG and the conventional grinding points in **phase 2.B** are shown in **Figure 5.23**. The obtained force signals from DynoWare are shown in **Appendix A.2(b)**. The grinding forces of the ceramics machined using UAG showed an order of high to low that was similar to that in conventional grinding, where the highest forces were obtained by Si_3N_4 (F_X = 154 N, F_Y = 147 N, and F_Z = 143 N), followed by ZrO_2 (F_X = 65 N, F_Y = 19 N, and F_Z = 33 N), Al_2O_3 (F_X = 22 N, F_Y = 20 N, and F_Z = 36 N), and SiC (F_X = 16 N, F_Y = 15 N, and F_Z = 19 N).

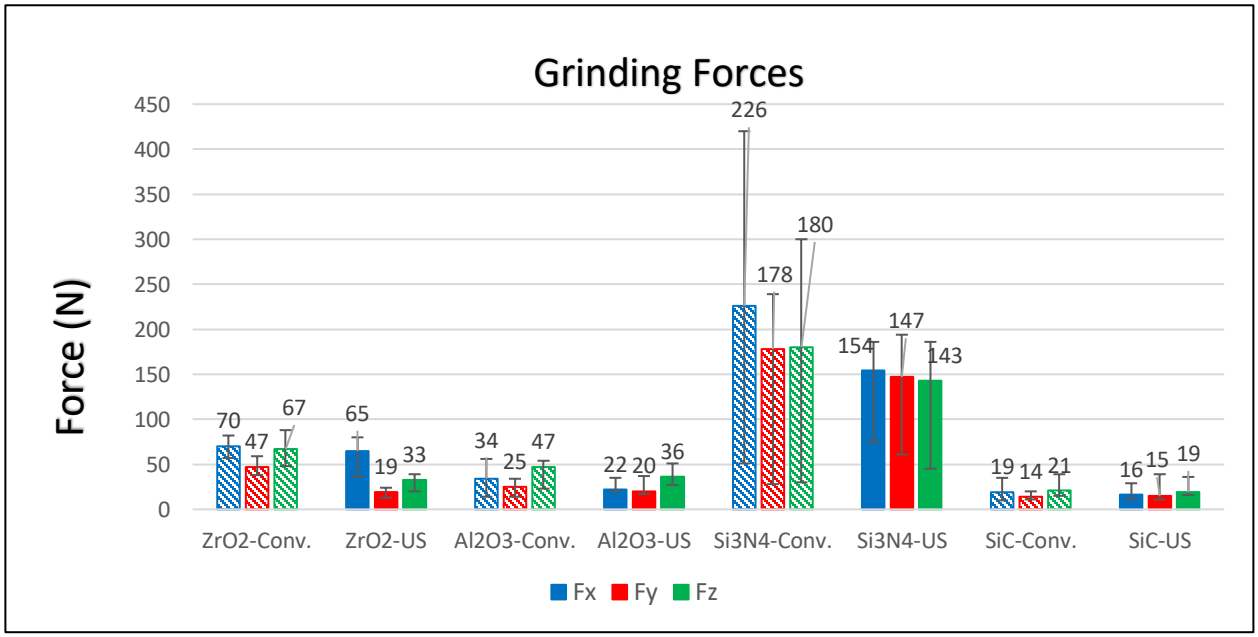


Figure 5.23 Average maximum absolute peak-to-peak grinding forces of ZrO_2, Al_2O_3, Si_3N_4, and SiC obtained using conventional grinding points and UAG (**phase 2.D**)

The reduction in grinding forces caused by UAG was significant compared with that obtained using conventional point grinding similar to Zhang et al. [30]. In ZrO_2, the grinding force F was reduced from 107 N to 75 N, indicating a decrease of almost 30%. In Al_2O_3, the F has reduced from 63 N to 46 N, which is a decrease of approximately 26%. In Si_3N_4, the reduction was from

339 N to 256 N, which is a decrease of approximately 24%. For SiC, the forces were within an almost similar range from 31 to 29 N, without significant reduction.

However, the reduction in the percentage of ZrO_2 forces was higher than that of Al_2O_3 forces because the effect of the hammering vibration in conventional point grinding already overcame the fracture toughness resistance of Al_2O_3, causing a relatively lower improvement in Al_2O_3. For Si_3N_4, the reduction percentage of the forces was limited owing to its other superior mechanical properties, which were the relatively higher shear (480–960 MPa), which might have resisted the improvement, even if its fracture toughness (5–8 MPam½) was at the same range as that of ZrO_2.

Moreover, the reason for the improvement in the reduced force in SiC is its relatively low fracture toughness of 2–4 MPam½, which is the lowest among the four ceramics. Thus, SiC does not require US vibration or hammering to produce or elongate cracks to reduce the material removal forces and hence improve machinability. The grinding point topography of the geometries and heights of several grains, with some of them rubbing (functioning as hammering) and others scratching without US vibration, overcomes the fracture toughness resistance of SiC.

However, unexpectedly, the reduction in grinding forces obtained using UAG did not improve the tool lives of the grinding points. The tool wear images of ZrO_2, Al_2O_3, Si_3N_4, and SiC are shown in **Figures 5.14**, **5.18**, **5.19**, and **5.20**, respectively. At all grinding points, an attrition wear can be observed on the electroplated bond, which indicates that the diamond grains continued to wear out until the start of cutting with the electroplated bond. In the conventional grinding points, none of the tools showed any trace of scratches on the electroplated bond that ground ZrO_2, Al_2O_3, Si_3N_4, and SiC, as shown in **Figures 5.2**, **5.6**, **5.7**, and **5.8**, respectively. Therefore, the utilised diamond grains could withstand higher grinding forces applied gradually as in conventional point grinding, without the grain wear reaching the electroplated bond. Unlike those

in UAG, the forces obtained in conventional point grinding were significantly lower, but the grains were worn faster and resulted in bond wearing. It believed that the US hammering might increase the mechanical fractures of the diamond grains, which led to a shorter tool life. Thus, the type of grinding force, whether applied gradually or suddenly and frequently, not only the magnitude, should be considered in analysing machining forces. Better quality diamond grinding points might have greater resistance against the influence of US vibration.

5.5 Summary of Results

The following **Table 5.1** is summarizing the obtained technical results of **Phase 2**, where it shows the reduction in the cutting forces that took place in all tested ceramics. However, the reduction in grinding forces did not associate with any improvement in the tools lives. The surface roughness Ra of Oxides ceramics has increased when UAG method used. Unlike the non-Oxides that almost had the same Ra values.

Table 5.1 Summary of the technical results of Phase 2

Material	**Conventional Point Grinding**		**UAG**	
	Surface Roughness Ra (µm)	Grinding Force (N)	Surface Roughness Ra (µm)	Grinding Force (N)
ZrO_2	0.33	107	0.58	75
Al_2O_3	0.52	63	0.63	46
Si_3N_4	0.16	339	0.17	256
SiC	0.08	31	0.07	29

6. CONCLUSIONS

This chapter need to be read with reference to the study aim and objectives mentioned in **section 1.3**:

1. **Conduct a literature review to establish the current state of the art for research on the machinability of advanced ceramics**

   On the basis of the literature review, it can be concluded that machining advanced ceramics using techniques such as LBM, EDM, and AWJ still have major limitations, including low MRR, heat-affected zone, and low dimension accuracy. In EDM and LBM, the workpieces must be electrically conductive or conductive materials should be added to the material base before sintering. However, UAM produces no thermal damage on ceramic workpieces with relatively high MRR and dimensional accuracy, making it a suitable machining method. Moreover, only few studies have conducted benchmarking or comparisons of advanced ceramics. Mostly, studies have been conducted using the conventional diamond abrasive grinding wheel. No study has investigated the effect of UAM using CVD diamond-coated end mills or conducted benchmarking using diamond grinding points, either conventionally or by using UAG.

2. **Investigate the operating parameters and conditions for the use of diamond-coated end mills on ZrO_2 with a 4-mm-diameter tool.**

   End milling ZrO_2 at a deeper axial cutting depth and lower cutting width (side milling) increased the tool life more than machining did by slot milling of shallow axial cutting depth and full tool width.

3. **Benchmark Al_2O_3, Si_3N_4, and SiC against ZrO_2 for the use of diamond-coated end mills conventionally. The standard assessment criteria included tool wear, surface roughness, material removal mechanism, and cutting forces.**

The findings show that advanced ceramic machinability varies significantly. ZrO_2 (HV = 1200 kgf/mm^2) exhibited superior machinability by obtaining tool life of 1500 mm. Al_2O_3 (HV = 1500–1650 kgf/mm^2), Si_3N_4 (HV = 1700–2200 kgf/mm^2), and SiC (HV = 2400–2800 kgf/mm^2) obtained tool lives of 100, 40, and 10 mm, respectively. This indicates that the tool life decreased as the hardness increased. In terms of surface roughness, the **non-oxides**, Si_3N_4 and SiC, obtained lower Ra values than the **oxides**, ZrO_2 and Al_2O_3. However, ZrO_2 was the only ceramic that had a material removal mechanism dominated by ductile fractures. The cutting forces increased as the hardness increased linearly, proportionally to tool life. The highest tool life of ZrO_2 obtained the lowest cutting force of F = 51 N, and the lowest tool life of SiC obtained the highest force of F_Z = 118 N. This indicates that ceramic hardness had a significant effect on the cutting forces.

4. **Establish the improvements that can be achieved using UAM, a non-conventional method.**

The non-conventional machining of UAM improved the machinability of Al_2O_3, Si_3N_4, and SiC, but not ZrO_2, which showed a drawback. This indicates that the hardness value of the ceramics was no longer the main factor that affected their machinability when UAM was applied. Owing to the material removal mechanism of US hammering that created and elongated the surface/sub-surface cracks, material removal became easier. The cutting forces were not proportional to the hardness value and tool life. The fracture toughness values of the ceramics were the main influencing factor on the reduction of the cutting forces. The percentage of reduction in the cutting

forces was proportional to the fracture toughness value, where the reduction of *F* was higher in SiC and Al_2O_3 than in ZrO_2 and Si_3N_4. The highest reduction obtained was by SiC (fracture toughness = 2–4 MPam½), from 118 N to 20 N. This was followed by Al_2O_3 (fracture toughness = 2.5–4 MPam½, decreasing from 61 N to 23 N), ZrO_2 (fracture toughness = 6–9 MPam½, decreasing from 51 N to 23 N), and Si_3N_4 (fracture toughness = 5–8 MPam½, from 96 to 57 N).

Moreover, it believed the low thermal conductivity of ZrO_2 caused its drawback when machined using US vibration. The very low thermal conductivity of ZrO_2 (1.5–2.5 W m^{-1} K^{-1}) maintained the generated heat in the contact zone to be concentrated and not to be transferred to the surrounded area rapidly, which resulted in weakened the bonding forces of diamond coating, due to poor dissipating of the generated heat by UAM vibration.

5. **Establish the effect of using electroplated diamond grinding points with a small diameter (4 mm) on ZrO_2 at a relatively high cutting speed.**

   Machining ZrO_2 using diamond grinding points at a relatively high cutting speed (5 m/s) close to that used in hard metal machining resulted in higher cutting forces, higher surface roughness, and shorter tool life than those obtained at a lower cutting speed (1 m/s).

6. **Benchmark Al_2O_3, Si_3N_4, and SiC against ZrO_2 for the use of diamond grinding points conventionally. The standard assessment criteria include tool wear, surface roughness, material removal mechanism, and cutting forces.**

   Among the grinding forces obtained from the grinding points, the lowest were obtained by the hardest ceramic, SiC. Al_2O_3 and SiC obtained forces lower or equal to

those of ZrO_2. This indicates that grinding ceramics using diamond grinding points could significantly reduce the influence of hardness on the grinding forces.

It believed that the force reduction was might due to the act of rubbing of some grains on the machined surface, causing hammering movements that created or elongate cracks. Some higher and sharper grains scratched the cracked and weekend surface. As a result, the grinding forces were reduced. It believed the results of **phase 1** could support this observation, because when ceramics machined using US vibration, including hammering movements, the cutting forces are reduced significantly.

7. Establish the improvements that can be achieved using UAG, a non-conventional method.

When the non-conventional method of UAG was applied, the grinding forces were reduced. In ZrO_2, Al_2O_3, and Si_3N_4, the *F* forces were reduced by almost 30%, 26%, and 24%, respectively. However, in SiC, the forces were almost similar owing to the grinding point topography, which believed has overcame lower SiC fracture toughness resistance already. The results indicate that the US vibration boosted the hammering effect that existed owing to the tool topography producing grains with negative rake angles at variable heights. However, this boosting of the hammering caused by UAG reduced the lives of the tools used. All the grinding points utilised exhibited abrasion wear on their electroplated bonds, indicating that the diamond grains were worn out faster because of the increase in mechanical fracture. The lowest tool wear was obtained using the point that machined SiC, and the highest wear was obtained by the point that machined Si_3N_4. Which indicates that the grinding forces were proportional to the tool wear.

7. SUGGESTIONS FOR FUTURE WORK

- More benchmarking investigations on advanced ceramics, conventionally and non-conventionally, could be conducted using PCD end mills that has higher quality, so higher MRR could be obtained. Also, different coating types such as PVD diamond coating that used in precise machining or cheaper coating such as nickel boron could be investigated. Using thermocouple to investigate the heat in cutting zone. Designing tool which might with thicker coating, more than 15 µm, to withstand the thermal softening and mechanical fractures caused by UAM, especially Liu et al. [45] work had similar suggestion of investigating tools with thicker (15µm) CVD coating. Moreover, a different cutter grind geometry, such as ball-nose, could be investigated at different diameters.
- More point grinding benchmarking investigations might be conducted with better diamond grain quality than that in this study to optimise the grit size and bonding type for each ceramic.
- The usefulness of different types of cutting fluid, such as nano-particles or vegetable oil using a different technique of MQL at different concentrations and pressures, must be explored.
- The machining parameters, tooling, machining method (conventional or US assisted), and economic machining feasibility for a specific product such as hip-joint replacement made of Al_2O_3, tooth crowns made of ZrO_2, or turbocharger rotors made of Si_3N_4 might be optimised. Further investigation on surface integrity and further study on the effects of the grain sizes of ceramics on the material cutting mode must be conducted. This will concentrate the efforts effectively and efficiently to improve advanced ceramics machining.

8.REFERENCE S

1. Fine Ceramics Production Process | Introduction to Fine Ceramics | Fine Ceramics World | Kyocera. [Online] Available at: https://global.kyocera.com/fcworld/first/process.html [Accessed 12 Feb. 2019].
2. Inoue, M., Kihara, Y., & Arakida, Y., 1989. Injection moulding machine for high-performance ceramics. Interceram, 38(2), 53-57.
3. Davim, J. P., 2010. Surface integrity in machining (Vol. 1848828742). London: Springer.
4. Inasaki, I., 1987. Grinding of hard and brittle materials. CIRP annals, 36(2), 463-471.
5. Jahanmir, S., 1998. Mechanisms of material removal in abrasive machining of ceramics. Machining of ceramics and composites, 11-84.
6. Marinescu, I., Rowe, B., Ling, Y., & Wobker, H. G., 1999. Abrasive processes. In Handbook of Ceramic Grinding & Polishing (pp. 94-189). William Andrew Publishing.
7. Gorin, A., & Reddy, M. M., 2014. Advanced Ceramics: Some Challenges and Solutions in Machining by Conventional Methods. In Applied Mechanics and Materials (Vol. 624, pp. 42-47). Trans Tech Publications Ltd.
8. Heimann, R., 2010. Classic and advanced ceramics: from fundamentals to applications. John Wiley & Sons.
9. Somiya, S. ed., 2012. Advanced technical ceramics. Elsevier.
10. Early, J.G. and Rook, H.L., 1996. Versailles project on advanced materials and standards (VAMAS). Advanced Materials, 8(1), pp.9-12.
11. Uhlmann, D.R., Bowen, H.K. and Kingery, W.D., 1976. Introduction to Ceramics.
12. Pittayachawan, P., 2009. *Comparative study of physical properties of zirconia based dental ceramics* (Doctoral dissertation, UCL (University College London)).
13. Täffner, U., Carle, V., Schäfer, U. and Hoffmann, M.J., 2004. Preparation and microstructural analysis of high-performance ceramics. In *Metallography and Microstructures* (pp. 1057-1066). ASM International.
14. Riley, F.L., 2000. Silicon nitride and related materials. *Journal of the American Ceramic Society*, *83*(2), pp.245-265.
15. Collins, J.F. and Gerby, R.W., 1955. New refractory uses for silicon nitride reported. *JOM*, *7*(5), pp.612-615.
16. International Syalons. 2022. Silicon Nitride Ceramics - International Syalons. [online] Available at: <https://www.syalons.com/resources/articles-and-guides/silicon-nitride-ceramics/> [Accessed 10 January 2022].
17. Roccaforte, F., Giannazzo, F. and Raineri, V., 2010. Nanoscale transport properties at silicon carbide interfaces. Journal of Physics D: Applied Physics, 43(22), p.223001.
18. Basu, B. and Balani, K., 2011. Advanced structural ceramics. John Wiley & Sons.
19. Doi, T., Uhlmann, E. and Marinescu, I.D. eds., 2015. *Handbook of ceramics grinding and polishing*. William Andrew.
20. Neimeier, B., 1991. Zirconia materials used in manufacturing applications. SME Tech. Paper Society of Manufacturing Engineers, pp.1-10.
21. Guo, C. and Chand, R.H., 1998. Ceramic machining primer. Ceramic industry, 148(4), p.71.
22. Ramanath, S., Kopp, R.N. and Dudley, J.A., 2000. Progress in Precision Grinding of Technical/advanced/fine Electronic Ceramics. Society of Manufacturing Engineers.

23. Dhara, S. and Su, B., 2005. Green machining to net shape alumina ceramics prepared using different processing routes. International Journal of Applied Ceramic Technology, 2(3), pp.262-270.
24. Besshi, T., Sato, T. and Tsutsui, I., 1999. Machining of alumina green bodies and their dewaxing. Journal of Materials Processing Technology, 95(1-3), pp.133-138.
25. Singh, R.P. and Singhal, S., 2016. Rotary ultrasonic machining: a review. Materials and Manufacturing Processes, 31(14), pp.1795-1824.
26. Jahanmir, S., Ramulu, M. and Koshy, P. eds., 1999. Machining of ceramics and composites. Marcel Dekker.
27. Chattopadhyay, A.B. 2017. *Machining And Machine Tools*. Wiley India.
28. Pei, Z.J. and Ferreira, P.M., 1999. An experimental investigation of rotary ultrasonic face milling. International Journal of Machine Tools and Manufacture, 39(8), pp.1327-1344.
29. Pei, Z. J., Ferreira, P. M., Kapoor, S. G., & Haselkorn, M. B. A. C. (1995). Rotary ultrasonic machining for face milling of ceramics. International Journal of Machine Tools and Manufacture, 35(7), 1033-1046
30. Zhang, C., Feng, P., Zhang, J., Wu, Z. and Yu, D., 2012. Investigation into the rotary ultrasonic face milling of K9 glass with mechanism study of material removal. International journal of manufacturing technology and management, 25(4), pp.248-266.
31. Olortegui-Yume, J.A. and Kwon, P.Y., 2007. Tool wear mechanisms in machining. International journal of machining and machinability of materials, 2(3-4), pp.316-334.
32. Stephenson, D.A. and Agapiou, J.S., 2016. Metal cutting theory and practice. CRC press.
33. Rabinowicz, E., 1995. Friction and Wear of Materials, Jhon Wiley & Sons. Inc., New York.
34. Rabinowicz, E., 1977. Abrasive wear resistance as a materials test.
35. Childs, T.H., Maekawa, K., Obikawa, T. and Yamane, Y., 2000. Metal machining: theory and applications. Butterworth-Heinemann.
36. Arriandiaga, A., Portillo, E., Sánchez, J.A., Cabanes, I. and Zubizarreta, A., 2017. Recurrent ANN-based modelling of the dynamic evolution of the surface roughness in grinding. Neural Computing and Applications, 28(6), pp.1293-1307.
37. Shimada, S., Ikawa, N., Inamura, T., Takezawa, N., Ohmori, H. and Sata, T., 1995. Brittle-ductile transition phenomena in microindentation and micromachining. CIRP annals, 44(1), pp.523-526.
38. Bifano, T.G., Dow, T.A. and Scattergood, R.O., 1991. Ductile-regime grinding: a new technology for machining brittle materials.
39. Beltrão, P.A., Gee, A.E., Corbett, J. and Whatmore, R.W., 1999. Ductile mode machining of commercial PZT ceramics. CIRP Annals, 48(1), pp.437-440.
40. Zhong, Z.W., 2003. Ductile or partial ductile mode machining of brittle materials. *The International Journal of Advanced Manufacturing Technology*, *21*(8), pp.579-585.
41. Yanyan, Y., Bo, Z. and Junli, L., 2009. Ultraprecision surface finishing of nano-ZrO 2 ceramics using two-dimensional ultrasonic assisted grinding. The International Journal of Advanced Manufacturing Technology, 43(5-6), p.462.
42. Matsumura, T. and Ono, T., 2008. Cutting process of glass with inclined ball end mill. Journal of Materials Processing Technology, 200(1-3), pp.356-363.
43. Cheng, X., Nakamoto, K., Sugai, M., Matsumoto, S., Wang, Z.G. and Yamazaki, K., 2008. Development of ultra-precision machining system with unique wire EDM tool fabrication system for micro/nano-machining. CIRP annals, 57(1), pp.415-420.

44. Wu, X., Li, L., He, N., Zhao, G., Jiang, F. and Shen, J., 2018. Study on the tool wear and its effect of PCD tool in micro milling of tungsten carbide. International Journal of Refractory Metals and Hard Materials, 77, pp.61-67.
45. Bian, R., He, N., Ding, W. and Liu, S., 2017. A study on the tool wear of PCD micro end mills in ductile milling of ZrO ceramics. International Journal of Advanced Manufacturing Technology, 92.
46. Bian, R., Ferraris, E., Ynag, Y. and Qian, J., 2018. Experimental investigation on ductile mode micro-milling of ZrO2 ceramics with diamond-coated end mills. Micromachines, 9(3), p.127.
47. Liu, J. and Camfield, R., 2015. Machinability experimental study of sintered alumina (Al2O3) ceramics material by chemical vapor deposition diamond coating milling tools. Proceedings of the Institution of Mechanical Engineers, Part B: Journal of Engineering Manufacture, 229(9), pp.1535-1546.
48. Inasaki, I. and Nakayama, K., 1986. High-efficiency grinding of advanced ceramics. CIRP Annals, 35(1), pp.211-214.
49. Yin, L. and Huang, H., 2004. Ceramic response to high-speed grinding. Machining Science and Technology, 8(1), pp.21-37.
50. Chen, J., Shen, J., Huang, H. and Xu, X., 2010. Grinding characteristics in high-speed grinding of engineering ceramics with brazed diamond wheels. Journal of Materials Processing Technology, 210(6-7), pp.899-906.
51. Ramesh, K., Yeo, S.H., Gowri, S. and Zhou, L., 2001. Experimental evaluation of super high-speed grinding of advanced ceramics. The International Journal of Advanced Manufacturing Technology, 17(2), pp.87-92.
52. Yin, L., Huang, H., Ramesh, K. and Huang, T., 2005. High speed versus conventional grinding in high removal rate machining of alumina and alumina–titania. International Journal of Machine Tools and Manufacture, 45(7-8), pp.897-907.
53. Huang, H. and Liu, Y.C., 2003. Experimental investigations of machining characteristics and removal mechanisms of advanced ceramics in high-speed deep grinding. International Journal of Machine Tools and Manufacture, 43(8), pp.811-823.
54. Agarwal, S. and Rao, P.V., 2008. Experimental investigation of surface/subsurface damage formation and material removal mechanisms in SiC grinding. International Journal of Machine Tools and Manufacture, 48(6), pp.698-710.
55. Huang, H., Yin, L., and Zhou, L.,2003. High speed grinding of silicon nitride with resin bond diamond wheels. Journal of Materials Processing Technology, 141(3), 329-336.
56. Li, K.M., Hu, Y.M., Yang, Z.Y. and Chen, M.Y., 2012. Experimental study on vibration-assisted grinding. Journal of manufacturing science and engineering, 134(4).
57. Zheng, S.Y., Feng, P.F. and Xu, X.P., 2009. Development trends of rotary ultrasonic machining technology. Journal of Tsinghua University (Science and Technology), 49(11), pp.1799-1804.
58. Zheng, W., Zhou, M. and Zhou, L., 2017. Influence of process parameters on surface topography in ultrasonic vibration-assisted end grinding of SiCp/Al composites. *The International Journal of Advanced Manufacturing Technology*, *91*(5), pp.2347-2358.
59. Chen, Z., Wu, Y., Yang, Y., Li, J., Xie, B., Li, X., Lei, S., Ou-Yang, J., Yang, X., Zhou, Q. and Zhu, B., 2018. Multilayered carbon nanotube yarn based optoacoustic transducer with high energy conversion efficiency for ultrasound application. *Nano Energy*, *46*, pp.314-321.

60. Ni, C., Zhu, L., Liu, C. and Yang, Z., 2018. Analytical modeling of tool-workpiece contact rate and experimental study in ultrasonic vibration-assisted milling of Ti–6Al–4V. *International Journal of Mechanical Sciences*, *142*, pp.97-111.
61. Sun, C., Niu, Y., Liu, Z., Wang, Y. and Xiu, S., 2017. Study on the surface topography considering grinding chatter based on dynamics and reliability. *The International Journal of Advanced Manufacturing Technology*, *92*(9), pp.3273-3286.
62. Abdo, B., Darwish, S.M., Al-Ahmari, A.M. and El-Tamimi, A.M., 2013. Optimization of process parameters of rotary ultrasonic machining based on Taguchis method. In Advanced Materials Research (Vol. 748, pp. 273-280). Trans Tech Publications Ltd.
63. Abdo, B.M., El-Tamimi, A. and Alkhalefah, H., 2020. Parametric Analysis and Optimization of Rotary Ultrasonic Machining of Zirconia (ZrO2) Ceramics. In IOP Conference Series: Materials Science and Engineering (Vol. 727, No. 1, p. 012009). IOP Publishing.
64. Abdo, B., El-Tamimi, A. and Nasr, E.A., 2020. Rotary ultrasonic machining of alumina ceramic: An experimental investigation of tool path and tool overlapping. Applied Sciences, 10(5), p.1667.
65. Gong, H., Fang, F.Z. and Hu, X.T., 2010. Kinematic view of tool life in rotary ultrasonic side milling of hard and brittle materials. International Journal of Machine Tools and Manufacture, 50(3), pp.303-307.
66. Inamura, T., Shimada, S., Takezawa, N. and Ikawa, N., 1999. Crack initiation in machining monocrystalline silicon. CIRP Annals, 48(1), pp.81-84.
67. Jasinevicius, R.G., Porto, A.J.V., Duduch, J.G., Pizani, P.S., Lanciotti Jr, F. and Dos Santos, F.J., 2005. Multiple phase silicon in submicrometer chips removed by diamond turning. Journal of the Brazilian Society of Mechanical Sciences and Engineering, 27(4), pp.440-448.
68. Geng, D., Lu, Z., Yao, G., Liu, J., Li, Z., & Zhang, D. 2017. Cutting temperature and resulting influence on machining performance in rotary ultrasonic elliptical machining of thick CFRP. International Journal of Machine Tools and Manufacture, 123, 160-170.

APPENDICES

APPENDIX A: Additional Experimental Results

A.1 Phase 1, End Milling

a) Phase 1.B: Benchmarking Al_2O_3, Si_3N_4, and SiC Against ZrO_2

Figures A1 to **A3** shows cutting forces signals from DynoWare when end milling ZrO_2

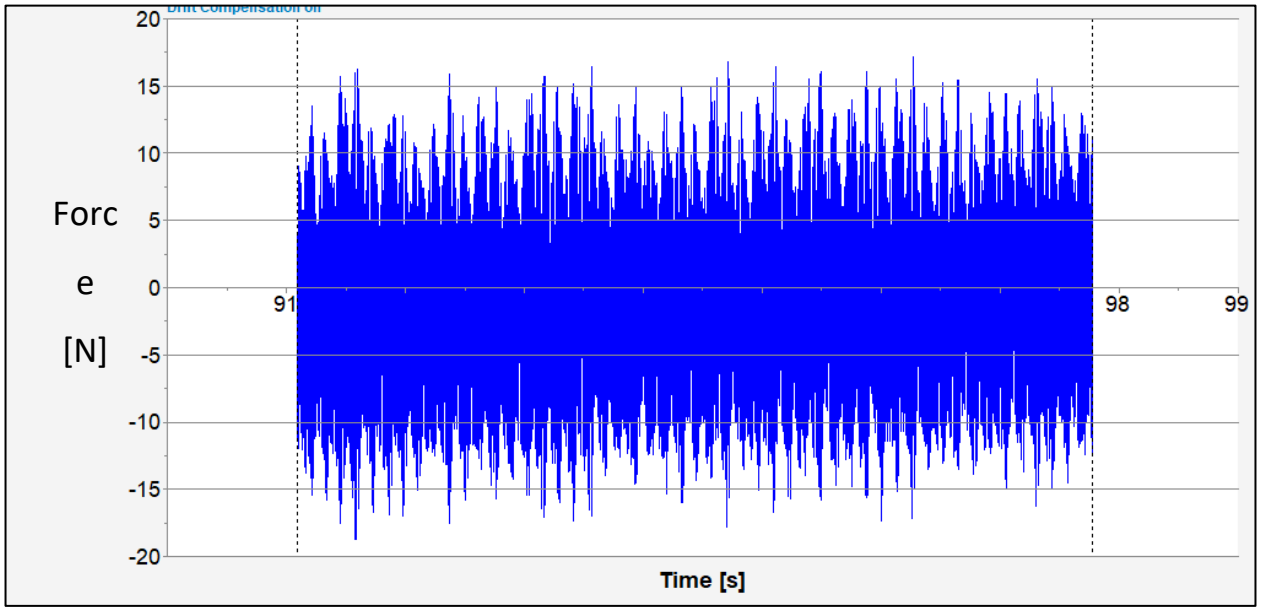


Figure A1 Cutting force signal of ZrO_2 in X axis F_X **(end milling)**

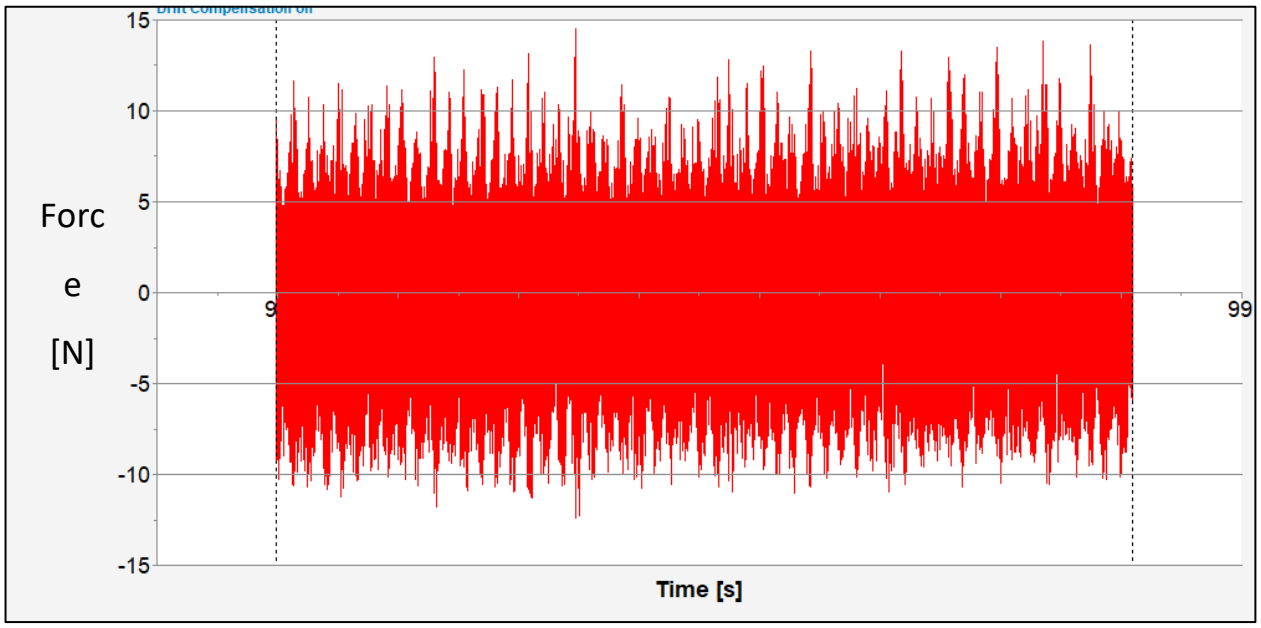


Figure A2 Cutting force signal of ZrO_2 in Y axis F_Y **(end milling)**

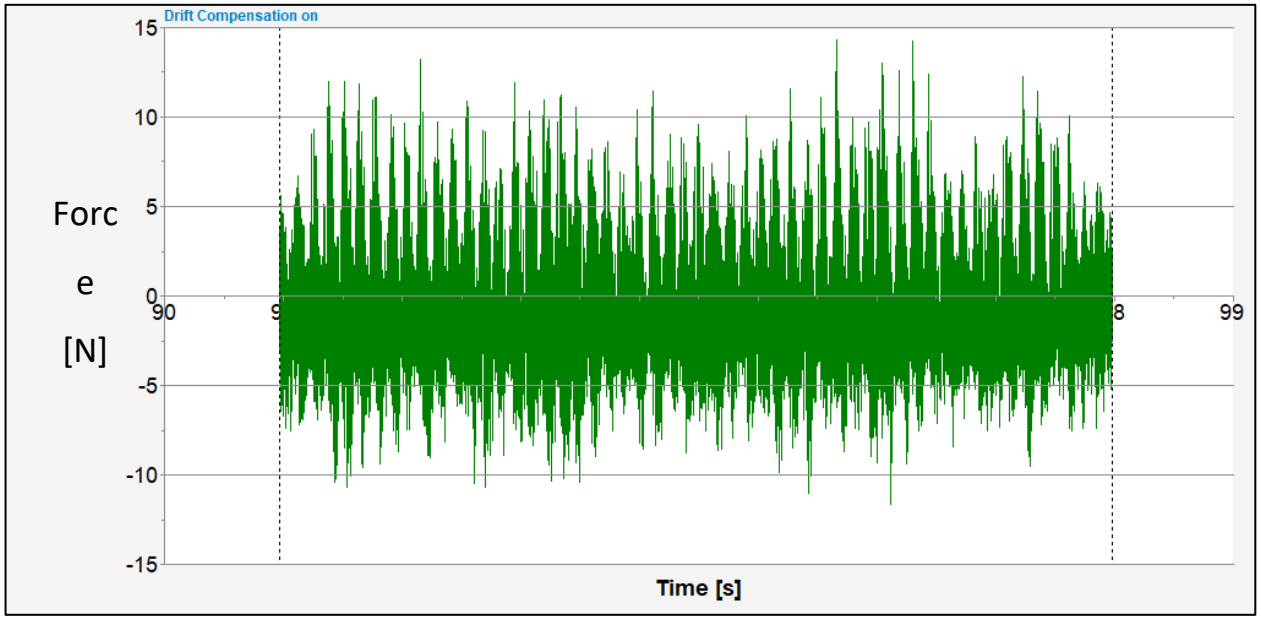


Figure A3 Cutting force signal of ZrO_2 in Z axis F_Z **(end milling)**

Figures A4 to **A6** shows cutting forces signals from DynoWare when end milling Al_2O_3

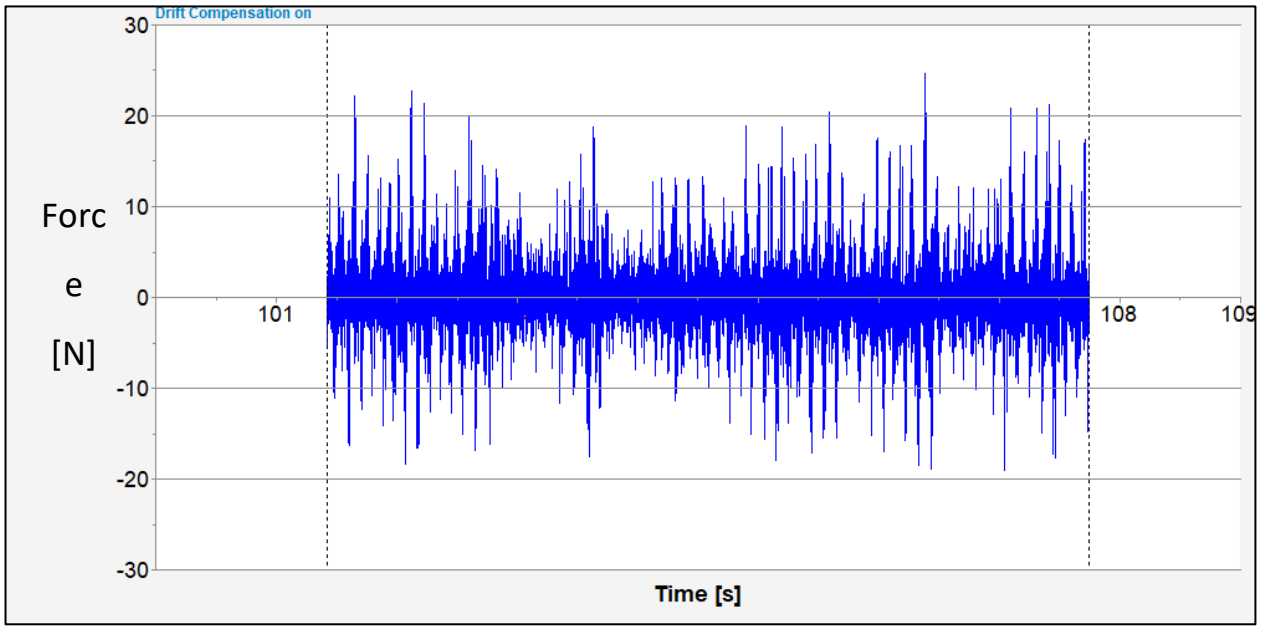


Figure A4 Cutting force signal of Al_2O_3 in X axis F_X **(end milling)**

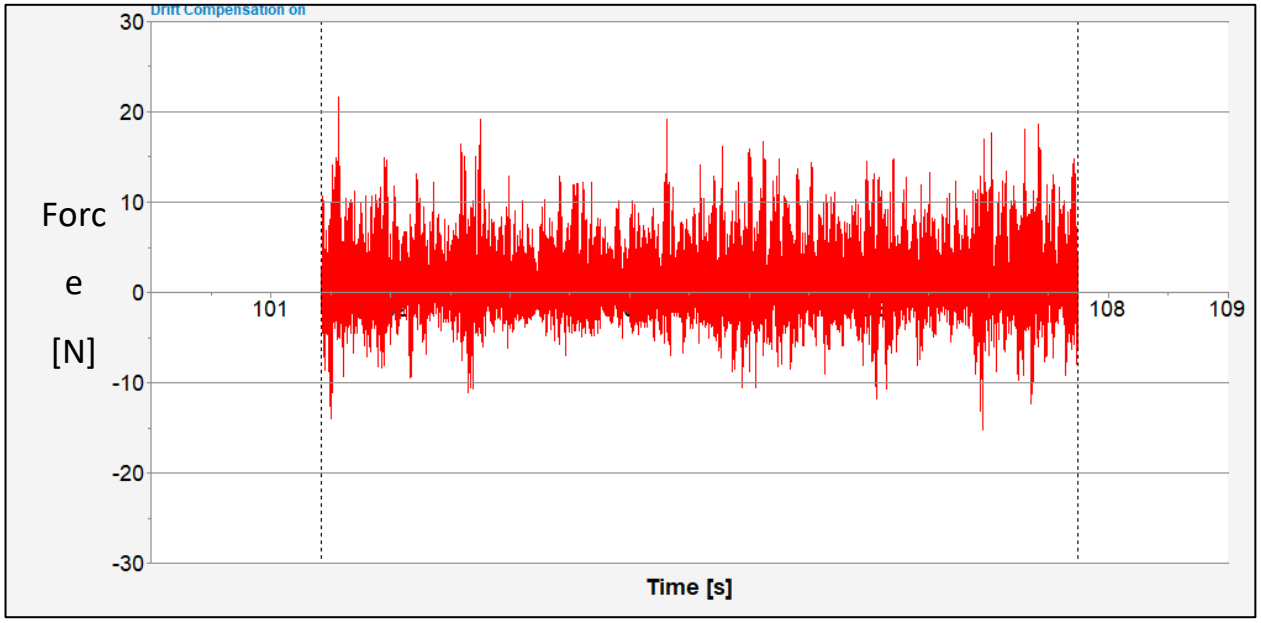


Figure A5 Cutting force signal of Al_2O_3 in Y axis F_Y **(end milling)**

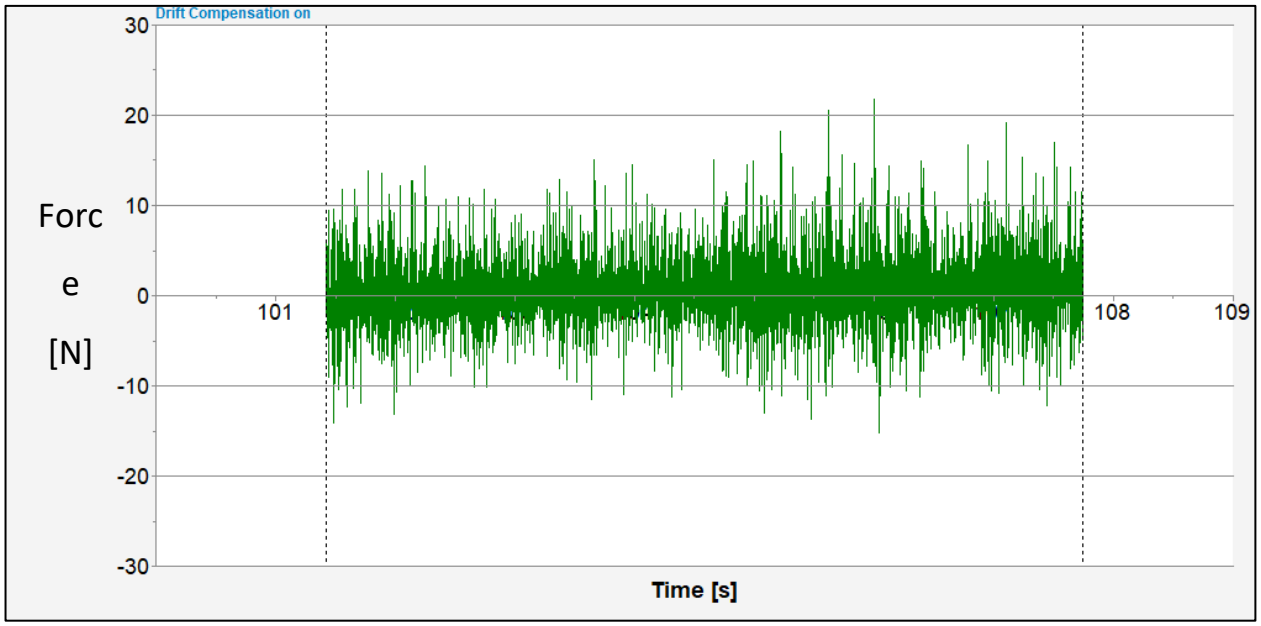


Figure A6 Cutting force signal of Al_2O_3 in Z axis F_Z **(end milling)**

Figures A7 to **A9** shows cutting forces signals from DynoWare when end milling Si_3N_4

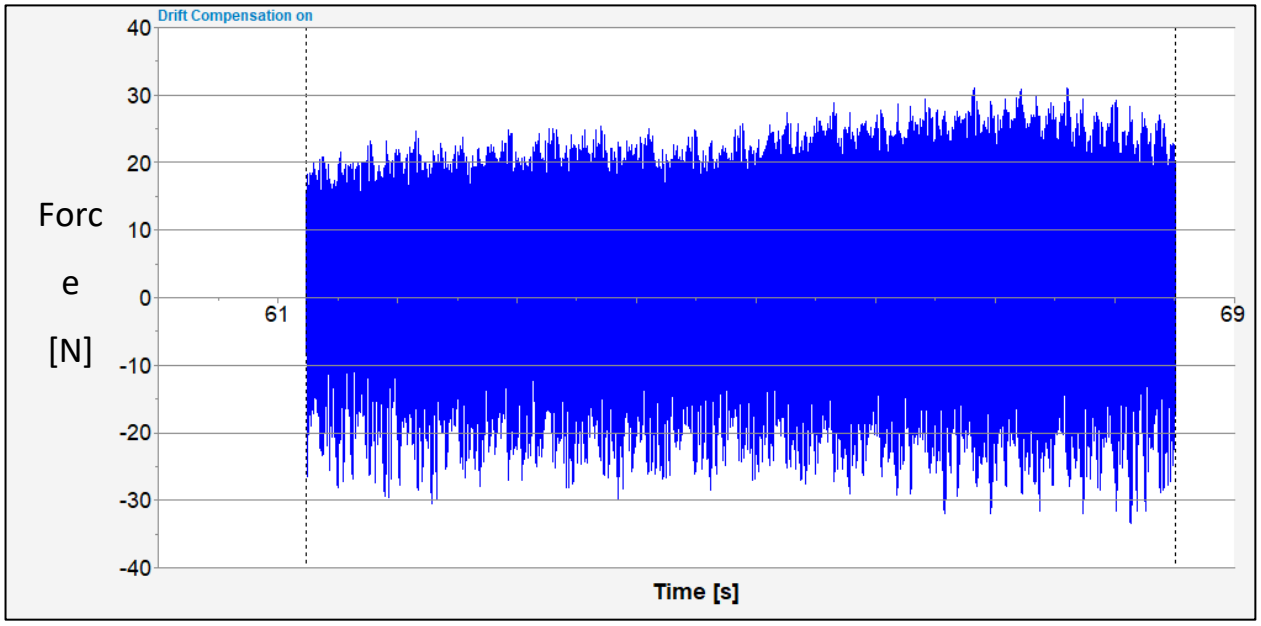


Figure A7 Cutting force signal of Si_3N_4 in X axis F_X **(end milling)**

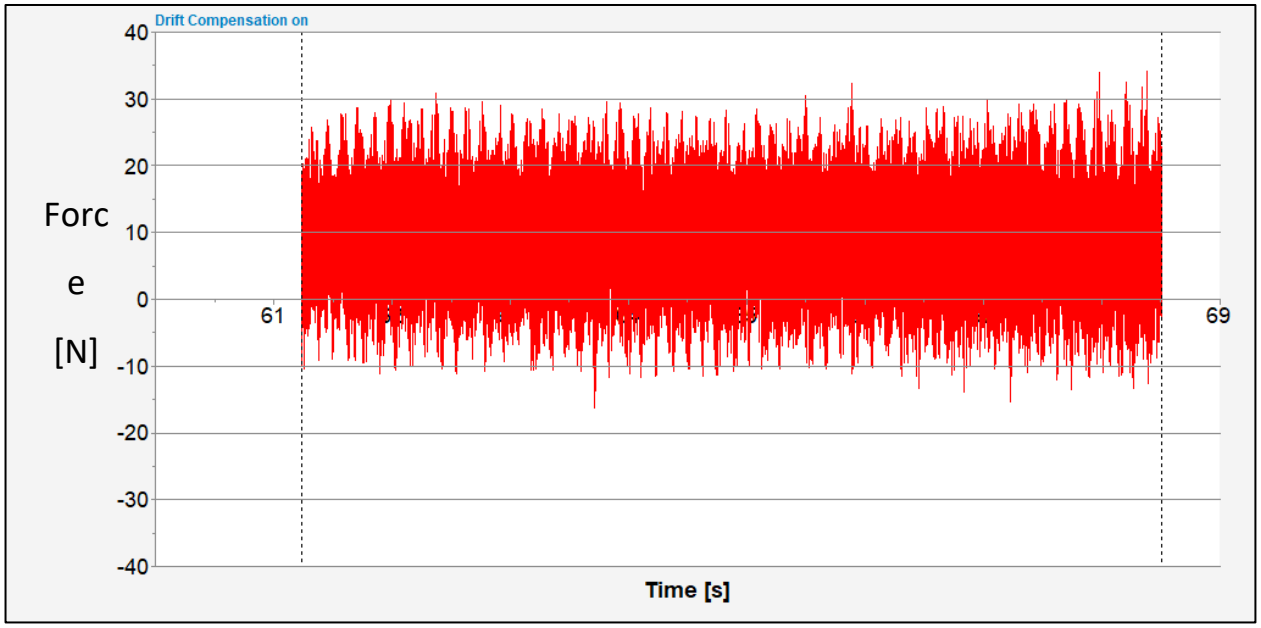


Figure A8 Cutting force signal of Si_3N_4 in Y axis F_Y **(end milling)**

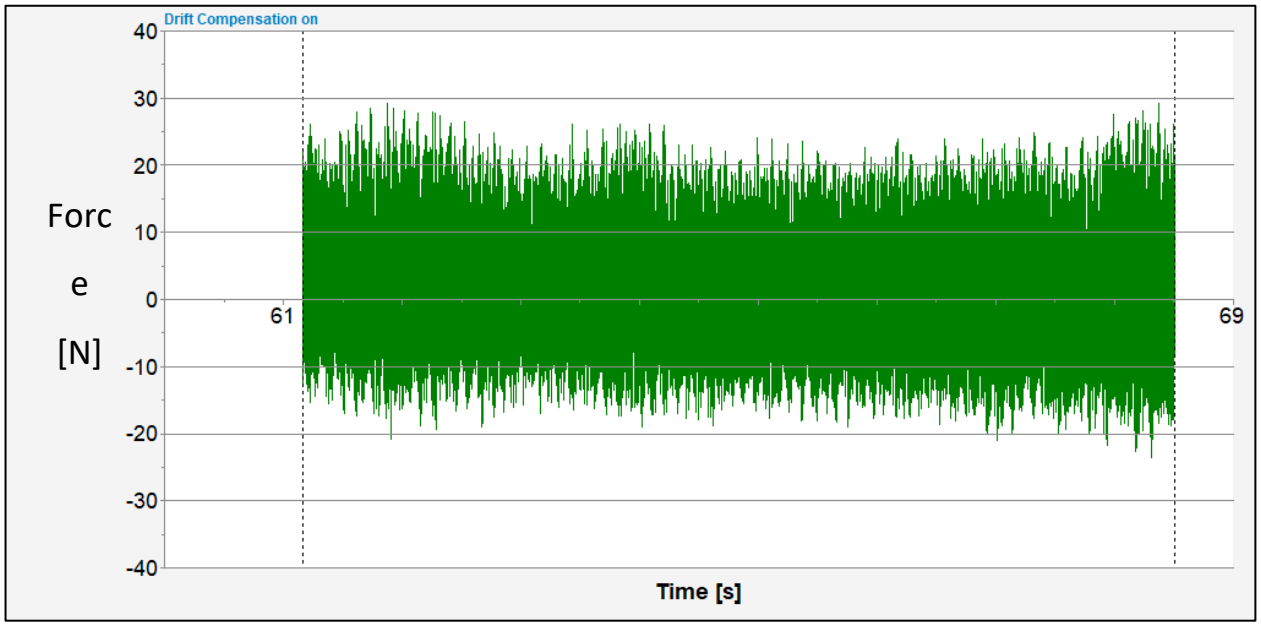


Figure A9 Cutting force signal of Si_3N_4 in Z axis F_Z **(end milling)**

Figures A10 to **A12** shows cutting forces signals from DynoWare when end milling SiC

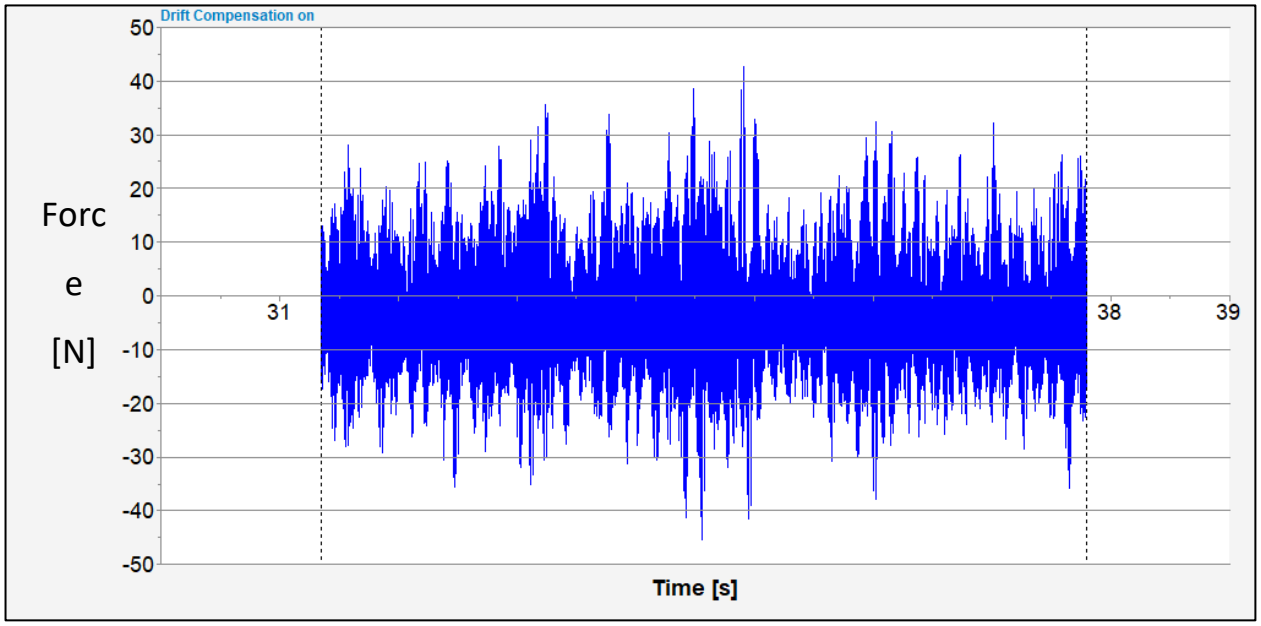


Figure A10 Cutting force signal of SiC in X axis F_X **(end milling)**

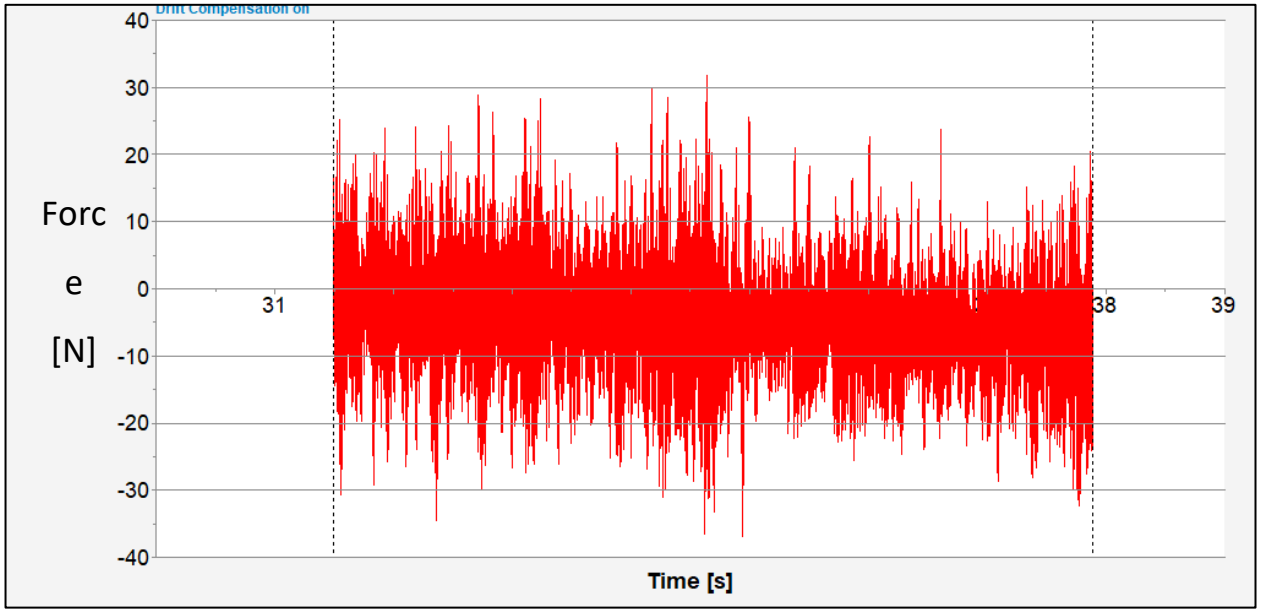


Figure A11 Cutting force signal of SiC in Y axis F_Y **(end milling)**

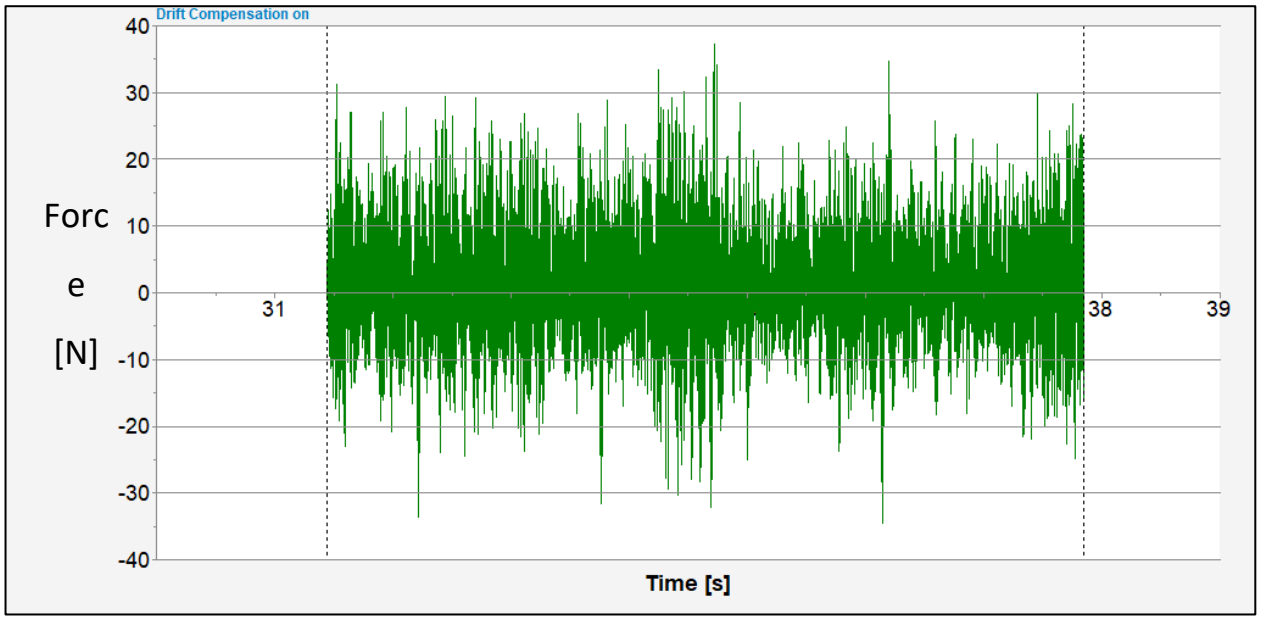


Figure A12 Cutting force signal of SiC in Z axis F_Z **(end milling)**

b) Phase 1.D: Benchmarking Al_2O_3, Si_4N_3, and SiC Against ZrO_2 When UAM Used, and Comparing Conventional Milling to Ultrasonic Assisted one.

Figures A13 to **A15** shows cutting forces signals from DynoWare when end milling ZrO_2 by UAM method

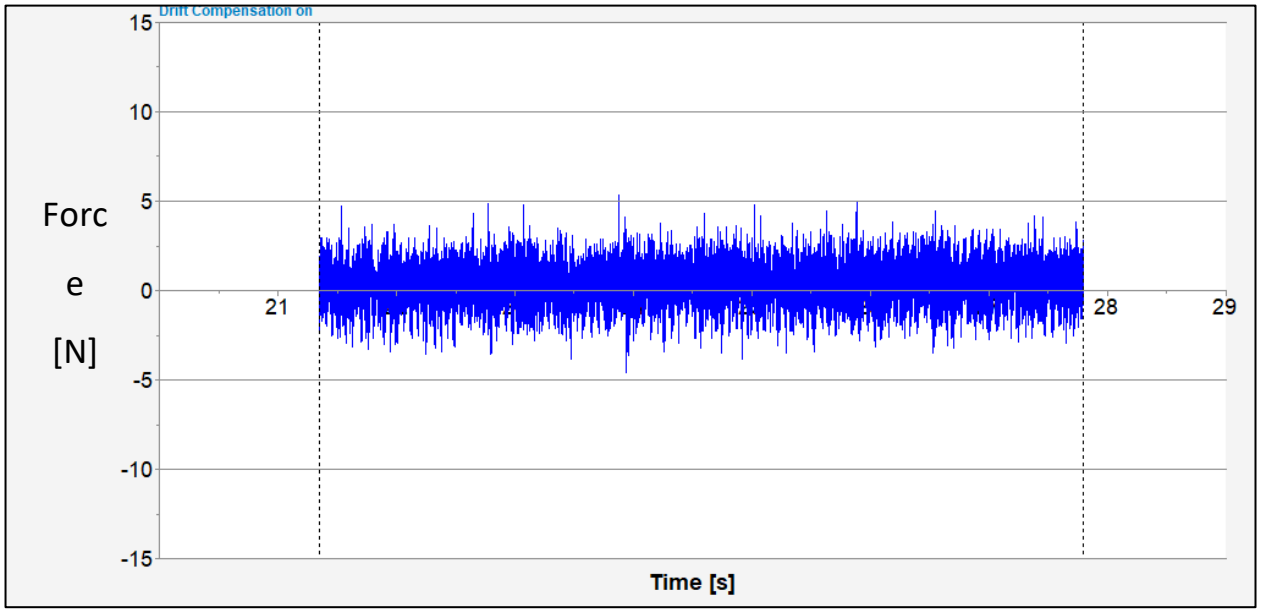


Figure A13 Cutting force signal of ZrO_2 in X axis F_X **(UAM)**

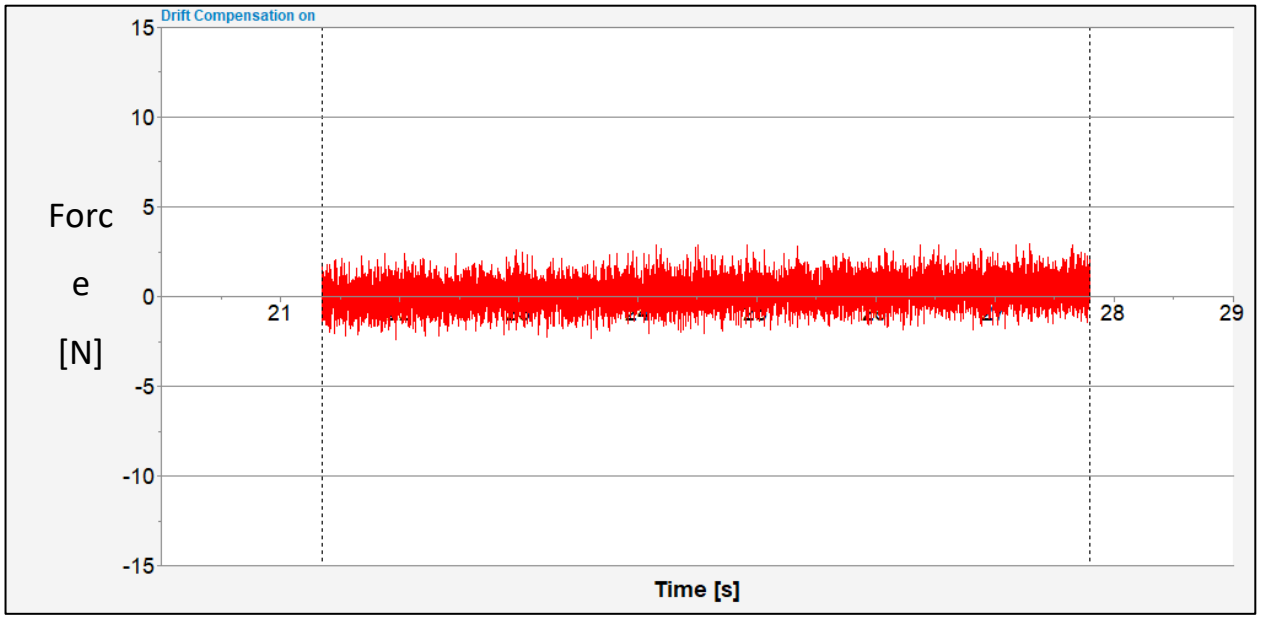


Figure A14 Cutting force signal of ZrO_2 in Y axis F_Y **(UAM)**

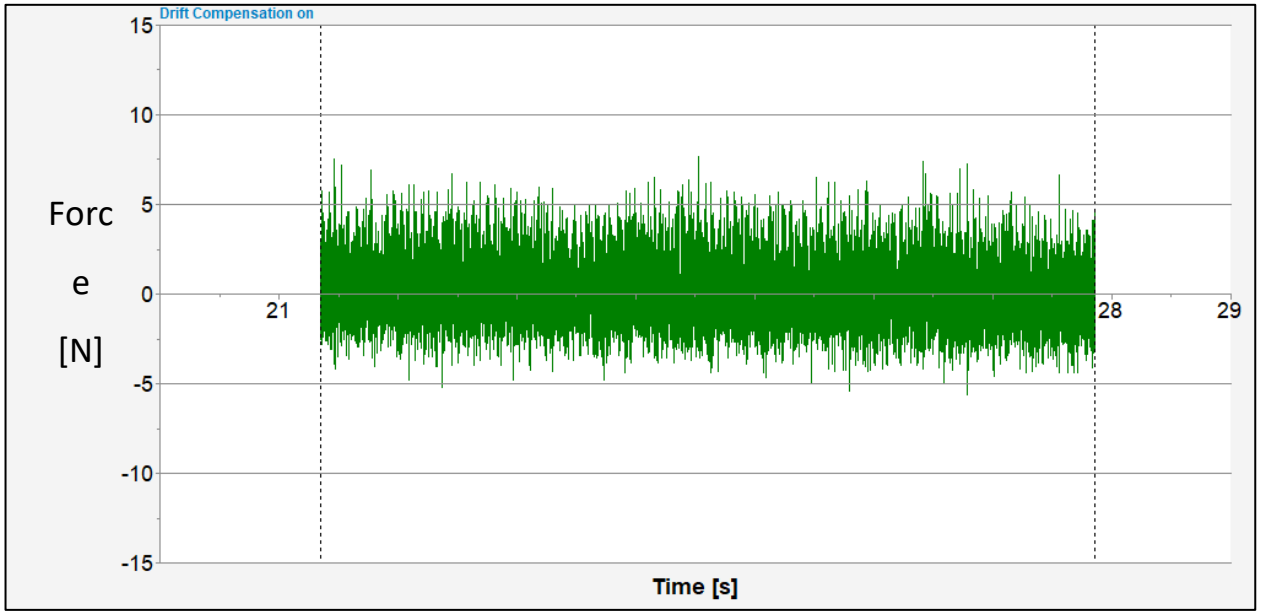


Figure A15 Cutting force signal of ZrO_2 in Z axis F_Z **(UAM)**

Figures A16 to **A18** shows cutting forces signals from DynoWare when end milling Al_2O_3 by UAM method

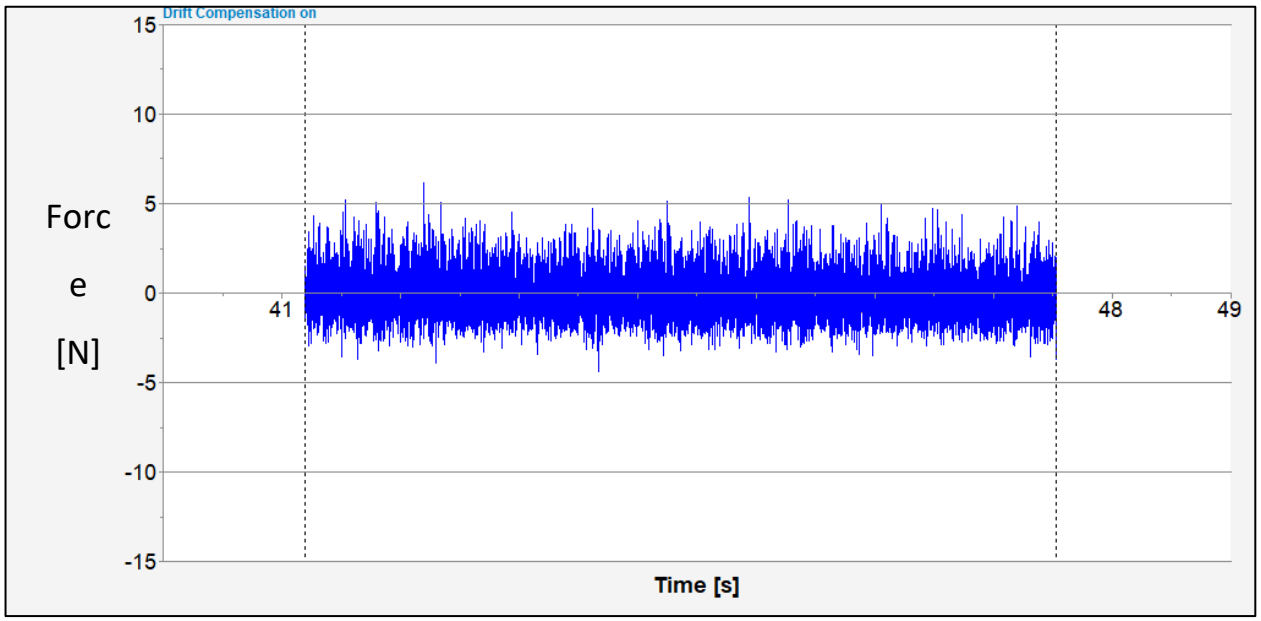


Figure A16 Cutting force signal of Al_2O_3 in X axis F_X **(UAM)**

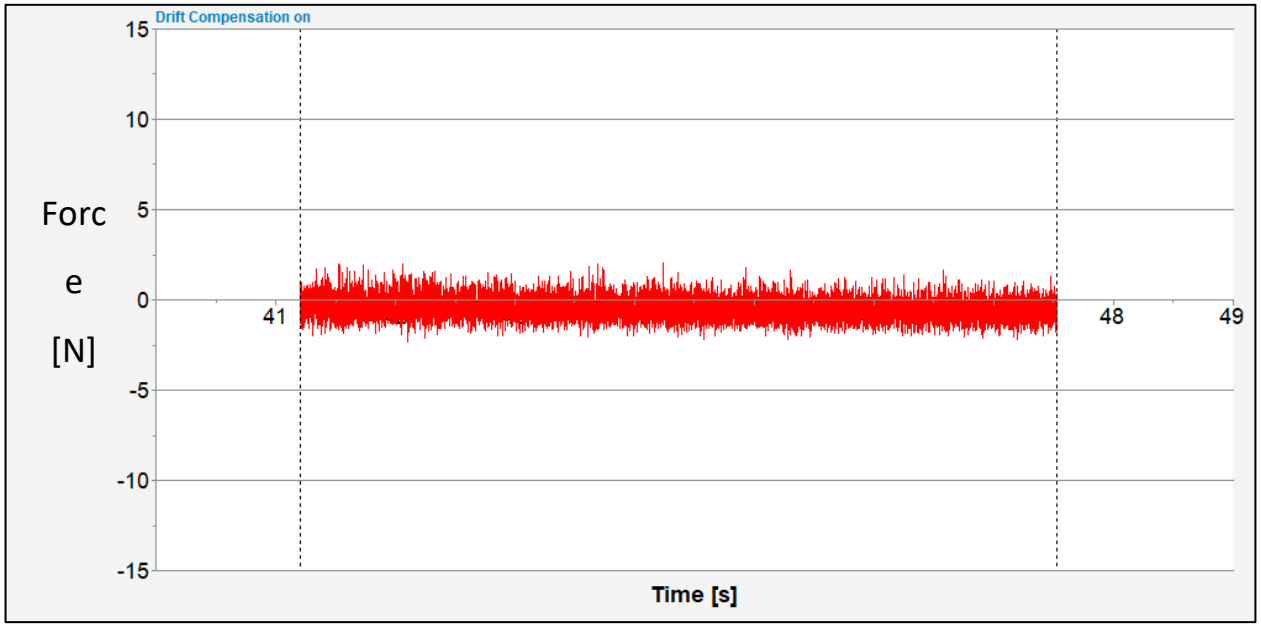


Figure A17 Cutting force signal of Al_2O_3 in Y axis F_Y **(UAM)**

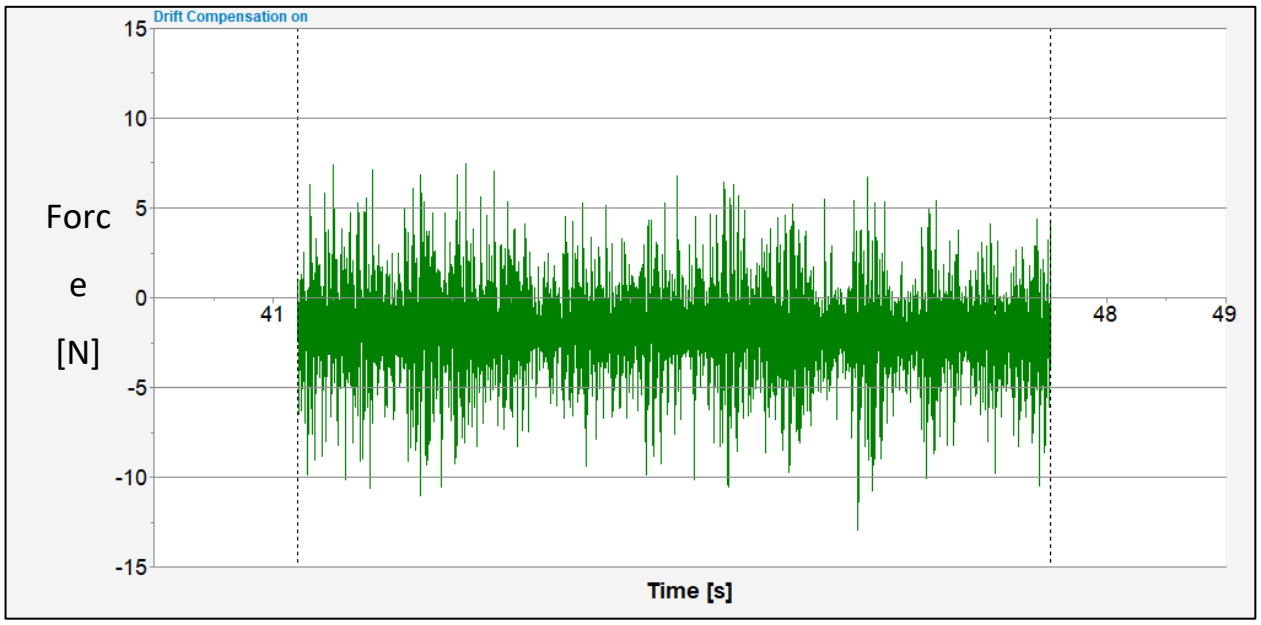


Figure A18 Cutting force signal of Al_2O_3 in Z axis F_Z **(UAM)**

Figures A19 to **A21** shows cutting forces signals from DynoWare when end milling Si_3N_4 by UAM method

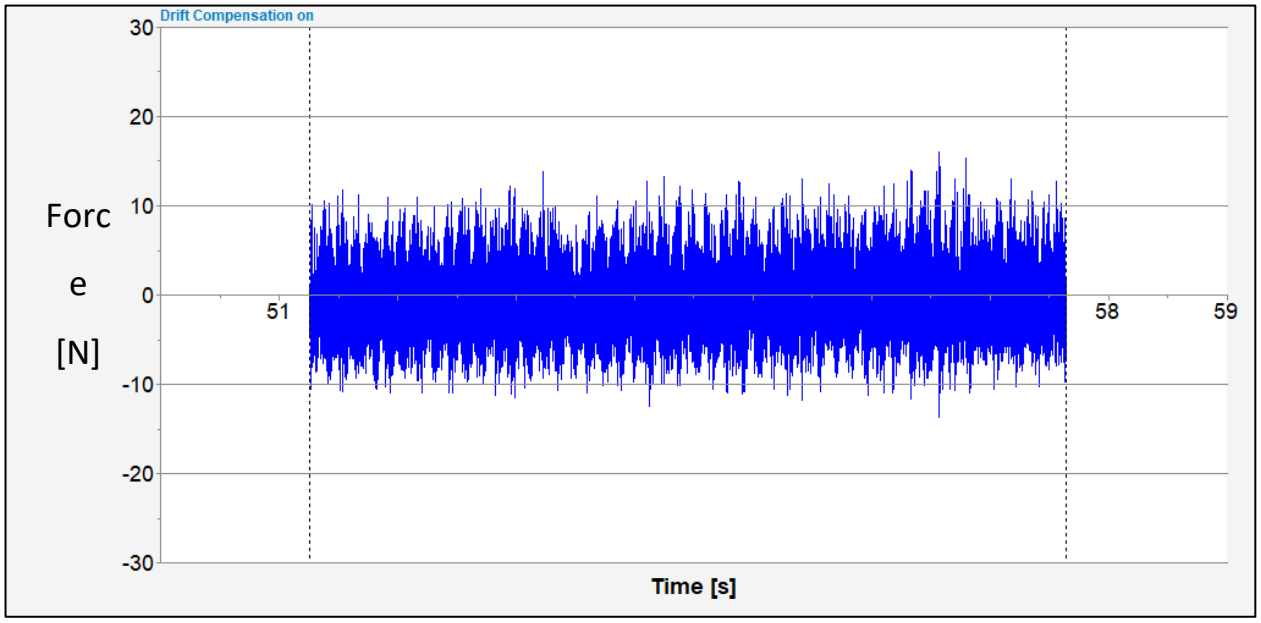


Figure A19 Cutting force signal of Si_3N_4 in X axis F_X **(UAM)**

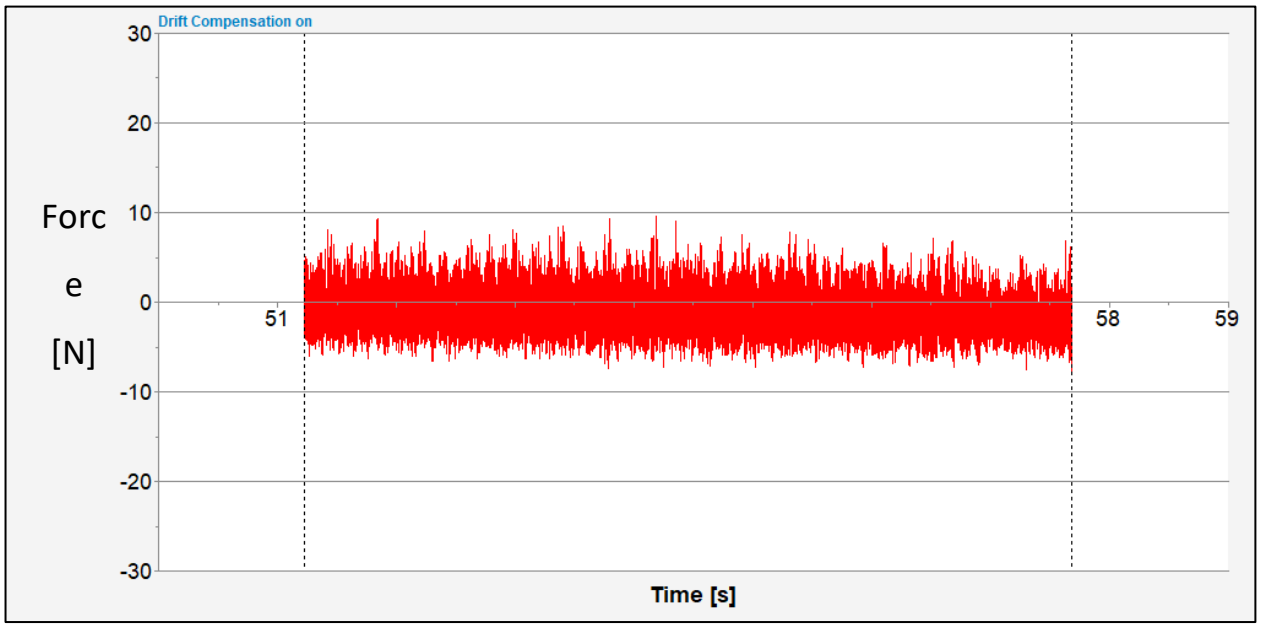


Figure A20 Cutting force signal of Si_3N_4 in Y axis F_Y **(UAM)**

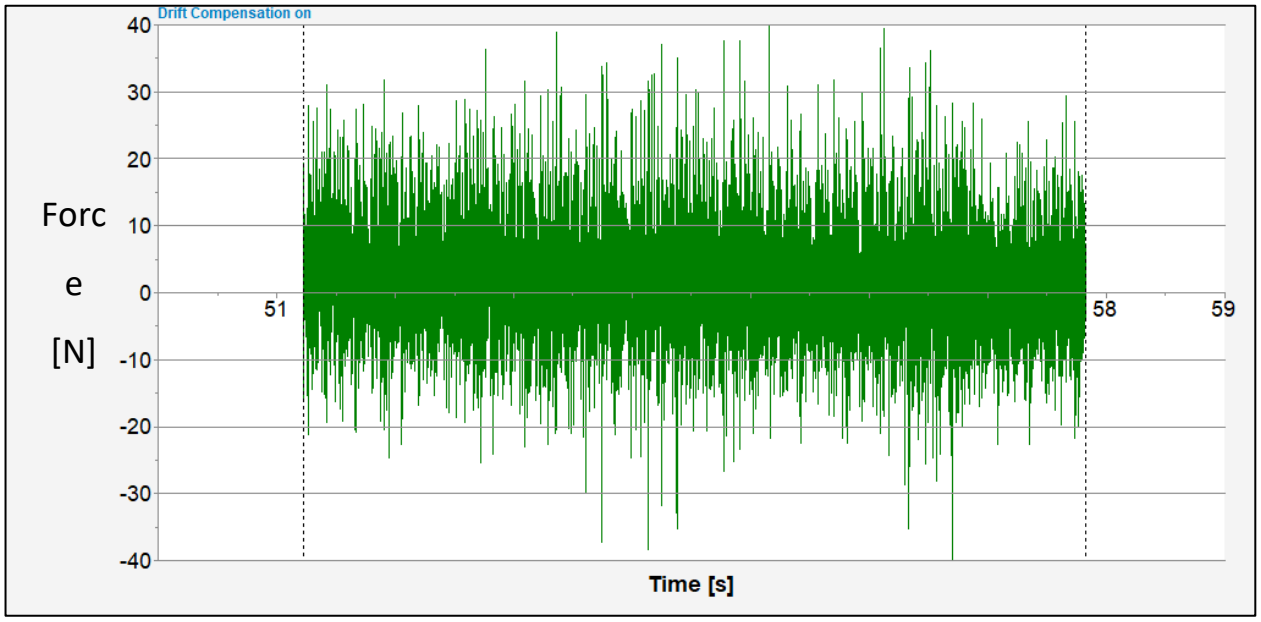


Figure A21 Cutting force signal of Si_3N_4 in Z axis F_Z **(UAM)**

Figures A22 to **A24** shows cutting forces signals from DynoWare when end milling SiC by UAM method

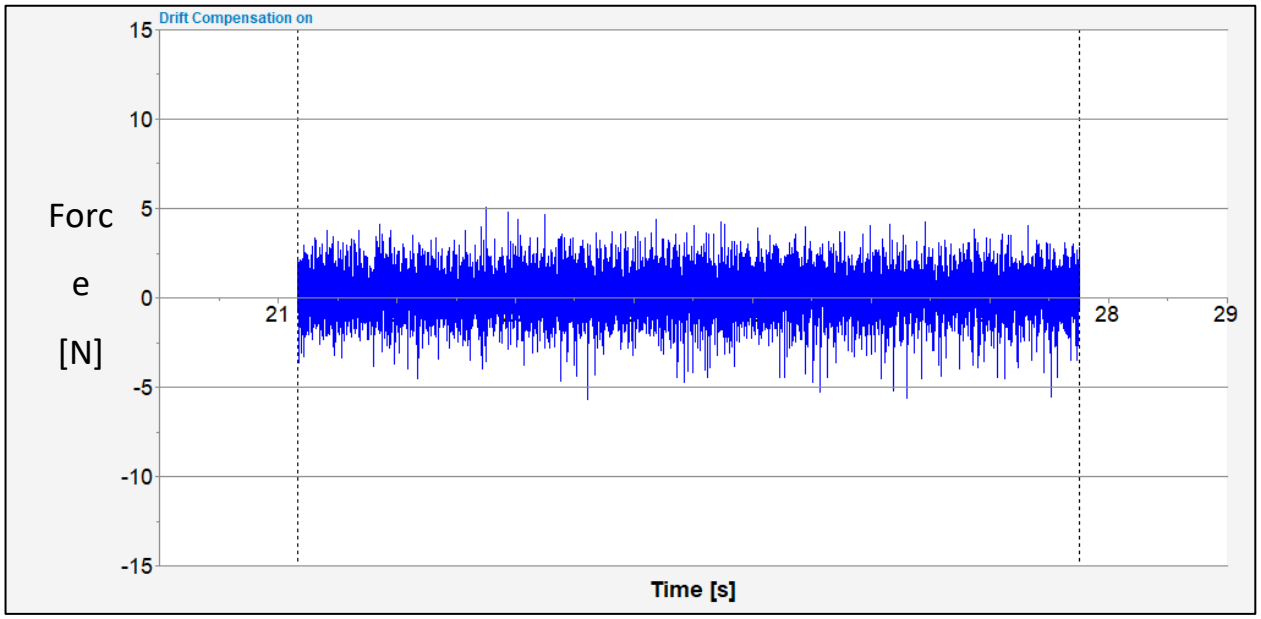


Figure A22 Cutting force signal of SiC in X axis F_X **(UAM)**

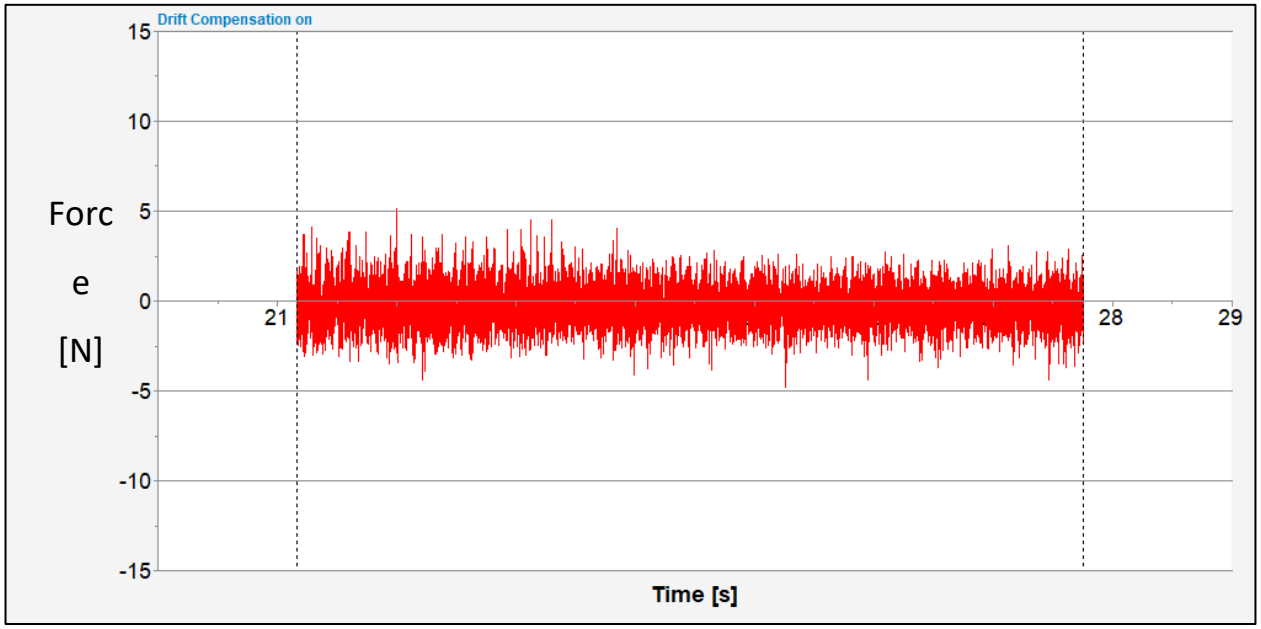


Figure A23 Cutting force signal of SiC in Y axis F_Y **(UAM)**

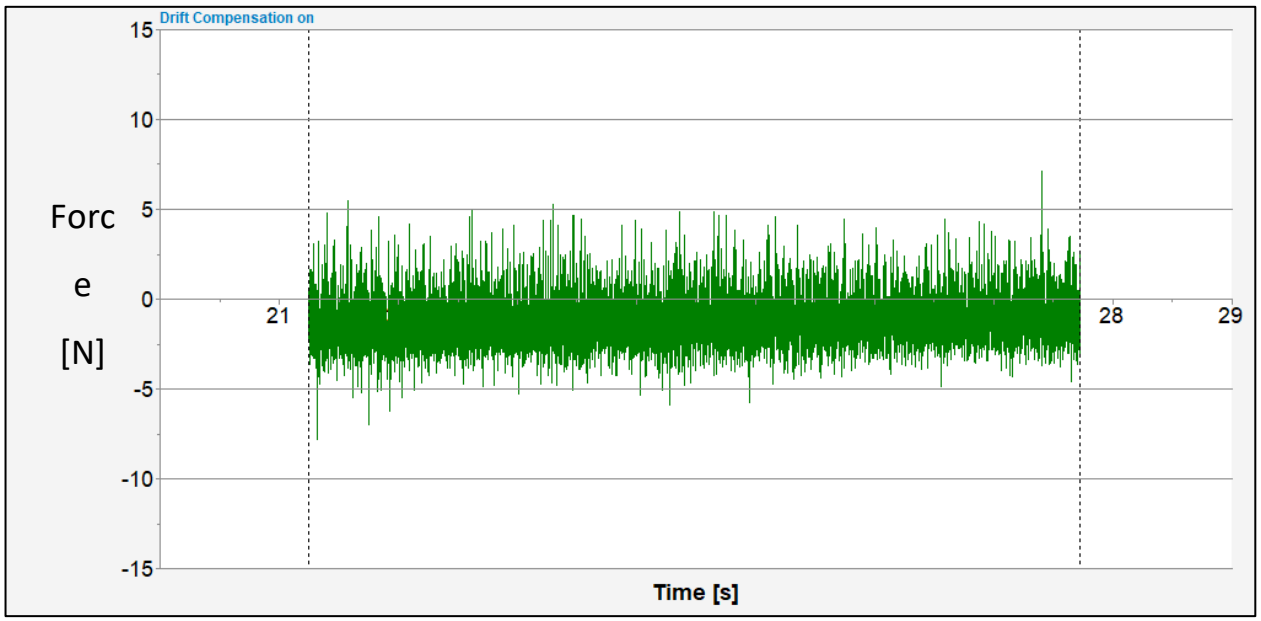


Figure A24 Cutting force signal of SiC in Z axis F_Z **(UAM)**

A.2 Phase 2, Point Grinding

a) Phase 2.B: Benchmarking Al_2O_3, Si_3N_4, and SiC against ZrO_2

Figures A25 to **A27** shows cutting forces signals from DynoWare when point grinding ZrO_2

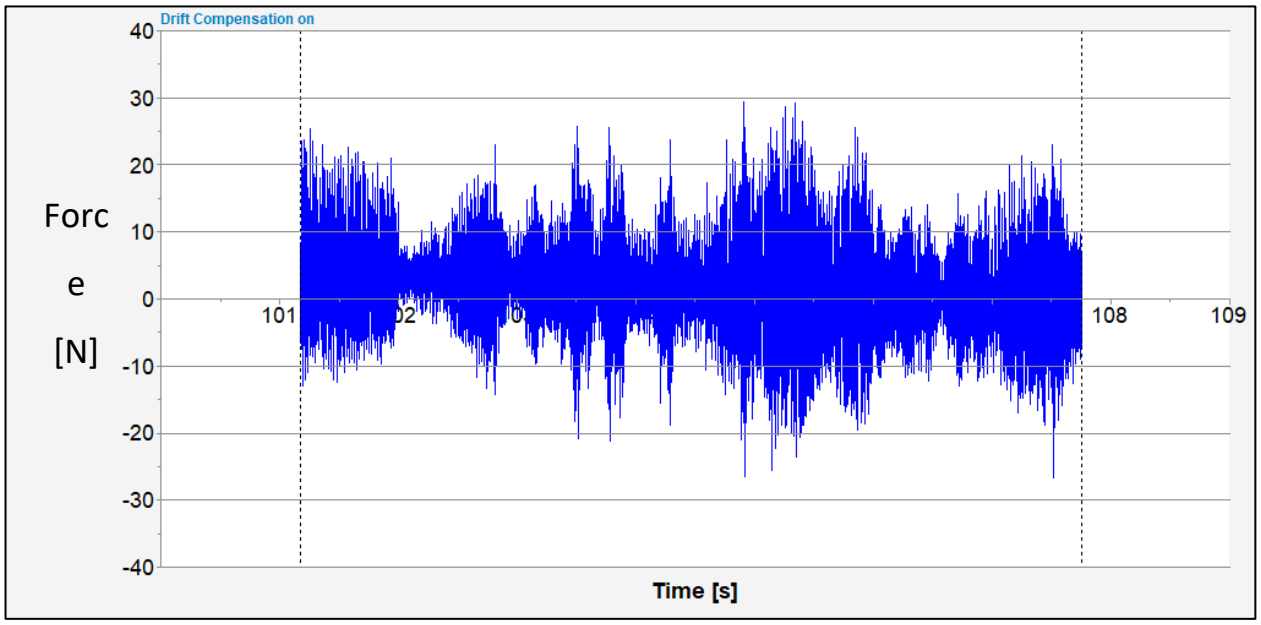


Figure A25 Cutting force signal of ZrO_2 in X axis F_X **(point grinding)**

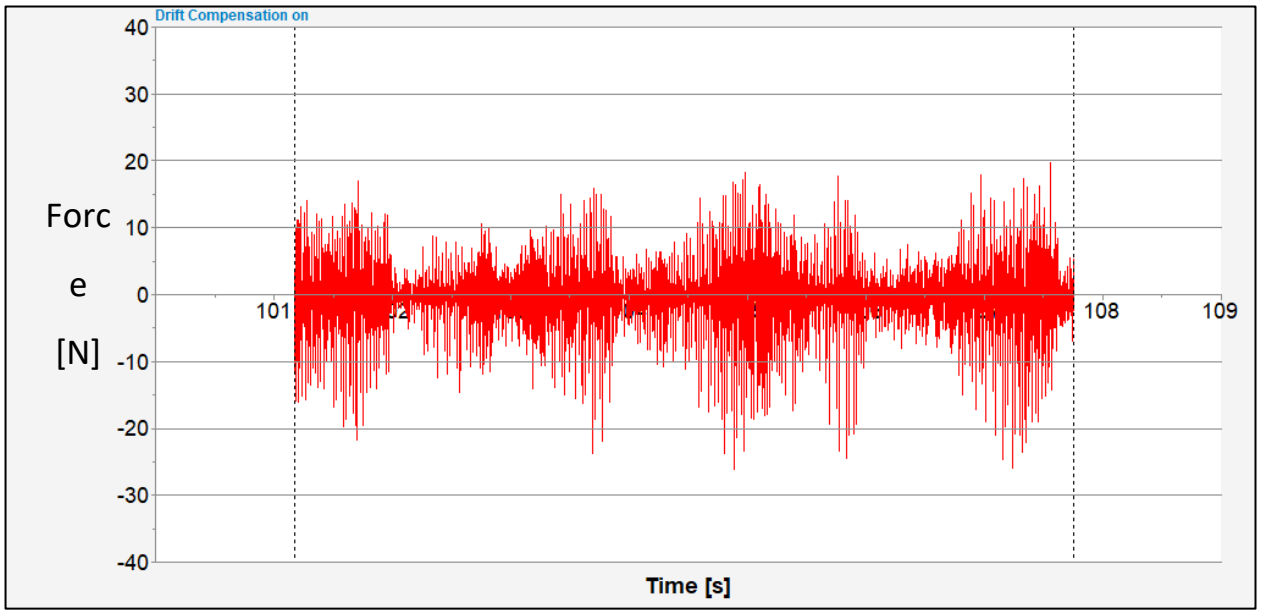


Figure A26 Cutting force signal of ZrO_2 in Y axis F_Y **(point grinding)**

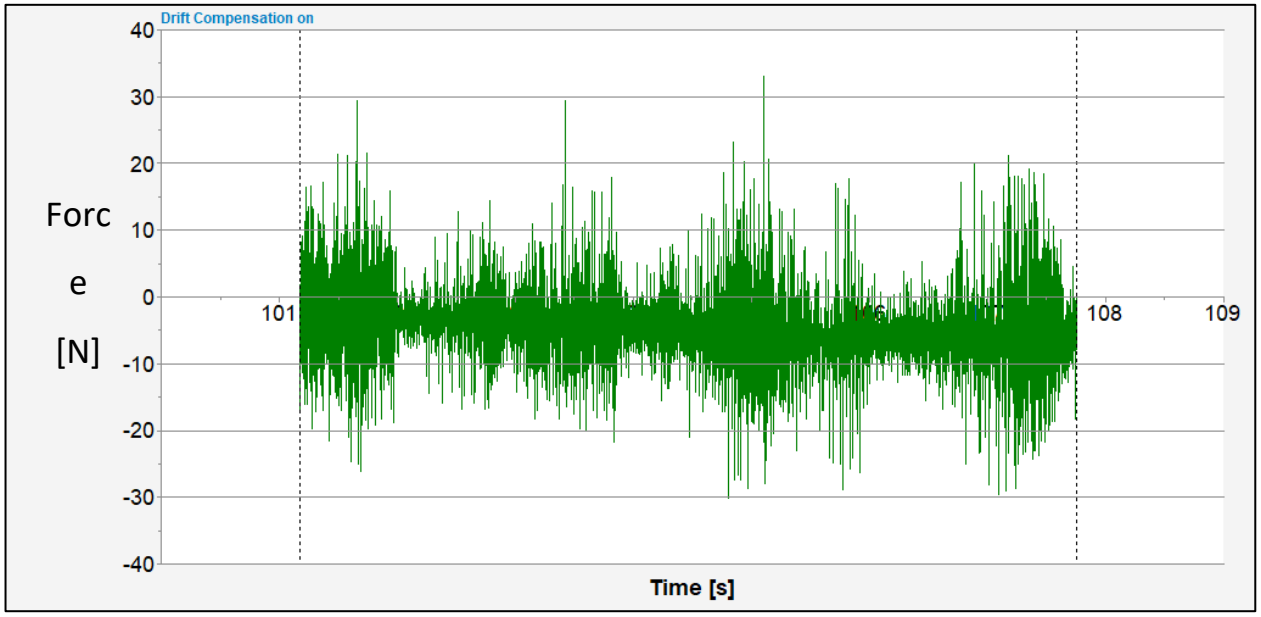


Figure A27 Cutting force signal of ZrO_2 in Z axis F_Z **(point grinding)**

Figures A28 to **A30** shows cutting forces signals from DynoWare when point grinding Al_2O_3

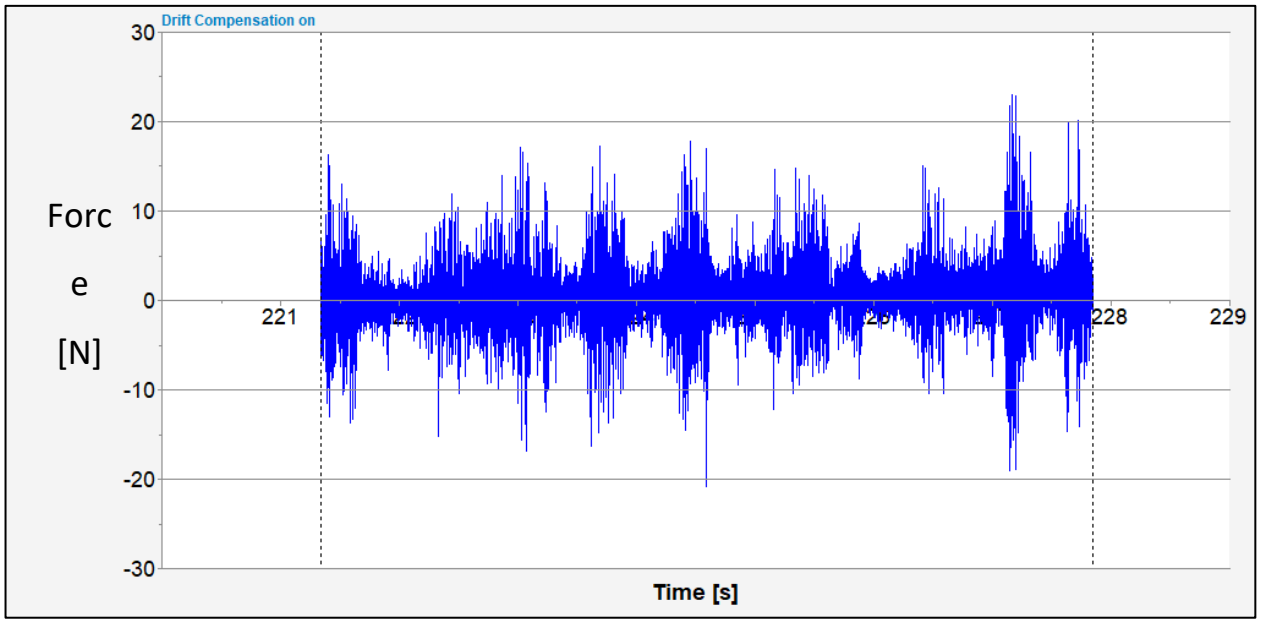


Figure A28 Cutting force signal of Al_2O_3 in X axis F_X **(point grinding)**

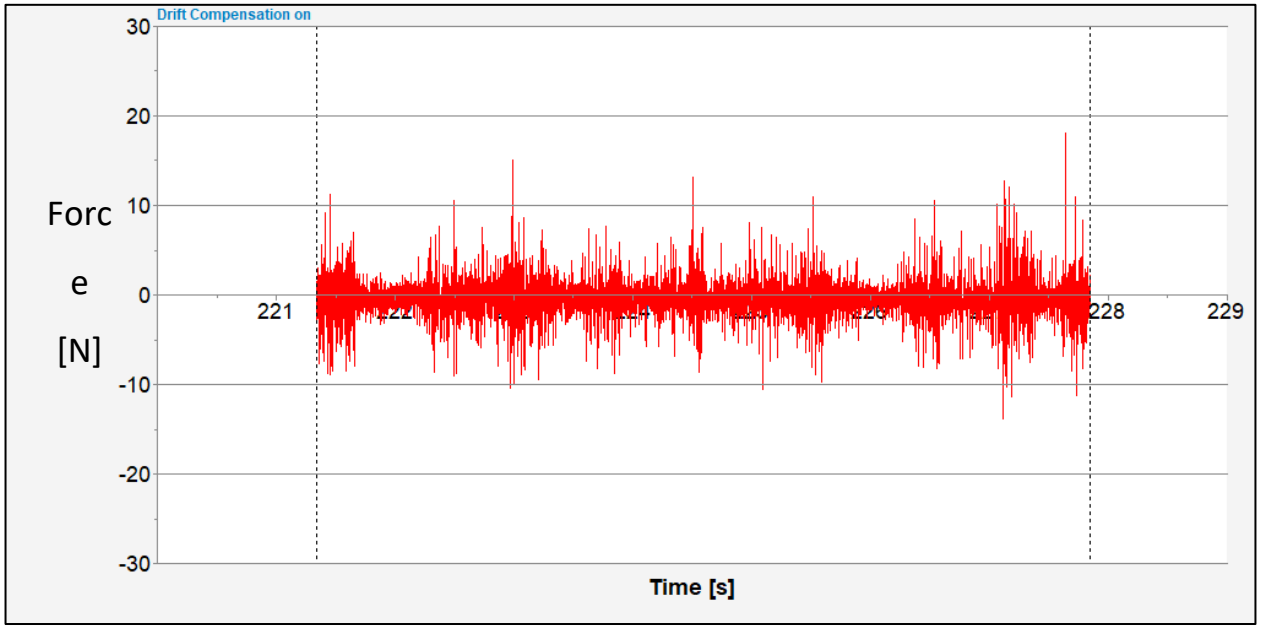


Figure A29 Cutting force signal of Al_2O_3 in Y axis F_Y **(point grinding)**

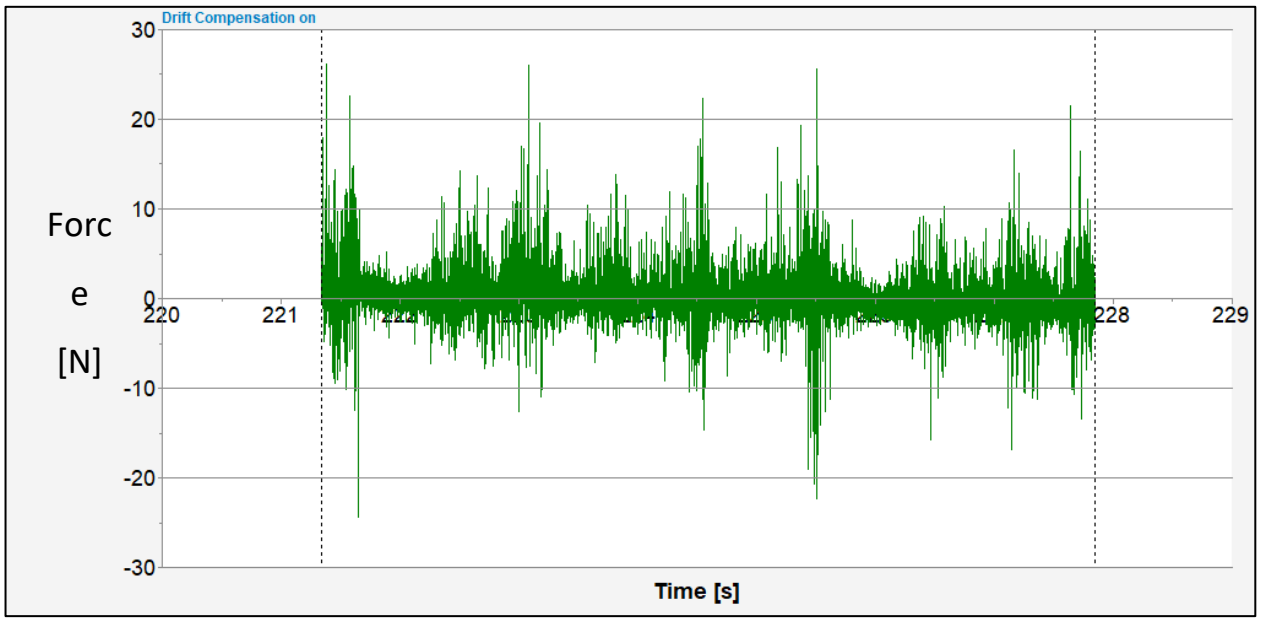


Figure A30 Cutting force signal of Al_2O_3 in Z axis F_Z **(point grinding)**

Figures A31 to **A33** shows cutting forces signals from DynoWare when point grinding Si_3N_4

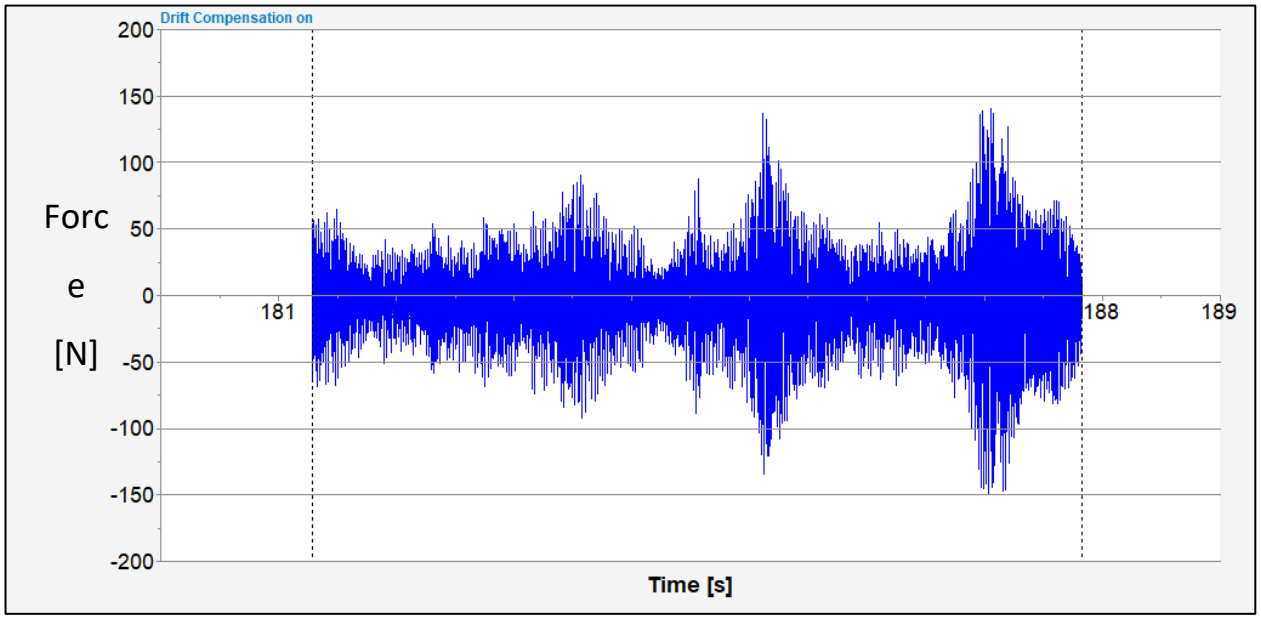


Figure A31 Cutting force signal of Si_3N_4 in X axis F_X **(point grinding)**

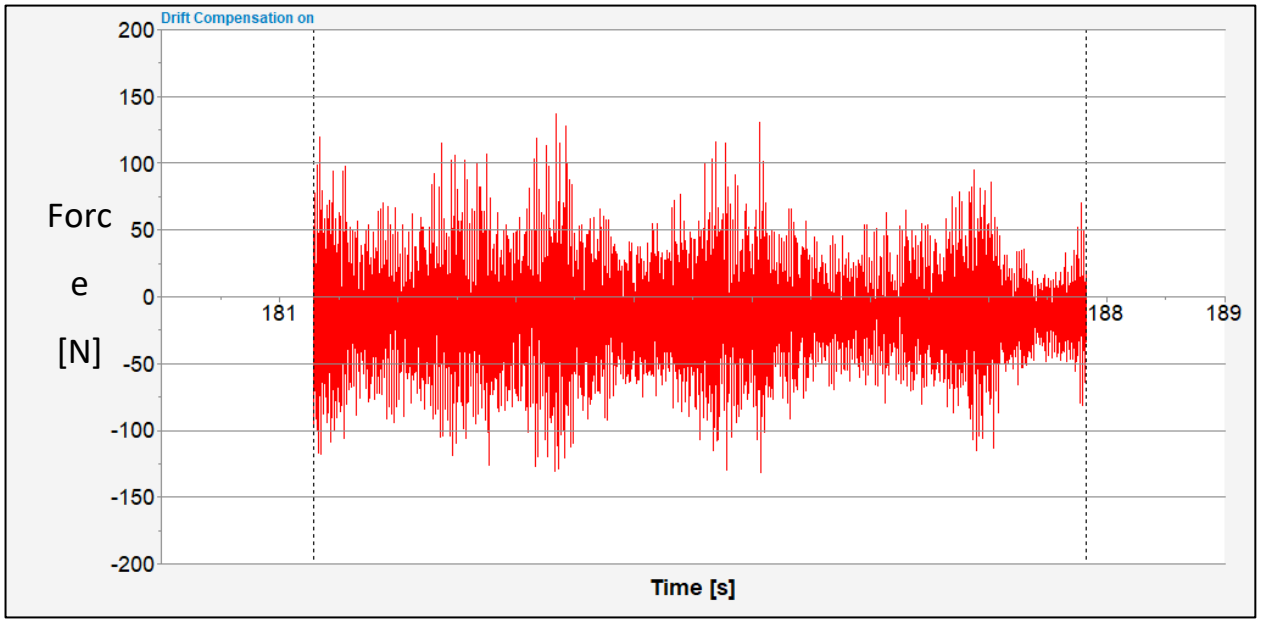


Figure A32 Cutting force signal of Si_3N_4 in Y axis F_Y **(point grinding)**

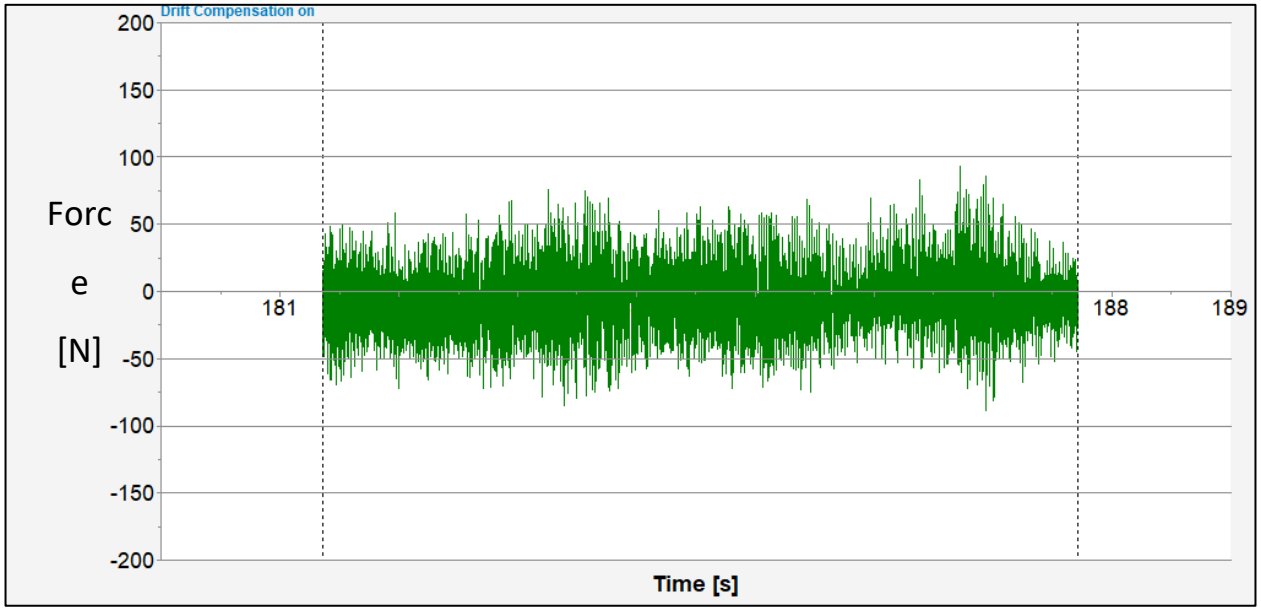


Figure A33 Cutting force signal of Si_3N_4 in Z axis F_Z **(point grinding)**

Figures A34 to **A36** shows cutting forces signals from DynoWare when point grinding SiC

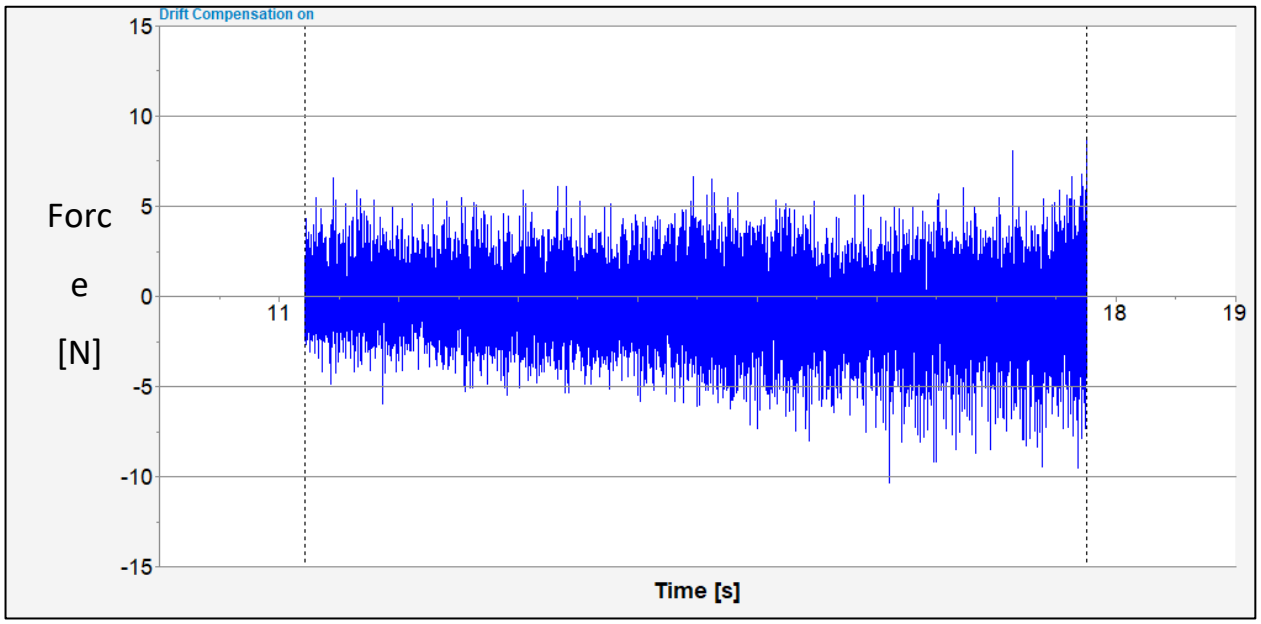


Figure A34 Cutting force signal of SiC in X axis F_X **(point grinding)**

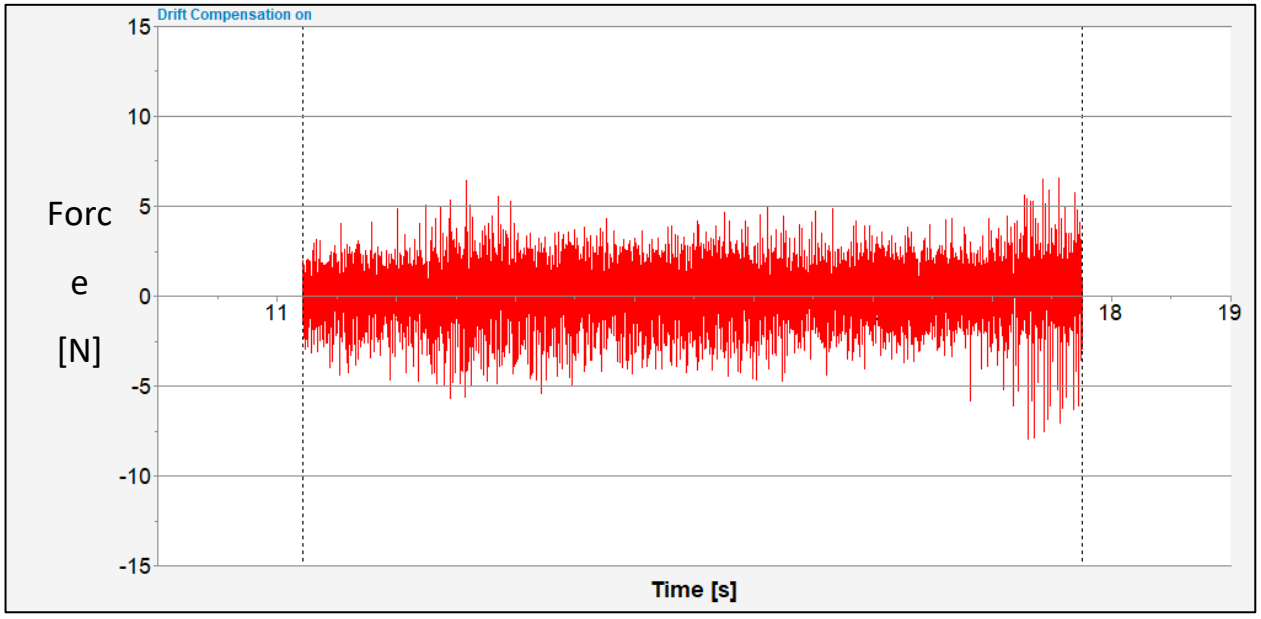


Figure A35 Cutting force signal of SiC in Y axis F_Y **(point grinding)**

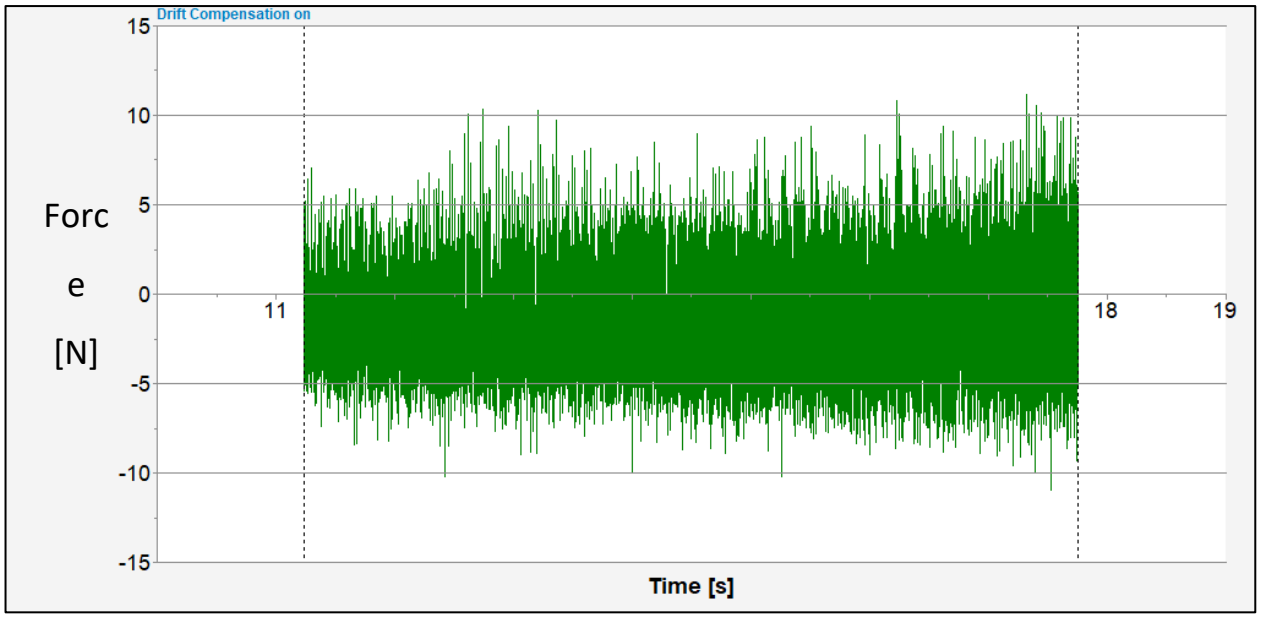


Figure A36 Cutting force signal of SiC in Z axis F_Z **(point grinding)**

b) Phase 2.D: Benchmarking Al_2O_3, Si_4N_3, and SiC Against ZrO_2 When Using UAG Method, and Comparing the Conventional Point Grinding to Ultrasonic Assisted Grinding

Figures A37 to **A39** shows cutting forces signals from DynoWare when point grinding ZrO_2 by UAG method

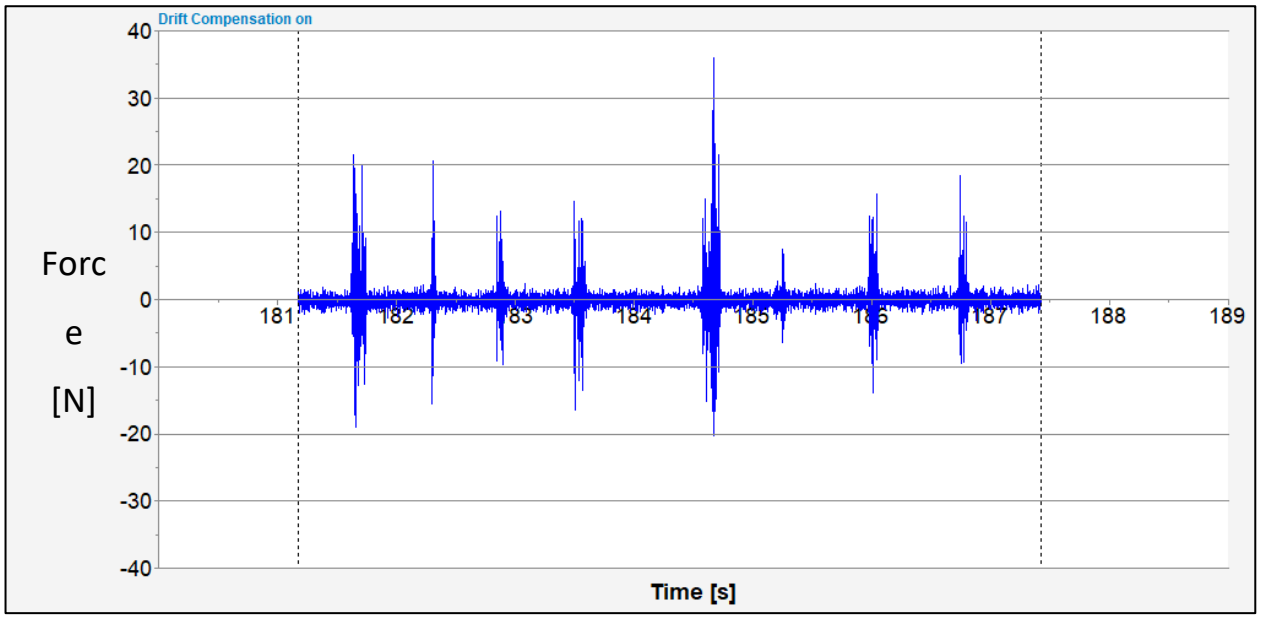


Figure A37 Cutting force signal of ZrO_2 in X axis F_X **(UAG)**

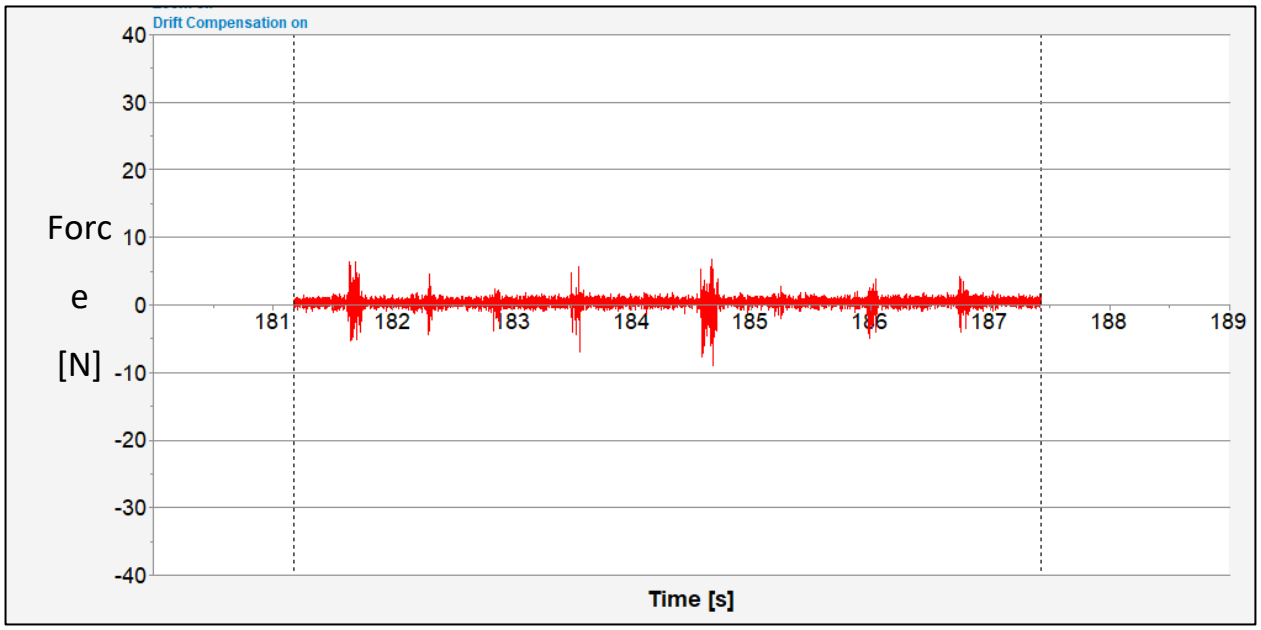


Figure A38 Cutting force signal of ZrO_2 in Y axis F_Y **(UAG)**

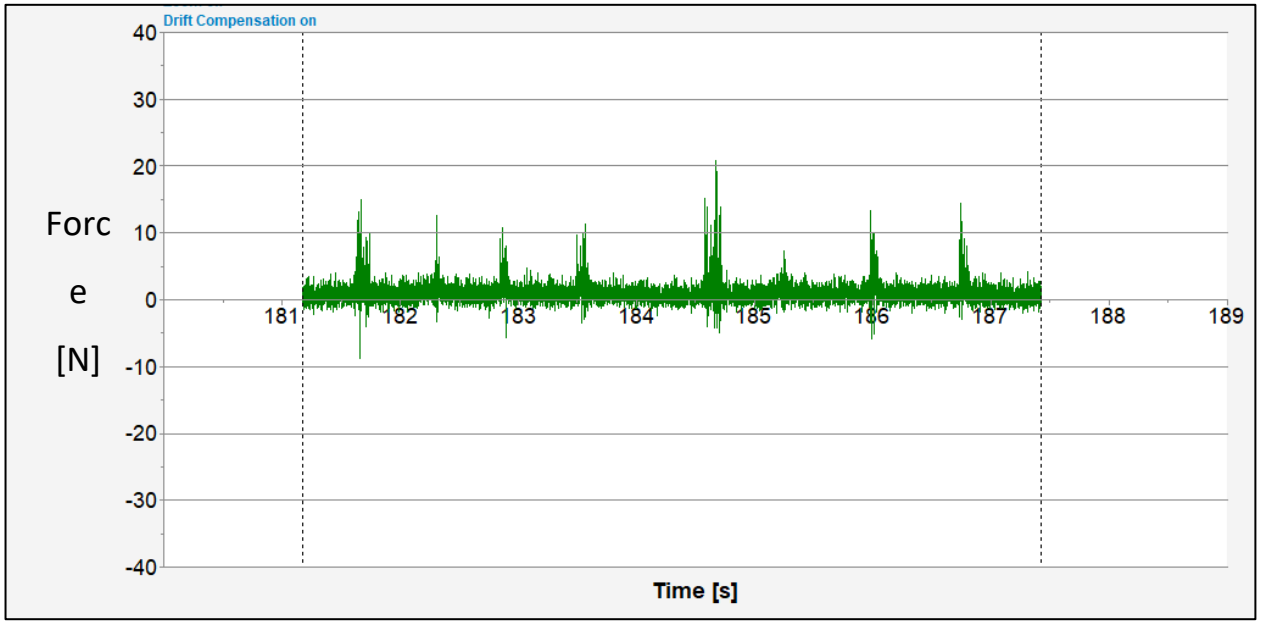


Figure A39 Cutting force signal of ZrO_2 in Z axis F_Z **(UAG)**

Figures A40 to **A42** shows cutting forces signals from DynoWare when point grinding Al_2O_3 by UAG method

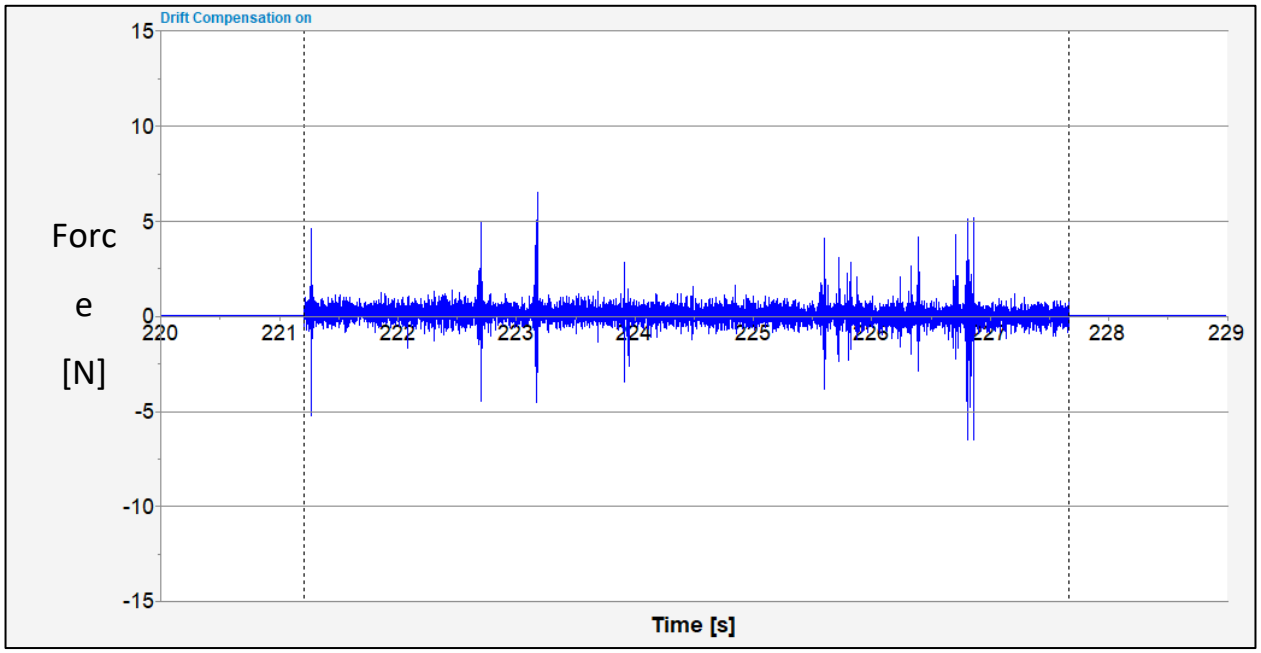


Figure A40 Cutting force signal of Al_2O_3 in X axis F_X **(UAG)**

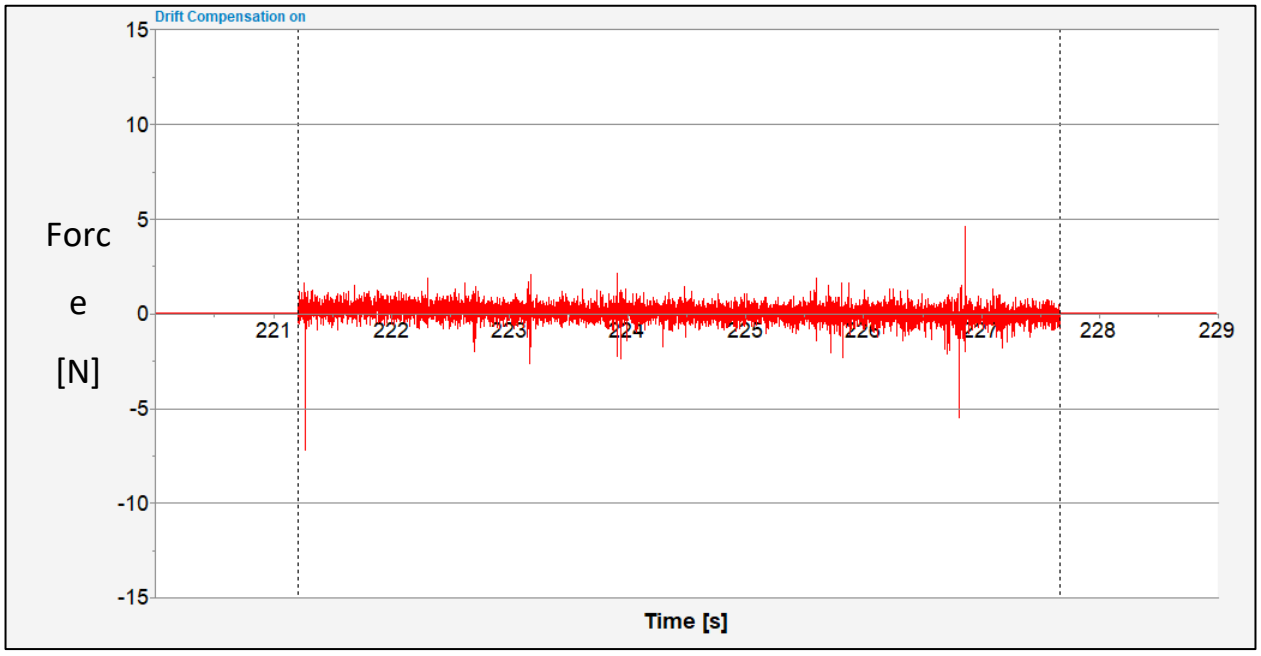


Figure A41 Cutting force signal of Al_2O_3 in Y axis F_Y **(UAG)**

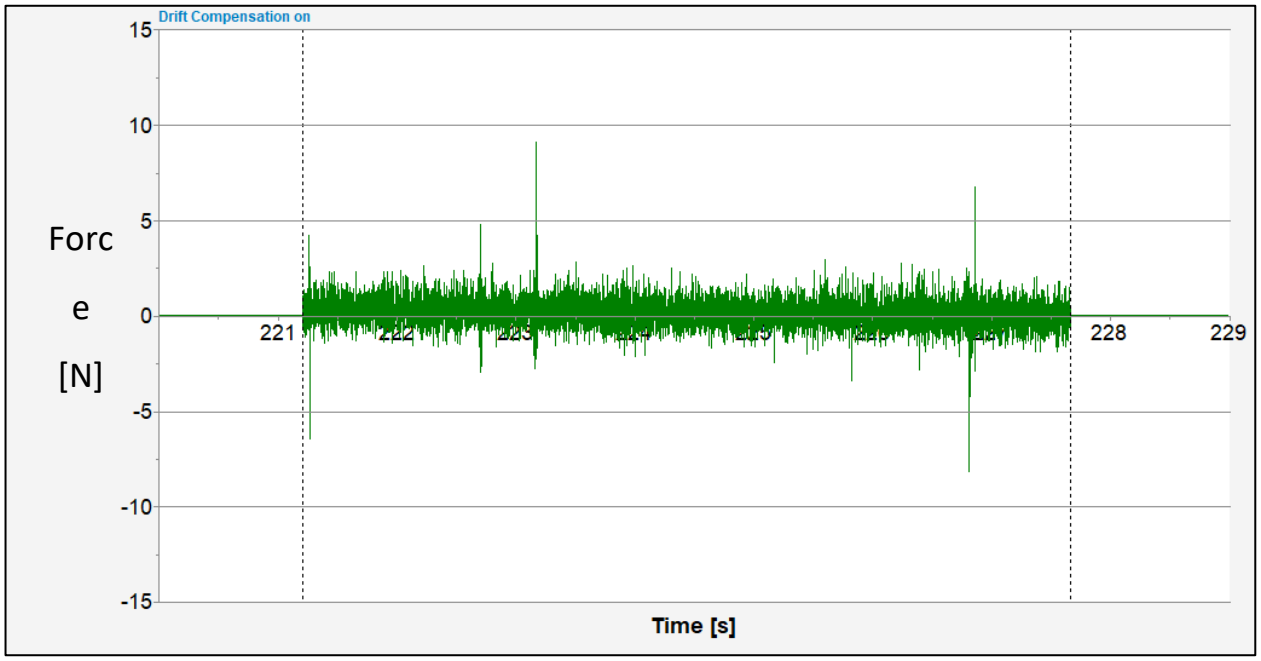


Figure A42 Cutting force signal of Al_2O_3 in Z axis F_Z **(UAG)**

Figures A43 to **A45** shows cutting forces signals from DynoWare when point grinding Si_3N_4 by UAG method

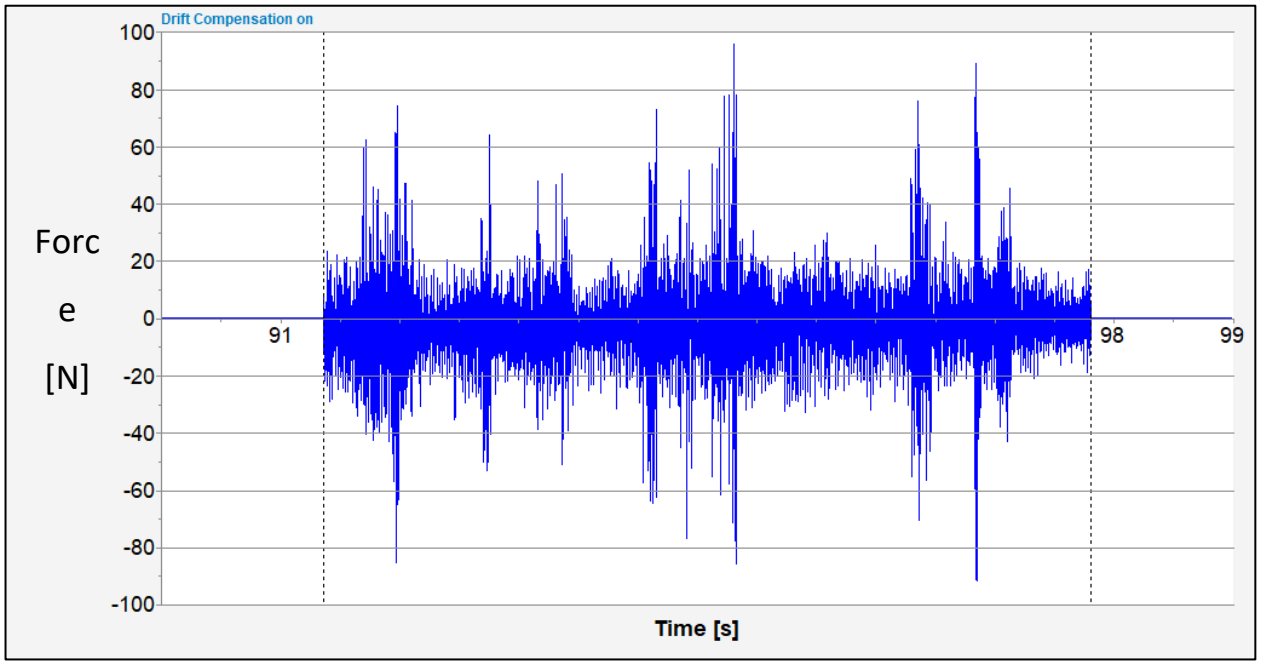


Figure A43 Cutting force signal of Si_3N_4 in X axis F_X **(UAG)**

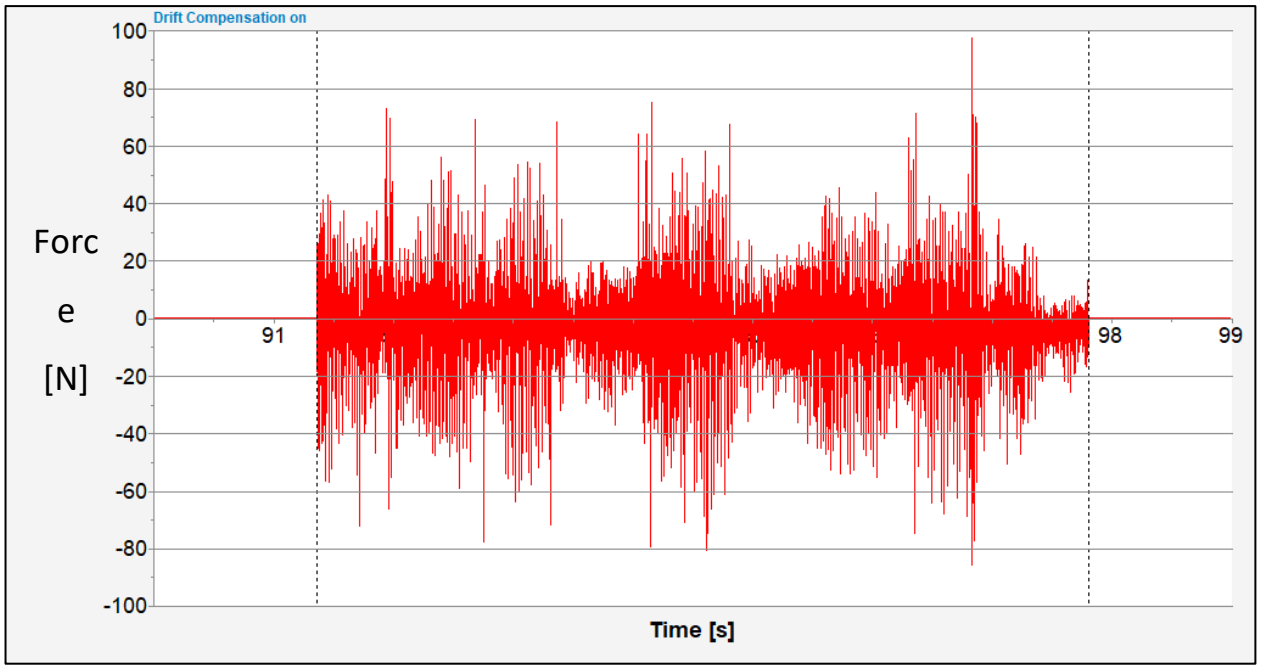


Figure A44 Cutting force signal of Si_3N_4 in Y axis F_Y **(UAG)**

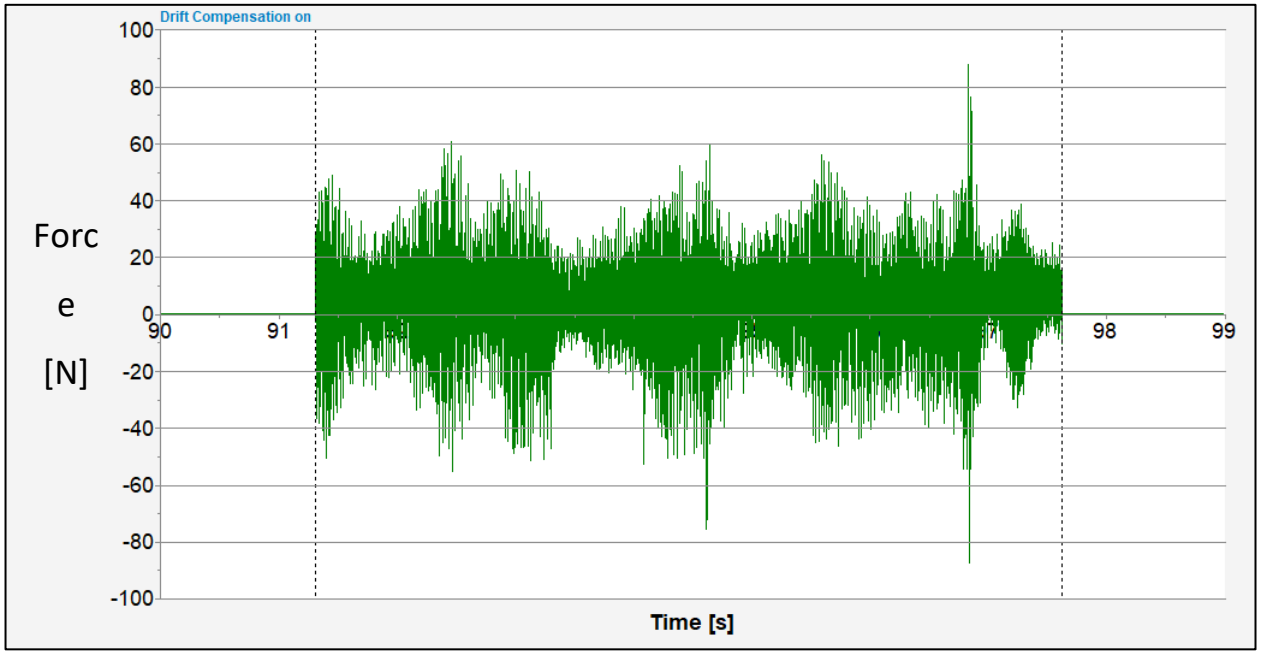


Figure A45 Cutting force signal of Si_3N_4 in Z axis F_Z **(UAG)**

Figures A46 to **A48** shows cutting forces signals from DynoWare when point grinding SiC by UAG method

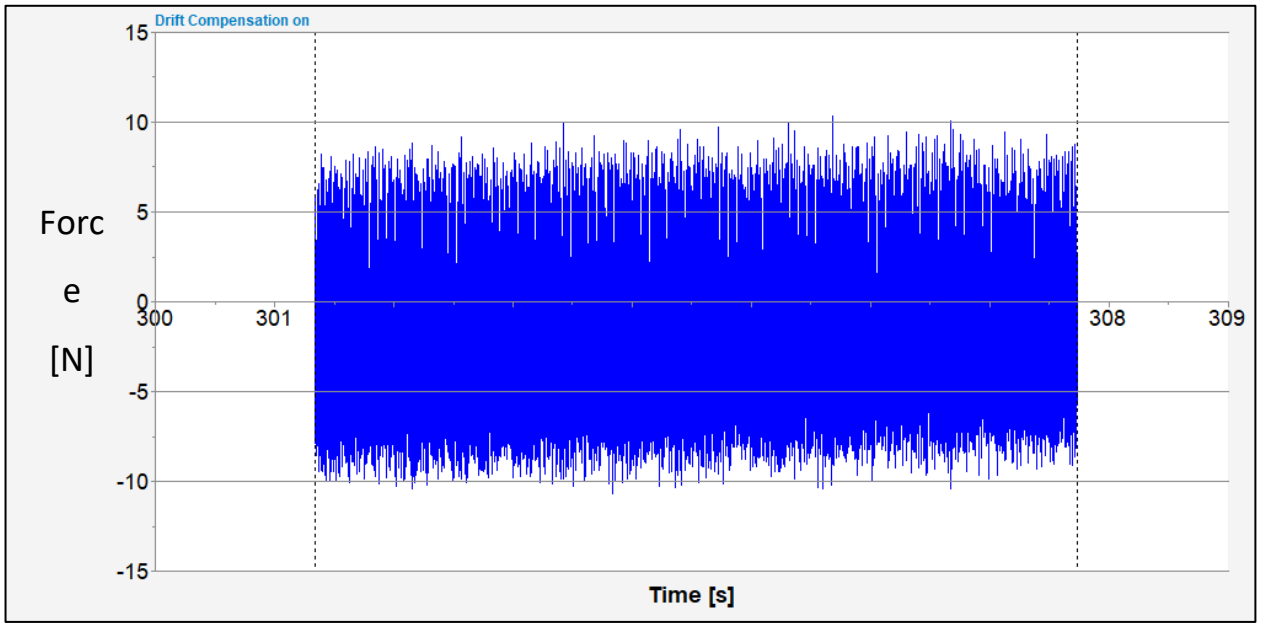


Figure A46 Cutting force signal of SiC in X axis F_X **(UAG)**

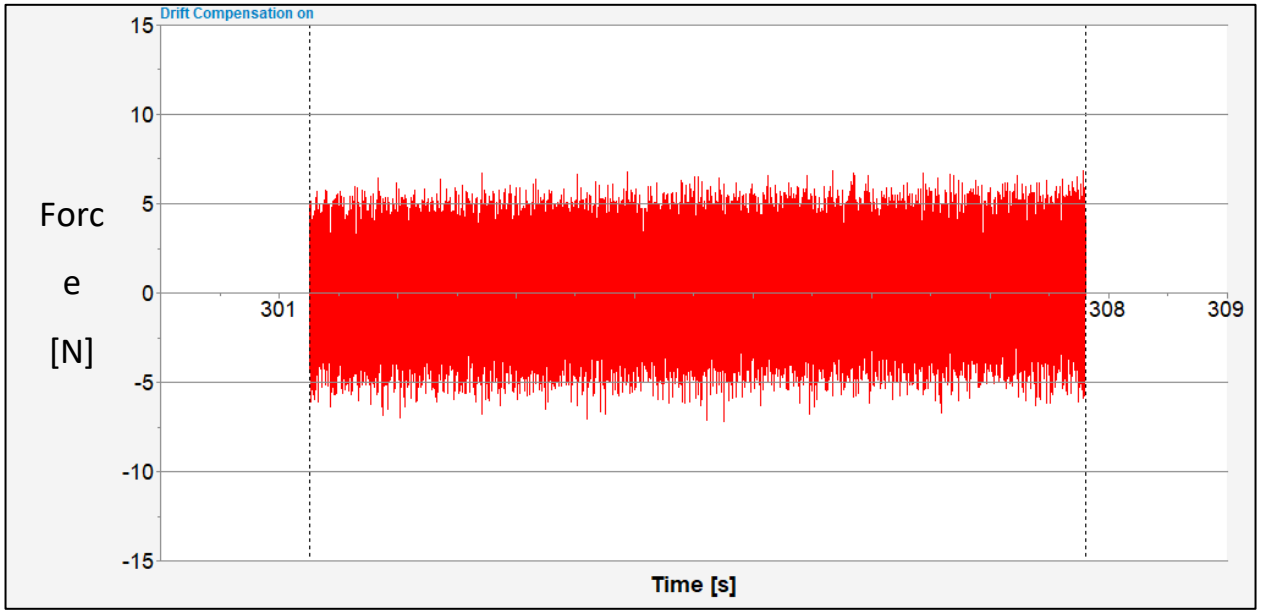


Figure A47 Cutting force signal of SiC in Y axis F_Y **(UAG)**

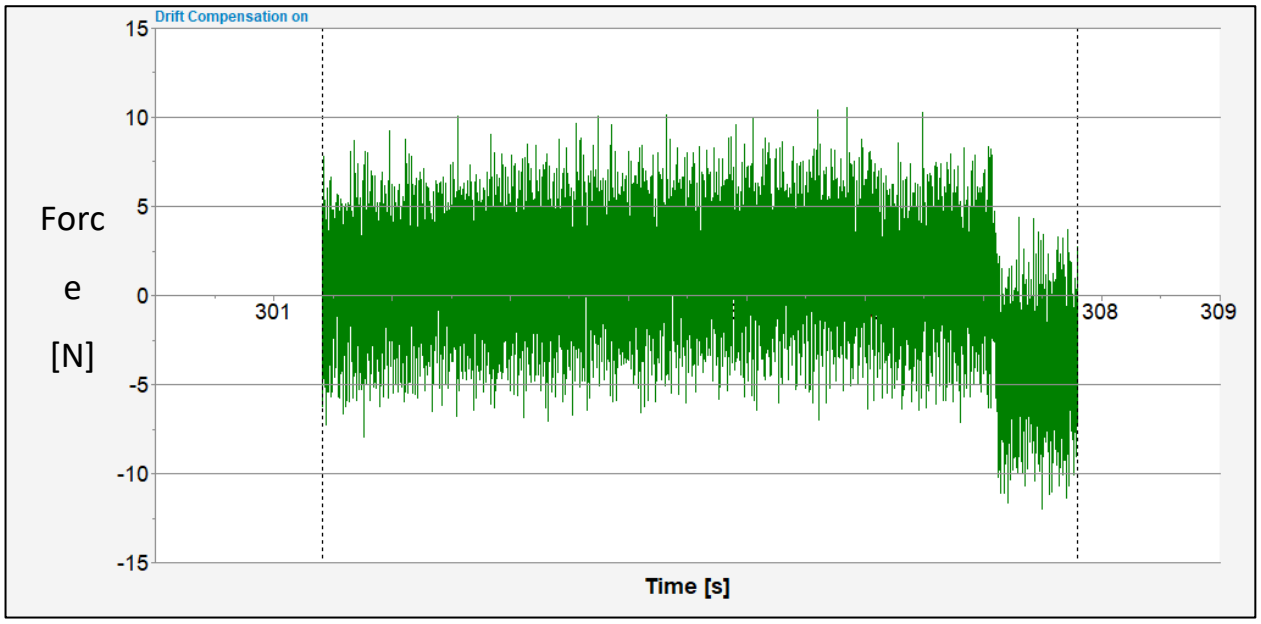


Figure A48 Cutting force signal of SiC in Z axis F_Z **(UAG)**